Contribution to System Level Modelling of Power Quality and EMC for Design of Aircraft Grids

Blazej Czerniewski

THÈSE

Pour obtenir le grade de

DOCTEUR DE L'UNIVERSITÉ GRENOBLE ALPES

préparée dans le cadre d'une cotutelle entre l'*Université Grenoble Alpes* et University of Nottingham

Spécialité : **Génie Electrique**

Arrêté ministériel : 25 mai 2016

Présentée par

Błażej CZERNIEWSKI

Thèse dirigée par **Jean-Luc Schanen, Professeur des universités, Université Grenoble Alpes** et codirigée par **Pericle Zanchetta, Professeur des universités, University of Nottingham**

préparée au sein des **Laboratoires G2ELab**

dans **les École Doctorale EEATS**

Contribution à la modélisation système pour la qualité de l'énergie et la CEM dans la conception des réseaux d'avions

Contribution to System Level Modelling of Power Quality and EMC for Design of Aircraft Grids

Thèse soutenue publiquement le **6 décembre 2022** devant le jury composé de :

M. Nicolas RETIERE
Professeur à l'Université Grenoble Alpes (G2Elab), Président du jury
M. Arnaud BREARD
Professeur à l'Ecole Centrale de Lyon, Rapporteur
M. Nicolas ROUX
Maitre de Conference à l'INP Toulouse, Rapporteur
M. Dave THOMAS
Professeur à University of Nottingham, Examinateur
M. Christian Klumpner
Maitre de Conference à University of Nottingham, Invité
M. Jean-luc SCHANEN
Professeur à l'Université Grenoble Alpes (G2Elab), Directeur de thèse
M. Pericle ZANCHETTA
Professeur à University of Nottingham, Co-directeur de thèse

Contribution to System Level Modelling of Power Quality and EMC for Design of Aircraft Grids

by Błażej Czerniewski, MSc

Thesis submitted to The University of Nottingham for the degree of Doctor of Philosophy, December 2022

Acknowledgements

At the beginning, I would like to thank my supervisors Prof. Zanchetta and Dr. Andrea Formentini for their guidance, help and support. Especially, I want to give my biggest thanks to Prof. Jean-Luc Schanen who gave me the opportunity to study as a PhD student. His expertise, engagement and faith allowed me to succeed in this part of academic journey.

I also address my thanks to the jury committee members: Prof. Nicolas Retiere, Prof. Arnaud Breard, Dr. Nicolas Roux and Prof. Dave Thomas who read carefully my work, proposed valuable improvements to the manuscript and made a very insightful discussion during the defence.

I would like to give my thanks to Prof. Laurent Gerbaud and Dr. Hervé Chazal for their valuable help and academic support which allowed me to proceed with my research.

I would also like to thank my colleagues from Électronique de Puissance team from G2ELab and Power Electronics, Machines and Control research group from University of Nottingham. It was a pleasure to work with you all during the years of my PhD.

Last but not least, I would love to express my biggest gratitude to my family and friends, especially my beloved wife Aleksandra and my dear friend Pawel for their constant support and believing in me. Without them, I would not be able to achieve this.

Contents

Introduction 1

I Design and Optimization of AC Aircraft Grid Harmonic Filters. 3

I.1 Research motivation. . . . 6

I.1.1 Role of the filters in a power electronics converter. . . . 6

I.1.2 Filters design challenges and issues. . . . 7

I.2 Description of the Study Case. . . . 8

I.2.1 Research objectives. . . . 8

I.2.2 AC grid description. . . . 8

I.2.3 Filters in the study case. . . . 10

I.2.4 Control system description. . . . 12

I.3 Aircraft standards requirements. . . . 17

I.3.1 Power quality requirements. . . . 17

I.3.2 Dynamic behaviour requirements. . . . 18

I.4 AC grid components interaction study. . . . 19

I.4.1 Matlab Simulink switching model. . . . 19

I.4.2 Interactions analysis. . . . 22

I.5 Control system simulation tool. . . . 25

I.5.1 Average model description. . . . 25

I.5.2 Simulation tool description. . . . 28

I.6 Experimental validation of the tool. . . . 30

I.6.1 Experimental rig description. . . . 30

I.6.2 Control system of the rig. . . . 32

I.6.3 Experimental tests. . . . 33

I.7 Area of Design definition. 37
I.8 Harmonic filters design optimization. 39
I.8.1 Optimization Algorithms. 39
I.8.1.1 Stochastic Optimization Methods. 40
I.8.1.2 Deterministic Optimization Methods. 41
I.8.2 Optimization Problem – reduction of the grid filters weight. 43
I.8.3 Weight dependent filters modelling. 44
I.8.3.1 Inductor model. 44
I.8.3.2 Capacitor model. 46
I.8.4 Frequency-domain grid model. 47
I.8.4.1 Grid THD frequency modelling description. 47
I.8.4.2 Model verification. 48
I.8.5 Optimization with THD constraints. 49
I.8.6 Optimization including dynamic requirements constraints. 50
I.8.6.1 Dynamic constraints definition. 50
I.8.6.2 Optimization results. 52
I.9 Conclusion. 54

II EMC Grid System Level Interaction Study and Modelling. 57
II.1 Research motivation 59
II.1.1 Electromagnetic Compatibility in Power Electronics. 59
II.1.2 EMI impact in Power Electronics grid. 61
II.2 Description of the study Case. 63
II.2.1 Research objectives. 63
II.2.2 The study case DC grid 64
II.2.3 Grid components description. 65
II.2.3.1 Boost converters. 65
II.2.3.2 EMI filters 66
II.2.3.3 Line Impedance Stabilization Network. 67
II.3 Aircraft standards EMC requirements. 68
II.3.1 Conducted EMI measurement according to DO-160. 68

II.3.2 Conducted EMI requirements according to DO-160. 69
II.4 Conducted EMI Grid Interactions Study. 71
II.4.1 Electromagnetic Interference modelling. 71
II.4.2 Electrical grid components modelling. 72
II.4.3 Time-domain simulation interactions study. 77
II.5 EMC Black Box modelling. 82
II.5.1 Terminated Black Box model description. 83
II.5.2 Blackbox model identification. 83
II.5.2.1 Model impedances identification. 84
II.5.2.2 Equivalent sources identification. 86
II.5.2.3 Black Box model identification based on simulation. 87
II.5.2.4 Black Box model identification based on experimental measurement. 93
II.5.3 Black Box model verification. 98
II.5.3.1 Simulation Black Box model validation. 100
II.5.3.2 Experimental Black Box model validation. 106
II.6 System level EMI modelling. 112
II.6.1 The study case grid Black Box modelling. 112
II.7 Conclusion. 115

General Conclusion **117**

Bibliography **127**

Abstract **129**

Résumé **140**

Annex A Control System Simulation Tool **151**

Annex B Harmonic Filters Optimization **157**

Annex C Computation of the Black Box model parameter **159**

Annex D Black Box model identification **161**

Annex E Frequency-domain circuit solver **169**

List of Figures

I.1 Harmonic content filtering. . . . 6

I.2 Standard design approach. . . . 7

I.3 Schematic of the study case AC aircraft grid. . . . 9

I.4 VSI control system. . . . 13

I.5 VSI PI controller loops. . . . 13

I.6 AFE control system. . . . 15

I.7 AFE PI controller loops. . . . 15

I.8 AFE control system based on PI controllers. . . . 15

I.9 THD requirements in AC grid. . . . 17

I.10 Envelope of normal AC voltage transient(top), DC voltage transient (bottom). [55] . . . 18

I.11 Simulink model of the VSI. . . . 19

I.12 Simulink control system of the VSI. . . . 20

I.13 Simulink model of the AFE. . . . 20

I.14 Simulink control system of the AFE. . . . 20

I.15 Simulink model of the study case grid. . . . 21

I.16 Output waveforms of the VSI converter. The maximum current ripple is around 20% as it was stated in a previous section. . . . 21

I.17 Output waveforms of the AFE converter. . . . 21

I.18 Step-load operation for dynamic behaviour study. . . . 22

I.19 Rescaled VSI dynamic behaviour requirements from *MIL704F* standard (AC grid). . . . 23

I.20 Rescaled AFE dynamic behaviour requirements from *MIL704F* standard (DC grid). . . . 23

I.21 Comparison of VSI and AFE output voltage response for a step load for different AFE input inductor values. Any other parameter is not changed. Red lines showing the dynamic requirements. 24
I.22 Small-signal circuit dq model of the VSI converter. 25
I.23 Small-signal circuit dq model of the AFE converter. 26
I.24 Example waveforms of the VSI average model run by simulation tool. 29
I.25 Example waveforms of the AFE average model run by simulation tool. . . . 29
I.26 Settling time and voltage undershoot in the VSI. 30
I.27 View of experimental test rig. 31
I.28 View of inductors and capacitors used in experiments. 32
I.29 FPGA PCB board view. [78] 32
I.30 Measurement board based on LEM sensors. 33
I.31 Transient waveforms acquired during the experiments for one set of the filters. L_{VSI}=260μH C_{VSI}=33μF L_{AFE}=630μH. 33
I.32 Comparison between simulation and experimental results of step-load response of the system. The passive components parameters are L_{VSI}=260μH C_{VSI}=33μF L_{AFE}=630μH. 34
I.33 Comparison between simulation and experimental results of step-load response of the system. The passive components parameters are L_{VSI}=260μH C_{VSI}=33μF L_{AFE}=345μH. 35
I.34 Comparison between simulation and experimental results of step-load response of the system. The passive components parameters are L_{VSI}=260μH C_{VSI}=33μF L_{AFE}=345μH. 35
I.35 Comparison between simulation and experimental results of step-load response of the system. The passive components parameters are L_{VSI}=260μH C_{VSI}=25μF L_{AFE}=345μH. 36
I.36 Decreasing amount of variables by elimination of non-physical ones. 37
I.37 Area of Design. Blue points indicates the design which meets the requirements, red which does not. 38
I.38 General classification of the optimization algorithms. 40
I.39 Outline of a genetic algorithm. 41

I.40 Example of gradient based algorithm solving methodology (gradient descent method). [37] . . . 42
I.41 View of optimization result from CADES software. . . . 44
I.42 Relation of Inductance versus Mass obtained from preliminary optimizations. 45
I.43 Relation of Capacitance versus Mass obtained from manufacturer datasheet. 46
I.44 Frequency-domain model of the grid. . . . 48
I.45 V_{VSI} voltage source both in time and frequency-domain. . . . 48
I.46 Verification of the frequency-domain grid model. . . . 49
I.47 Pole-Zero stability analysis of designed controller with optimized harmonic filters. Controllers bandwidths fi_{VSI}=1000Hz, fv_{VSI}=100Hz, fi_{AFE}=600Hz, fv_{AFE}=40Hz . . . 50
I.48 L_{VSI} design constraint. . . . 51
I.49 C_{VSI} design constraint. . . . 51
I.50 L_{AFE} design constraint. . . . 52
I.51 Simulation result with optimized filters. . . . 53
I.52 Optimized solutions in the Area of Design. . . . 54

II.1 Different EMI disturbances generated by a device. . . . 60
II.2 EMC disturbances present in grid including power electronics converters. . . 61
II.3 Study case DC grid. . . . 64
II.4 Boost converter schematic including the parasitic components. . . . 65
II.5 Schematic of the EMI filter used in the study case. . . . 66
II.6 Schematic of the LISN used in the study case. LISN parameters are the one used in DO160 standard. . . . 67
II.7 LISN impedance characteristic defined in DO-160 [34]. . . . 68
II.8 Typical conducted EMI setup defined in DO-160 [34]. . . . 69
II.9 Maximum conducted emission level for power lines defined in DO-160 [34]. . 70
II.10 One of the constructed boost converters. . . . 72
II.11 One of the constructed EMI filters. . . . 73
II.12 Input impedance characterization using an impedance analyser. . . . 74
II.13 Model of boost converter used in the work. . . . 75

II.14 Model of a cable used in the simulation. 75
II.15 Model of designed EMI filter including components parasitics. 76
II.16 Model of the LISN used in the study case based on DO160 standard. 76
II.17 Model of the DC grid which consist of DO160 LISN, cables, EMI Filter and a single boost converter. 77
II.18 Model of the DC grid which consist of DO160 LISN, cables, EMI Filter and three boost converters connected in parallel. 78
II.19 Comparison between triple emission from single converter grid versus emission from grid of parallel converters for I_1 and I_2 currents in frequency-domain. 80
II.20 Comparison between triple emission from single converter grid versus emission from grid of parallel converters for I_{CM} and I_{DM} currents in frequency-domain. 80
II.21 Various Black Box model topologies. On the left Norton based, on the right Hybrid. 83
II.22 The impedance measurement configurations allowing identify the impedances of the model. First is Z_{PG} with Plus and Ground connected, the second Z_{MG} with Minus and Ground connected and the last one Z_{PM} with Plus and Minus connected. 84
II.23 Reducing CM circulation in measurement circuit by shorting impedance measurement device to the ground. 86
II.24 Example of line currents measurement for Black Box model identification. . 86
II.25 Time-domain SPICE simulation model for line currents measurement. . . . 88
II.26 Obtained line currents FFT result. 88
II.27 AC Sweep simulation for model for Z_{PG} impedance measurement. 89
II.28 Measured Z_{PG} impedance with presented both module and phase shift. . . . 90
II.29 AC Sweep simulation for model for Z_{MG} impedance measurement. 90
II.30 Measured Z_{MG} impedance with presented both module and phase shift. . . 91
II.31 AC Sweep simulation for model for Z_{PM} impedance measurement. 91
II.32 Measured Z_{PM} impedance with presented both module and phase shift. . . 92
II.33 Comparison between Black Box model impedances Z_{21} and Z_{Z22} obtained from simulation identification. 92

II.34 Line currents measurement setup for Black Box model identification. 94
II.35 Line currents obtained from experimental measurement processed by FFT. . 94
II.36 View of impedance measurement procedure: on the left impedance measurement interface, impedance measurement setup on the right. 95
II.37 Measured Z_{PG} impedance with presented both module and phase shift. . . . 96
II.38 Measured Z_{MG} impedance with presented both module and phase shift. . . 96
II.39 Measured Z_{PM} impedance with presented both module and phase shift. . . 97
II.40 Comparison between Black Box model impedances Z_{21} and Z_{Z22} obtained from experimental identification. 97
II.41 Validation case "Asymmetrical grid". Minus to ground LISN's impedance is modified to 5Ω to create asymmetry in the grid. 98
II.42 Validation case "Minus to ground". High current asymmetry is introduced by shorting minus and ground terminals. 99
II.43 Validation case "EMI Filter". Significant change of line currents according to identification process due to high attenuation of the filter. 99
II.44 Time-domain model for validation Black Box model. Case "Asymmetrical grid". LISN has line-ground impedances unbalance to introduce assymetry. 100
II.45 Asymmetrical LISN. Changed resistor is marked blue. 101
II.46 Frequency-domain Black Box model circuit. Case "Asymmetrical grid". . . 101
II.47 Comparison between line current obtained by time-domain simulation with FFT – red coloured spectrum and line currents obtained by solving frequency-domain circuit with Black Box model representing EMI of the converter – black dots. Case "Asymmetrical grid". 102
II.48 Time-domain model for validation Black Box model. Case "Minus to ground". The connection impedance is marked blue. 102
II.49 Frequency-domain Black Box model circuit. Case "Minus to ground". . . . 103
II.50 Comparison between line current obtained by time-domain simulation with FFT – red coloured spectrum and line currents obtained by solving frequency-domain circuit with Black Box model representing EMI of the converter – black dots. Case "Minus to ground". 103
II.51 Time-domain model for validation Black Box model. Case "EMI Filter". . . 104

II.52 Frequency-domain Black Box model circuit. Case "EMI Filter". 104
II.53 Comparison between line current obtained by time-domain simulation with FFT – red coloured spectrum and line currents obtained by solving frequency-domain circuit with Black Box model representing EMI of the converter – black dots. Case "EMI Filter". 105
II.54 Experimental validation of the Black Box model."Asymmetrical grid" case with using CISPR 16 LISN. Changed minus to ground grid impedance can be seen in zoom. 107
II.55 Comparison between line current obtained by exepriments with FFT – red coloured spectrum and line currents obtained by solving frequency-domain circuit with Black Box model representing EMI of the converter – black dots. Case "Asymmetrical grid". 107
II.56 Experimental validation of the Black Box model."Minus to ground" case. Minus to ground connection on the converter side can be seen in zoom. . . . 108
II.57 Comparison between line current obtained by exepriments with FFT – red coloured spectrum and line currents obtained by solving frequency-domain circuit with Black Box model representing EMI of the converter – black dots. Case "Minus to ground". 109
II.58 Experimental validation of the Black Box model."EMI Filter" case. 110
II.59 Comparison between line current obtained by exepriments with FFT – red coloured spectrum and line currents obtained by solving frequency-domain circuit with Black Box model representing EMI of the converter – black dots. Case "EMI Filter". 110
II.60 Schematic view of a grid based on Black Box models. 112
II.61 Grid-level EMI modelling based on Black Box approach. Study case grid. . 113
II.62 Grid currents I_1 and I_2" in frequency domain. The comparison between time-domain simulation results and Black Box frequency-domain results. . . 114
II.63 Schematic of the study case AC aircraft grid. 130
II.64 Comparison of VSI and AFE output voltage response for a step load for different AFE input inductor values. Any other parameter is not changed. Red lines showing the dynamic requirements. 130

II.65 Small-signal circuit dq model of the VSI converter. 131
II.66 Small-signal circuit dq model of the AFE converter. 131
II.67 View of experimental test rig. 132
II.68 Comparison between simulation and experimental results of step-load response of the system. Example result with filter parameters L_{VSI}=260μH C_{VSI}=33μF L_{AFE}=630μH. 132
II.69 Area of Design. Blue points indicates the design which meets the requirements, red which does not. 133
II.70 Frequency-domain model of the grid. 133
II.71 Study case DC grid. 135
II.72 Comparison between triple emission from single converter grid versus emission from grid of parallel converters for I_{CM} and I_{DM} currents in frequency-domain. 136
II.73 Terminated Asymmetrical Black Box model. 136
II.74 Black Box model identification of the physical converter. 137
II.75 Frequency-domain Black Box model circuit. Case "Minus to ground". . . . 137
II.76 Comparison between line current obtained by time-domain simulation with FFT – red coloured spectrum and line currents obtained by solving frequency-domain circuit with Black Box model representing EMI of the converter – black dots. Case "Minus to ground". 138
II.77 Grid-level EMI modelling based on Black Box approach. Study case grid. . 138
II.78 Grid currents I_1 and I_2" in frequency domain. The comparison between time-domain simulation results and Black Box frequency-domain results. . . 139
II.79 Schéma de réseau de l'avion AC du cas d'étude. 141
II.80 Comparaison de la réponse de la tension de sortie du VSI et de l'AFE pour une charge échelonnée pour différentes valeurs d'inductance d'entrée de l'AFE. Aucun autre paramètre n'est modifié. Les lignes rouges montrent les exigences dynamiques. 141
II.81 Modèle dq du circuit à petits signaux du convertisseur VSI. 142
II.82 Modèle de circuit à petit signal dq du convertisseur AFE. 142
II.83 Vue du banc d'essai expérimental. 143

II.84 Comparaison entre les résultats de la simulation et les résultats expérimentaux de la réponse du système à la charge par paliers. Exemple de résultat avec le paramètre du filtre L_{VSI}=260μH C_{VSI}=33μF L_{AFE}=630μH. 143
II.85 Une aire de dimensionnement. Les points bleus indiquent la conception qui répond aux exigences, les rouges celle qui n'y répond pas. 144
II.86 Modèle de réseau dans le domaine de la fréquence. 144
II.87 Cas d'étude réseau DC. 146
II.88 Comparaison entre l'émission triple du réseau d'un seul convertisseur et l'émission du réseau de convertisseurs parallèles pour les courants I_{CM} et I_{DM} dans domaine de la fréquence. 147
II.89 Terminated Asymmetrical Black Box model. 148
II.90 Black Box model identification du convertisseur réel. 148
II.91 Circuit modèle Black Box dans le domaine de la fréquence. Cas "Minus to ground". 149
II.92 Comparaison entre le courant de ligne obtenu par simulation dans le domaine temporel avec FFT – spectre de couleur rouge et les courants de ligne obtenus par la résolution du circuit dans le domaine de la fréquence avec le modèle Black Box représentant l'interférence électromagnétique du convertisseur – points noirs. Cas "Minus to ground". 149
II.93 Modélisation des interférences électromagnétiques au niveau du réseau basée sur l'approche Black Box. Cas d'étude réseau. 150
II.94 Courants de réseau I_1 et I_2" dans le domaine des fréquences. La comparaison entre les résultats de la simulation dans le domaine temporel et les résultats de la Black Box dans le domaine des fréquences. 150

List of Tables

I.1 Nominal parameters of the converters. 10

I.2 Simulation tool input parameters. 28

I.3 Experimental setup parameters 31

I.4 Optimization results with THD constraints. 49

I.5 Comparison between the total filter mass. Before optimization, with THD constraints only and with all constraints. 52

II.1 Parameters of DO160 LISN. 67

II.2 Parameters of the boost converter including parasitics. 73

II.3 Parameters of the EMI filter. 74

II.4 Comparison between the total filter mass. Before optimization, with THD constraints only and with all constraints. 134

II.5 Comparaison entre la masse totale du filtre. Avant optimisation, avec les contraintes THD uniquement et avec toutes les contraintes. 145

Notations

AC – Alternate Current

AFE – Active Front End

AoD – Area of Design

BNC – Bayonet Nut Coupling

CADES – Component Architecture for Design of Engineering Systems

CM – Common Mode

CMC – Common Mode Chocke

DC – Direct Current

DM – Differential Mode

DSP – Digital Signal Processor

DUT – Device Under Test

EMC – Electromagnetic Compatibility

EMI – Electromagnetic Interference

EPC – Equivalent Parallel Capacitance

EPR – Equivalent Parallel Resistance

ESL – Equivalent Series Inductance

ESR – Equivalent Series Resistance

EUT – Equipment Under Test

FFT – Fast Fourier Transform

FPGA – Field Programmable Gate Array

GA – Genetic Algorithm

MEA – More Electric Aircraft

MOSFET – Metal-Oxide Semiconductor Field-Effect Transistor

MPF – Metallized Polypropylene Film

PCB – Printed Circuit Board

LISN – Line Impedance Stabilization Network

THD – Total Harmonic Distortion

PCB – Printed Circuit Board PWM – Pulse Width Modulation

PI Controller – Proportional Integral Controller

RMS – Root Mean Square

SMPS – Switching Mode Power Supply

SQP – Sequential Quadratic Programming

VSI – Voltage Source Inverter

Introduction

One of the main features of a modern world is a dynamic technology development. This results in a drastic growth of emission which is a cause of many environmental issues such as global warming [69, 22]. Current science including engineering constantly tries to variety of solutions to fight with the negative impact of technology on environment.

Among many industries aviation is one of the most pollutant fields. The origin of the pollution is a huge CO_2 emission of all air traffic [23]. The proposed solution of CO_2 reduction is an aircraft electrification. This approach can lead to significant decrease of the aircraft's mass which will result with a reduction of exploitation costs and therefore of CO_2 emission and its environmental impact. Moreover, current study show that having more electrified aircraft can lead to improvement of its distribution system reliability and efficiency. The major concept in engineering which deals with the aircraft electrification is More Electric Aircraft (MEA). The main goal is to replace conventional devices, which usually are powered by pneumatic, hydraulic or mechanical power sources, by electrical systems including power electronics converters [63].

When power electronic converter is designed all electrical parts such as power switches, passive components, printed circuit boards (PCB), cables etc... are chosen individually for a demanded power, current and voltage ratings. The control is often designed with a local perspective of the device but the interactions might occur in the global system. This is also true for EMI filters which are designed with individual LISNs to meet the standards, but which global behaviour in a full system is still unknown. When several converters are connected together some interactions might occur not only inside the single device but between many of them. This might be good phenomena (e.g. filter of the one device can partly another one) but in this case some converter's parts might be oversized. In some scenarios those interactions can lead to problems with converters malfunction or standard compliance. Therefore, it is necessary to identify, understand and if needed consider all

interactions in order to properly size multiple converters including all aspects. This thesis main focus is the analysis of those interactions and proposed solution of their consideration through global design and optimization approach.

The thesis is composed of two parts. Both of them describe the global design and optimization for aircraft application. The first part is focused on analysis of AC avionic grid interactions. The study case considers two typical aircraft converters connected to the AC grid – Voltage Source Inverter (VSI) and Active Front End (AFE). In this part the interactions between both converters are studied in terms of power quality and dynamic behaviour and their influence on the avionic standard compliance. Then, the global design of both converters' harmonic filters is performed. Finally, the optimization including both aspects is presented.

The second part is focused on the EMI interactions in the aircraft grid composed on several power electronic converters. The study case includes three Boost converters connected to a DC grid. This part contains analysis of occurring interactions between converters in terms of EMC. Afterwards, a specific EMC model for system level studies is introduced approach is introduced for lightweight EMI modelling. Finally, the grid-level EMC modelling including the lightweight so-called Black Box model is described.

Part I

Design and Optimization of AC Aircraft Grid Harmonic Filters.

Chapter Abstract

This part focuses on interactions of harmonics filters connected to the AC aircraft grid. At first interactions are identified and described for a given study case considering both aspects: power quality (harmonics) and control (dynamic response). Consequently the optimization constraints are defined in order to comply the dynamic and power quality aircraft standards. Finally a global design optimization is performed including filters of both converters and considering all constraints in order to obtain an optimal design.

Contents

I.1 Research motivation. . . . 6
I.1.1 Role of the filters in a power electronics converter. . . . 6
I.1.2 Filters design challenges and issues. . . . 7
I.2 Description of the Study Case. . . . 8
I.2.1 Research objectives. . . . 8
I.2.2 AC grid description. . . . 8
I.2.3 Filters in the study case. . . . 10
I.2.4 Control system description. . . . 12
I.3 Aircraft standards requirements. . . . 17
I.3.1 Power quality requirements. . . . 17
I.3.2 Dynamic behaviour requirements. . . . 18
I.4 AC grid components interaction study. . . . 19
I.4.1 Matlab Simulink switching model. . . . 19
I.4.2 Interactions analysis. . . . 22
I.5 Control system simulation tool. . . . 25
I.5.1 Average model description. . . . 25
I.5.2 Simulation tool description. . . . 28
I.6 Experimental validation of the tool. . . . 30
I.6.1 Experimental rig description. . . . 30
I.6.2 Control system of the rig. . . . 32
I.6.3 Experimental tests. . . . 33
I.7 Area of Design definition. . . . 37

I.8 Harmonic filters design optimization. 39
I.8.1 Optimization Algorithms. 39
I.8.2 Optimization Problem – reduction of the grid filters weight. 43
I.8.3 Weight dependent filters modelling. 44
I.8.4 Frequency-domain grid model. 47
I.8.5 Optimization with THD constraints. 49
I.8.6 Optimization including dynamic requirements constraints. 50
I.9 Conclusion. 54

I.1 Research motivation.

I.1.1 Role of the filters in a power electronics converter.

The switching phenomena, which is the basic principle of the converter's operation, generates a harmonic content. If the converter is connected to any device or a grid, the harmonic content might be transferred outside the converter and generate some drawbacks at grid level, such as additional losses, aging of cables and some devices, low frequency radiated emission etc. [27]. Therefore, the electrical power quality standards such as IEEE-519 define harmonic content limits which can be injected to the grid in order to prevent the grid disruptions. For AC grids limits are usually defined as Total Harmonic Distortion (THD) and its value should be below 5-15%. The THD definiton is a ratio of the all harmonic components and fundamental frequency voltage [65].

$$THD = \frac{\sqrt{\sum_{k=2}^{n} U_k^2}}{U_1} \tag{I.1}$$

Where:

– U_1 is a fundamental frequency rms voltage

– U_k is a k-th harmonic frequency rms voltage

The common practice to attenuate the harmonics generated by the converter and consequently respect the limits defined by standards is use of passive filters. They are an integral part of power electronics converter and play a significant role in the design process. They are usually play a major role of the converter's size and weight [75], especially the inductors due to their bulkiness.

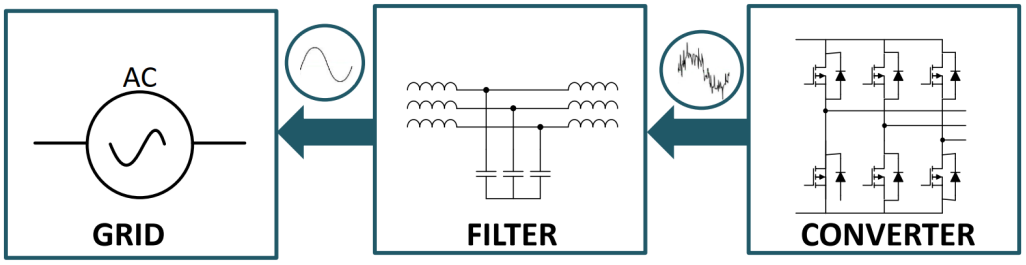

Figure I.1: Harmonic content filtering.

I.1.2 Filters design challenges and issues.

Nowadays, high expectations are placed for a modern power electronics converter, especially in the aircraft industry. Converters size and weight tends to be minimized while keeping high efficiency and standards compliance.

Harmonic filters, as an integral part of the converter, play a major role of its size and weight. Therefore, the common design practice, while optimizing the converter, is to reduce the filters, especially the inductors due to their bulkiness and relatively high cost [59, 62]. This is usually done by increasing converter's switching frequency. Nevertheless, this approach drastically increase switching losses and might generate additional electromagnetic interference (EMI) issues. Minimizing the filters can also cause some problems related to control system stability and the dynamic behaviour of the converter. Changing filter values can result with dynamic performance decrease which can lead to issues with standard compliance and in some extreme cases can cause control system instability [16].

The common approach is to design a converter in separate steps. Harmonic filters in order to attenuate the noise generated by converter and comply power quality standard, electromagnetic compatibility (EMC) filters depending on the disturbances generated by the whole converter (including harmonic filters since their parasitics have an influence on EMI) and finally control system based on all converters passive components and demanded voltage and current ratings. In reality all those aspects are connected and have influence on each other.

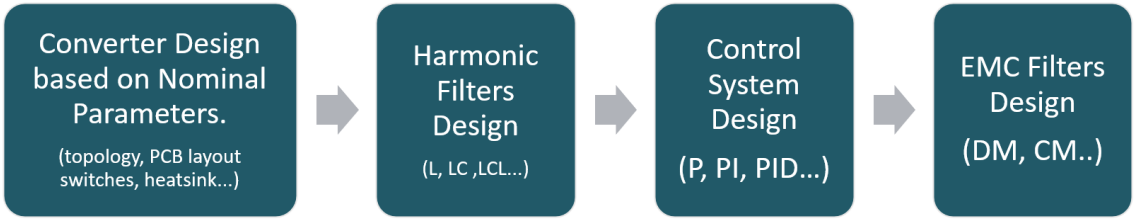

Figure I.2: Standard design approach.

The case is even more complex since in reality converters usually do not work standalone. They are often a part of a grid with several devices such as: other converters, electric motors, cables, non-linear loads. They might interact with each other which can be an advantage (filter of one device can attenuate noise of the other, for instance) but

also an origin of issues (e.g. noise injected to the grid by one device can cause malfunction on the others).

In order to have an optimal design which comply all standards is necessary to consider all design aspects together but also influence of another devices connected with the designed one.

I.2 Description of the Study Case.

I.2.1 Research objectives.

The goal of the conducted research is to study the interactions between power electronics converters considering two aspects: power quality, control and their influence on the design process of their harmonic filters. On the basis of obtained results optimization constraints considering interactions will be defined to optimally design the harmonic filters respecting the standards.

I.2.2 AC grid description.

The study case is a generic AC aircraft notional grid composed of two converters which are commonly used in aircraft applications – Active Front END (AFE) and Voltage Source Inverter (VSI). The VSI is supplied by DC voltage source and generates 115V ac rms 400 Hz output which are the standard parameters for an aircraft grid. The AFE is supplied by the AC grid generated by VSI. AFE generates 350V dc output voltage. The output is connected to a resistive load including the switch used for dynamic behaviour analysis (step load response). Both converters are controlled separately with Pulse Width Modulation (PWM) signals send to the gates of power switches which are modified thanks to PI controllers [48]. The switching frequency of both converters is constant and set to 20kHz. The control of both converters is realized as closed-loop systems. The modulation indexes are computed by controllers based on VSI output voltage and current and AFE input current and output voltage measurements. The filters are used in the two converters on both input and output sides. On the DC sides of both converters a DC link capacitor is placed. On AC side of the VSI there is LC filter and of the AFE an inductor (L) filter. The AC grid schematic is presented below in Fig. I.3. The values of the components used in the preliminary simulations are given in Table I.1.

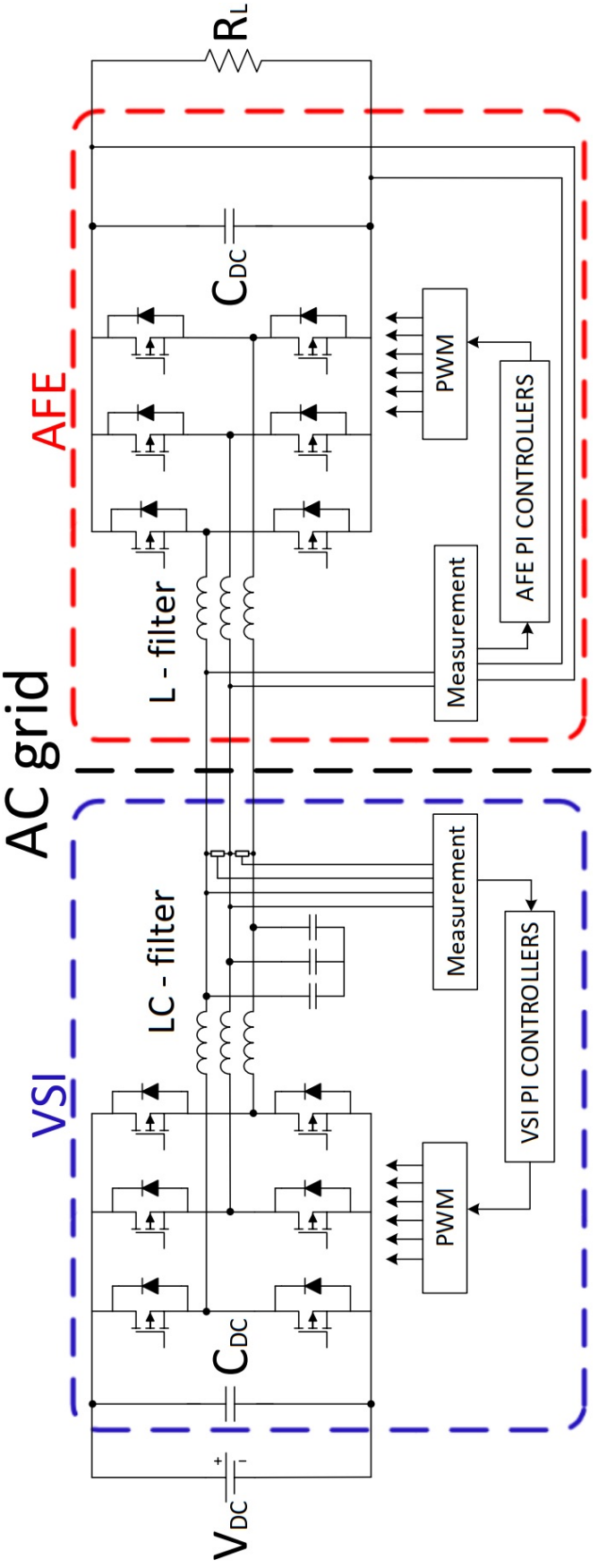

Figure I.3: Schematic of the study case AC aircraft grid.

Table I.1: Nominal parameters of the converters.

Parameters	Unit	VSI	AFE
Power P_N	[kW]	1.5	1.5
Input Voltage V_{in}	[V]	350 dc	115 ac rms
Output Voltage V_{out}	[V]	115 ac rms	350 dc
Switching Frequency f_{sw}	[kHz]	20	20
Nominal Frequency f_n	[Hz]	400	–
AC Filter Inductance L_{VSI} L_{AFE}	[µH]	260	630
AC Filter Capacitance C_{VSI}	[µF]	33	–
DC Filter Capacitance C_{DC}	[µF]	100	100

I.2.3 Filters in the study case.

Filters in the generic study case are used in both VSI and AFE converters and are connected to their inputs and output. The filters have been designed based to empiric engineering approach.

The DC side filters of both converters are DC link capacitors and their role is to limit the voltage ripple to meet aircraft standard requirements. Due to the fact that the DC link capacitor is not a direct part of the AC grid which is a main focus of the study and the interaction study (described in Section I.4.2) did not reveal any significant impact on the grid dynamic behaviour, the input DC capacitor of VSI is not under concern in the design process. The DC link capacitance of the AFE was computed based on the most dominant harmonic current approximation which has been taken from the switching model (described in I.4.1). The formula is given below [32].

$$C_{DC} = \frac{I_{mD}}{2\pi f_{sw} \Delta V_{DC}} = 10.6\mu F \tag{I.2}$$

Where:

– I_{mD} most dominant current harmonic

– f_{sw} converter switching frequency

– ΔV_{DC} maximum voltage ripple

According to Eq.I.2 in order to meet aircraft standard of maximum voltage ripple smaller than 5% the DC link capacitance C_{DC}=10.6μF, however, this value is too small

according to maximum current ripple of the capacitor. Therefore, significantly bigger filter has been chosen C_{DC}=100μF which is another limitation for designing this capacitor [19].

On the AC side which is the core of this study, the main role of the VSI output filter is to attenuate voltage harmonics originated from the inverter switching [12, 42]. The VSI output filter was designed in order to meet THD requirements defined by aircraft standard (max THD = 5%). The inductor itself has been designed in order to ensure maximum peak-to-peak current ripple 40% (expert engineering rule). The ripple current depends on the DC link voltage, inductance, and the switching frequency. The DC link voltage and switching frequency are constant, thus the inductance can be calculated from equation given below [4].

$$L_{VSI} = \frac{1}{8}\frac{V_{dc}}{\Delta I_{L_{VSI}} f_{sw}} = 296.5\mu H \tag{I.3}$$

Where:

– V_{dc} converter input voltage

– $\Delta I_{L_{VSI}}$ is inductor current maximum ripple

– f_{sw} converter switching frequency

Then, the LC filter capacitor has been chosen according to filter's cut-off frequency (Eq.I.4). The cut-off frequency should be above the fundamental one but not too high to be still able to attenuate all harmonics (at least one decade below the 20kHz switching frequency). The chosen cut-off frequency was 1.5kHz, however, there was no available actual capacitor for a given frequency. Thus, LC filter capacitor value which has been chosen is $C_{VSI} = 33\mu F$ for a cut-off frequency computed in the equation below.

$$f_c = \frac{1}{2\pi\sqrt{L_{VSI}C_{VSI}}} = 1.609kHz \tag{I.4}$$

Fundamental frequency $f_n = 400Hz$, thus LC filter cut-off frequency was set to value which ensure sufficient attenuation of the converter's harmonics and therefore standard compliance.

The input filter of the AFE is a series inductor. The filter role is to prevent AFE switching harmonics to be injected in the AC grid. The filter is designed to reduce input current ripple and therefore minimize harmonic content in the AC grid [44]. The filter inductance was computed based on maximum current ripple which was assumed as 20% [36]. This rule of thumb also allows limiting the losses in the inductor.

$$L_{AFE} = \frac{V_{in}}{\sqrt{6} f_{sw} \Delta I_L} = 636.3 \mu H \tag{I.5}$$

Where:

– V_{in} converter input voltage

– ΔI_L AFE inductor maximum current ripple

– f_{sw} converter switching frequency

I.2.4 Control system description.

The control system has been designed separately for each converter. Both converters' control is realized with PI Controllers based dq-frames decomposition [77].

The VSI has a closed-loop control system based on output values measurements. The controller send PWM signal to power switches which control the VSI output parameters. The system schematic is presented in Fig.I.4 and Fig.I.5. The measured output voltage (V_{ab},V_{bc}) and current (I_a,I_b) are transformed to the dq-frames which are inputs of two control loops. The loops control the VSI output voltage and current through PI controllers. The VSI output voltage reference in d-frame is set to converter nominal value V_{cd}=115V rms, whereas V_{cq} is set to 0 in order to keep unity power factor. The control loops outputs are modulation indexes (m_d and m_q) which are changed to abc frame again and control PWM signal of the converter's switches.

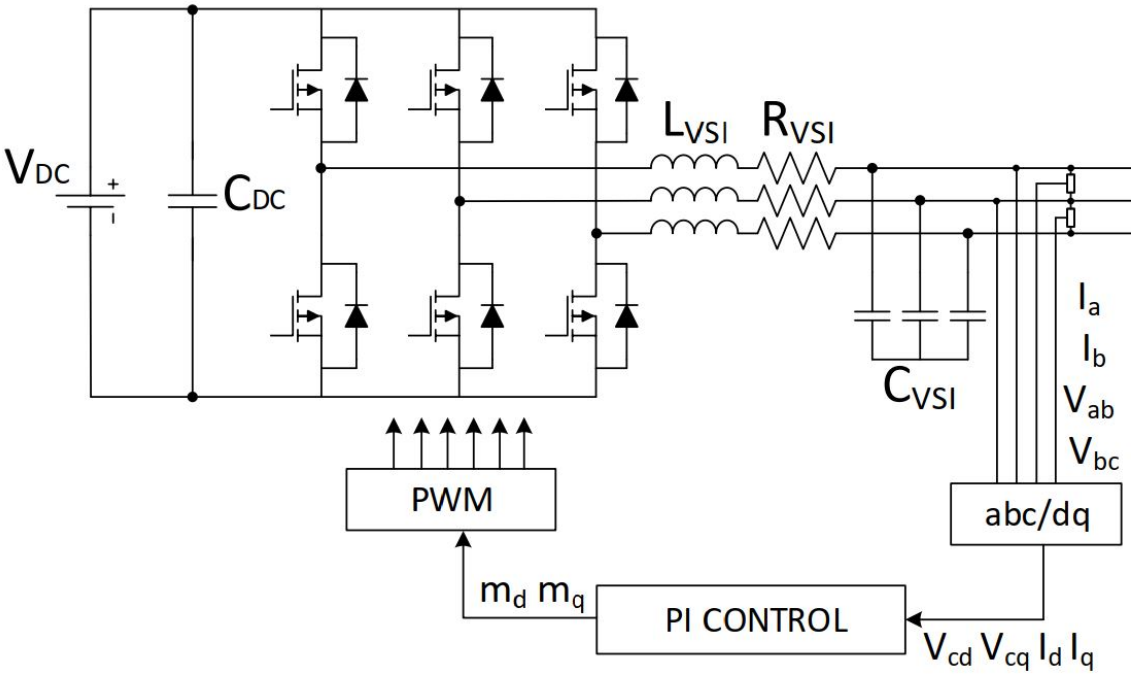

Figure I.4: VSI control system.

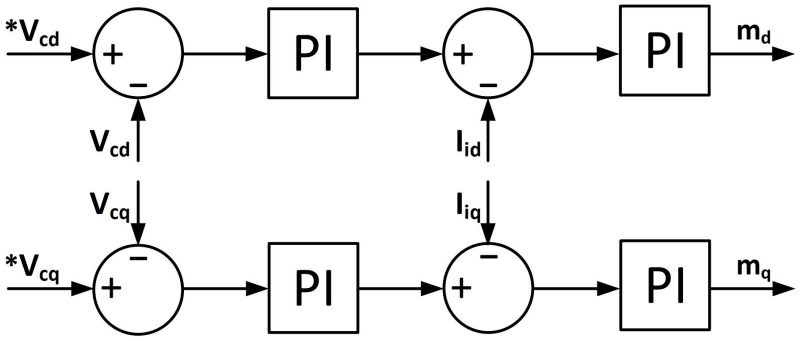

Figure I.5: VSI PI controller loops.

The PI voltage and current control gains are computed based controlled system transfer function. The computation of the PI gains is presented below (Eq. I.6).

$$\begin{aligned} K_{pv_{VSI}} &= 2\zeta C_{VSI} f_{v_{VSI}} 2\pi \\ K_{iv_{VSI}} &= C_{VSI} (f_{v_{VSI}} 2\pi)^2 \\ K_{pi_{VSI}} &= 2\zeta L_{VSI} f_{i_{VSI}} 2\pi - R_{VSI} \\ K_{ii_{VSI}} &= L_{VSI} (f_{i_{VSI}} 2\pi)^2 \end{aligned} \tag{I.6}$$

Where:

– $K_{pv_{VSI}}$, $K_{iv_{VSI}}$ proportional and integral gains of the VSI voltage loop

– $K_{pi_{VSI}}$, $K_{ii_{VSI}}$ proportional and integral gains of the VSI current loop

– L_{VSI} LC filter inductance

– R_{VSI} inductor parasitic resistance

– C_{VSI} LC filter capacitance

– $f_{v_{VSI}}$, $f_{i_{VSI}}$ VSI PI controllers bandwidths of VSI current and voltage loops

– ζ damping factor

The controllers bandwidths ($f_{v_{VSI}}$, $f_{i_{VSI}}$) are set in a way to comply the dynamic requirements dictated by aircraft standards (which will be introduced in next Section I.3) – decently fast controller to pass settling time requirement and reasonable voltage undershoot to pass overshoot/undershoot requirement. The damping factor was arbitrary set to unity.

The AFE has a closed-loop control based on the measurement of the input current and output voltage. The control system schematic is presented in Fig.I.2.4. The measured output voltage (V_{dca}) and input current (I_a,I_b) are transformed to the dq-frames which are inputs of two control loops. Similarly to the VSI control system, the loops controlling the AFE output voltage and input current with PI controllers.

The AFE output voltage reference is set to converter nominal value V_{dca}=350V, whereas I_{aq} is set to 0 in order to keep unity power factor. The control loops outputs are modulation indexes (p_d and p_q) which are transferred to abc-frame and modify PWM signal of the converter's switches.

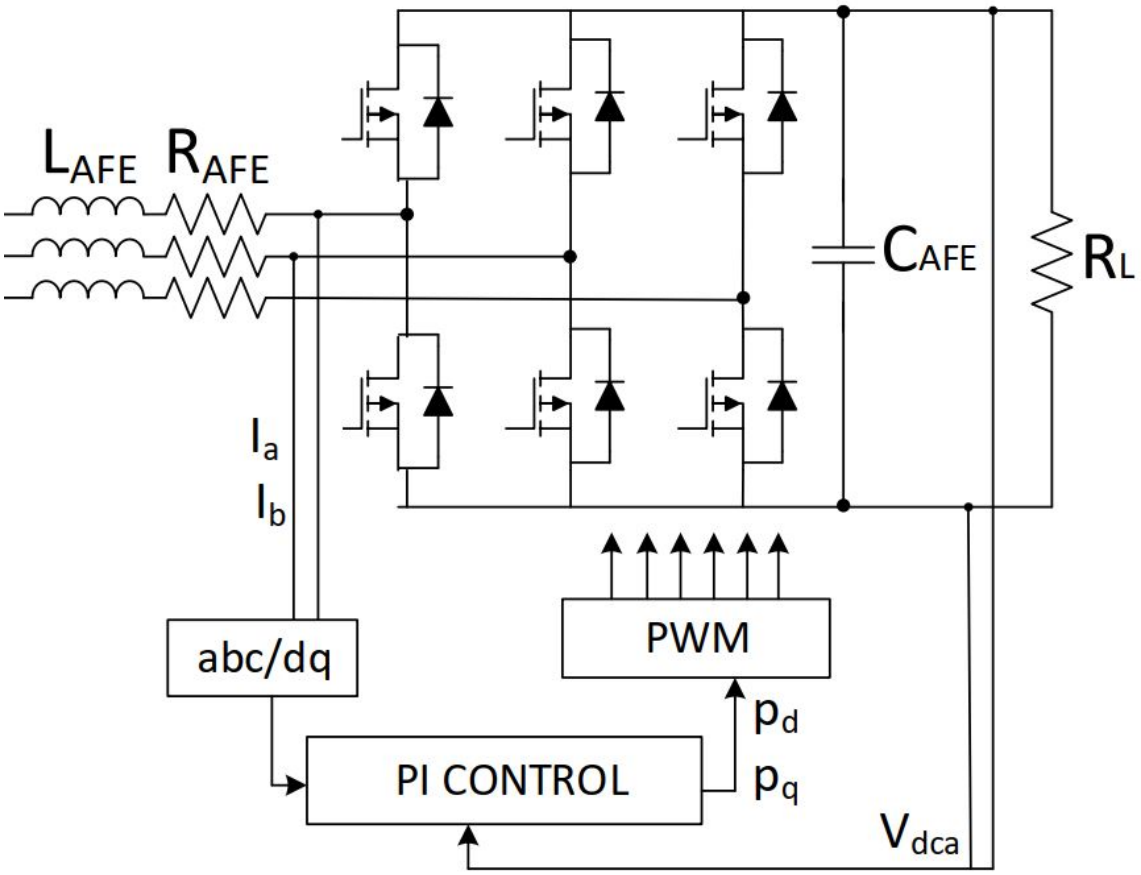

Figure I.6: AFE control system.

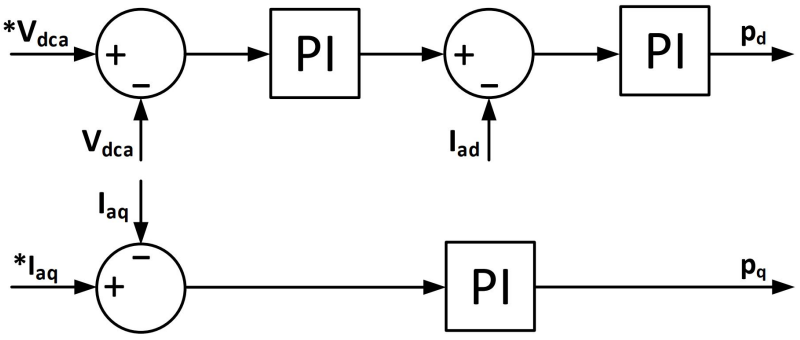

Figure I.7: AFE PI controller loops.

Figure I.8: AFE control system based on PI controllers.

The AFE PI controllers gains are computed on the basis of the system transfer function. The PI voltage and current control gains are computed as follows (Eq. I.7).

$$\begin{aligned} K_{pv_{AFE}} &= 2\zeta C_{AFE} f_{v_{AFE}} 2\pi \\ K_{iv_{AFE}} &= C_{AFE}(f_{v_{AFE}} 2\pi)^2 \\ K_{pi_{AFE}} &= -2\zeta L_{AFE} f_{i_{AFE}} 2\pi - R_a \\ K_{ii_{AFE}} &= -L_{AFE}(f_{i_{AFE}} 2\pi)^2 \end{aligned} \tag{I.7}$$

Where:

– $K_{pv_{AFE}}$, $K_{iv_{AFE}}$ proportional and integral gains of the AFE voltage loop

– $K_{pi_{AFE}}$, $K_{ii_{AFE}}$ proportional and integral gains of the AFE current loop

– L_{AFE} AFE input filter

– R_{AFE} input filter parasitic resistance

– C_{AFE} output DC filter capacitance of the AFE

– $f_{v_{AFE}}$, $f_{i_{AFE}}$ AFE PI controllers bandwidths

Similarly to VSI control, the bandwidths are set in order to comply dynamic behaviour requirements of the aircraft standard and damping factor is set to unity.

I.3 Aircraft standards requirements.

There are two aircraft standards which have been taken into consideration. The first one is *RTCA DO-160 Environmental Condition and Test Procedures for Airborne Equipment* is a civil standard. It considers not only the electrical aspects of the equipment but also another aspects such as Humidity, Icing resistance, Flammability etc. The second standard is *MIL-STD-704F Aircraft Electric Power Characteristics and Utilization.* This is a military standard which focuses just on the aircraft electricity. The standard chosen for the analysis is *MIL-STD-704F* due to the fact that it is more strict that then civil one. The requirements which are necessary to design the grid filters are power quality and dynamic behaviour requirements.

I.3.1 Power quality requirements.

Power quality requirements play a major role in harmonic filters design. The filters should be designed in a way to sufficiently attenuate harmonic content injected to the grid. *RTCA DO-160* requirement of grid voltage THD is 8%-12% depending of the equipment category [34]. However, the military standard limitation is more strict and therefore was chosen in the analysis. The requirement for AC grid with frequency of 400 Hz is maximum voltage THD=5%.

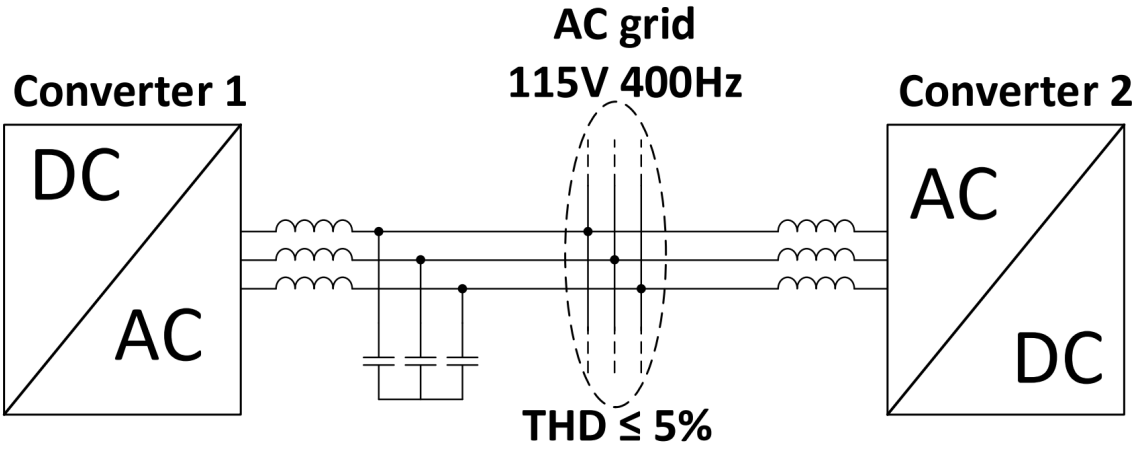

Figure I.9: THD requirements in AC grid.

I.3.2 Dynamic behaviour requirements.

Dynamic behaviour requirements are defined for transient situations in the grid. They usually occurs as a result of normal disturbances such as electric load change or engine speed change. A transient may also occur as a result of a momentary power interruption or an abnormal disturbance such as fault clearing [55]. The requirements chosen for analysis are defined by *MIL-STD-704F* standard. The limits consider voltage overshoot/undershoot and settling time. They are shown in figures below (I.10) for both AC and DC grids.

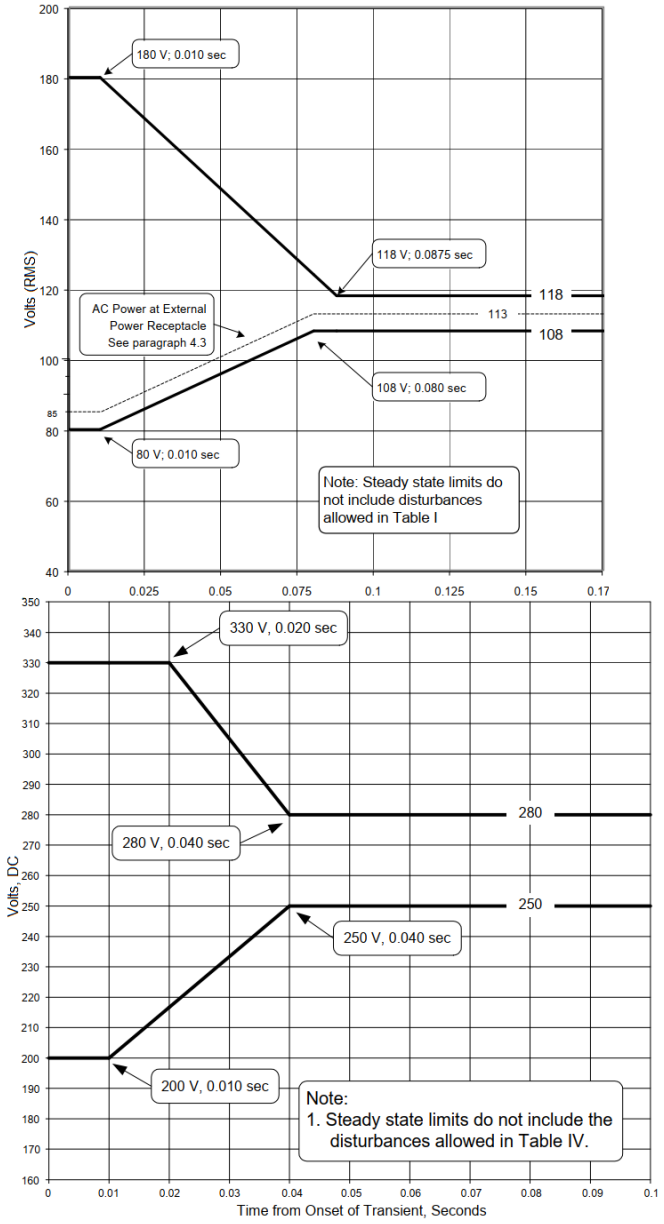

Figure I.10: Envelope of normal AC voltage transient(top), DC voltage transient (bottom). [55]

I.4 AC grid components interaction study.

The first step in the analysis was to find what are the interactions in the AC grid and their influence on power quality and control system performance. In order to do that the switching simulation model has been created in Matlab Simulink environment.

I.4.1 Matlab Simulink switching model.

The switching model composed of the VSI, AFE converters connected together. Moreover, the control system is also included to the model. Detailed description of the grid was presented in a chapter I.2. The switching models of VSI and AFE converters with their control system and converters' output waveforms are presented below. The waveforms present the loaded system in steady state.

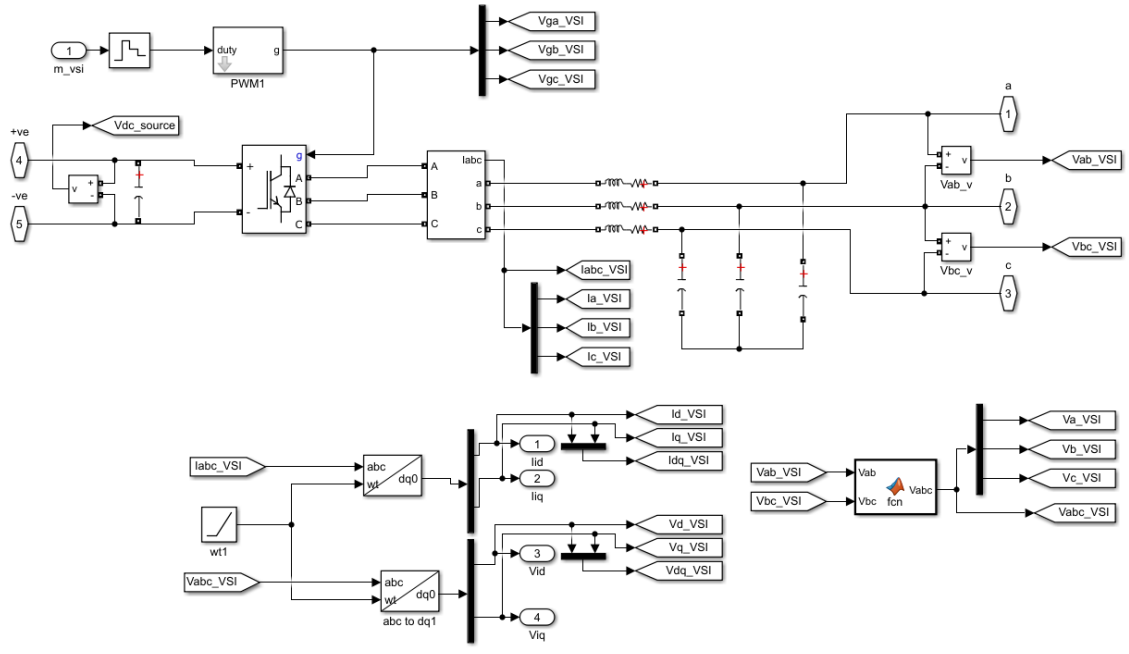

Figure I.11: Simulink model of the VSI.

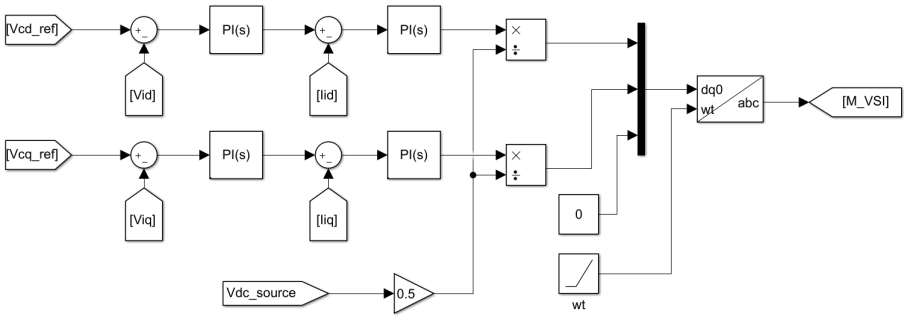

Figure I.12: Simulink control system of the VSI.

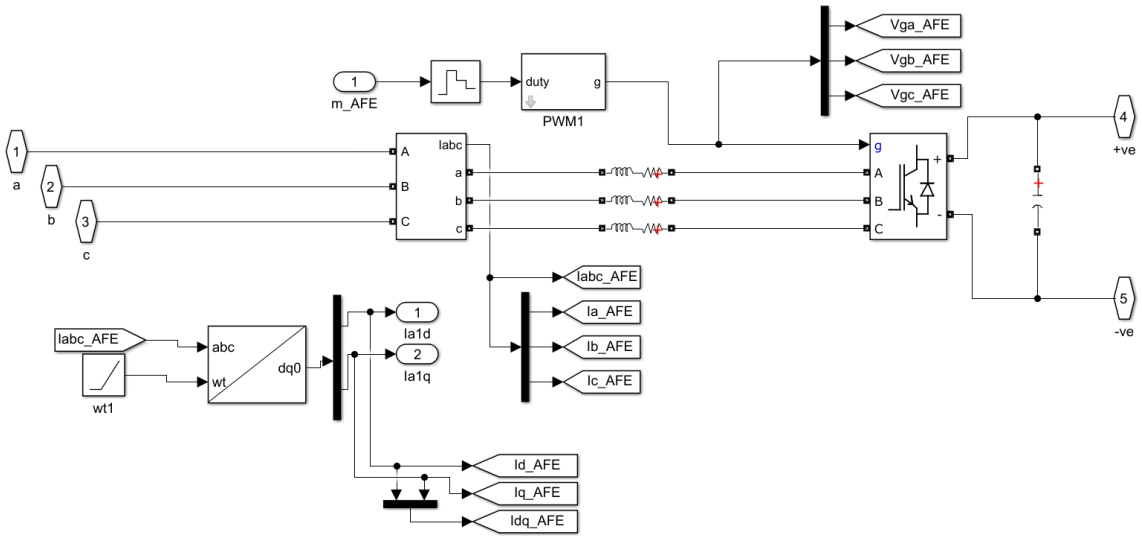

Figure I.13: Simulink model of the AFE.

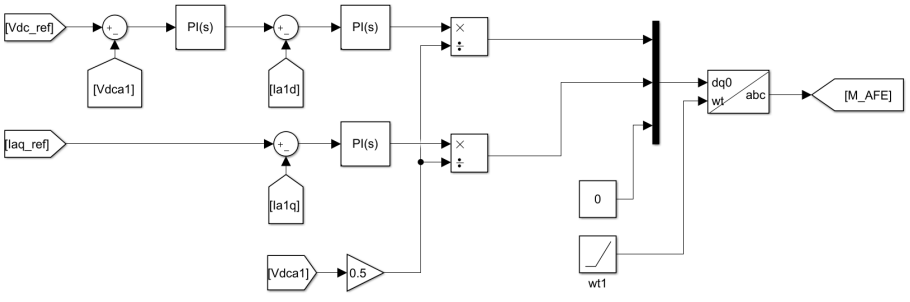

Figure I.14: Simulink control system of the AFE.

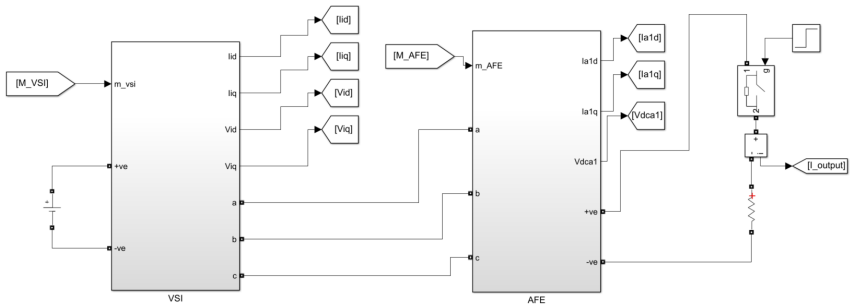

Figure I.15: Simulink model of the study case grid.

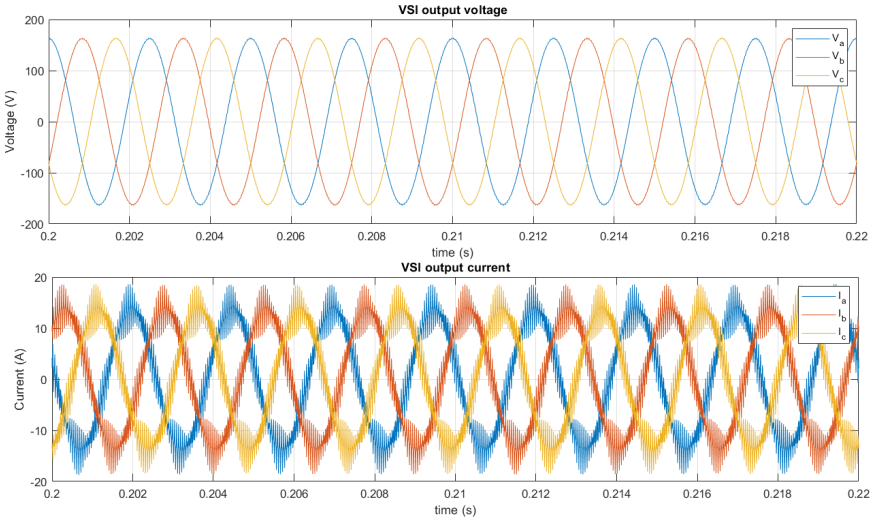

Figure I.16: Output waveforms of the VSI converter. The maximum current ripple is around 20% as it was stated in a previous section.

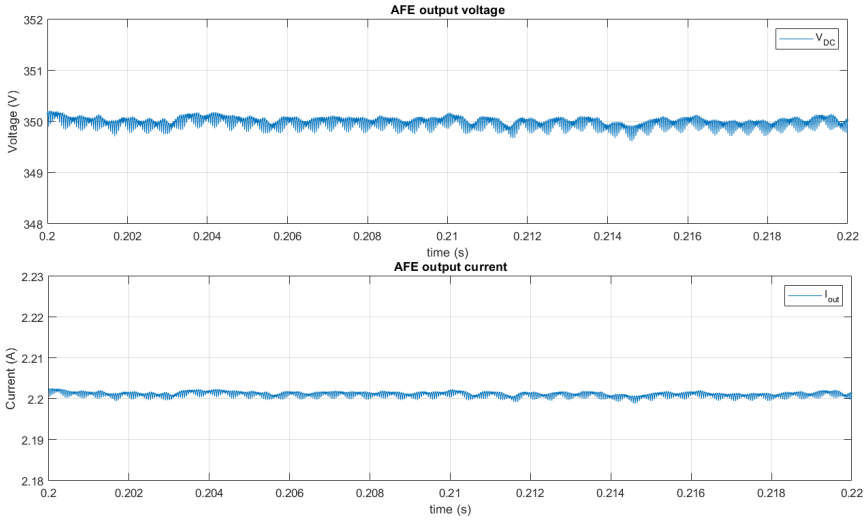

Figure I.17: Output waveforms of the AFE converter.

I.4.2 Interactions analysis.

In order to check the grid components influence on the system dynamic behaviour the step-load response of the system has been check for various values of the converter's filters without changing the control parameters (bandwidths). The resistive load $R_L = 86\Omega$ was connected to the AFE output at time $t_s = 0.5s$. The control system response was compared with dynamic requirements from *MIL704F* standard.

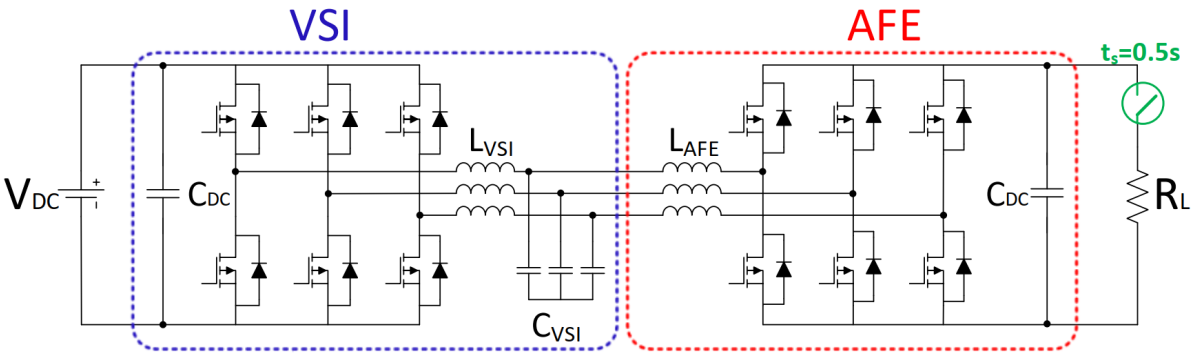

Figure I.18: Step-load operation for dynamic behaviour study.

The dynamic requirements defined in the standard have been rescaled for the study case analysis purpose. The AC voltage have been rescaled from 115V to 162.63V to have the requirement for peak value instead of RMS. It has been done since the average model which will be described in the next chapter gives peak value of the output voltage. The VSI output voltage was transformed to dq-frame in order to better present its dynamic behaviour and then compared with the standard. The DC voltage requirement have been rescaled from 270V to 350V to have the requirement for nominal output voltage value of the AFE. However, the shape of both requirements remains the same to the ones from the standard. The rescaled requirements with VSI, AFE examples is presented below (Fig.I.19 and Fig.I.20). Red lines presenting the rescaled requirements and blue lines the step-load response of VSI and AFE accordingly.

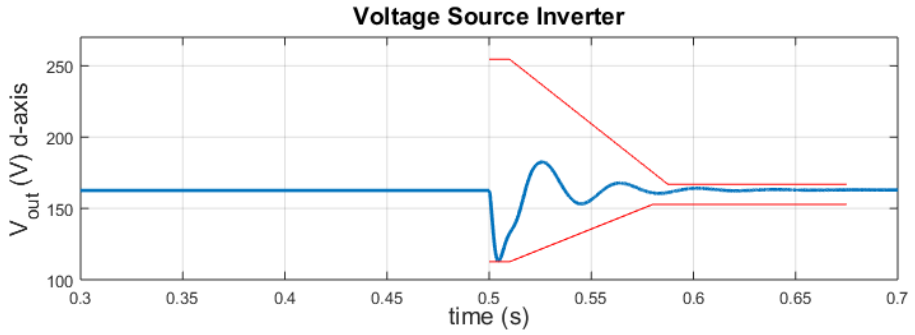

Figure I.19: Rescaled VSI dynamic behaviour requirements from *MIL704F* standard (AC grid).

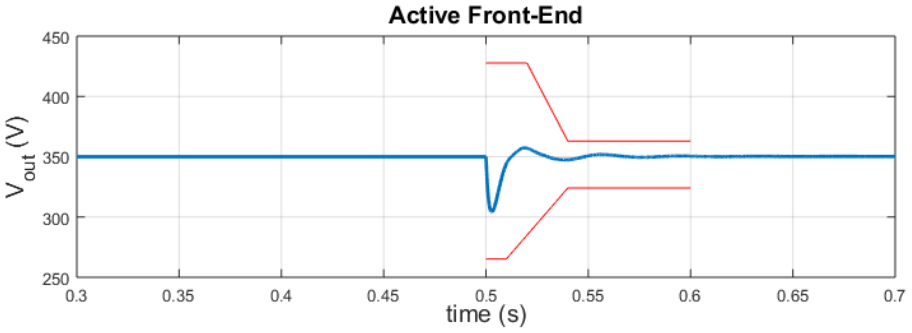

Figure I.20: Rescaled AFE dynamic behaviour requirements from *MIL704F* standard (DC grid).

Various simulations with changing the grid parameters showed that the most impactful parameters of the grid on the dynamic behaviour of the system are LC filter of the VSI and L filter of the AFE, so the AC grid harmonic filters. Reducing their values decreases the control performance of both systems. The simulation study revealed that there is an interaction between harmonic filters and dynamic behaviour of the control system. The interaction occur not in each converter separately but between both of them. Manipulation of the VSI LC filter affects the AFE output voltage step load response as well as changing AFE input filter values affect VSI output voltage response. Example results are presented in Fig.I.21. The step load response of the VSI AC output and AFE DC output voltages for different values of AFE input filter. The VSI output voltage is modified without changing any parameters of this converter. Fig.I.21 shows that for significantly small values of the L filter both VSI and AFE converter's response do not meet the requirements. There is a similar effect with manipulation of LC filter values.

For very small values of LC filter capacitor it was not possible to find any solution meeting the dynamic requirements even with manipulation of the PI controllers bandwidths.

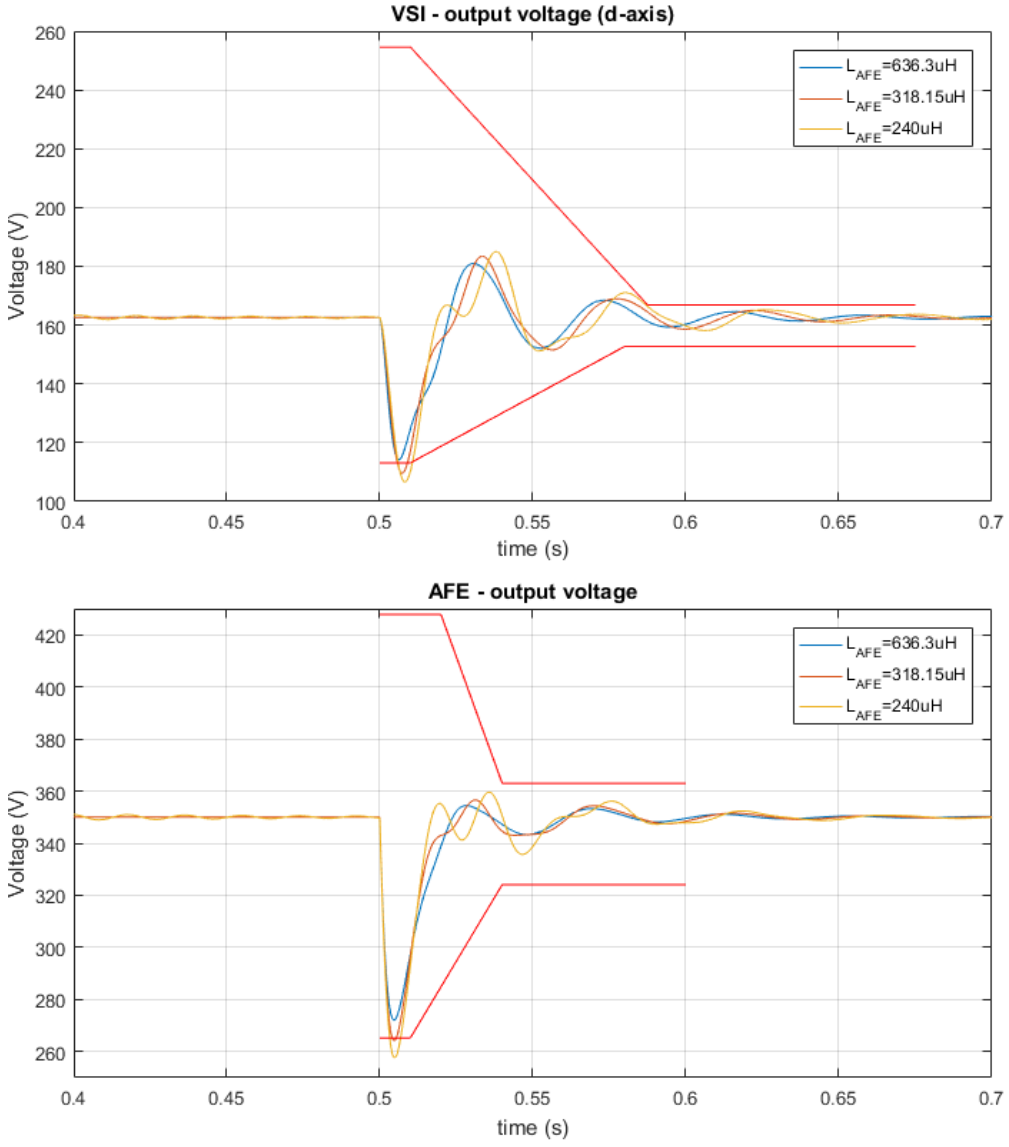

Figure I.21: Comparison of VSI and AFE output voltage response for a step load for different AFE input inductor values. Any other parameter is not changed. Red lines showing the dynamic requirements.

The focus of the study was on the parameters of the AC grid where the interactions occur (LC VSI filter and L AFE filter), therefore, DC capacitors on the DC grids were kept constant.

I.5 Control system simulation tool.

The preliminary analysis revealed that the interactions occur between several elements of the grid. Moreover, the dynamic response also depends of the controllers bandwidth. This results in numerous possible cases. Conventional simulation method which has been used in preliminary analysis is time consuming and needs a lot of computational power and thus it is not viable for further study. Moreover, mathematical description of the electrical system including the control would be incredibly complex task since due to high order of the system [13]. Therefore, the dedicated simulation tool, based on small-signal average modelling approach, was created.

I.5.1 Average model description.

The small-signal average model of both VSI and AFE which was obtained thanks to linearization of the system in the specified operating point (nominal parameters) [33]. The system is represented in dq-frame as a form of two coupled DC systems for VSI converter and another two for AFE converter. The dq-frame models are presented below in Fig.I.22 and Fig.I.23.

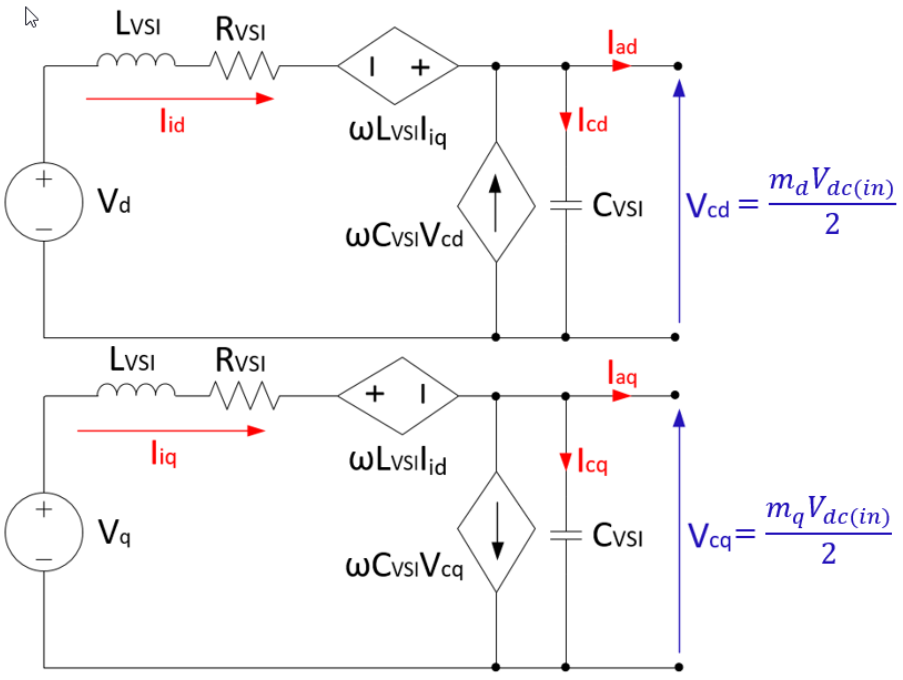

Figure I.22: Small-signal circuit dq model of the VSI converter.

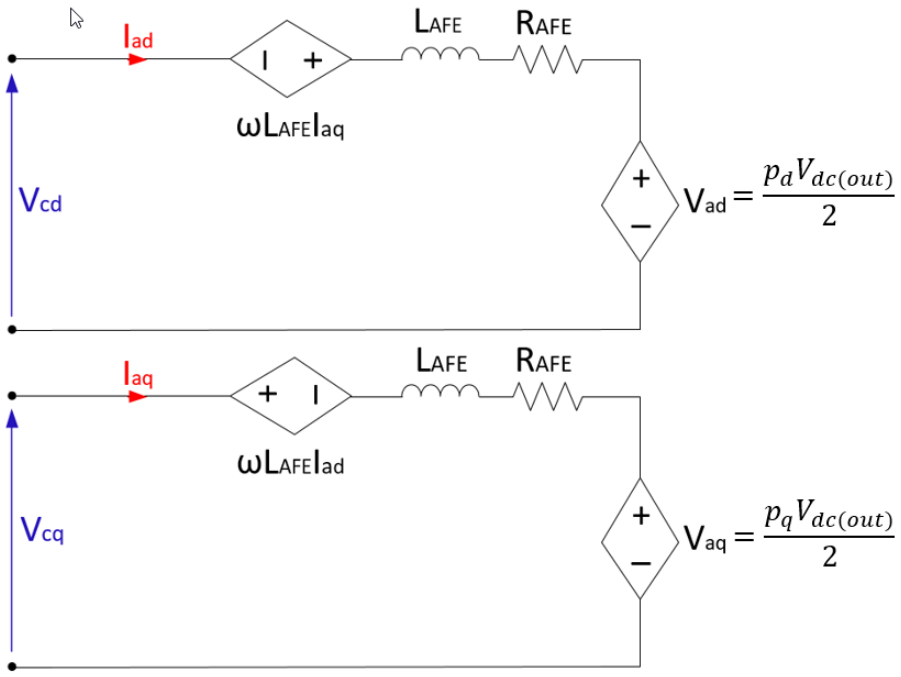

Figure I.23: Small-signal circuit dq model of the AFE converter.

Eq.I.8 describes VSI converter model including the control system (realized by modulation indexes m_d and m_q). Equation Eq.I.9 describes AFE model with its control system (p_q and p_q). The average model representation significantly simplify the circuit but it is still able to simulate dynamic behaviour of the system accurately with much less computational need and time effort. The average model ignores all switching effects of converters, however, the switching does not affect dynamic behaviour of the system and therefore can be neglected [76].

$$\begin{aligned}
\frac{dI_d}{dt} &= -\frac{R_{VSI}}{L_{VSI}} I_d + \omega I_q - \frac{1}{L_{VSI}} V_{cd} + \frac{1}{2L_{VSI}} V_{dc_i} m_d \\
\frac{dI_q}{dt} &= -\frac{R_{VSI}}{L_{VSI}} I_q - \omega I_d - \frac{1}{L_{VSI}} V_{cq} + \frac{1}{2L_{VSI}} V_{dc_i} m_q \\
\frac{dV_{cd}}{dt} &= \frac{1}{C_{VSI}} I_d + \omega V_{cq} - \frac{1}{C_{VSI}} I_{ad} \\
\frac{dV_{cq}}{dt} &= \frac{1}{C_{VSI}} I_q - \omega V_{cd} - \frac{1}{C_{VSI}} I_{aq}
\end{aligned} \tag{I.8}$$

Where:

– I_d, I_q VSI output currents in dq-frames respectively

– V_{cd}, V_{cq} VSI output voltages in dq-frames respectively

– L_{VSI} VSI output filter inductor

– R_{AFE} output filter inductor parasitic resistance

– C_{VSI} VSI output filter capacitance

– m_d,m_q modulation indexes in dq-frames respectively

– V_{dc_i} VSI input voltage

$$\begin{aligned}
\frac{dI_{ad}}{dt} &= -\frac{R_{AFE}}{L_{AFE}} I_{ad} + \frac{1}{L_{AFE}} V_{cd} + \omega I_{aq} - \frac{1}{2L_{AFE}} V_{dc_a} p_d \\
\frac{dI_{aq}}{dt} &= -\frac{R_{AFE}}{L_{AFE}} I_{aq} + \frac{1}{L_{AFE}} V_{cq} - \omega I_{ad} - \frac{1}{2L_{AFE}} V_{dc_a} p_q \\
\frac{dV_{dc_a}}{dt} &= -\frac{3}{4C_{AFE}} I_{ad} p_d + \frac{3}{4C_{AFE}} I_{aq} p_q - \frac{1}{C_{AFE} R_L} V_{dc_a}
\end{aligned} \tag{I.9}$$

– I_{ad}, I_{aq} AFE input currents currents in dq-frames respectively

– V_{dc_a} AFE DC output voltage

– L_{AFE} AFE input filter inductor

– R_{AFE} input filter inductor parasitic resistance

– C_{AFE} AFE output filter capacitance

– p_d,p_q modulation indexes in dq-frames respectively

– R_L load resistance connected to the AFE output for step-load response study

Both systems are coupled VSI dq-frame output voltage time derivatives ($\frac{dV_{cd}}{dt}$ and $\frac{dV_{cq}}{dt}$) depend on AFE instantaneous currents (I_{ad} and I_{aq}) and AFE current time derivatives ($\frac{dI_{ad}}{dt}$ and $\frac{dI_{aq}}{dt}$) depend on VSI instantaneous voltages (V_{cd} and V_{cq}). This corresponds to the real situation in the analysed study case.

I.5.2 Simulation tool description.

The simulation tool was created in Matlab environment. The tool is a script generating all possible combinations of the system variables which play significant role in the dynamic behaviour. VSI LC filter, AFE input filter, both VSI and AFE controllers bandwidths. Any other values of the system (such as both converters DC capacitors and damping factor) were constant in the analysis. The variables range were set according the control system estimated limits (for instance there was not possible to find stable system with a C_{VSI} capacitance smaller than 16μF) and technological limits (possible sampling frequency of the measurement setup used in experiments – described in Chapter I.6). The table with both variables and fixed values is presented in Table I.2. The variables are defined as input vectors in the script. Then tool runs simulation numerous times in order to check all possible combinations for each variable value.

Table I.2: Simulation tool input parameters.

Parameters	**Unit**	**VSI**	**AFE**
DC Filter Capacitance	[µF]	C_{DC} = 100	C_{AFE} = 100
Output Filter Inductor Parasitic Resistance	[µΩ]	R_{VSI} = 120	R_{AFE} = 90
Damping Factor	[–]	$\zeta = 1$	$\zeta = 1$
Input Filter Inductance	[µH]	L_{VSI} = 10-2000	L_{AFE} = 10-2000
Input Filter Capacitance f_n	[µF]	C_{VSI} = 16-160	–
Current controller bandwidth	[Hz]	$f_{i_{VSI}}$ = 100-1000	$f_{i_{AFE}}$ = 100-1000
Voltage controller bandwidth	[Hz]	$f_{v_{VSI}}$ = 10-100	$f_{v_{AFE}}$ = 10-100 Hz

Each simulation ran by the tool was similar to the one described in section I.4.2. However, thanks to use of the average model the simulation time decreased from several few minutes to few milliseconds. The waveforms for single combination of input variables are presented below as an example (Fig.I.24 and Fig.I.25).

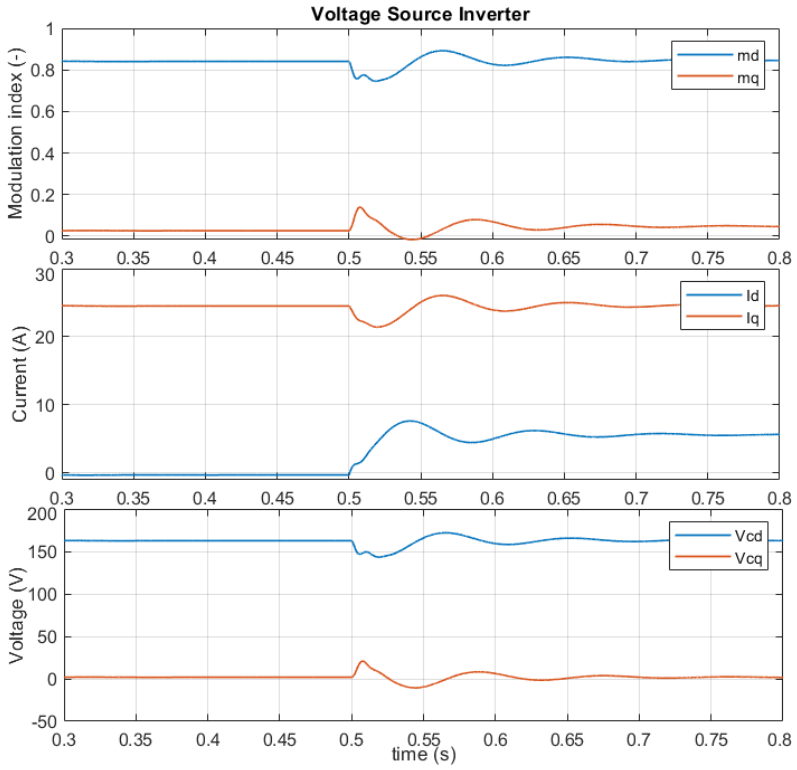

Figure I.24: Example waveforms of the VSI average model run by simulation tool.

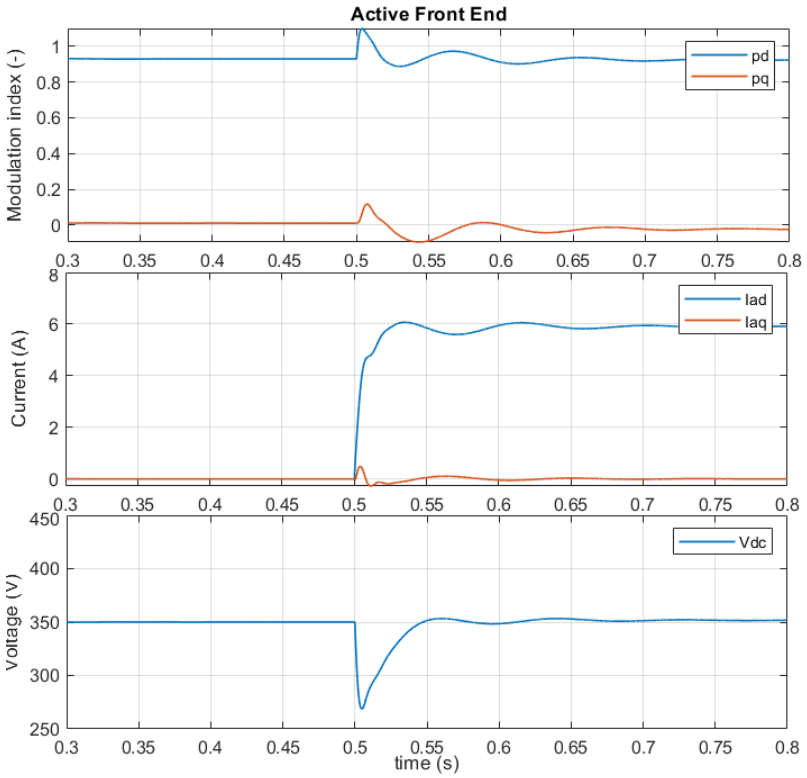

Figure I.25: Example waveforms of the AFE average model run by simulation tool.

The tool checks system stability based on eigenvalues of the control system for every combination of input parameters before the simulation starts, then it captures the key waveforms, measure the step load response undershoot and settling time and finally compare the result with the standard requirements. Data such as settling time, undershoot (Fig. I.26) and the flag indicating whether the standard is met for both converters are the tool output and saved in the lookup table for each set of input variables.

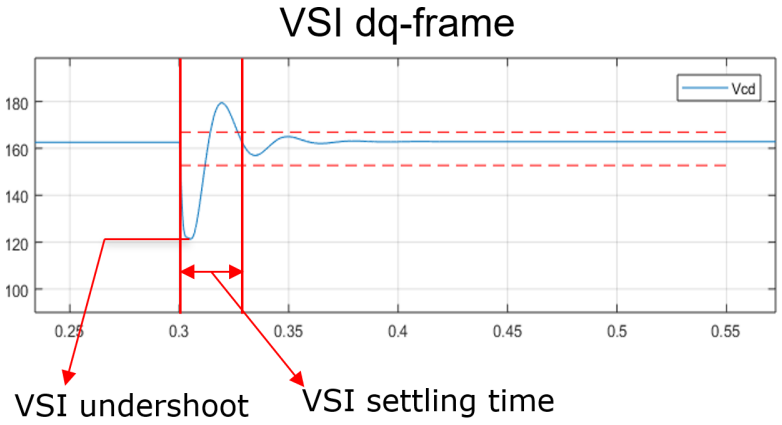

Figure I.26: Settling time and voltage undershoot in the VSI.

I.6 Experimental validation of the tool.

To check the control system simulation tool the experimental validation has been conducted. In order to verify the tool a prototype rig has been built. The experimental results were compared for different sets of harmonic filters with the results obtained by simulation tool.

I.6.1 Experimental rig description.

The experimental rig was built with following components: DC power supply, VSI and AFE converters, grid harmonic filters, FPGA/DSP control board, LEM sensors and resistive load with a switch for step-load operations and oscilloscope for dynamics measurements. The experimental setup is presented in Fig. I.27. The rig's parameters used in experiments are shown in Table I.3. The values are slightly different to the design ones due to manufacturing limits.

Table I.3: Experimental setup parameters

Parameters	**Unit**	**VSI**	**AFE**
Power P_N	[kW]	1.5	1.5
Input Voltage V_{in}	[V]	350 dc	115 ac rms
Output Voltage V_{out}	[V]	115 ac rms	350 dc
Switching Frequency f_{sw}	[kHz]	20	20
Nominal Frequency f_n	[Hz]	400	–
AC Filter Inductance L_{VSI} L_{AFE}	[µH]	260	345/630
AC Filter Capacitance C_{VSI}	[µF]	18/25/33	–
DC Filter Capacitance C_{DC}	[µF]	100	100

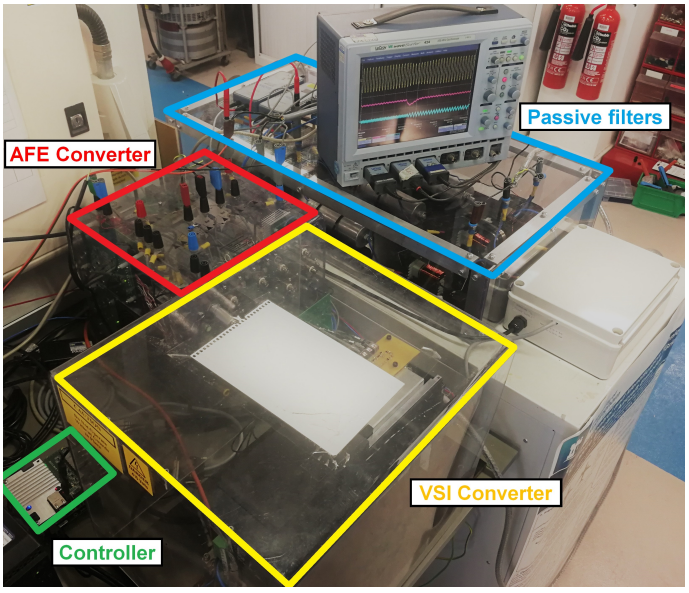

Figure I.27: View of experimental test rig.

The inductors used as harmonic filters were designed and manufactured in the lab for tests purposes. The coils were wounded on a plastic frame with a copper wire. All inductors have U shape powder magnetic cores with an air gap [70][45]. The capacitors used as a part of harmonic filters are manufactured by TDK EPCOS with metallized polypropylene film technology. Several capacitance values from manufacturer's product range were chosen for tests [24]. The values of designed inductors and used capacitors are presented in the Table I.3.

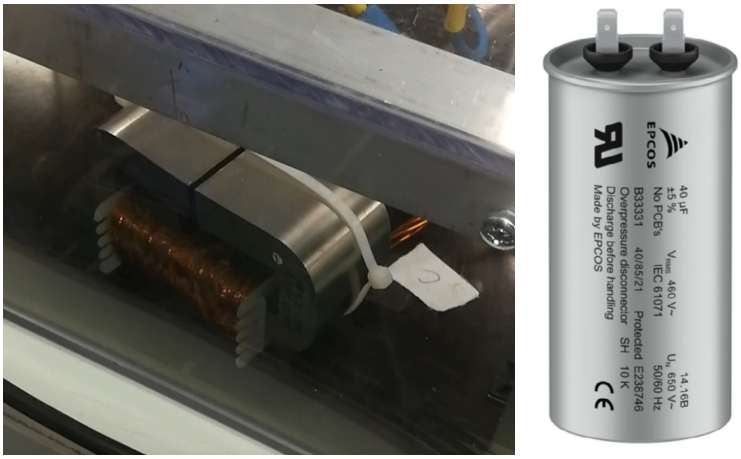

Figure I.28: View of inductors and capacitors used in experiments.

I.6.2 Control system of the rig.

The converter's control in the experimental rig was realized with Xlinix Zynq FPGA/DSP control board. Substantial voltages and currents were measured with LEM sensors and then transmitted to the FPGA ADCs through optic fibres. The control was realized with software written in C language where abc/dq conversion algorithm and PI controllers for both current and voltages in dq-frames were included. The control system output is demodulated to abc-frame and send for each converter power module drivers through optic fibres.

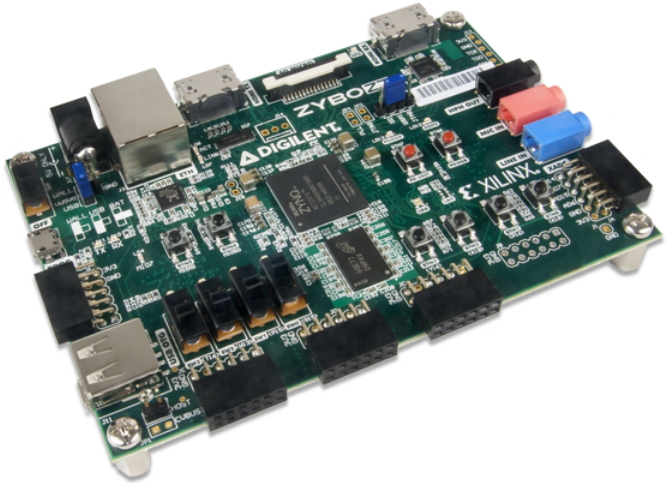

Figure I.29: FPGA PCB board view. [78]

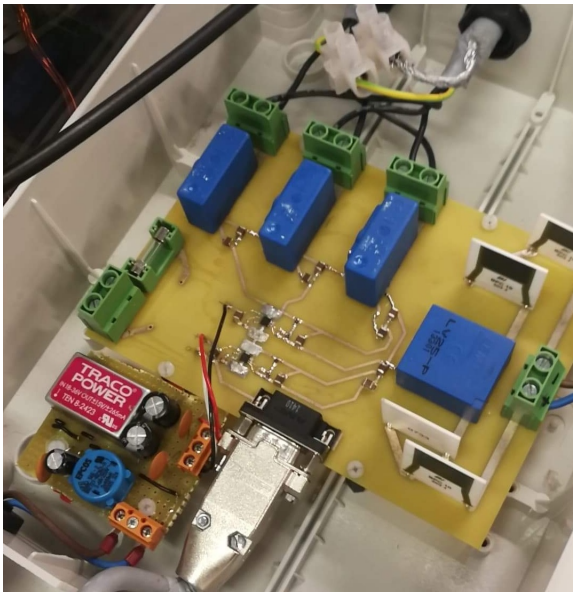

Figure I.30: Measurement board based on LEM sensors.

I.6.3 Experimental tests.

In order to check the validity of the simulation control tool the step-load response was tested and then compared with the tool results. The load used in experiments is the same used in previous analysis and in the control simulation tool (R_L=86Ω). The load was connected to the working converters through the switch and the response transient was recorded with using an oscilloscope and ADC channels of the FPGA. The tests were done for several times for different sets of the harmonic filters. The view of the oscilloscope measurement is presented in Fig. I.31.

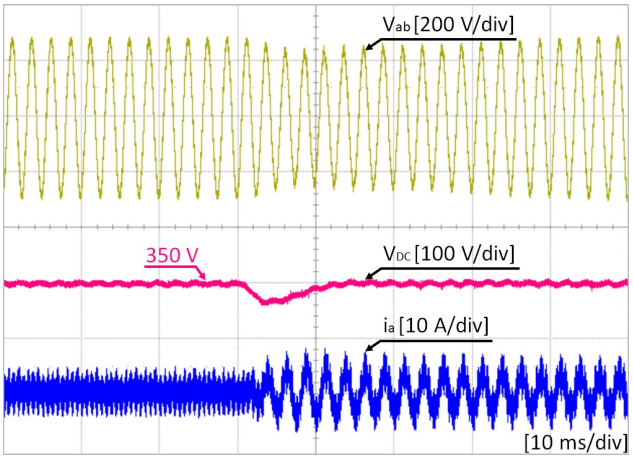

Figure I.31: Transient waveforms acquired during the experiments for one set of the filters. L_{VSI}=260μH C_{VSI}=33μF L_{AFE}=630μH.

It order to compare simulation with measurement the VSI output voltage had to be presented be in dq-frame. The controller internally did abc-dq transformation and thus measurement used for comparison was based on controller ADC channels. The results are presented below. Orange coloured waveforms are the ADC channels measurement results, blue waveforms are obtained by control simulation tool and red the dynamic requirement from the standard.

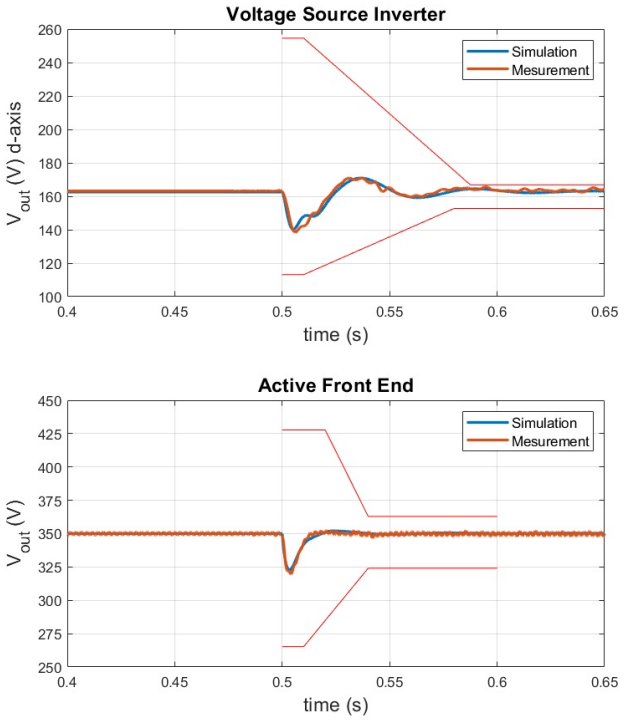

Figure I.32: Comparison between simulation and experimental results of step-load response of the system. The passive components parameters are L_{VSI}=260μH C_{VSI}=33μF L_{AFE}=630μH.

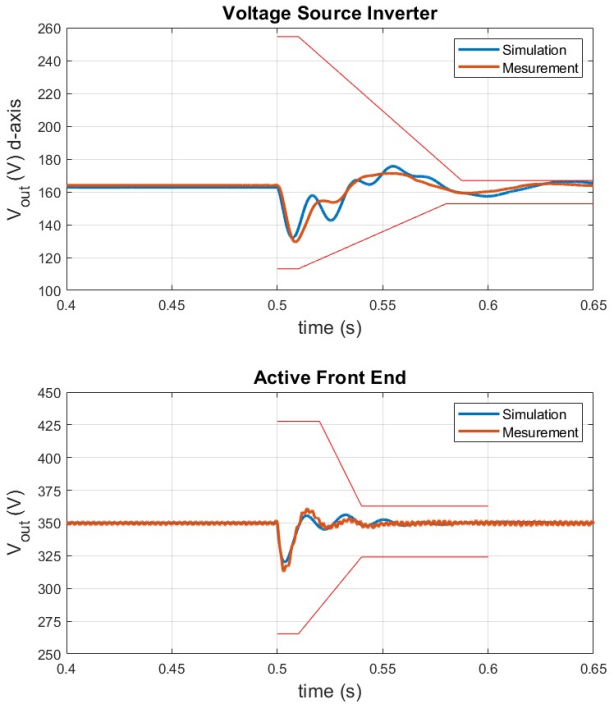

Figure I.33: Comparison between simulation and experimental results of step-load response of the system. The passive components parameters are L_{VSI}=260μH C_{VSI}=33μF L_{AFE}=345μH.

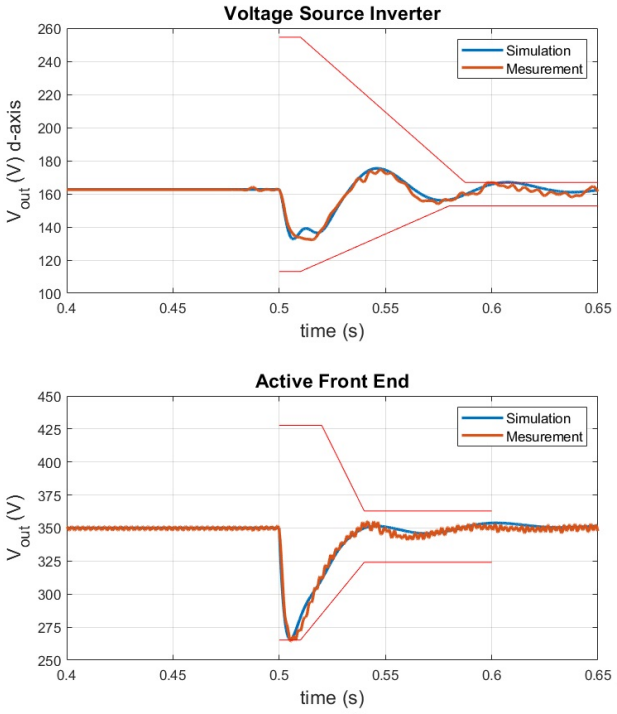

Figure I.34: Comparison between simulation and experimental results of step-load response of the system. The passive components parameters are L_{VSI}=260μH C_{VSI}=33μF L_{AFE}=345μH.

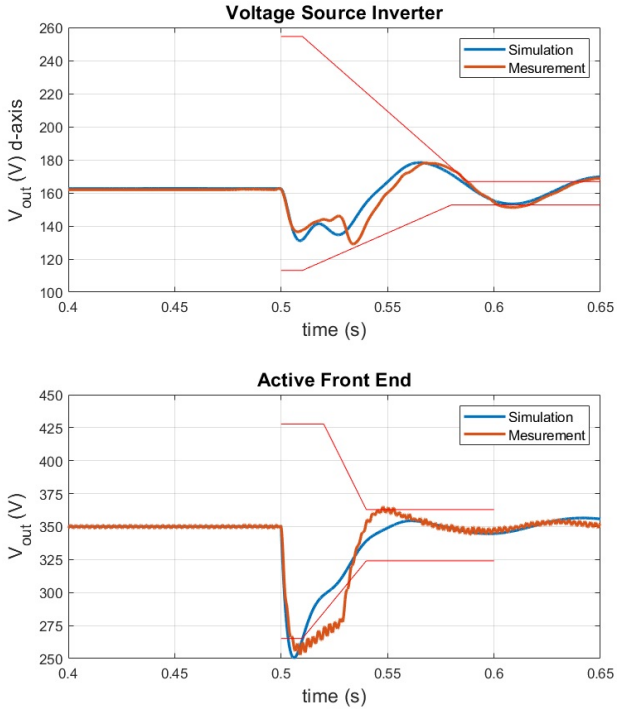

Figure I.35: Comparison between simulation and experimental results of step-load response of the system. The passive components parameters are L_{VSI}=260μH C_{VSI}=25μF L_{AFE}=345μH.

The test results proved the validity of control system simulation tool. The average model used in the tool is sufficiently accurate according to the obtained results. In some cases the waveforms do not match perfectly which can be caused by not accurately setting the simulation passive component values to the actual ones from the experimental setup. However, even if the waveforms do not fit perfectly, the dynamic behaviour is well reproduced, in every checked case. Regardless of requirements compliance, the result of the simulation and experiments are corresponding. Among the selected results are presented for different filter components and controller parameters Fig.I.32 and Fig.I.33 are the cases where the standards were met whereas Fig.I.34 and Fig.I.35 present the cases where requirements were not met.

I.7 Area of Design definition.

Once the simulation tool was validated by experimental measurements, the obtained data from the tool was processed. The obtained lookup table contained combination of each input variable which resulted with millions of records. Therefore, it was necessary to reduce amount of data in order to be able to process it. For each set of physical variables (LC and L filters components values) it was checked whether exist at least one set of non-physical variables (controllers bandwidths) where the system is able to meet the dynamic requirements. In other words, if it is possible to design controller which is able to meet the standards for particular set of passive components values. Thanks to that amount of variables decreased from 7 to 3 (Fig. I.36) and amount of data from millions to thousands data points. The simplified results were composed together and presented as the Area of Design (AoD) (Fig.I.37). Blue dots showing the design where meeting the requirements is possible and the red ones where it is not. It needs to be mentioned that the Area of Design considers only control aspect, there might be a lot of designs which do not comply power quality standard. This feature will be studied in the last following chapter of this part.

The AoD shows that control aspect needs to be considered when designing the filters and thus the link between power quality and control aspects. For some sets of the grid filters even if they meet the power quality standards, it might be not possible to design a control system which meets the dynamic standards [41]. Therefore, some design constraints have to be defined especially when there is a need of minimizing the filters (e.g. through optimization) for saving converter's weight or cost, for instance.

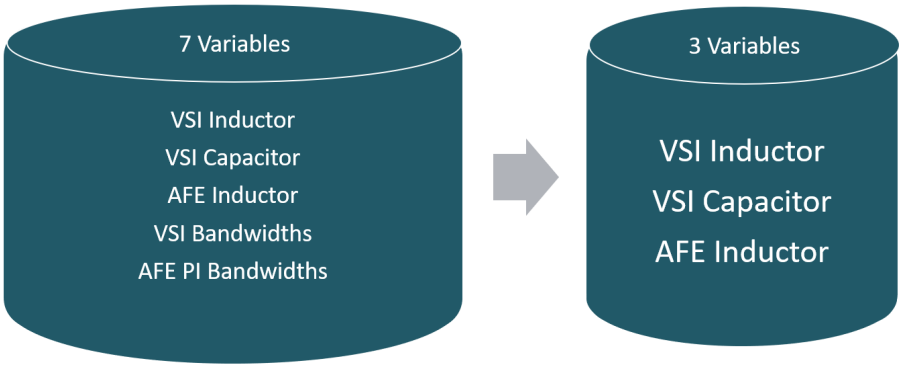

Figure I.36: Decreasing amount of variables by elimination of non-physical ones.

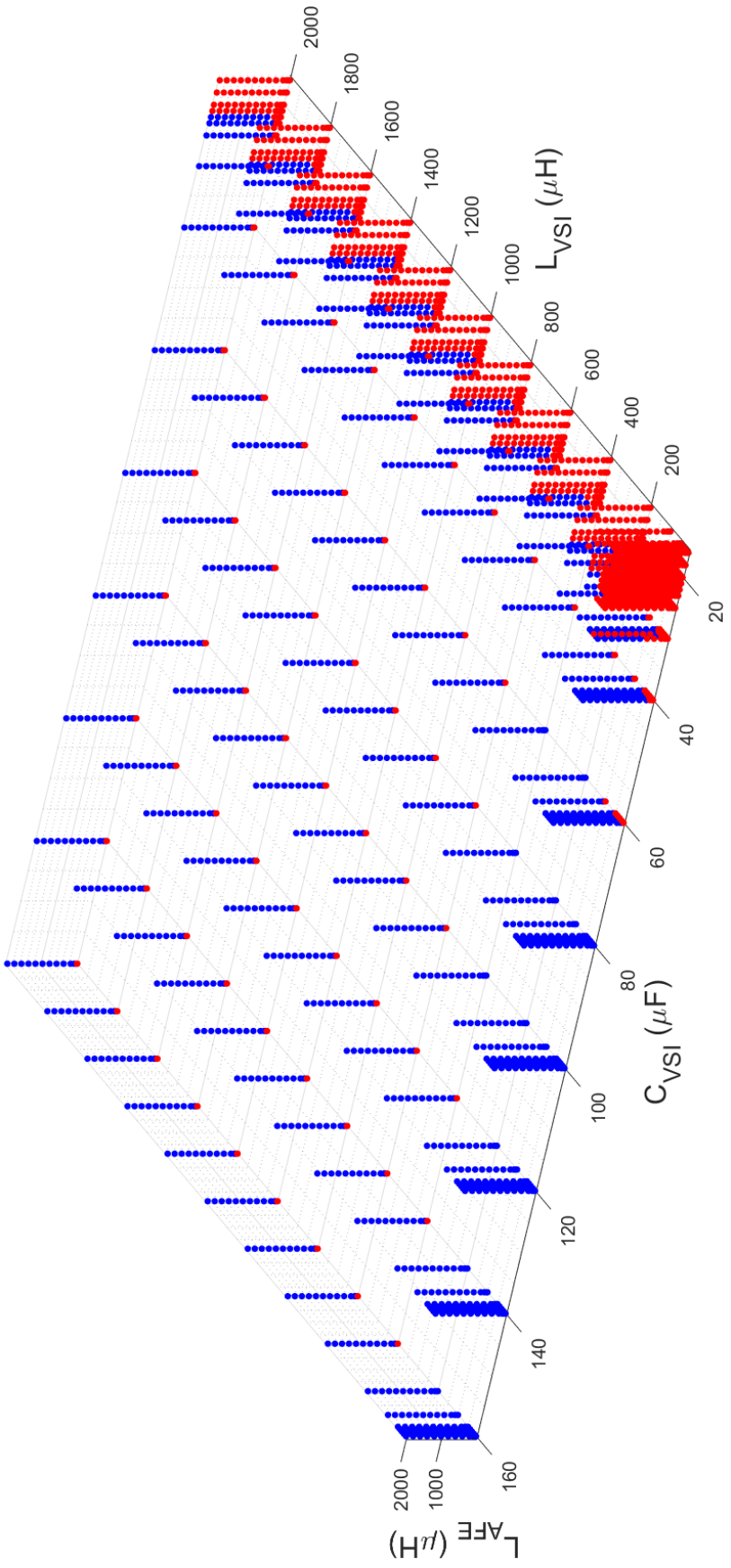

Figure I.37: Area of Design. Blue points indicates the design which meets the requirements, red which does not.

I.8 Harmonic filters design optimization.

In order to properly design grid filters including power quality, dynamic requirements and the interactions harmonic filters optimization has been conducted. The objective was to minimize the filters' weight while respecting the standard requirements (major concern in Aircraft [14]). Thanks to minimizing the filters and consequently aircraft weight the exploitation cost can be drastically reduced.

I.8.1 Optimization Algorithms.

The main goal of the optimization problem is to find the best solution from all feasible ones [11]. In general, the objective and constraint functions can be linear or non-linear and can be explicit or implicit functions. The standard form for a single-objective, non-linear constrained optimization problem could be defined as follows (Eq. I.10).

$$\begin{aligned} &Minimize: f(x) \\ &Subject\ to: g_j(x) \leq 0 \qquad j = 1, m \\ &\qquad\qquad h_k(x) = 0 \qquad k = 1, p \\ &\qquad\qquad x_{iL} \leq x_i \leq x_{iU} \qquad i = 1, n \end{aligned} \tag{I.10}$$

Where $f(x)$ represents the objective function, $g_j(x)$ an inequality constraint and $h_k(x)$ an equality constraint function. The x vector represents the n design variables that are modified to obtain the optimum. The searchable design space is defined by lower and upper bounds (x_{iL} and x_{iU}) of the design variables which are the side constraints [72].

There are plenty of optimization methods and algorithms. Their classification is presented in Fig. I.38. Majority of algorithms consider the side constraints separately from the equality and inequality constraints. The side constraints can be handled efficiently by direct implementation in the algorithm. The optimization methods are divided to deterministic and stochastic [79].

Both of them have pros and cons and therefore the choice should be dictated by many factors such as:

- type objective function (whether is differentiable or not)
- type and number of input variables and constraints
- complexity of optimization problem.

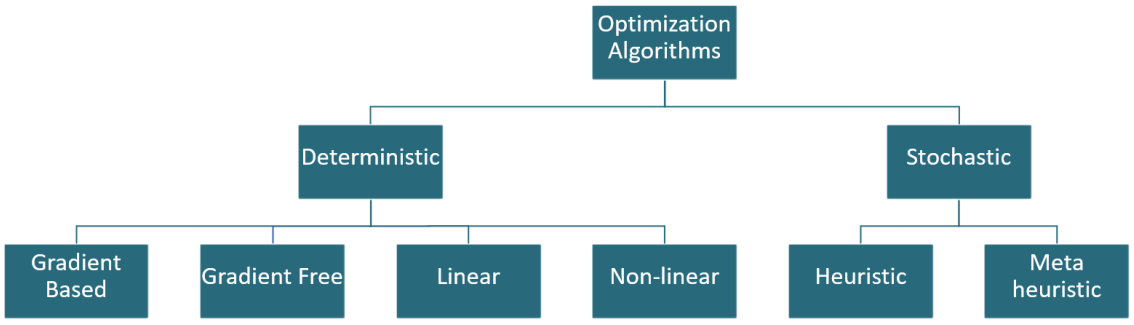

Figure I.38: General classification of the optimization algorithms.

I.8.1.1 Stochastic Optimization Methods.

Stochastic optimization algorithms uses the randomness in the search procedure for objective functions for which derivatives cannot be calculated. The stochastic algorithms usually consider a lot of sampling of the objective function and therefore, necessitate high performance computation. The stop criterion is not obvious to define and thus global optimum is not guaranteed.

There are numerous amount of stochastic algorithms which are widely used in machine learning [43]. Some of them have an origin in biology and they are named evolutionary algorithms. They are based on mechanisms that occurs in nature such as natural selection, species migration, bird swarms, human culture, and ant colonies [67].

Among these algorithms the most popular used in engineering are Genetic Algorithms (GA) which operation is divided on 5 phases. In the first phase the algorithm gather the characteristics of each individual from all populations from the previous iteration or generate them randomly if it is the first iteration. Then, the choice of populations is made by usually following processes – duels between populations, random selection weighted by the performance of the solution or identification of best solution. When the selection has been

made the individuals are be genetically crossed (recombination), which can again there are several ways. Crosses can be single, multiple or unequal depending on the crossing rate chosen. Finally, a certain proportion of populations mutate randomly. The proportion of mutation is often low to keep the benefit of recombination and selection. Thanks to mutation it is possible to expand solutions in space and avoid focusing on a local extrema, especially at start of the process. Once all phases are complete it is necessary to determine whether the algorithm has succeeded in converging towards the optimum or if the populations generated must start the cycle again. The optimal solution is obtained when the characteristics of the individuals are close for instance when the population is uniformed [8, 80]. The outline of a general genetic algorithm where example of evolution stages are shown is presented in Fig. I.39.

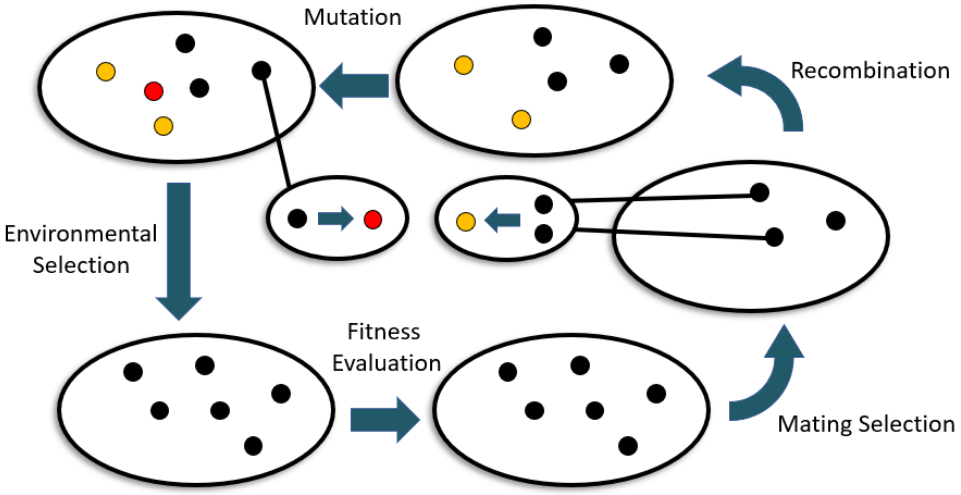

Figure I.39: Outline of a genetic algorithm.

I.8.1.2 Deterministic Optimization Methods.

The main feature of deterministic algorithms is the fact that they follow a precise sequence of actions. Thus, design variables and objective function can have the same values and repeat the same route. Unlike stochastic algorithms, they are never random and therefore the optimization solution will be always identical. The main advantage of the deterministic algorithms is the fact that they need less evaluation of the objective function to converge to the optima. Also, constraint are easier to be defined. They can be trapped into local optimia if the objective function is not convex [58].

- Zero-order methods – they do not use information on the derivative of the model but only make use of zero-order interval arithmetic. The popular examples of this method is a simplex algorithm or interval bisection [31].
- First-order methods – they use the model derivable aspects such as interval gradients or slopes to converge toward the optimum. In this method both objective function and its derivative is calculated which allows the algorithm to chose next step direction. The popular example is a Gradient descent method [61].
- Second-order methods – they additionaly to first-order methods calculate the second derivative which is called the Hessian [35]. This operation usually speed up the convergence, however it can need a lot of computational power and time effort. The popular example is the Newton-Raphson method.

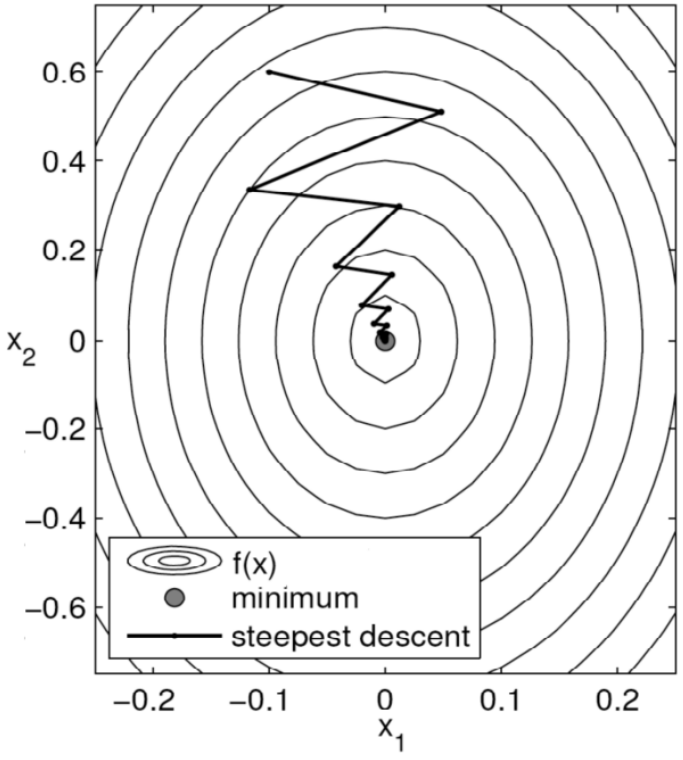

Figure I.40: Example of gradient based algorithm solving methodology (gradient descent method). [37]

I.8.2 Optimization Problem – reduction of the grid filters weight.

It would be much easier to develop sizing models for power electronics for the optimization using stochastic algorithm rather than deterministic. It is especially true for converters' elements such as power switches and capacitors since they are developed by manufacturer and therefore they are discrete variables in the algorithm what prevents computing the gradients. Moreover, in the study case constraints resulted from interactions are also delivered as discrete data. However, they main drawback of stochastic algorithms is drastic growth of computation time effort needed with an increase of input variables. Even if the study case is quite simple the future analysis would consider whole aircraft grid having numerous power electronics converter and thus large amount of input variables.

Despite all issues related with creating continuous models of discrete data, the deterministic algorithm has been chosen. Specifically, gradient-based the Sequential quadratic programming (SQP) algorithm. The SQP is able to maintain large problem with numerous constraints and has relatively small convergence time.

The objective of the optimization was to reduce the total weight of the AC aircraft grid filters. In order to perform optimization the objective function has been defined (Eq. I.11).

$$Filters_{mass} = min\, f(L_{VSI}, C_{VSI}, L_{AFE}) \tag{I.11}$$

The objective function has several constraints based on technological limits such as currents and voltages, core material etc... as well as the constraints based on the standards and the interactions described in Chapter I.4.

The grid filters optimizations has been carried out using a dedicated software – Vesta Systems CADES. It has implemented many optimization algorithms both deterministic and stochastic. In addition, CADES uses ADOL-C package dedicated for evaluation of first and higher derivatives of functions which decrease the computation time and increases the precision on function gradients [74]. The view of example optimization result is presented in Fig. I.41. The result shows that the THD constraint is slightly exceed, this is caused by the software's accuracy since it considers only 5 digits after the decimal.

Variable name	Orientation	Type of constraint	Value/Initial guess	Min	Max	Best result (13)
f	INPUT	FIXED				
Filters_Mass	OUTPUT	MINIMIZE	600.0			500.36908003...
Mass_CVSI	OUTPUT	FREE				164.0293520529
Mass_LAFE	OUTPUT	FREE				130.5112772907
Mass_LVSI	OUTPUT	FREE				205.8284506936
my_C_CVSI_va	INPUT	INTERVAL	3.3E-5	1E-5	1E-4	2.296626586E-5
my_L_LAFE_va	INPUT	INTERVAL	1.0E-4	2E-5	0.002	2.489833707E-5
my_L_LVSI_va	INPUT	INTERVAL	1.0E-4	2E-5	0.002	5.141846855E-5
THD	OUTPUT	INTERVAL		0.0	0.05	0.050000032675
v_RVSI_arg	OUTPUT	FREE				
v_RVSI_dB	OUTPUT	FREE				
v_RVSI_mod	OUTPUT	FREE				
Vharm_sum	OUTPUT	FREE				25319.11426489
Vharm_sum_n	OUTPUT	FREE				63.14001814314

Figure I.41: View of optimization result from CADES software.

I.8.3 Weight dependent filters modelling.

To minimize the total weight of the filters it was necessary to design models representing the relation between harmonic filters values and their weight. Moreover the models have to be continuous and derivable to be able to use it in SQP algorithm.

I.8.3.1 Inductor model.

Inductors are one of the bulkiest elements of power electronics converter. Their size and weight depends on many factors such as magnetic core material, size and shape, presence or absence of air gap, winding thickness, amount of turns type and size of frame. Moreover, inductors can be affected by physical phenomena like, skin and proximity effects and core saturation which need to be taken into consideration in order to correctly design them. This makes inductor modelling process even more complex [49]. Therefore, it is not an easy task to define the weight dependent model of the inductor.

The complex inductor model which take into account a saturation effect, magnetic core material type, shape and dimension, type and thickness winding was developed before for the same type of inductor (AC inductor for 115V aircraft grid). Therefore, this already available model was used for inductor weight estimation. The detailed description can be found [73].

In order to simplify the optimization the weight dependent model of the inductor was obtained through the interpolation of results of several preliminary optimizations for parameters used in study case. The magnetic core material and shape has been fixed into toroidal inductor with KoolMμ material which has low loss and relatively high saturation level. The results of the interpolation are presented below (Fig. I.42).

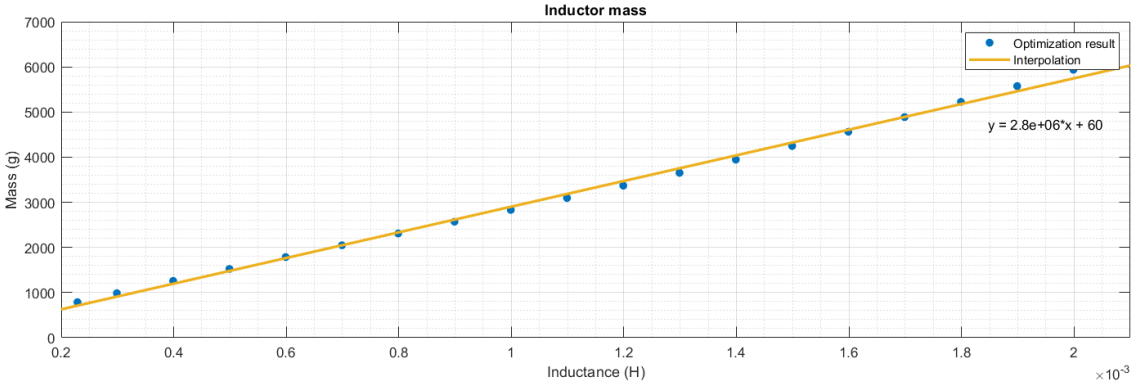

Figure I.42: Relation of Inductance versus Mass obtained from preliminary optimizations.

It is an almost linear increase of the inductor's weight with inductance on the chosen range of variation (200μH-2mH) To be noted that current and voltage ratings were kept constant during the optimization process. The interpolation resulted with weight dependent model of the inductor which was implemented in the optimization algorithm.

$$L_{mass} = (2.8 \cdot 10^6)\ L + 60 \tag{I.12}$$

Where:

– L_{mass} inductor weight [g]

– L inductance [H]

I.8.3.2 Capacitor model.

Due to the fact that the capacitors are devices already provided by manufacturer, the model was based on the datasheet [24]. The chosen capacitors were developed in Metallized Polypropylene Film (MPF) technology which is suitable for AC filtering application. The capacitor rated voltage has been chosen to withstand nominal voltage and transients in the AC grid – V_{RMS}=460V. For a given value of V_{RMS} all available capacitance values and their corresponding weight have been gathered and interpolated to obtain the continuous function and thus weight dependent model.

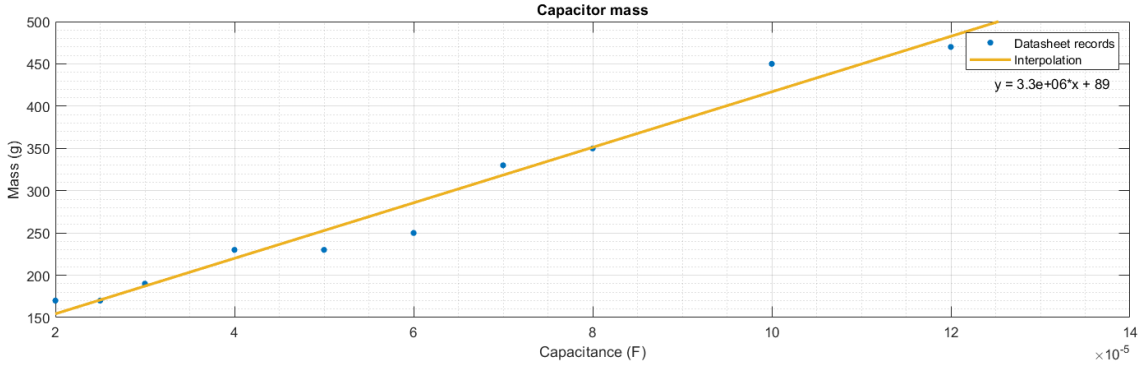

Figure I.43: Relation of Capacitance versus Mass obtained from manufacturer datasheet.

The interpolation resulted with weight dependent model of the capacitor which was implemented in the optimization algorithm.

$$C_{mass} = (3.3 \cdot 10^6)\ C + 89 \tag{I.13}$$

Where:

– C_{mass} capacitor weight [g]

– C capacitance [F]

It has been assumed that for this kind of AC filter application the maximum RMS current was not a limiting factor since the capacitors from datasheet has been chosen for RMS current above the nominal one.

As it can be seen, the weight models are quite simple (linear approximations) with some simplifications regarding the sizing constraints with respect to the RMS current. This was to keep the illustration of the optimization process quite simple. However, the full models have been developed and used in previous works [19][73] and the same optimization framework. They are full compatible with the approach and could easily be implemented in the optimization process. In this case, the design variable would be the core size and inductor turn number, in addition to capacitance.

I.8.4 Frequency-domain grid model.

One of the main requirements of the grid filters design which is also optimization constraint is the grid voltage THD which has to be smaller or equal 5%. The standard procedure for obtaining THD is to either measure a grid voltage, or simulate it in time-domain simulation, perform Fast-Fourier Transform (FFT) and then compute THD. However, that could not be the case if it has to be included in optimization algorithm as a constraint. Therefore, the frequency-domain grid voltage modelling approach has been conducted. This allows to estimate the grid voltage depending on filter values in a quick and computation lightweight way [52].

I.8.4.1 Grid THD frequency modelling description.

The frequency-domain grid model based on simplification to one-phase frame assuming the phase balance. The model is composed of two equivalent Voltage sources V_{VSI} and V_{AFE} in frequency-domain which are phase voltages of VSI and AFE respectively and the harmonic filters. The model is presented in Fig. I.44. To obtain the equivalent sources the time-domain voltage waveforms have been transformed to frequency-domain by FFT and then, in order to simplify the computation, only voltage peaks in the frequencies where the harmonics are present were included in the model. The sources waveforms both in time and frequency-domain are presented in Fig. I.45 the voltage peaks for which frequencies the model was evaluated are marked in orange. According phase shifts were also evaluated since they are crucial for frequency-domain computation. Thanks to this approach it was able to quickly evaluate the AC grid voltage and thus grid THD for different sets of the filter.

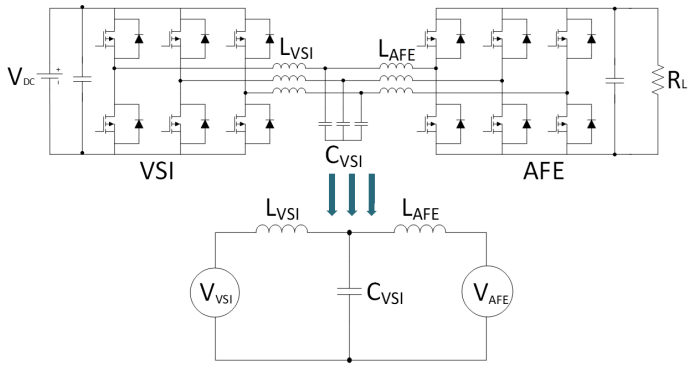

Figure I.44: Frequency-domain model of the grid.

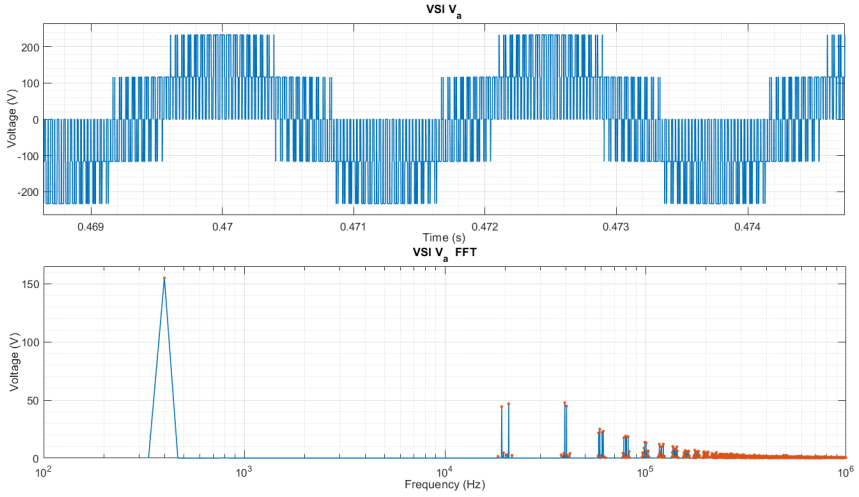

Figure I.45: V_{VSI} voltage source both in time and frequency-domain.

I.8.4.2 Model verification.

In order check the validity of the frequency-domain model a Matlab Simulink time-domain simulation has been done and then the results has been compared with the frequency-domain results. The Simulink model is described in Section I.4.1. The verification has been done for nominal parameters of the grid filters described in Chapter I.2. The comparison of frequency-domain model (orange points) and time-domain simulation AC grid voltage is presented in Fig. I.46. Moreover, AC grid voltage computed from both models is identical – THD=0.38%.

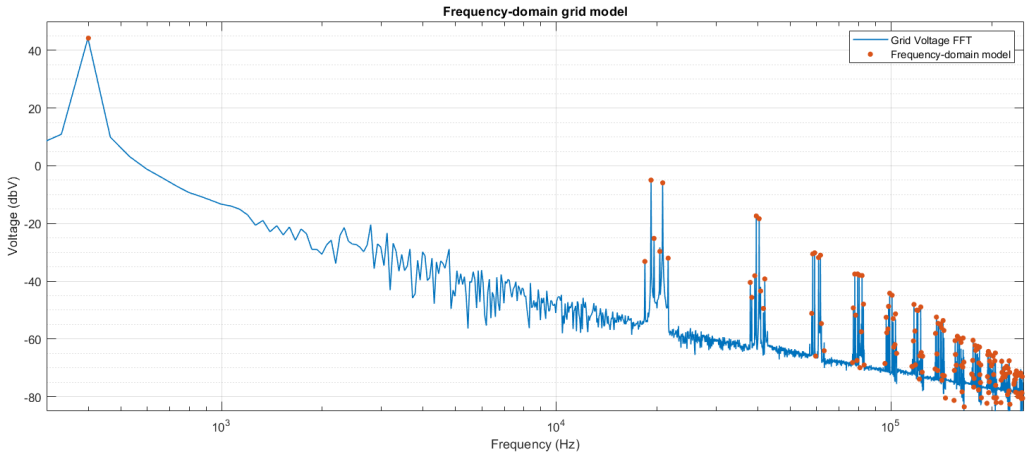

Figure I.46: Verification of the frequency-domain grid model.

I.8.5 Optimization with THD constraints.

The first optimization was performed with power quality constraints only. In addition, the technological limits of the filters have been considered by using approximation of the models which includes them. The power quality requirement used in optimization was taken from *MIL704F* standard which was maximum AC grid THD=5%. The optimization results are presented in the Table I.4.

Table I.4: Optimization results with THD constraints.

Parameters	**Unit**	**Before Optimization**	**After Optimization**
L_{VSI}	[µH]	260	51.4
C_{VSI}	[µF]	33	23
L_{AFE}	[]µH]	630	24.9
$FiltersMass$	[g]	1866.5	500.37
THD	[%]	0.38	4.99

The optimization result shows that the previous inductor design based on empiric engineering method was significantly oversized. The new design is almost 4 times lighter. However, in this case the optimization does concern only power quality standards and it is not certain if the result allows to design a controller which is able to meet dynamic requirements.

In order to check if the result is able to meet dynamic requirements the control system simulation tool has been run with filter parameters fixed. The simulation tool did not find any control able to meet the requirement, over 10 000 control designs has been checked where most of them was not even stable. Fig. I.47 shows example stability analysis result for one of controller designs with filters resulted from optimization.

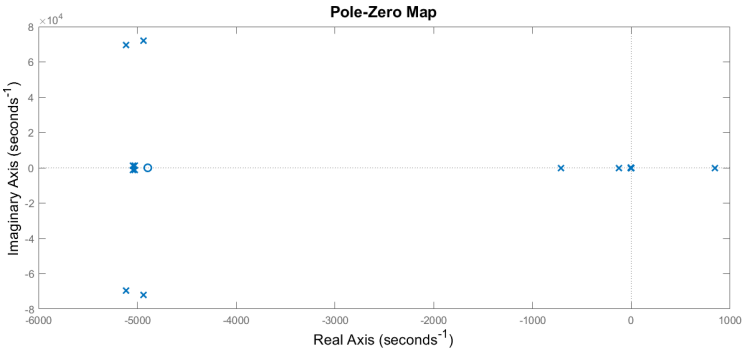

Figure I.47: Pole-Zero stability analysis of designed controller with optimized harmonic filters. Controllers bandwidths fi_{VSI}=1000Hz, fv_{VSI}=100Hz, fi_{AFE}=600Hz, fv_{AFE}=40Hz

I.8.6 Optimization including dynamic requirements constraints.

Previous optimization showed that it is necessary to consider dynamic behaviour requirements during harmonic filters optimization. Therefore, the second optimization has been run including both.

I.8.6.1 Dynamic constraints definition.

In order to include dynamic requirements in the optimization algorithm the constraints describing relation between harmonic filters and system dynamics must be defined. Therefore, previously developed Area of Design has been used (described in Chapter I.7).

However, the data in AoD is scattered which cannot be a case if gradient-based algorithm will be used. Thus, interpolation of the AoD data was performed with resulted in 3 continuous functions used as constraints in the algorithm. The interpolation has been performed with used a java code script which use bicubic interpolation algorithm. The constraints' functions are presented as follows.

$$L_{VSI} \geq f(C_{VSI}, L_{AFE})$$

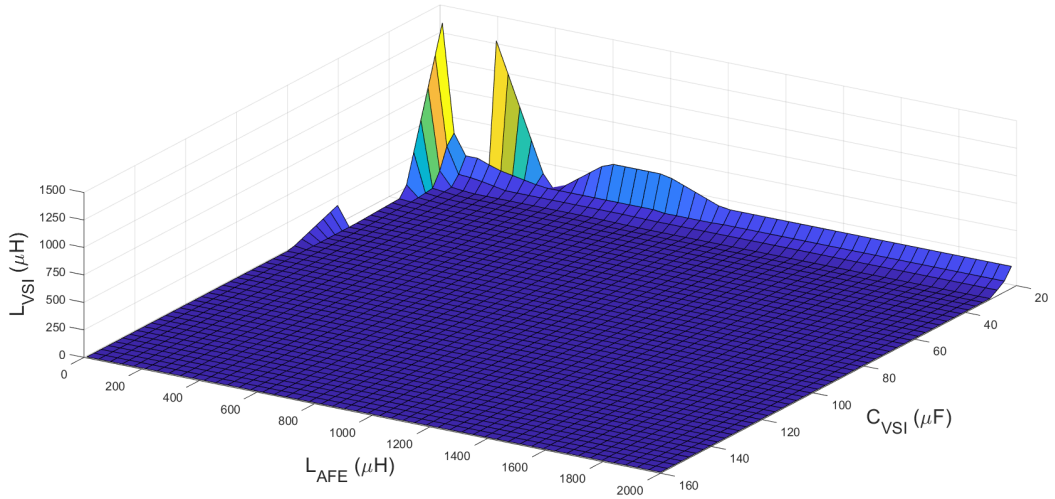

Figure I.48: L_{VSI} design constraint.

$$C_{VSI} \geq f(L_{VSI}, L_{AFE})$$

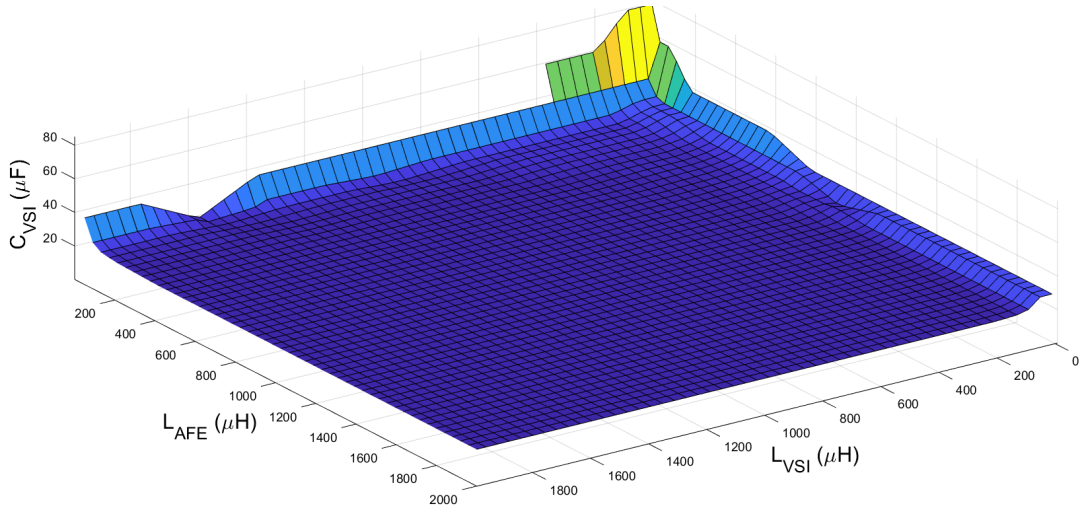

Figure I.49: C_{VSI} design constraint.

$$L_{AFE} \geq f(L_{VSI}, C_{VSI})$$

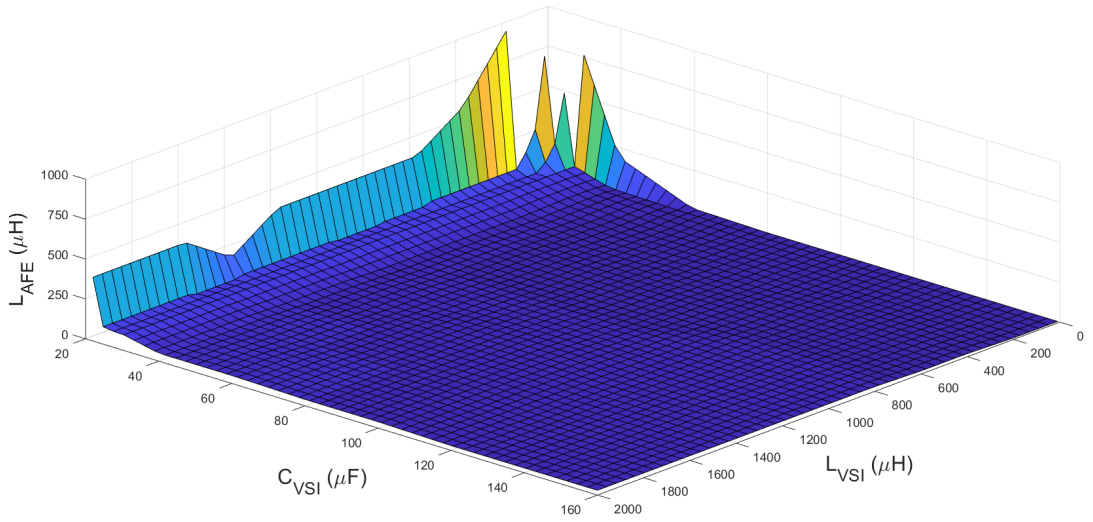

Figure I.50: L_{AFE} design constraint.

I.8.6.2 Optimization results.

The second optimization has been performed including both power quality and dynamic behaviour constraints. Both constraints are based on *MIL704F* standard. The power quality one is directly defined in the standard (THD≤5%) and the second one is based on AoD constraint definition explained in the previous section. Second optimization results are presented in the Table II.4.

Table I.5: Comparison between the total filter mass. Before optimization, with THD constraints only and with all constraints.

Parameters	**Unit**	**Before Optimization**	**Optimization without Dynamic Constraints**	**Optimization with Dynamic Constraints**
L_{VSI}	[µH]	260	51.4	64.4
C_{VSI}	[µF]	33	23	40
L_{AFE}	[µH]	630	24.9	45.67
$FiltersMass$	[g]	1866.5	500.37	652.2
THD	[%]	0.38	4.99	2.09

The obtained result is slightly heavier than the one from the previous optimization. Nevertheless, it is still much lighter than the original design. In addition, THD decreased from 4.99% to 2.09% which shows that it is no more an active constraint. The obtained result has been checked with control system simulation tool and it found several controller designs which meets the standard. Waveforms presenting control system step-load response which meets dynamic requirements for harmonic filters obtained from second optimization is presented in Fig. I.51. it is clear from this figure that there is still some margin in the dynamic, since the results show that there is not a hard limit, neither on the dynamic response nor on the THD point of view. Nevertheless, if the obtained value is not a "real" optimum, it is guaranteed that both criteria are met.

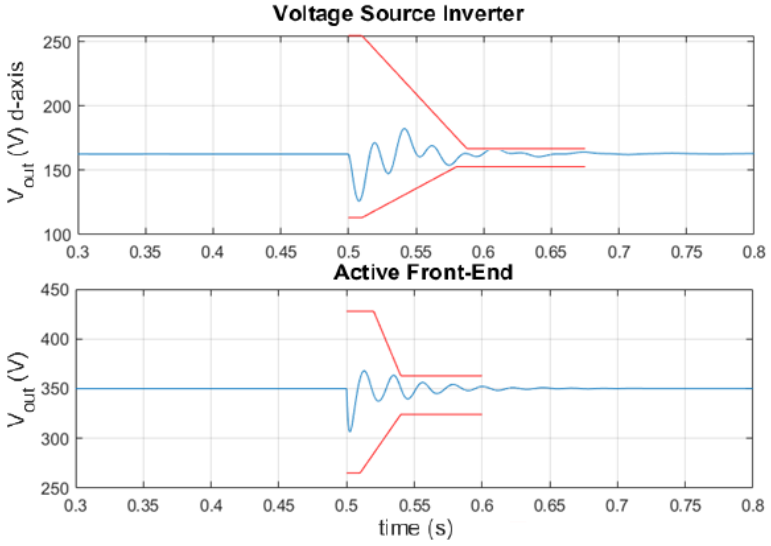

Figure I.51: Simulation result with optimized filters.

Harmonic filters' designs obtained from both optimizations were placed in AoD which is shown in Fig. I.52. The first designed is marked with yellow and the second with green colour. It is clear in this figure that the dynamic constraints have moved the filter values to another location of the AoD.

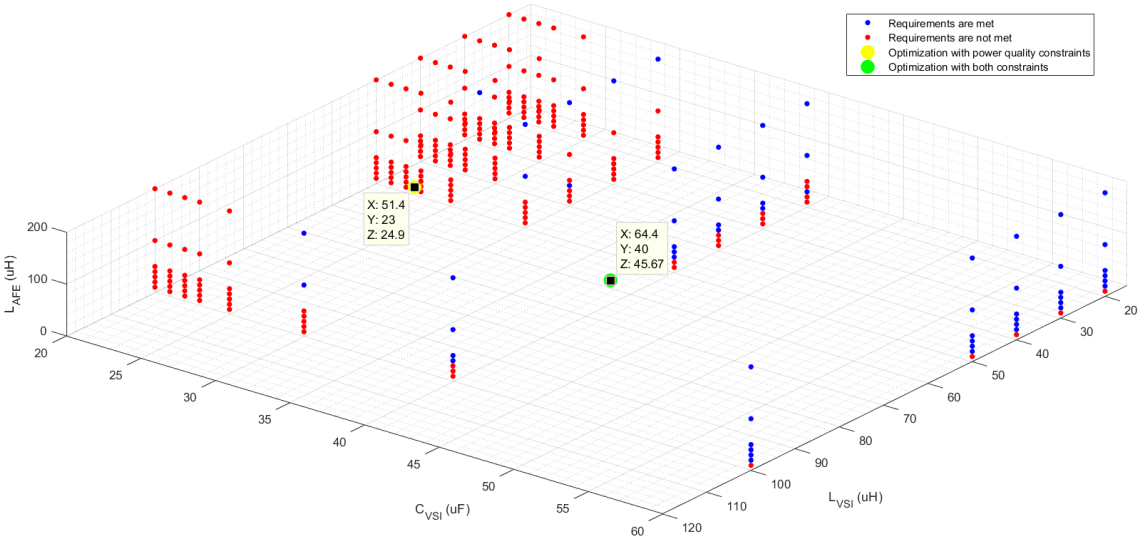

Figure I.52: Optimized solutions in the Area of Design.

I.9 Conclusion.

In this part an extensive analysis of interactions in an AC grid for a notional study case has been done. In an AC grid THD constraints as well as dynamic constraints need to be met. If we want to reduce the weight of the grid, filters have also to be reduced. This can be done as long as we keep an acceptable THD (i.e. meeting the standard). However, on a control point of view, the dynamic response of the AC grid voltage is also constrained by standards. It has been shown that it is influenced by all filters connected to the AC grid, and even some of the DC grid.

The control design defines some constraints on the filter values. These ones have been identified through preliminary simulation, what leads to "forbidden areas" and therefore filter design constraints. The method presented here is not the most generic, since it necessitates these preliminary simulations, and to check controller design at each step, but it underlines the necessity to account simultaneously for all filters during their design, and not only the THD constraints, but also te dynamic requirements.

Usually, the general design approach every converter is treated individually. In addition converter electrical design and control are performed separately.

The work described in this part showed that for some designs even if filters met harmonic requirements it was not possible to design a control which would be able to comply the dynamic requirements which was proven with optimization example.

All standards either civil or military describe requirements for a single device. The presented interactions indicates that treating the requirements individually for each device as defined in the standards might not be enough.

The solution which was presented and described in this part is a global design approach using optimization. The global design allow to consider numerous aspects of power converter design and clever modelling approach can allow to design several converters at the same time allowing to consider interactions between them.

The control approach analysed in this work was based on PI control technology. It is a standard method commonly used in industrial applications. It has its limits but it is quite easy to tune and therefore could be used by a regular engineer. However, there are many advanced control strategies which can greatly improve control system performance which could remove the design limit. Some work about advanced control strategy has been already done for this particular study case and can be found in [26, 21, 20]. Nevertheless, designing this kind of control is a task demanding the expertise knowledge in mathematics and control engineering thus is not commonly used in industry. Moreover advanced control design strongly depend on the grid impedance which is now always known and depend on filter to be designed. Therefore, it still necessitates a global vision.

Part II

EMC Grid System Level Interaction Study and Modelling.

Chapter Abstract

This part is focused on EMC interactions that occur between power electronics converters connected to the same grid. In the example studied in this chapter, a DC grid is considered. Firstly, EMI disturbances are modelled with a typical approach – a time-domain simulation with a frequency-domain analysis of the obtained results where EMC interactions in the grid were studied. Then, a lightweight Black Box modelling approach is introduced and verified. Finally the system-level EMI modelling based on Black Box models is presented.

Contents

II.1 Research motivation . . . 59
II.1.1 Electromagnetic Compatibility in Power Electronics. . . . 59
II.1.2 EMI impact in Power Electronics grid. . . . 61
II.2 Description of the study Case. . . . 63
II.2.1 Research objectives. . . . 63
II.2.2 The study case DC grid . . . 64
II.2.3 Grid components description. . . . 65
II.3 Aircraft standards EMC requirements. . . . 68
II.3.1 Conducted EMI measurement according to DO-160. . . . 68
II.3.2 Conducted EMI requirements according to DO-160. . . . 69
II.4 Conducted EMI Grid Interactions Study. . . . 71
II.4.1 Electromagnetic Interference modelling. . . . 71
II.4.2 Electrical grid components modelling. . . . 72
II.4.3 Time-domain simulation interactions study. . . . 77
II.5 EMC Black Box modelling. . . . 82
II.5.1 Terminated Black Box model description. . . . 83
II.5.2 Blackbox model identification. . . . 83
II.5.3 Black Box model verification. . . . 98
II.6 System level EMI modelling. . . . 112
II.6.1 The study case grid Black Box modelling. . . . 112
II.7 Conclusion. . . . 115

II.1 Research motivation

Power Electronics development in recent years resulted with a noticeable improvement in semiconductor technology [66]. This led to a significant increase of switching frequency in the power electronics devices which resulted in higher performances of the converters. Nevertheless, high switching and thus high transients can cause numerous issues related to electromagnetic interference which became one of the major concerns of modern Power Electronics field. In addition, due to extensive technology development, number of power electronic converters drastically increased. Frequently, several switched mode systems are somehow connected together which make EMI issues even more complex due to potential interaction between them [18]. The current qualification procedures do not account for these interactions, since each converter is tested individually on a standards grid (the Line Impedance Stabilization Network, introducted in section II.2.3.3). Therefore, it is necessary to find a way to accurately predict EMI behaviour in electric environment to prevent any potential issues.

II.1.1 Electromagnetic Compatibility in Power Electronics.

The concept which deals with Power Electronics issues related to EMI is electromagnetic compatibility (EMC). EMC is an ability of a device, equipment or system to function satisfactory in its electromagnetic environment without introducing any intolerable electromagnetic disturbances to anything in that environment [3]. In order to avoid any issues related to EMI there are several EMC standards which must be complied by a device.

EMI emission can be of a different nature depending on the propagation path. According to EMC standards, electromagnetic interference can by classified as follows:

Conducted emissions – electromagnetic disturbance in a form of an electrical current which flows through power cords (150KHz – 30MHz)

Radiated emissions – electromagnetic disturbance released in a form of electromagnetic field that propagate through a medium away of the device (30MHz – 1GHz)

It is worth to mention that the frequency ranges of both conducted and radiated emission might vary depending on the standard. In addition, due to a dynamic growth of switching mode power supplies' (SMPS) switching frequencies the classification will probably shift in the future to a higher limit.

This work focuses on conducted electromagnetic interference which is generated and propagates through power electronics converters. Conducted emission can be divided into two modes[50]. Common mode (CM) which is a disturbance conducted on all lines simultaneously in the same direction and phase, the signal returns through a ground. Differential mode (DM) which is a disturbance conducted on two lines of closed loop but current flow in the opposite directions. All kinds of EMI disturbances generated by a device, including radiated emission (EUT – equipment under test) are presented Fig. II.1.

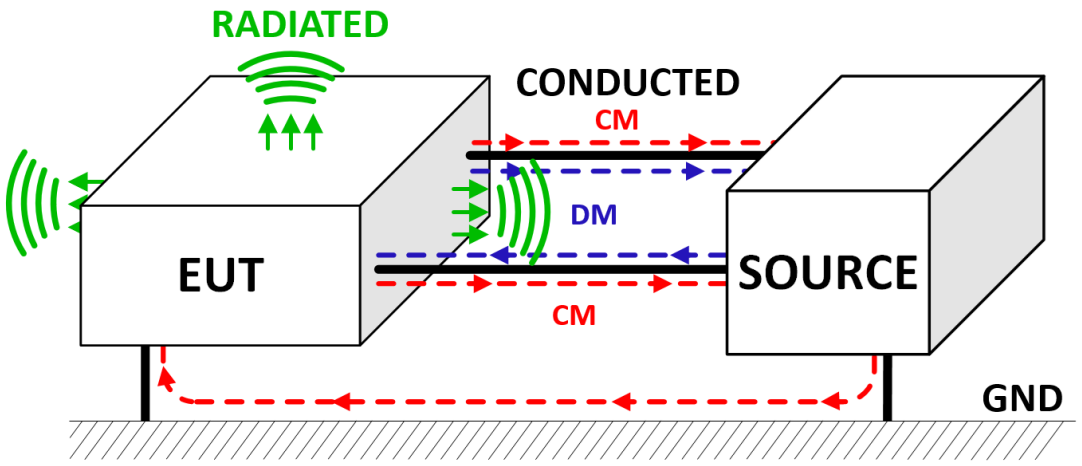

Figure II.1: Different EMI disturbances generated by a device.

EMI impact regardless its type can be reduced in many ways. The design might be improved in terms of EMI by a proper routing and components placement on the PCB. Moreover using components with smaller parasitics and their optimal connection in the device (e.g. having as short as possible mounting of the component which decrease its parasitics) can also improve EMI performance of the device [38]. Very often some shielding have to be used in the device in order to prevent self-interference of the device and decrease its radiated emission [28]. Lastly, modification of control algorithms can also improve EMI [39]. Nevertheless, in most cases, in order to comply emission limits defined the EMC standards, is necessary to include EMI filter in a converter design.

II.1.2 EMI impact in Power Electronics grid.

A standard approach of SMPS design in terms of EMC is to treat it individually. Moreover, all EMC standards are defined for testing an individual device in a standardized environment using a Line Impedance Stabilization Network (LISN) to reproduce a "real" grid impedance [54]. However, in many applications there are several converters connected to the same grid which can interact with each other. In addition, grid also consists numerous elements such as cables, casings, cabinets, loads etc... which can have a real impact on EMI propagation [51] and it is not well represented by the standard impedance of the LISN. Moreover, conducted interactions can occur even in a scenario when another devices are not turned on or even when devices are not physically connected, the propagation may take place through parasitic coupling (capacitive coupling with a common ground for instance). Finally, radiated emissions can also have an impact on devices nearby which can increase number of possible interactions in a grid. Fig. II.2 presents possible EMI interactions in an example grid composed of several power electronics converters.

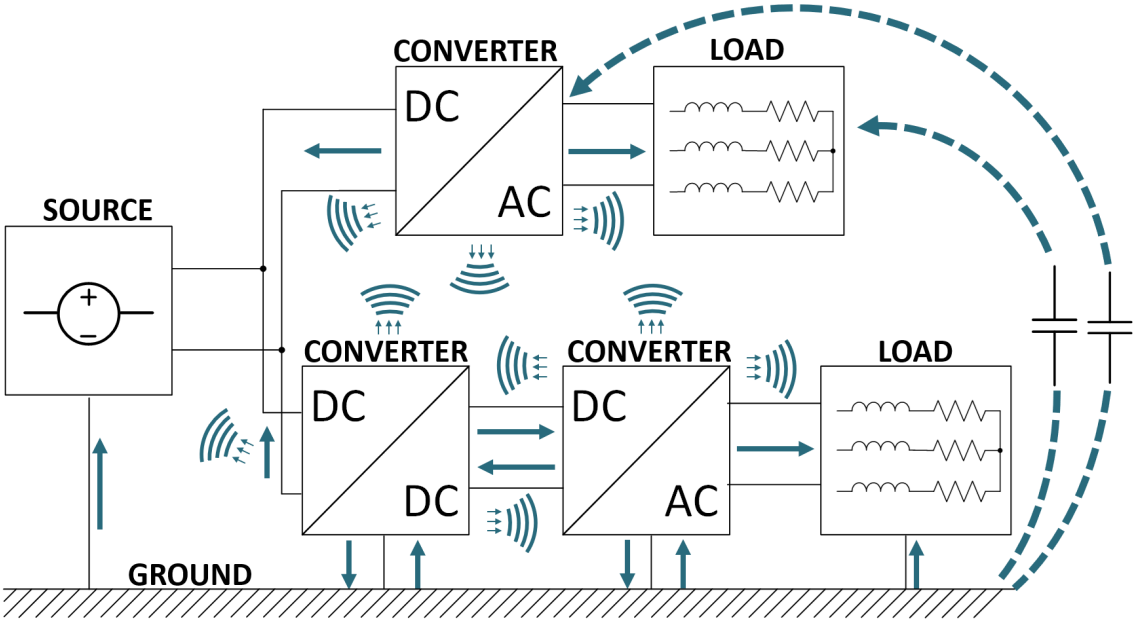

Figure II.2: EMC disturbances present in grid including power electronics converters.

There are numerous possible ways of the interactions in EMI environment, therefore, a typical approach, which is defined by the standards, where each device is treated individually might not be sufficient. It can lead to either some EMI-related issues or over-design of the EMI filter if the interactions happen to have a positive impact.

To have a proper Switched Mode Power Supply design in terms of EMC which is connected to any grid, it is necessary to know a total generated EMI level of the grid and to know possible propagation paths in order to foresee possible noise amplification or cancellation. Some prediction could be done with non-standardized measurement using a LISN connected to the whole grid, in this situation, the LISN would supply all converters, therefore all interactions within the grid would be considered. However, this would be a specific measurement situation, not generic. Furthermore, especially in high power applications, the connection to the grid must have mounted EMI filters already to prevent any malfunction caused by extensive emission injected to the gird. In that case the only solution is to model and simulate EMI in the considered grid. Unfortunately, a standard modelling based on time-domain simulation cannot be always convenient due to very long simulating time and convergence issues if model is too complex (especially if numerous converters including all parasitics are considered). The goal of this part of the thesis is to propose, identify and validate the use of a system level EMC model, suitable to be used directly in the frequency-domain to get rid of the issues of time-domain simulation.

II.2 Description of the study Case.

EMI-related interactions between power electronics converters and other parts of the grid can be very complex. In fact, every component can have an influence in many ways and can interact with several parts of the grid. Therefore, to recognize the basic principles of the interactions, it was decided to study a relatively simple DC grid composed of the basic power electronics devices based on the common topology of a boost converter. In consequence, it was easier to understand and identify EMC behaviour and be able to extend it in a future to more complex systems like the one described in Part I or even much more realistic system (e.g. real grid).

II.2.1 Research objectives.

A typical approach of conducted EMI identification in the device which is defined by the standards is to measure the disturbance in the power cords (input) with a device under test (DUT) connected to the LISN [2]. Based on that measurement and disturbance decomposition to CM and DM, EMI filter can be designed to provide a sufficient attenuation to pass emission limits defined by the EMC standards.

In reality, the device can be connected to the other ones (e.g. through the common bus bar) which can have an influence on its disturbance due to impedance of the other devices and their emission. It could have a positive impact such as, some disturbances between grid components cancels out or negative like different input filters ringing causing disturbance attenuation. Therefore, treating every device of the grid individually might not be an optimal approach.

The aim of this study is to check possible interactions and their impact on the total disturbance emission generated by the converters in the DC grid and therefore what influence it can have on EMI filter design process. Consequently, to find a proper lightweight modelling method which allows to predict EMI behaviour in the grid considering all interactions. Finally, to be able to properly design EMI filter for each grid component.

II.2.2 The study case DC grid

The grid which has been taken for consideration in the study is a DC grid composed of three typical DC/DC boost converters. Each converter have an EMI filter connected on the boosts' input side. Every converter is loaded by a resistor connected to their output R_L=42Ω. Converters are connected to each other in parallel pattern. They are all together connected to the LISN which is supplied by DC voltage source providing V_{in}=14V to the whole grid. The grid schematic is presented in Fig.II.3.

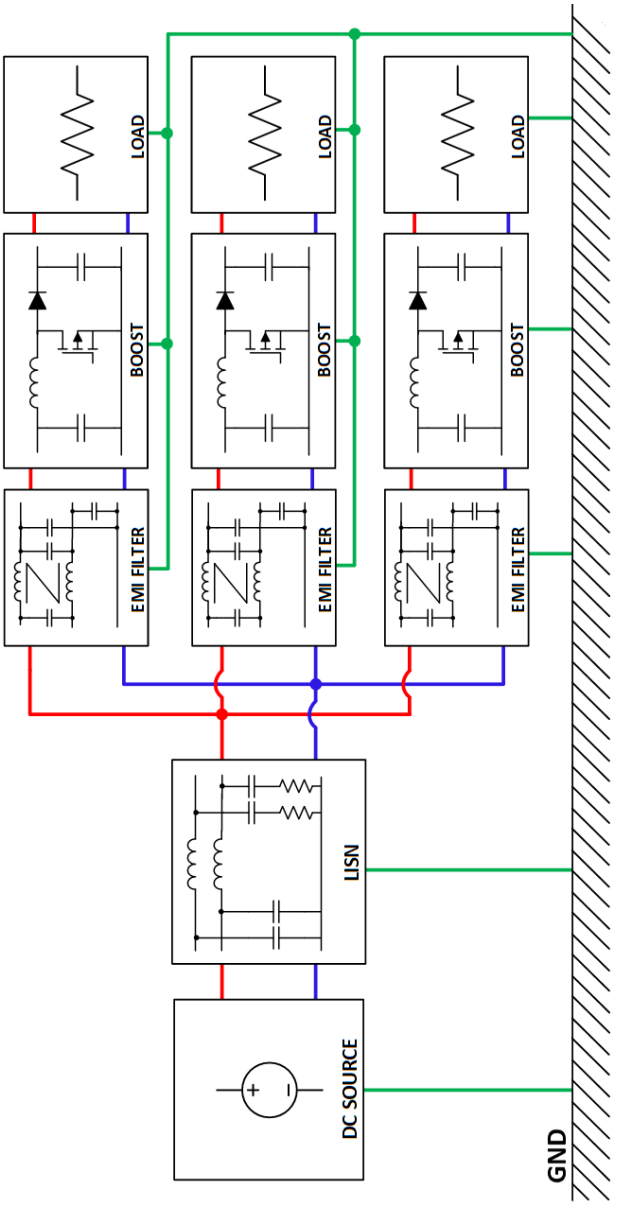

Figure II.3: Study case DC grid.

II.2.3 Grid components description.

II.2.3.1 Boost converters.

The converters used in the grid are typical boost topology power electronics devices. They are DC-DC converters increasing an output voltage magnitude which value depends on an input voltage of the converter and a duty factor of the switching part of the device [71]. All three considered converters are identical in terms of topology and components inside them. Their inputs are supplied by a voltage source V_{in}=14V and they generate V_{out}=42V on the output side where the loads are connected. The switches in each converter are MOSFETs. Their control is realized by an open-loop system based on square-shape generator which provides a gate signal changing the transistor state. The switching frequency of the converters is f_{sw}=115kHz and duty cycle DF=2/3. The schematic of the boost converter is presented in Fig.II.4. It shows all stray elements which are related to EMI behaviour of the converter. L_P and L_M are the parasitic inductances representing the wire connection between input filter and input connector present in the actual converter, $C_{in_{ESL}}$, $C_{in_{ESL}}$ are equivalent series inductance and resistance of the input filter and $C_{in_{ESL}}$, $C_{in_{ESL}}$ of the output filter respectively. L_{EPC} and L_{EPR} are equivalent parallel capacitance and resistance of the boost inductor. C_{dec} is a decoupling capacitor and C_{pg},C_{mg}, C_{pm} are stray ground capacitances of the boost converter. The stray elements which were used in the study have been identified from the actual converter availible. More details about the parasitics are described in a further Chapter II.4.2.

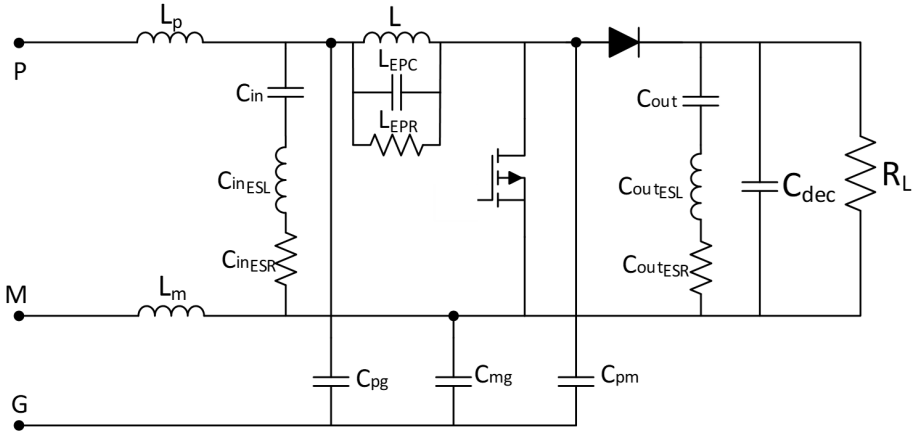

Figure II.4: Boost converter schematic including the parasitic components.

II.2.3.2 EMI filters

The role of the EMI filters is to attenuate conducted disturbances generated by a given electrical device [60]. In order to pass the conducted emission limits defined by the EMC standards the attenuation has to be sufficient in the frequency range up to 30MHz. The filters which has been used in the study case were designed with a standard approach: measuring CM / DM disturbances with a single converter connected to LISN, then comparing the disturbances to the limits defined by *DO-160* standard (the limits' details are explained in further section II.3.2) in order to define demanded filter attenuation and finally designing a filter for a given attenuation both in CM and DM. The chosen EMI filter topology is a very typical single-stage one for DC and AC single phase devices. It is composed of C_x capacitor connected between lines for DM emission filtering, Common Mode Chocke (CMC) and two C_y connected from each line (positive and negative) to the ground for CM filtering. Designed filter was constructed based on above-mentioned approach and then the physical filter was measured in order to identify all actual parasitics which led to create a precise model of the filter. The details about filter parasitics are presented in further chapter. Each boost converter has the filter which is connected between LISN and the converter itself. EMI filter schematic including parasitic components are presented below in Figure II.5.

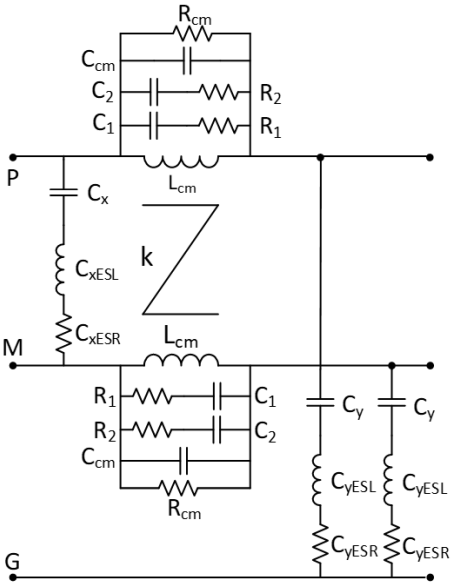

Figure II.5: Schematic of the EMI filter used in the study case.

II.2.3.3 Line Impedance Stabilization Network.

Line Impedance Stabilization Network is a device commonly used in EMI measurements. Its role is to provide a precise impedance value defined by the standard in a required frequency range (typically from 150kHz up to 30MHz). [1] Moreover, LISN acts as a low-pass filter separating the source grid from the EUT which allows to measure only disturbances generated by the device. LISN used in the study is the one defined by *DO160* standard and its role is to simulate the "real" grid impedance in the aircraft. In the analysed grid, LISN is connected between EMI filters of the converters and DC voltage source. The schematic and parameters are presented below in Fig.II.6 and Table II.1.

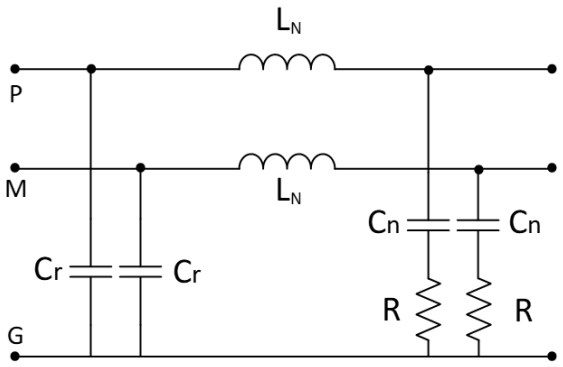

Figure II.6: Schematic of the LISN used in the study case. LISN parameters are the one used in DO160 standard.

Table II.1: Parameters of DO160 LISN.

Parameter	Unit	Value
L_N	[µH]	5
C_r	[µF]	10
C_n	[nF]	100
R	[Ω]	50

II.3 Aircraft standards EMC requirements.

There are several EMC standards where specific requirements for conducted emission are defined. Among them civil avionic standard *RTCA DO-160 Environmental Condition and Test Procedures for Airborne Equipment* has been chosen since it treats electromagnetic compatibility specifically for aircraft environment which is a subtopic of the research. *DO-160* standard has a detailed description of the conducted emission measurement setup and they level limits.

II.3.1 Conducted EMI measurement according to DO-160.

Conducted interference emission according to DO-160 should be measured from 150kHz up to 152MHz and the interference currents shall be measured by using a clamp-on interference measuring device such as current probe [34]. Moreover, Line Impedance Stabilization Network which should be inserted in each EUT power line. Standard specifies specific impedance characteristic which is presented in Fig.II.7 (with 5μ H inductor) to emulate a real aircraft grid impedance. The RF measurement port of the LISN should be terminated into 50Ω for all tests to correctly measure line current. Moreover, a 10μF capacitor has to be inserted between each LISN power input terminal and the ground plane to prevent LISNs self resonance above 10kHz. The typical conducted interference measurement setup is the Fig.II.8.

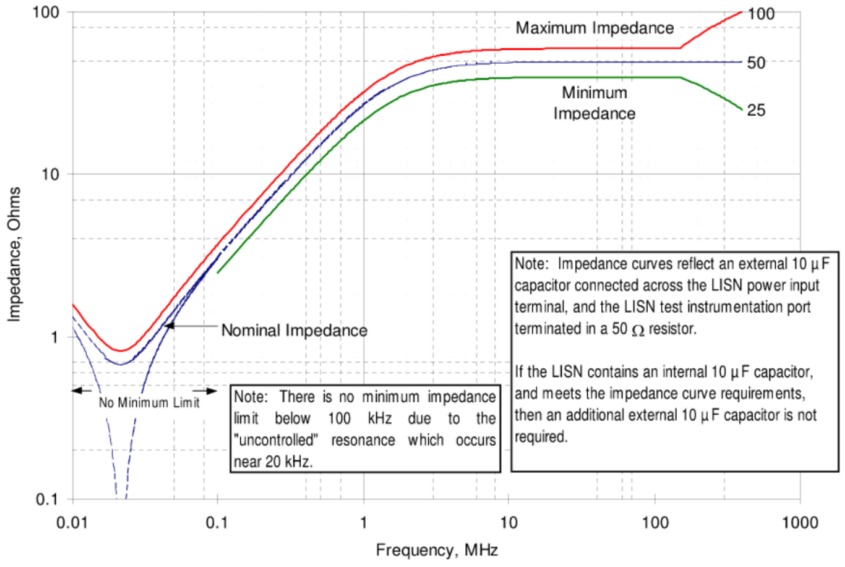

Figure II.7: LISN impedance characteristic defined in DO-160 [34].

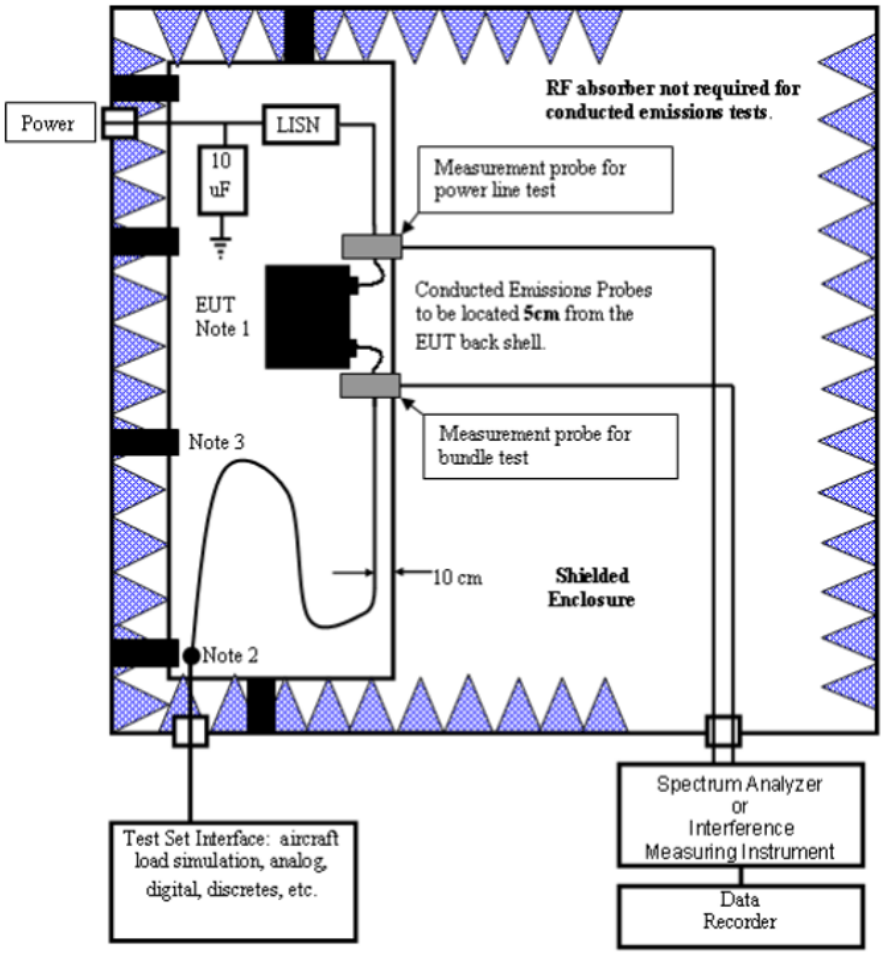

Figure II.8: Typical conducted EMI setup defined in DO-160 [34].

II.3.2 Conducted EMI requirements according to DO-160.

The standard defines many emission levels depending on equipment category. Each category definition is included in the standard. Due to the fact that converters used in the study case are simple ones and intended to use just for research purpose, the least demanding category B has been chosen. This category is intended primarily for equipment where interference should be controlled to tolerable levels. Based on this category requirement the EMI filter used in the study case has been designed.

Maximum level of conducted interference in power lines defined by DO-160 standard is presented below in Fig.II.9.

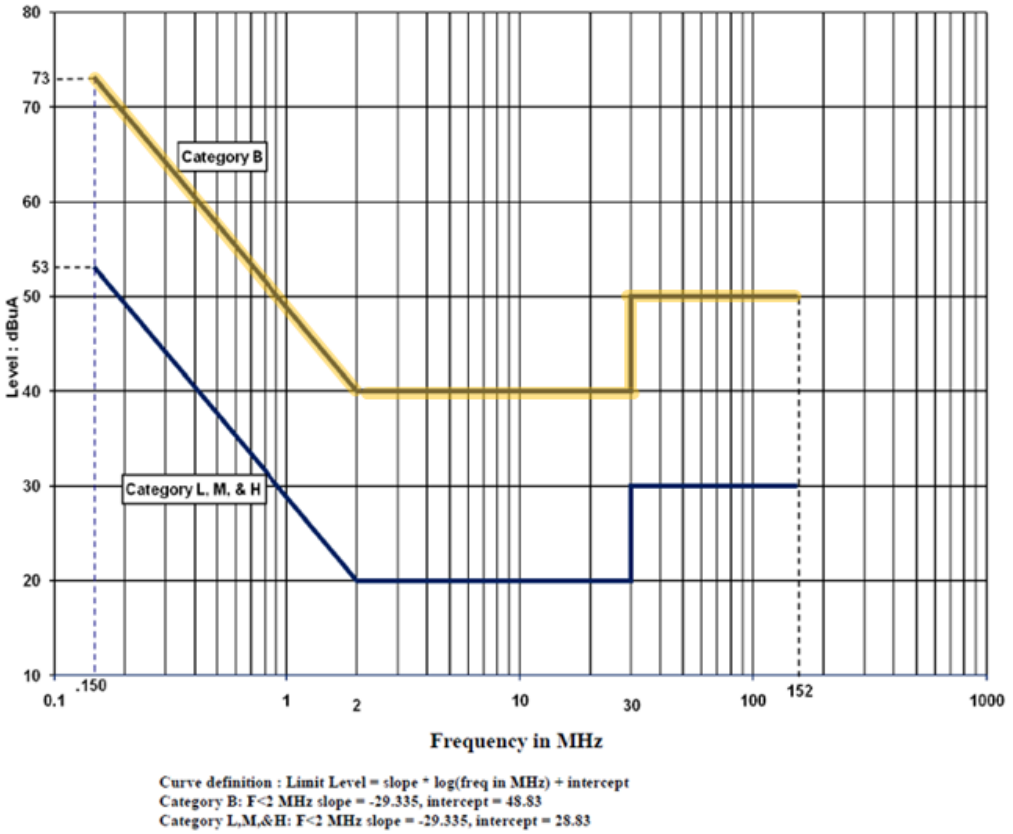

Figure II.9: Maximum conducted emission level for power lines defined in DO-160 [34].

The study do not consider the spectra until 152 MHz. A high frequency limit has been set to 100 MHz in both simulation and measurement, due to limitations of the experimental setup, the issue with time domain simulations, and also the accuracy of representation of actual converters and filters. In fact, the experimental results has shown (described in further chapters) that due to these limitations the accuracy is valid up to 10 MHz.

II.4 Conducted EMI Grid Interactions Study.

In order to study interactions between grid components in terms of conducted emission a time-domain modelling approach has been used. Despite the fact that simulation time is relatively long due to high number of components in the model which increase simulation time significantly, it was quite convenient method thanks to ability of freely changing parameters, and grid components and their composition.

II.4.1 Electromagnetic Interference modelling.

To model EMI behaviour of electrical devices and components, it is necessary to realize what is the source of EMI and what are propagation paths of the emission.

The main source of conducted electromagnetic interference are switching parts of power supplies such as MOSFETs, IGBTs etc. and in some cases DC motors. The main cause of EMI generation in the converters are quick changes of voltage (dV/dt) and current (dI/dt) which implies generation high-frequency currents in the circuit. Whereas, in DC motors interference is mainly generated by high raising edges of motor current and brush sparking which creates high-frequency noise [57].

The propagation path of the interference depends on the type of the noise and circuit components parasitics. CM propagation path is mainly dependent on stray capacitances to the ground, since common-mode current mainly flows from emission source to the ground through all lines simultaneously, while DM current circulates between lines and it highly depends on parasitics of the components, such as inductors' parasitic capacitances, capacitors' ESR and ESL etc. Moreover another propagation mechanisms can occur in a circuit through inductive and capacitive couplings [64].

II.4.2 Electrical grid components modelling.

In order to be able to predict emission in an actual grid it is necessary, in addition to the basic components of the grid, to model some parasitics which have influence on the EMI propagation and interference nature [7]. Moreover semiconductors (transistors, diodes etc.) which are present in the circuits have to be modelled more accurately than an ideal switch, since their parameters such as an inherent parasitic capacitance, resistance and inductance have a significant impact on emission.

All components of the grid has been modelled on the basis of actual ones which has been available in the lab. Boost converters, EMI filter design and the parasitics identification process has been conducted in the previous work [15] and therefore the details will be not described in this thesis.

Boost converter and EMI filter are the most impactful in the grid in terms of EMC. Their parameters were defined based of the actual components previously designed and constructed. The constructed boost converter and filter are presented in Figures II.10 and II.11.

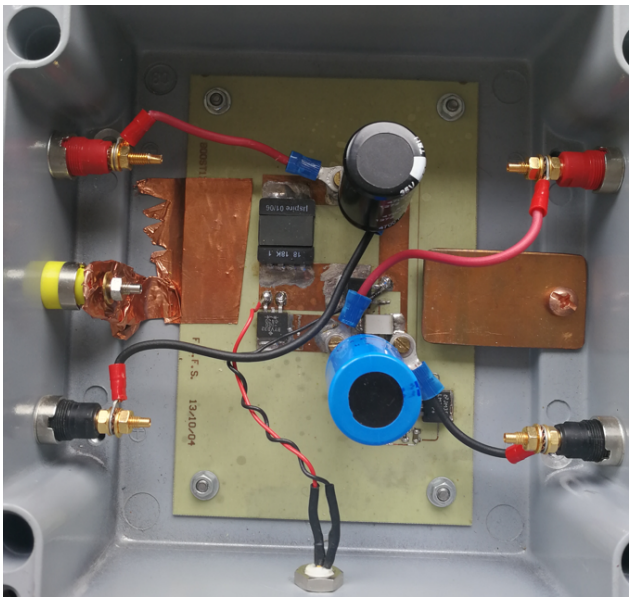

Figure II.10: One of the constructed boost converters.

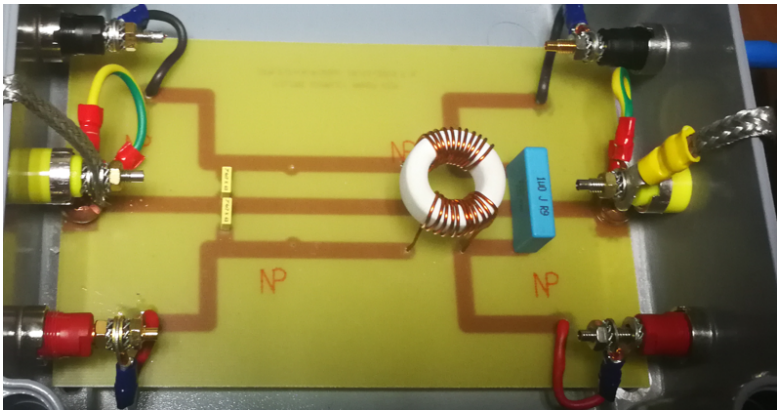

Figure II.11: One of the constructed EMI filters.

All parasitics of the gird components such as converters, filters has been identified using an impedance analyser . The detailed parameters including the parasitics which has been identified are presented in Table II.2 and Table II.3.

Table II.2: Parameters of the boost converter including parasitics.

Parameter	**Unit**	**Value**
L_p	[nH]	140
L_m	[nH]	140
C_{in}	[µF]	4700
$C_{in_{ESL}}$	[nH]	40
$C_{in_{ESR}}$	[mΩ]	60
L	[µH]	18.8
L_{EPC}	[pF]	13
L_{EPR}	[kΩ]	3.96
C_{pg}	[pF]	300
C_{mg}	[pF]	300
C_{pm}	[pF]	240
C_{out}	[µF]	470
$C_{out_{ESL}}$	[nH]	40
$C_{out_{ESR}}$	[mΩ]	60
C_{dec}	[µF]	1
R_L	[Ω]	42

In the study all three converters were based on the same physical converter (from Fig.II.10). Therefore, the stray elements in the further study are the same in each converter which would not be a case if we treat a real converters since the parasitics depends on many factors such as layout, grounding method etc. which cannot be perfectly repeatable.

Table II.3: Parameters of the EMI filter.

Parameter	Unit	Value
L_{cm}	[µH]	660
C_{cm}	[pF]	3.1
R_{cm}	[kΩ]	3.5
C_1	[pF]	10
R_1	[kΩ]	55
C_2	[pF]	75
R_2	[kΩ]	11.5
C_X	[µF]	1
$C_{X_{ESL}}$	[nH]	13
$C_{X_{ESR}}$	[mΩ]	20
C_Y	[nF]	4.5
$C_{Y_{ESL}}$	[nH]	300
$C_{Y_{ESR}}$	[mΩ]	300

It needs to be mentioned that EMI filter is constructed as a standalone device in an individual casing which is meant to be plugged to another devices (for research purposes), therefore its stray elements are quite unusual comparing to the typical ones.

Fig. II.12 shows an example measurement impedance of input capacitor including connection wires in order to determine wires inductance and capacitance ESR and ESL values.

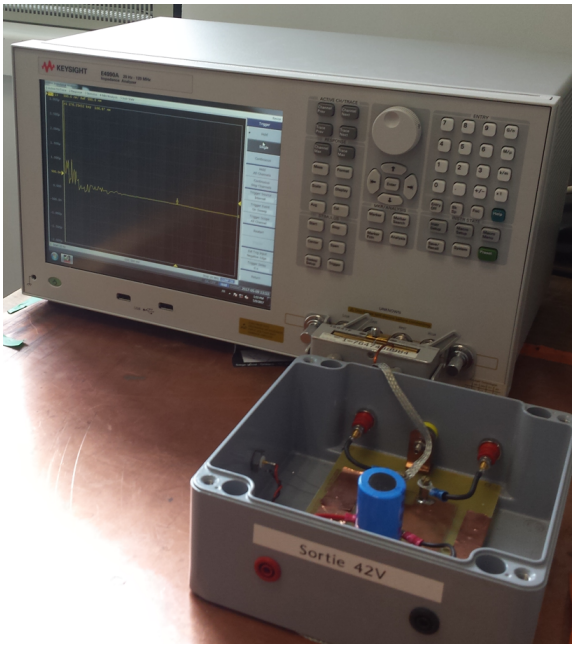

Figure II.12: Input impedance characterization using an impedance analyser.

The grid has been implemented in time-domain simulation model which allowed to simulate its standard operation of. All identified parameters (including parasitics) has been added to the models which allowed to simulate EMI behaviour of them. The models has been implemented to SPICE simulator software where time-domain analysis has been conducted. The detailed models of the converter, EMI filter, connecting cables and LISN are presented in the following Figures II.13, II.14, II.15, II.16.

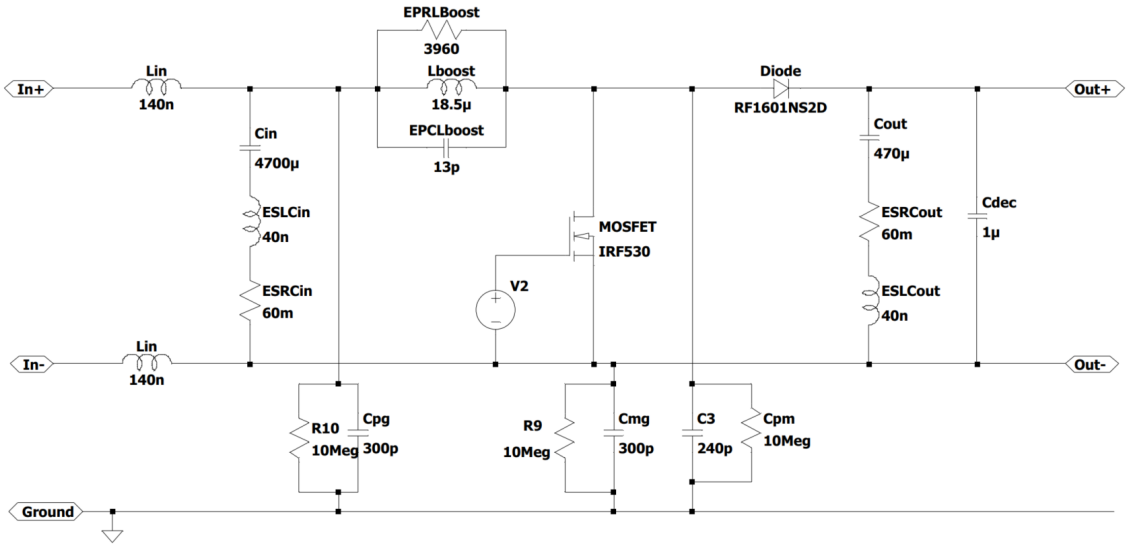

Figure II.13: Model of boost converter used in the work.

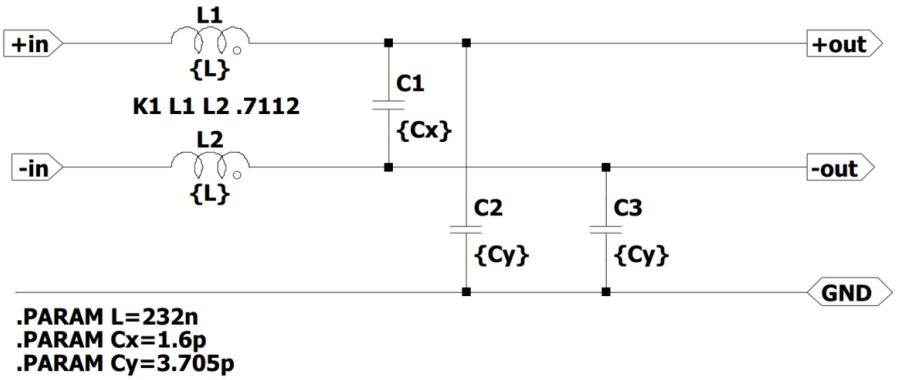

Figure II.14: Model of a cable used in the simulation.

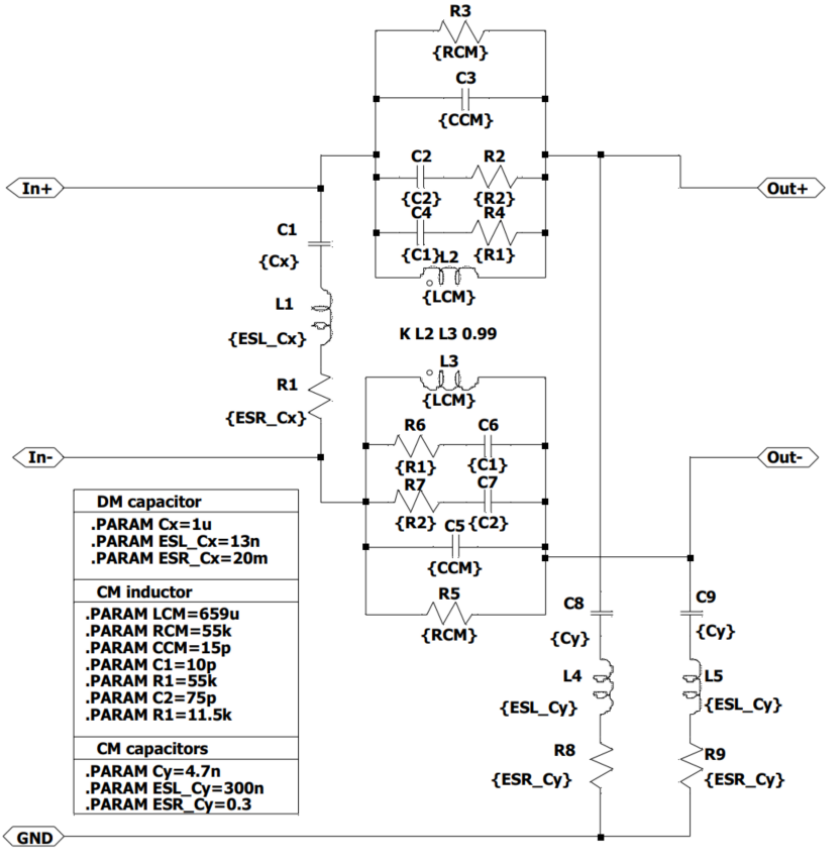

Figure II.15: Model of designed EMI filter including components parasitics.

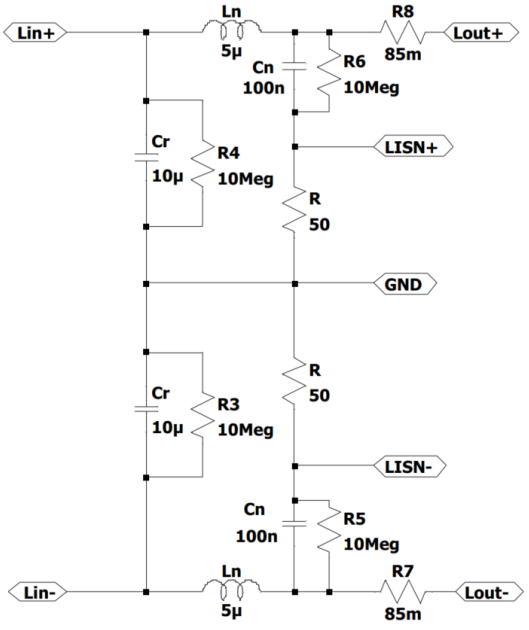

Figure II.16: Model of the LISN used in the study case based on DO160 standard.

II.4.3 Time-domain simulation interactions study.

In order to determine whether any EMI-related interactions occur in the grid, a study based time-domain simulation including accurate models described above has been conducted. The aim was to check what is the impact of number of converters on grid's total emission, in particular, whether it is a bare sum of emission generated by each converter or it is different due to impedance of another converters and other grid components such as cables, type of connections etc.

To check the influence two simulations has been conducted, one with a grid based on a single converter which was connected to the EMI Filter and LISN through cables and a second one where three boosts converters with EMI Filters were connected in parallel to LISN. The grid models implemented in SPICE software in order to perform time-domain simulation are presented in the following Fig.II.17 and Fig.II.18.

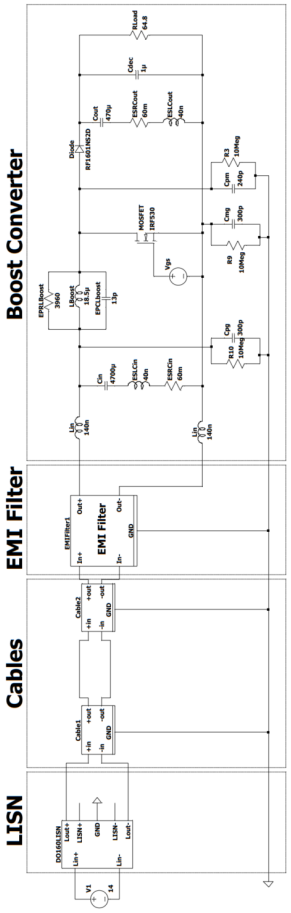

Figure II.17: Model of the DC grid which consist of DO160 LISN, cables, EMI Filter and a single boost converter.

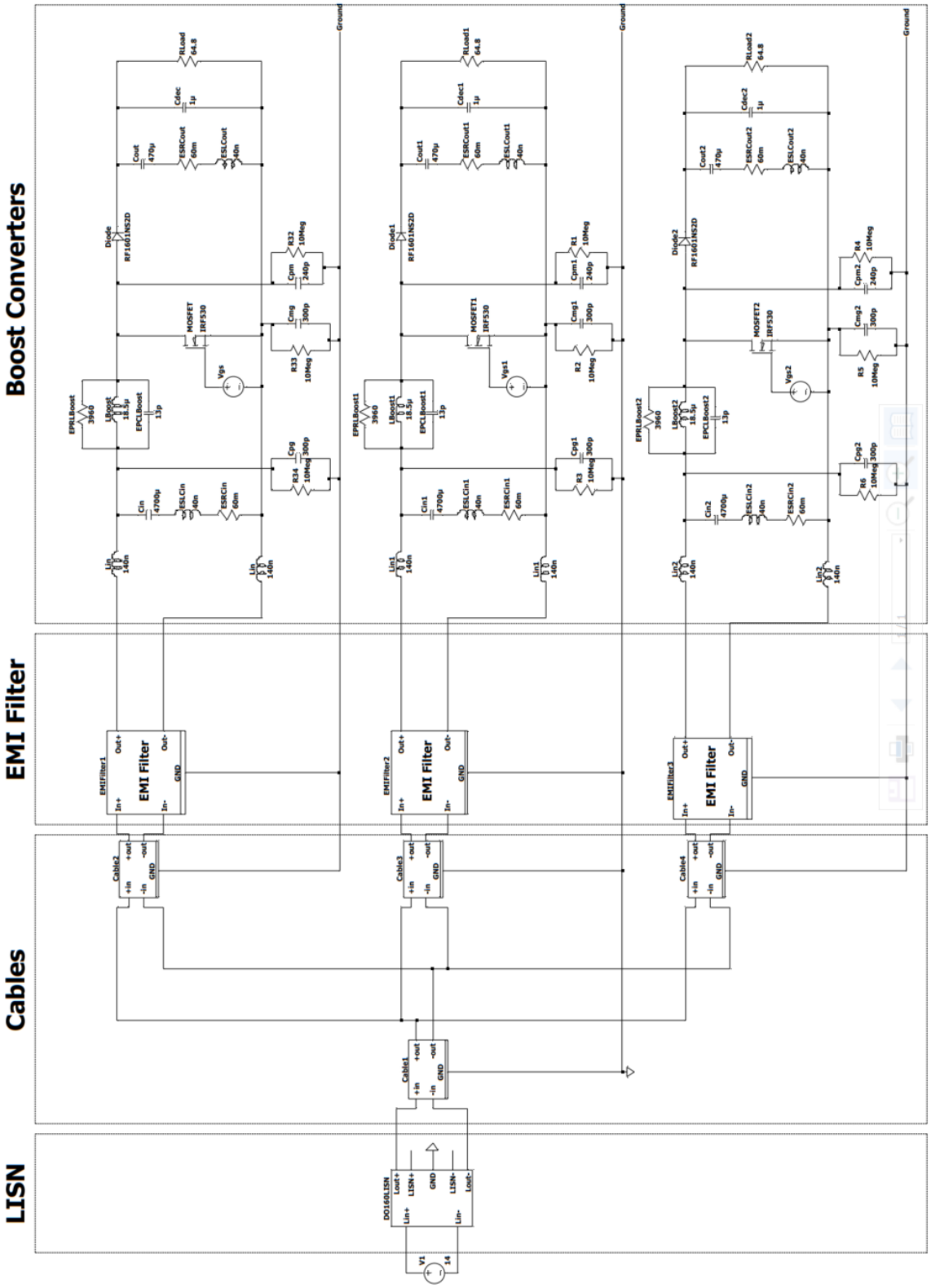

Figure II.18: Model of the DC grid which consist of DO160 LISN, cables, EMI Filter and three boost converters connected in parallel.

In both scenarios conducted emission was identified by measuring a line current flowing to the LISN (this method is determined by DO160 standard [34] which was explained in details in the Chapter II.3.1). Then based on current measurement a CM/DM decomposition [53] has been done by the following equations:

$$I_{DM} = \frac{I_P - I_N}{2} \tag{II.1}$$

$$I_{CM} = \frac{I_P + I_N}{2} \tag{II.2}$$

Where:

– I_{DM} differential mode current

– I_{CM} common mode current

– I_P positive line current flowing to LISN

– I_N negative line current flowing to LISN

Afterwards, based on the obtained results FFT was performed in order to transform time-domain data to frequency-domain which is more convenient for EMI analysis since disturbance currents contain wideband frequency components. Then a comparison has been done in order to determine possible interactions: three times the emission generated from single converter in a grid versus total emission from grid of converters connected in parallel. The converters in the simulation were exactly the same to simplify the computation but the converter which has been triplicate was firstly identified experimentally. The results for both I_1, I_2 (I_1 is positive current I_2 is negative current) and I_{CM}, I_{DM} currents in frequency domain are presented below in Fig. II.19 and Fig. II.20

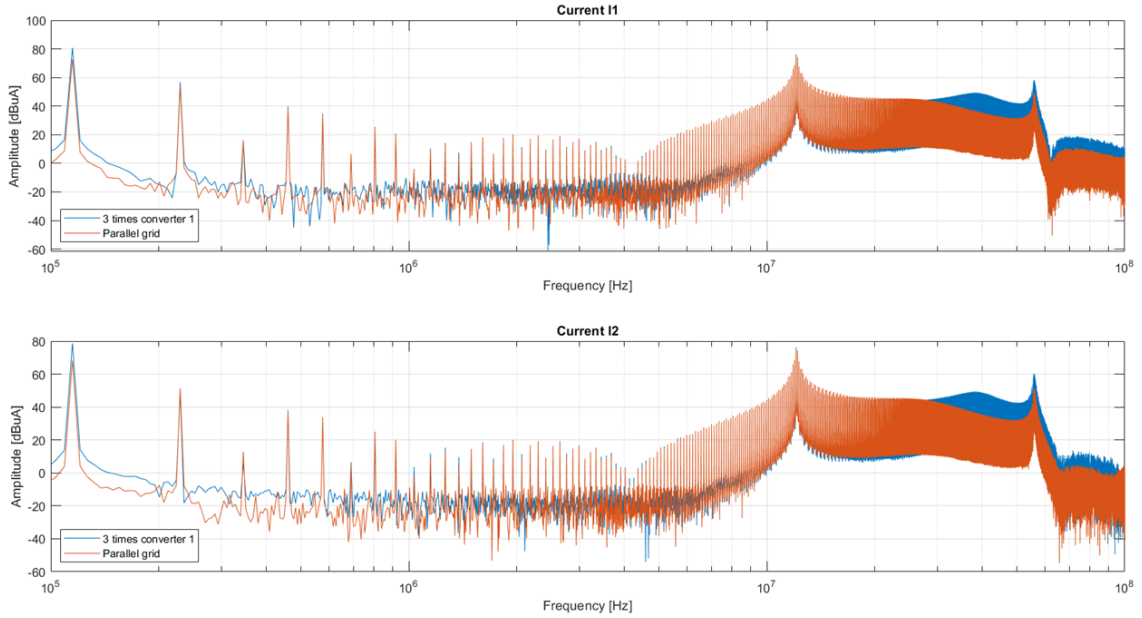

Figure II.19: Comparison between triple emission from single converter grid versus emission from grid of parallel converters for I_1 and I_2 currents in frequency-domain.

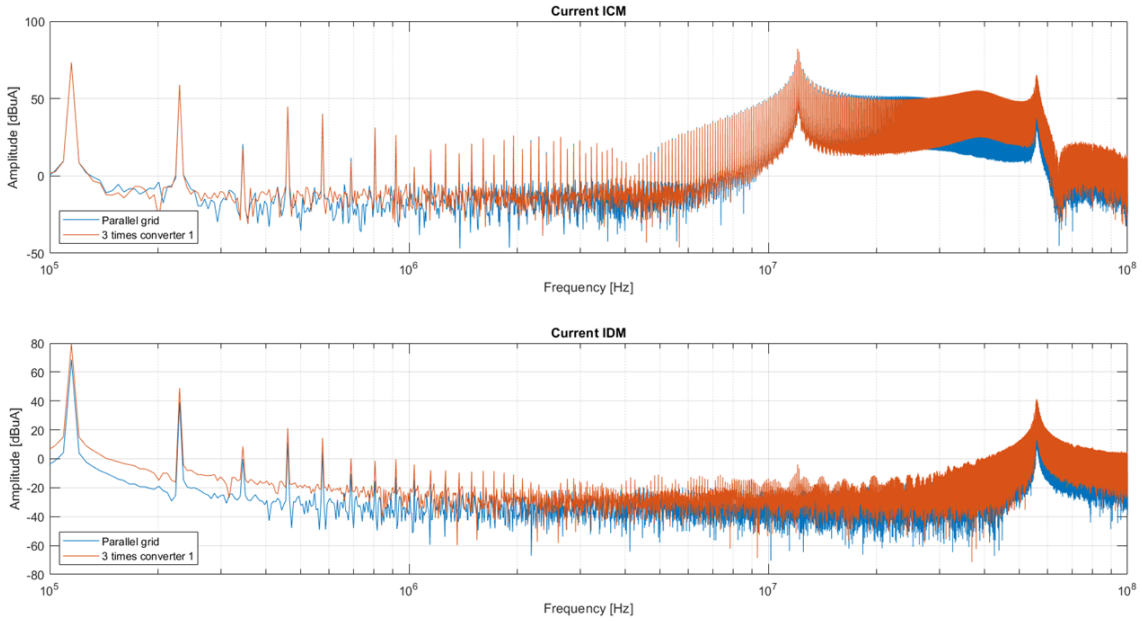

Figure II.20: Comparison between triple emission from single converter grid versus emission from grid of parallel converters for I_{CM} and I_{DM} currents in frequency-domain.

The analysis revealed that there is a significant difference of EMI level between the case when single converter is considered and the scenario when multiple converters are connected to the common grid. After the disturbance current decomposition to CM and DM it can be seen that the DM current is very much different in a parallel grid than a single converter scenario (10dB difference), whereas, CM current remaining the same up to around 20MHz, however, above the difference is up to 5dB. DM current generated by each converter in a parallel grid does not circulating just between converter and LISN but part of it flows through other grid components due to their DM impedance, in other words, another grid parts filter part of emission.

It can be seen that with multi converter scenario total emission can be lower due to positive interaction effect, however it must be taken into account that a ringing phenomenon can occur between grid components which can amplify level of disturbance for some frequencies where the resonance occurs, which in total can have a negative impact in terms of EMI.

To sum up, the study proved that the approach defined in the standards of treating each converter individually might not be an optimal solution, since in the case which has been studied it would lead to over-design of EMI filters for each converter. The method which has been used in the study described in this chapter would not be usable in a case of much more devices in the grid, in particular switching components. It is limited due to computing power, simulation time, convergence issues and some numerical error risks. Therefore, the study which will be described in the following chapters will be focused on lightweight EMI modelling to be able to simulate EMI in much more complex grids.

II.5 EMC Black Box modelling.

There are several modelling approaches which can be used for EMC analysis. The most common one is a time-domain simulation which has been utilized in the previously described analysis, however, as it was mentioned before, this method is not suitable for large systems including several electrical devices such as power supplies [40]. Another popular method is a frequency-domain modelling using equivalent sources which represent the switching cell of the device responsible for EMI generation. This method is much more efficient than the time-domain modelling since the sources can be expressed in the frequency-domain and therefore the circuit equations can be solved very quickly. Nevertheless, the main issue of this method is necessity of knowing perfectly the stray elements of the device in order to correctly reproduce its EMI behaviour. In addition, the equivalent sources localization is arbitrary and thus it can incorrectly represent disturbance current flow in the circuit [46],[30].

The other method and in fact the one which has been chosen is a Black Box modelling approach. In this method similarly to frequency-domain simulation all parameters can be represented in frequency-domain which makes it suitable for EMI-modelling application. In addition, in this approach the device is seen from its external connections only, therefore there is no need of identifying each component inside the device [6]. Moreover, it is not necessary to know how the device is built. There are two different types of Black Box models, terminated which are intended to use when the device output is constant [6],[9], and unterminated which allows EMI investigation on both source and load sides – this method is very interesting when load is changing or if the device works as interconnection of two different grids [68].

II.5.1 Terminated Black Box model description.

The Black Box model approach which has been chosen is a terminated one since in the study case grid loads are constant and there are no devices connected to converters outputs. There are several topologies of the models, among them two significant ones: a Norton based [25] and hybrid. The example of both models is presented below in Fig.II.21.

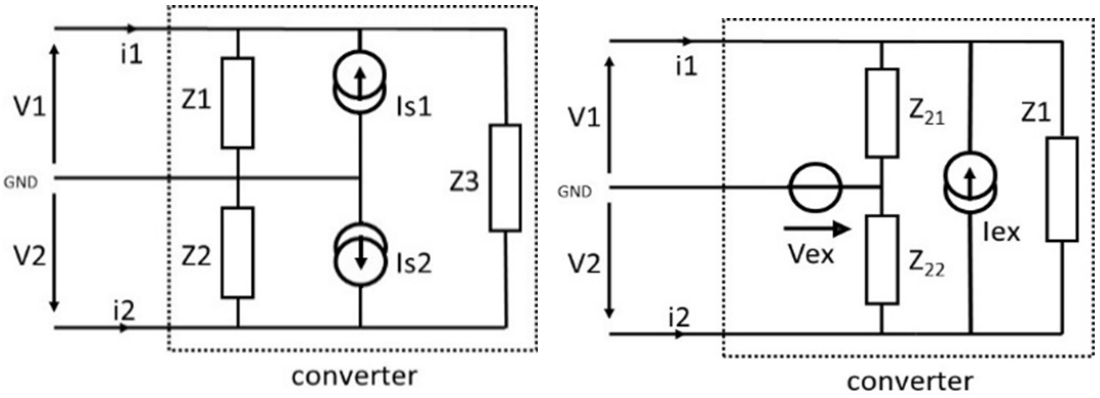

Figure II.21: Various Black Box model topologies. On the left Norton based, on the right Hybrid.

The hybrid Black Box modelling representation has been chosen. In this model current source is placed between lines and voltage source between line and the ground. V_{ex} mostly represents (but not only which will be expalined later) an excitation source of common mode in the device, whereas I_{ex} mostly represents differential mode excitation source. Impedances Z_{21} and Z_{22} are common mode impedances from each line to the ground. Impedance Z_1 is DM impedance between lines. The model can be used in both single-phase AC and DC applications to estimate EMI from the devices.

II.5.2 Blackbox model identification.

There are two methods of identification the terminated Black Box model parameters. The first one uses line current measurements when the device is operating on known impedances, then changing these impedances allows identifying the model parameters [9]. The second approach uses two types of measurement, first is offline impedance measurement on the device's input terminals and combines them with the second measurement of line currents recording when device operates on a known environment (such as LISNs). Combination of both measurements allows to obtain the two sources V_{ex} and I_{ex}.

The main assumption in this method (detailed in section II.5.1) is that the impedance measured offline (i.e. converter not switching) are not modified when the converter will be switching.

The common statement when using Black Box models assumes symmetry of both the model (Z_{21} =Z_{22}) and the grid [6],[9], to link CM current to Vex only, and DM current to Iex only. However, this situation is not common in the general case, and in usually both sources of the model contribute to CM and DM generation. Consequently, identifying a symmetrical model, even with symmetric grid, with the assumption of mode separation may be wrong. Also using a symmetrical model in an asymmetrical grid could lead to wrong results. Therefore, it was decided to identify an asymmetrical Black Box model with $Z_{21} \neq Z_{22}$ which can be more precise in asymmetrical environment conditions [17].

II.5.2.1 Model impedances identification.

According to work presented in [5] impedance seen from converter terminals is not modified significantly when the switches state changes, therefore, an assumption of "masking impedance" has been used allowing use constant impedance whatever the semiconductors state. Thus, the method of offline impedance measurement could used for the identification process.

In order to identify impedances in the model three different measurement configurations had to be performed since there are three input terminals in the model. The first one is an impedance measurement between negative and ground terminals with positive terminal shorted to the ground, the second is the measurement between positive and ground terminals with a negative terminal shorted to the ground and the last one is an impedance measurement between both positive and negative terminals and ground while they are shorted together. The measurement setup configurations are presented in Fig.II.22.

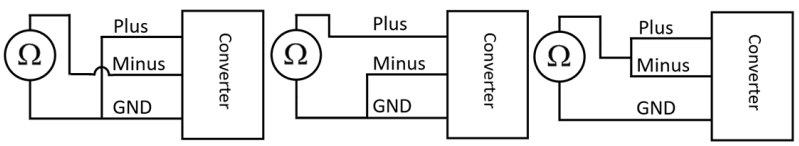

Figure II.22: The impedance measurement configurations allowing identify the impedances of the model. First is Z_{PG} with Plus and Ground connected, the second Z_{MG} with Minus and Ground connected and the last one Z_{PM} with Plus and Minus connected.

The measurement allowed to identify impedances used in the Black Box model by computing them with following equations:

$$Z_1 = \frac{2 \cdot Z_{MG} \cdot Z_{PG} \cdot Z_{PM}}{Z_{MG} \cdot Z_{PM} - Z_{MG} \cdot Z_{PG} + Z_{PG} \cdot Z_{PM}} \tag{II.3}$$

$$Z_{21} = \frac{2 \cdot Z_{MG} \cdot Z_{PG} \cdot Z_{PM}}{Z_{MG} \cdot Z_{PG} - Z_{MG} \cdot Z_{PM} + Z_{PG} \cdot Z_{PM}} \tag{II.4}$$

$$Z_{22} = \frac{2 \cdot Z_{MG} \cdot Z_{PG} \cdot Z_{PM}}{Z_{MG} \cdot Z_{PG} + Z_{MG} \cdot Z_{PM} - Z_{PG} \cdot Z_{PM}} \tag{II.5}$$

Where:

– Z_1 impedance between line terminals in the Black Box model

– Z_{21} impedance between positive terminal and Voltage source in the Black Box model

– Z_{22} impedance between negative terminal and Voltage source in the Black Box model

– Z_{PG} measured impedance in a configuration with positive and ground terminals shorted

– Z_{MG} measured impedance in a configuration with negative and ground terminals shorted

– Z_{PM} measured impedance in a configuration with positive and negative terminals shorted

The advantage of the chosen impedance identification method, beside the considering non-symmetry which can happen in the device, is the measurement method itself. In this measurement there is no "floating" measurement (a pure differential mode measurement necessitates the use of a balun for high frequencies [47], which complexifies the process.). One of the points in the measurement setup is always connected to the ground of the equipment under test. This reduces amount of CM current derived to the ground (known as common mode leakage phenomena) and therefore makes impedance identification process more accurate. This CM leakage reduction effect is presented in Fig.II.23.

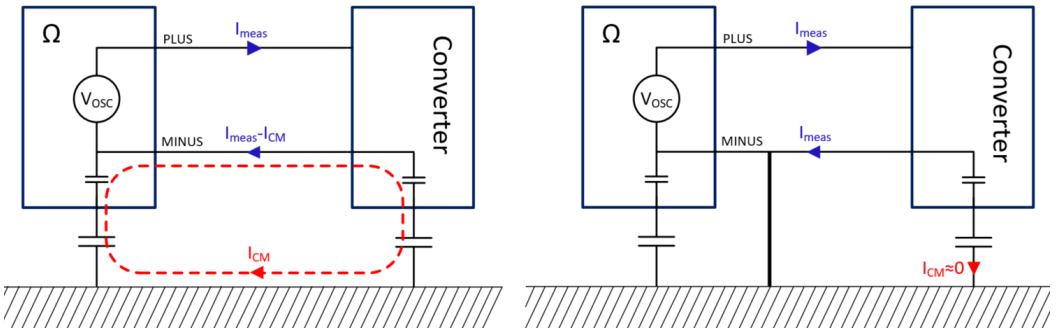

Figure II.23: Reducing CM circulation in measurement circuit by shorting impedance measurement device to the ground.

II.5.2.2 Equivalent sources identification.

In order to determine two remaining parameters of the Black Box model is necessary to perform line currents measurement in a known environment. The known environment used in identification process is a LISN since it has well defined impedance in a wide spectrum. The LISN used for the sources identification in simulation is the one based on DO160 standard requirement ans has been explained in detail in previous Chapter II.2.3.3, whereas for experimental identification another one based on CISPR 16 standard has been used (due to its availability in the lab). Figure II.24 presents an example view of line current measurement for equivalent sources identification.

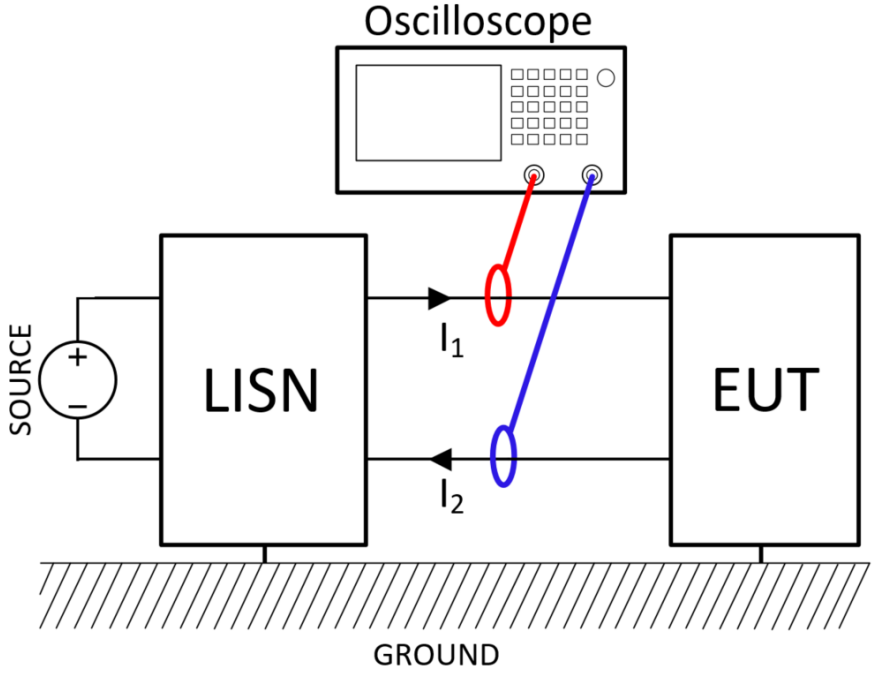

Figure II.24: Example of line currents measurement for Black Box model identification.

When both line currents and model's impedances have been obtained it is possible to determine V_{ex} and I_{ex} sources. The following equations present how equivalent sources can be computed.

$$V_{ex}(s) = I_1(s) \cdot \frac{Z_L \cdot Z_{22} + Z_{21} \cdot Z_{22}}{Z_{21} + Z_{22}} + I_2(s) \cdot \frac{Z_L \cdot Z_{21} + Z_{21} \cdot Z_{22}}{Z_{21} + Z_{22}} \tag{II.6}$$

$$\begin{aligned} I_{ex}(s) = -I_1(s) \cdot \frac{Z_1 \cdot Z_L + Z_1 \cdot Z_{21} + Z_L \cdot Z_{21} + Z_L \cdot Z_{22}}{Z_1 \cdot Z_{21} + Z_1 \cdot Z_{22}} + \\ + I_2(s) \cdot \frac{Z_1 \cdot Z_L + Z_1 \cdot Z_{22} + Z_L \cdot Z_{21} + Z_L \cdot Z_{22}}{Z_1 \cdot Z_{21} + Z_1 \cdot Z_{22}} \end{aligned} \tag{II.7}$$

Where:

– $V_{ex}(s)$ Black Box model equivalent voltage source

– $I_{ex}(s)$ eBlack Box model equivalent current source

– $I_1(s)$ measured positive line current in a function of frequency

– $I_2(s)$ measured negative line current in a function of frequency

– Z_L line to ground impedance of the LISN

– Z_1 impedance between line terminals in the Black Box model

– Z_{21} impedance between positive terminal and Voltage source in the Black Box model

– Z_{22} impedance between negative terminal and Voltage source in the Black Box model

It is worth noting that the line currents must be recorded together to keep the information of the phase shift. It is necessary since in the computation of the equivalent sources complex impedances are used. Therefore, in the scenario when the identification is performed in a physical setup, measuring devices such as Spectrum Analysers or EMI Receiver cannot be utilized since they do not record the phase shift. Thus, time domain waveforms with Fourier Transform processing have to be used.

II.5.2.3 Black Box model identification based on simulation.

The first Black Box model which has been identified was an EMI model of the boost converter based on time-domain SPICE simulation which has been used in the previous study.

In order to perform identification two types of simulation had to be run. The first one was a time-domain simulation with the converter connected to DO160 LISN since it is a known environment which is necessary for the identification procedure. Input line currents I_1 and I_2 have been measured and then have been processed with FFT in order to obtain frequency-domain currents for Black Box model's excitation sources computation. The simulation model used for line current measurement and the result processed by FFT are presented below in Fig.II.25 and Fig.II.26.

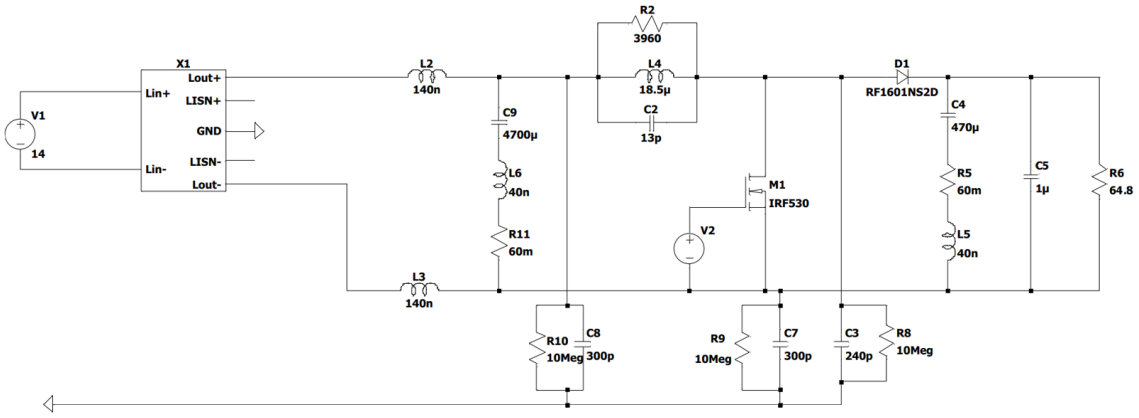

Figure II.25: Time-domain SPICE simulation model for line currents measurement.

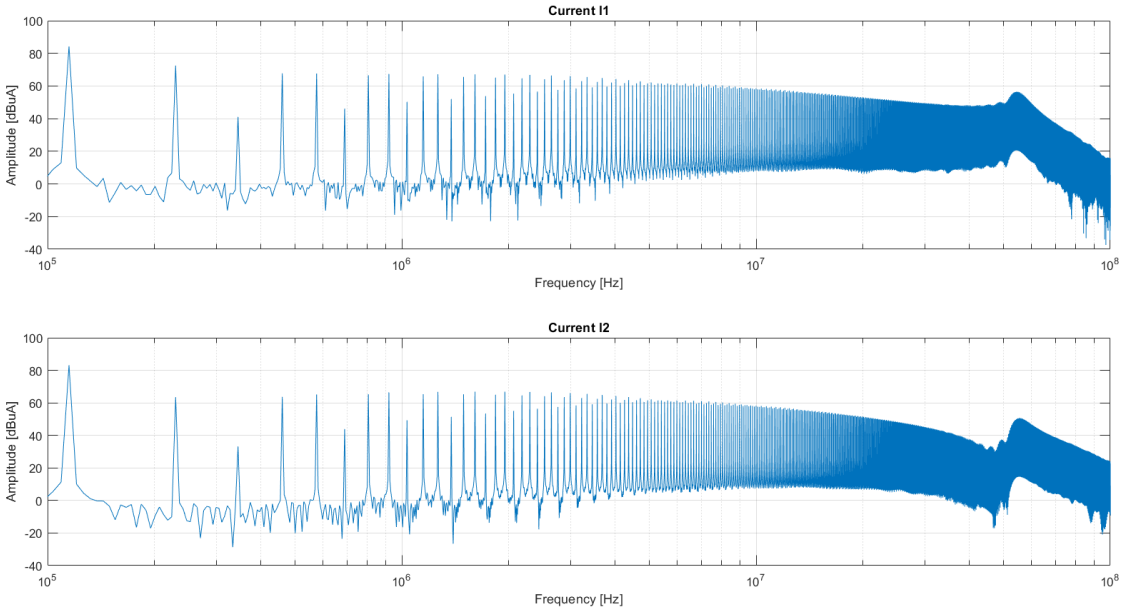

Figure II.26: Obtained line currents FFT result.

The second type of simulation which had to be performed in order to obtain necessary data for Black Box model was the AC Sweep simulation where the small-signal response of the circuit is obtained. Thanks to that it was possible to obtain impedance of the circuit in the defined frequency range. To obtain impedance with AC Sweep a current source with amplitude of 1A was connected between converter's input and the ground. Then, voltage across terminals connected to the source were measured which corresponds to the impedance across the terminals due to Ohm's law Z=U/I where I is equal to 1, thus Z=U. MOSFET switch has been shorted since as it was mentioned before its impedance has insignificant influence on the model accuracy. AC Sweep was performed in three configurations Z_{PG}, Z_{MG} and Z_{PM} to be able to obtain Black Box model impedances.
AC Sweep simulation with a measurement setup where a plus terminal is shorted to the ground is presented below on Fig.II.27 the measured Z_{PG} impedance is presented in Fig.II.28.

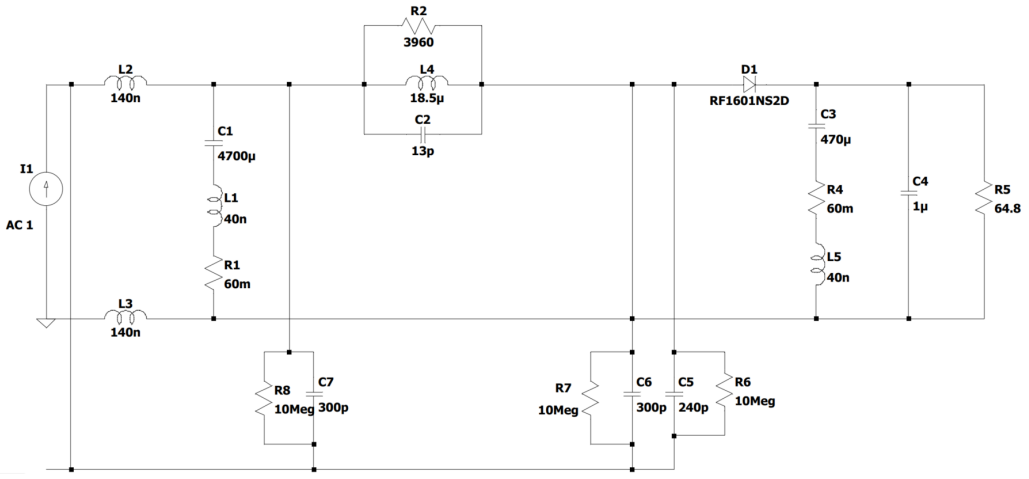

Figure II.27: AC Sweep simulation for model for Z_{PG} impedance measurement.

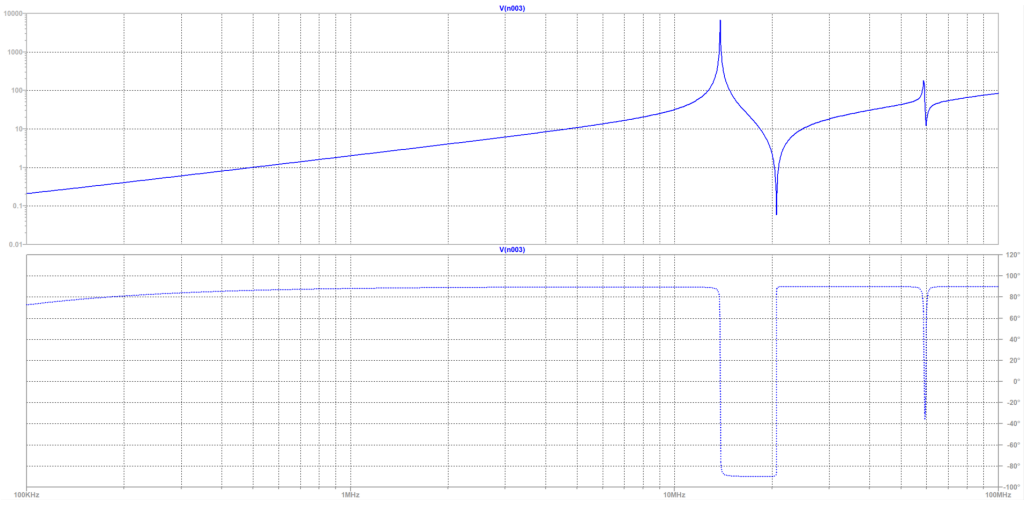

Figure II.28: Measured Z_{PG} impedance with presented both module and phase shift.

AC Sweep simulation with a measurement setup where a minus terminal is shorted to the ground is presented below on Fig.II.29 the measured Z_{MG} impedance is presented in Fig.II.30.

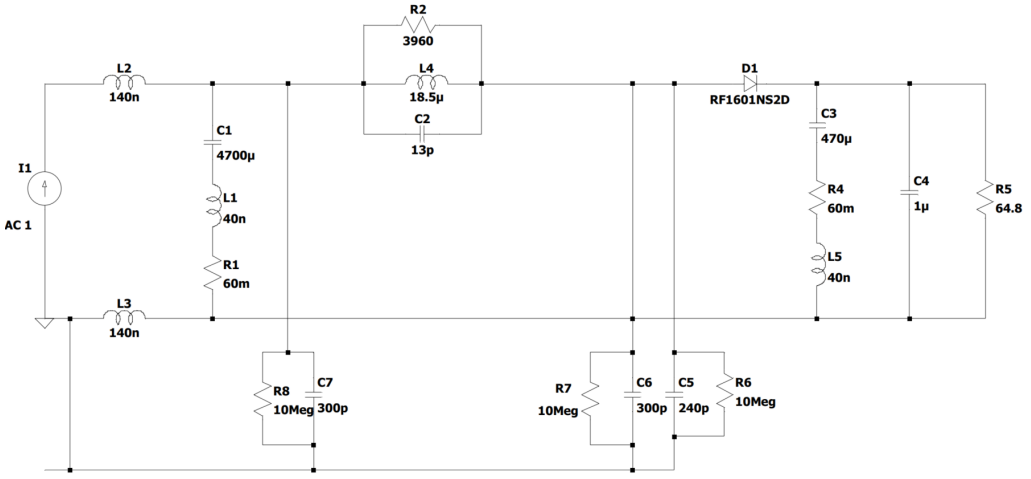

Figure II.29: AC Sweep simulation for model for Z_{MG} impedance measurement.

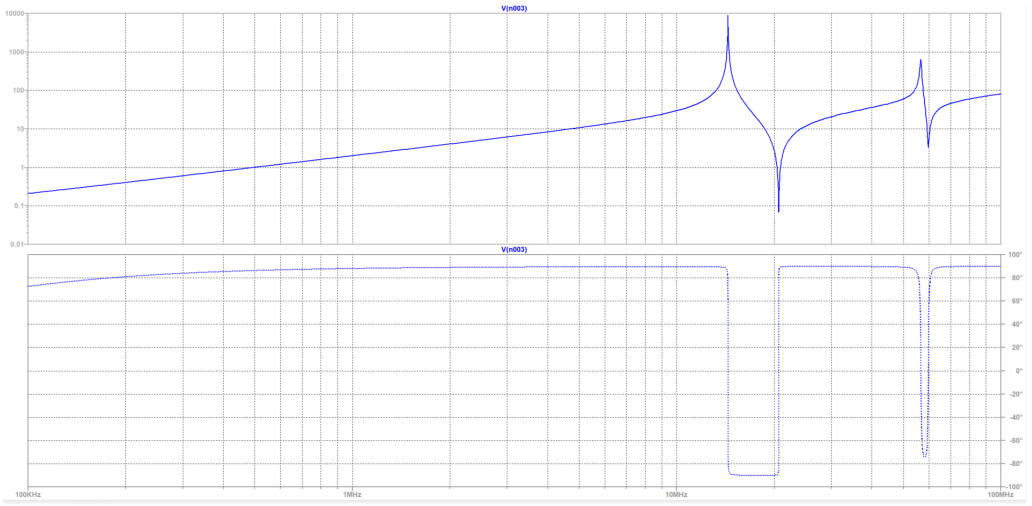

Figure II.30: Measured Z_{MG} impedance with presented both module and phase shift.

AC Sweep simulation with a measurement setup where a minus terminal is shorted to the ground is presented below on Fig.II.31 the measured Z_{PM} impedance is presented in Fig.II.32.

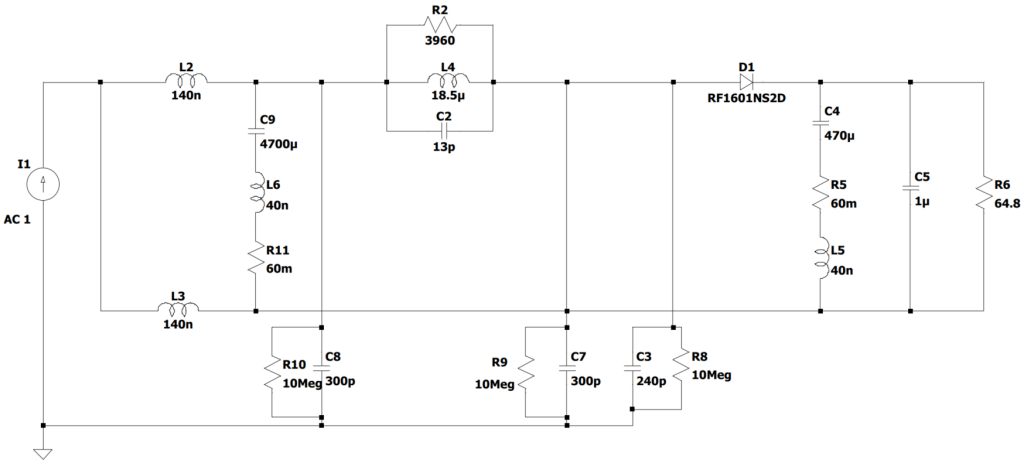

Figure II.31: AC Sweep simulation for model for Z_{PM} impedance measurement.

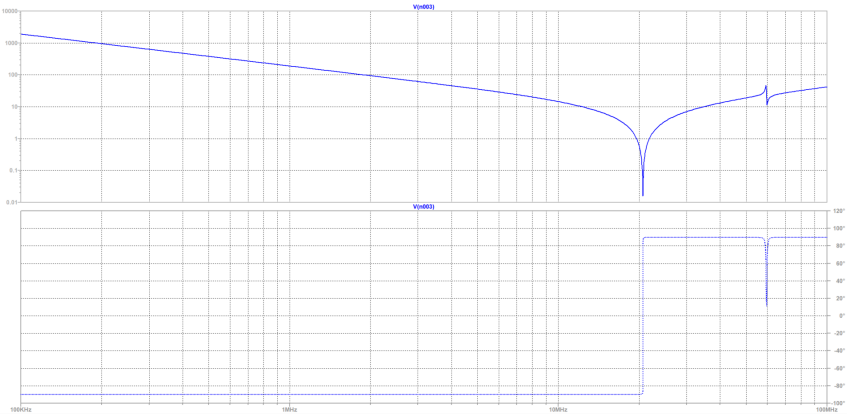

Figure II.32: Measured Z_{PM} impedance with presented both module and phase shift.

When all measurements which are needed for Black Box model identification were conducted, it was possible to compute Black Box model parameters thanks to previously presented equations Eq.(II.3),Eq.(II.4),Eq.(II.5),Eq.(II.6) and Eq.(II.7).

Figure II.33 presents the comparison between Z_{21} and Z_{Z22} computed from impedances obtained from time-domain model AC analysis. It can be seen that the impedances are matching quite well which is reasonable since no significant asymmetry is introduced in time-domain model (stray capacitances only). Nevertheless, there is a difference in high frequency (57MHz), therefore, is reasonable to assume asymmetry in the model.

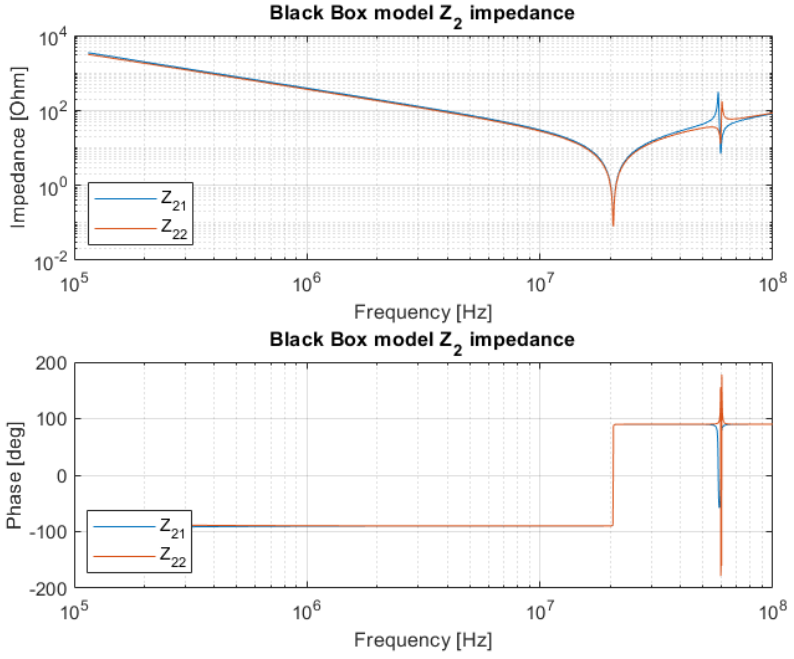

Figure II.33: Comparison between Black Box model impedances Z_{21} and Z_{Z22} obtained from simulation identification.

II.5.2.4 Black Box model identification based on experimental measurement.

The second Black Box model which has been identified was based on the actual converter which was available in the laboratory.

Similarly to the previous case, to perform identification two types of measurements have been done. The first one was the online measurement of line currents when converters was working in its operating point with LISN connected between converter input and the voltage source. Input line currents I_1 and I_2 have been measured with oscilloscope using a high amount of data points (500k) and a high dynamic range (11bits) in order to capture as accurate as possible data in a possibly high frequency range. Currents were recorded simultaneously in order to keep identical phase shift of both currents. Afterwards, recorded data have been processed with FFT in order to obtain frequency-domain currents. The identification is performed only on the relevant peaks (related to emission not to a background noise) of the FFT, therefore, care has to be taken to the numerical processing of the signals to avoid a bad evaluation of the amplitude of the peaks: a mismatch in the exact frequency may result in a large error in the peak amplitude and therefore in the model evaluation. This aspect was not critic in simulation, since the switching frequency was perfectly known, however, in measurement a small jitter is always present and peak search becomes critical.

The measurement setup composed of Bench Power Supply working as voltage source, LISN, Boost converter, rheostat (load with adjustable resistance) and oscilloscope with two high-frequency current probes for the measurement. The setup and the obtained current measurement after FFT process are presented in Fig.II.34 and Fig.II.35.

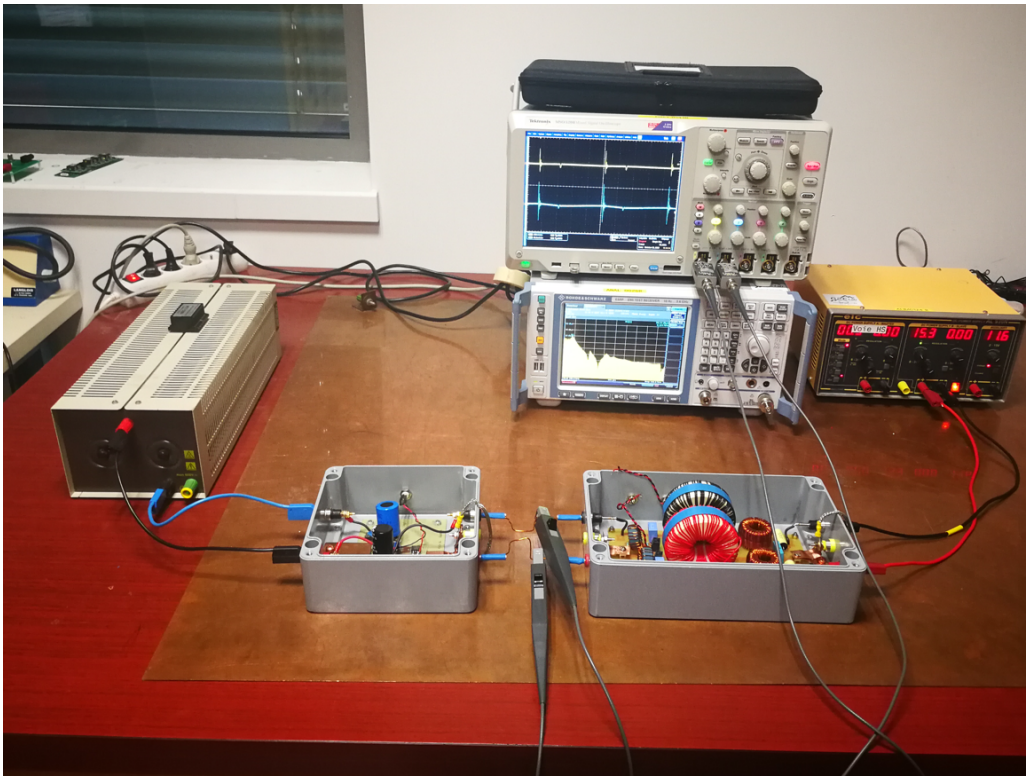

Figure II.34: Line currents measurement setup for Black Box model identification.

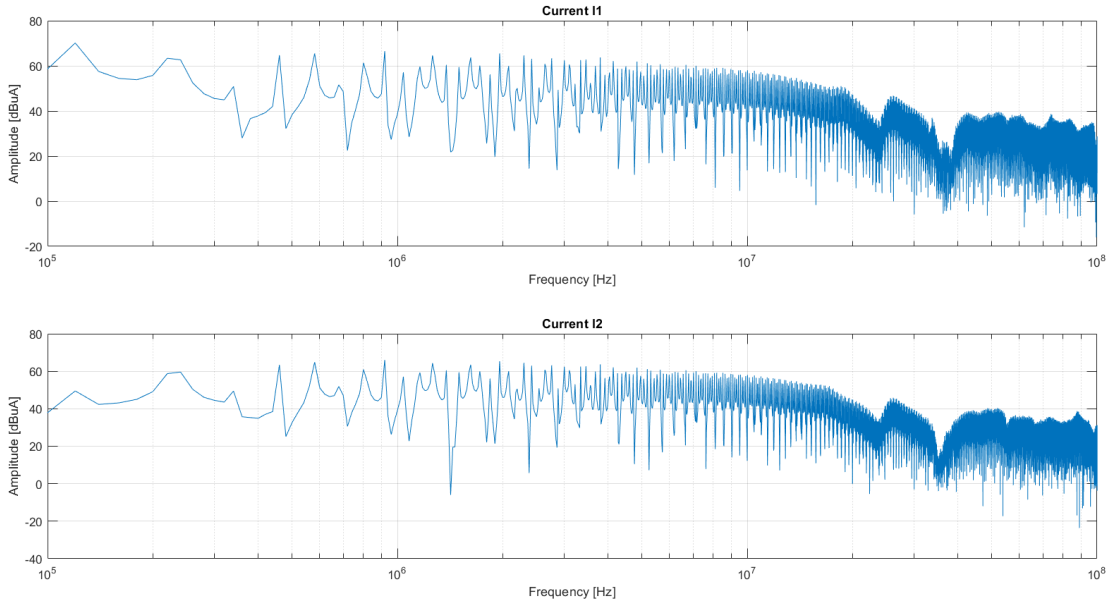

Figure II.35: Line currents obtained from experimental measurement processed by FFT.

The second step to obtain data necessary to identify the model was input impedance measurement. The device used for the measurement was Impedance Analyser with operating frequency up to 120MHz.

In order to possibly increase measurement accuracy and to provide measurement reproducibility, specific interface has been built for impedance measurement. It is composed of several BNC connectors to link the converter with the Impedance Analyser. In addition, the interface allows to short circuit some parts of the converter. Using a BNC short circuit and a BNC cable to the meter allows performing the three measurement configurations demanded for the model identification with good reproducibility. The Impedance Analyser is calibrated accounting for the BNC cable and the interface to reduce their influence on the measurement. The interface and impedance measurement setup are presented in Fig.II.36.

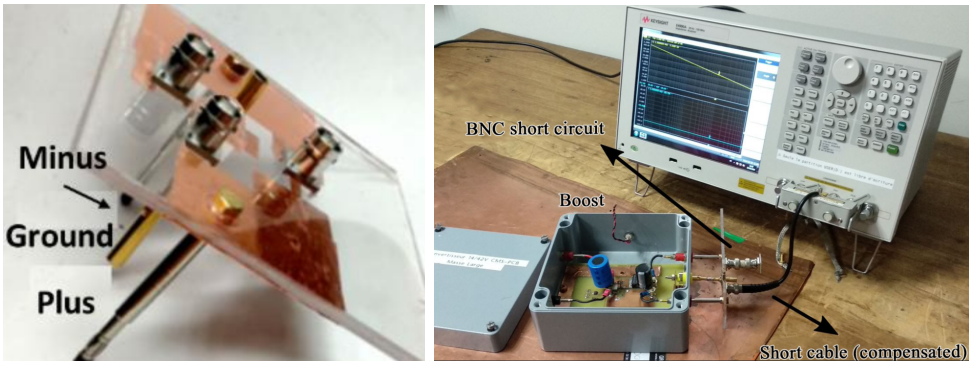

Figure II.36: View of impedance measurement procedure: on the left impedance measurement interface, impedance measurement setup on the right.

Similarly to the previous case, the impedances were measured for three different configurations Z_{PG}, Z_{MG} and Z_{PM}. The results are presented below in the following Figures II.37, II.38, II.39.

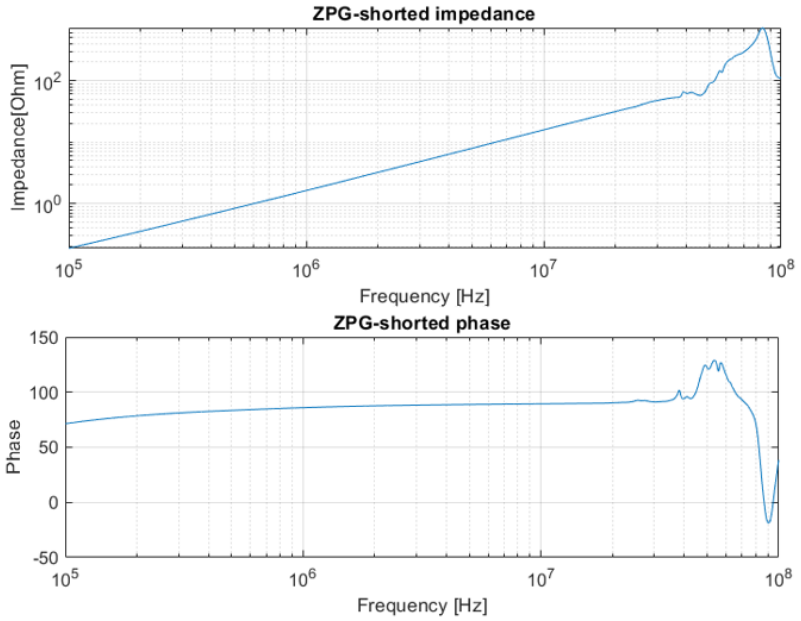

Figure II.37: Measured Z_{PG} impedance with presented both module and phase shift.

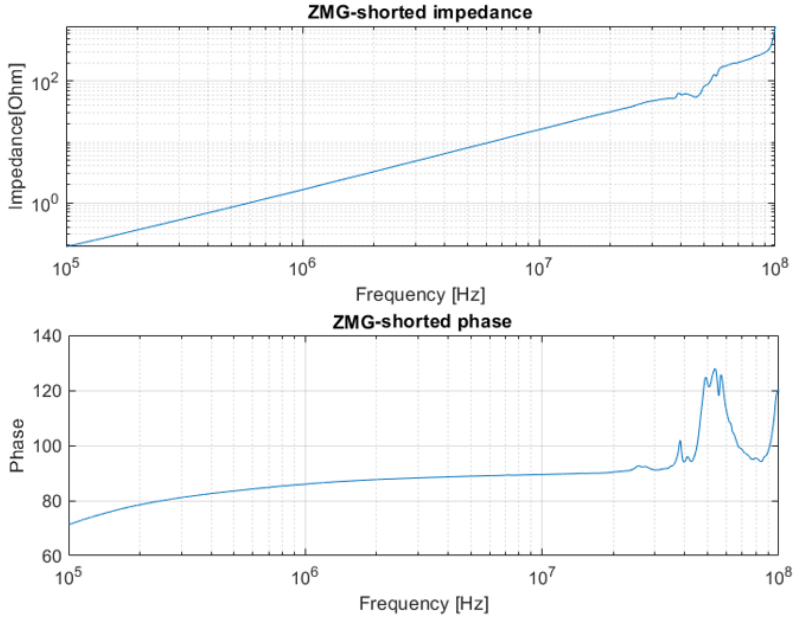

Figure II.38: Measured Z_{MG} impedance with presented both module and phase shift.

Based on all obtained measurements needed for Black Box model identification were conducted, the Black Box model parameters were computed on the basis of previously presented equations Eq.(II.3),Eq.(II.4),Eq.(II.5),Eq.(II.6) and Eq.(II.7). Afterwards, the model based on the physical boost converter has been identified.

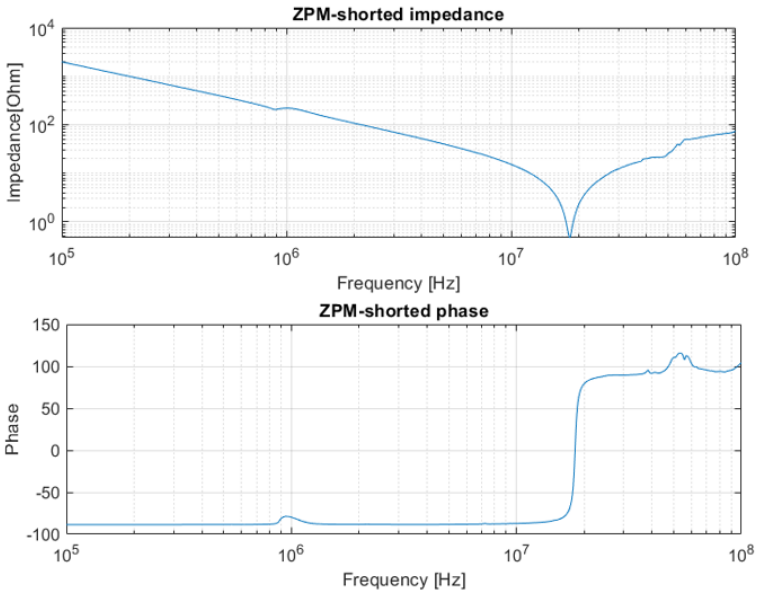

Figure II.39: Measured Z_{PM} impedance with presented both module and phase shift.

FigureII.40presents the comparison between Z_{21} and Z_{Z22} computed from impedances obtained from experimental measurements. It can be seen that this time the impedances, even if they remain similar shape, are different. In the frequencies 1MHz and 50MHz the difference is significant. This shows that the asymmetry of the Black Box model should be considered.

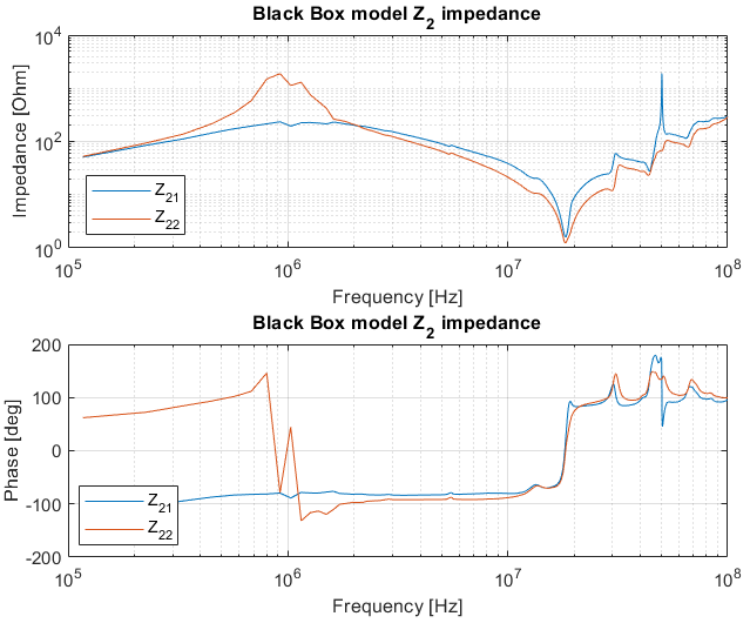

Figure II.40: Comparison between Black Box model impedances Z_{21} and Z_{Z22} obtained from experimental identification.

II.5.3 Black Box model verification.

Once the Black Box models for both time-domain simulation and the physical converter one were identified, the models were applied in three test configurations to validate them. In order to conduct a verification process a specific tool has been built to solve the circuit equations in the frequency domain. The solver computes I_1 and I_2 currents which flows between the Black Box model and the LISN for each configuration setup. Then, these results are compared with the measurements obtained by time-domain simulation or experiments for the same configuration depending which model is being validated.

The first configuration used for a validation is connecting the model to asymmetrical environment, in order to do that LISN impedance has been modified, in minus to ground connection R value has been changed from 50Ω to 5Ω. This validation case is presented in Fig.II.41.

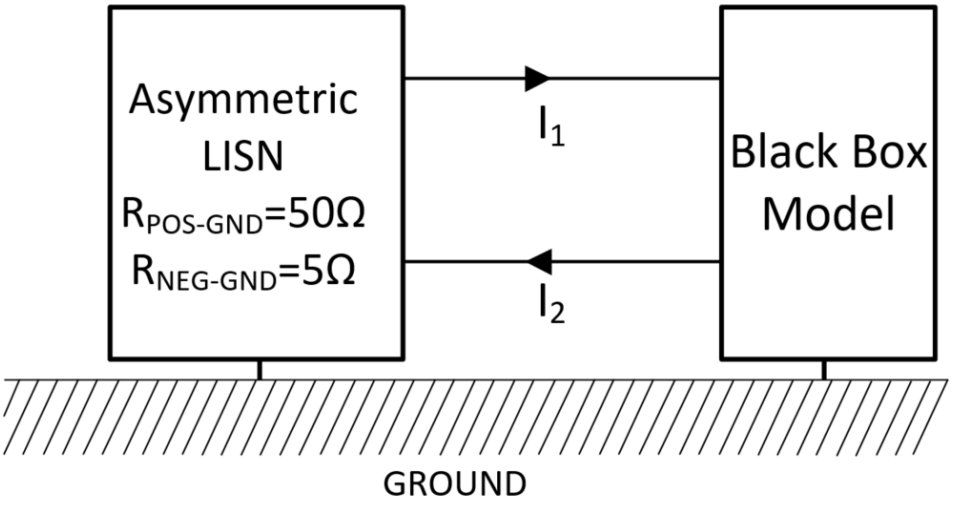

Figure II.41: Validation case "Asymmetrical grid". Minus to ground LISN's impedance is modified to 5Ω to create asymmetry in the grid.

The second configuration for model validation is a connection minus to the ground on the Black Box model terminals side, it creates high asymmetry of the current since in theory all current flows between plus and ground bypassing the minus wire. However, it is not really true in a higher frequencies. In reality due to some connection impedance, current in minus wire is not exactly zero which was noticed in experimental validation.

Therefore, even in simulation validation case some small impedance has been added in the minus to ground connection. "Minus to ground" validation case is presented in Fig.II.42.

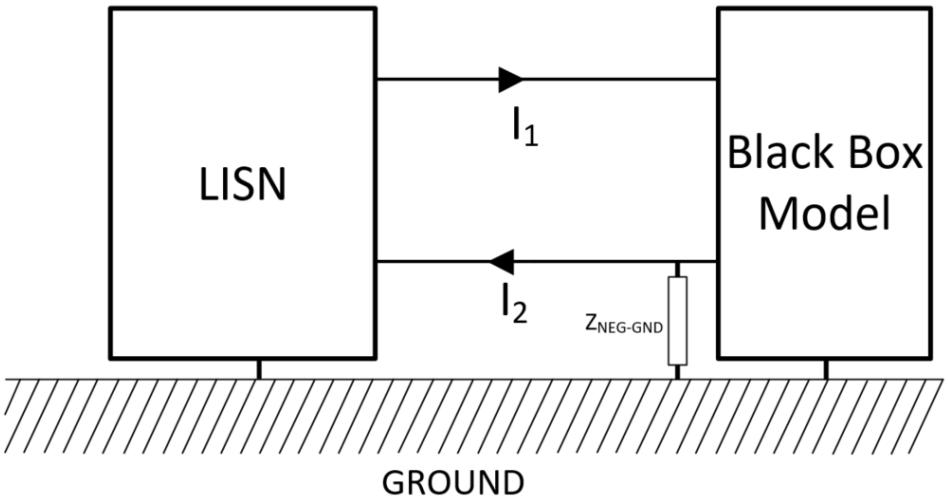

Figure II.42: Validation case "Minus to ground". High current asymmetry is introduced by shorting minus and ground terminals.

The third configuration is a case with EMI filter connected between Black Box model and the LISN. Filter's impedance significant modifies higher frequency content of line currents due to its attenuation. Therefore, it is a good validation setup since the line currents will be very much different to the ones from the identification process. EMI filter validation case is presented in Fig.II.43.

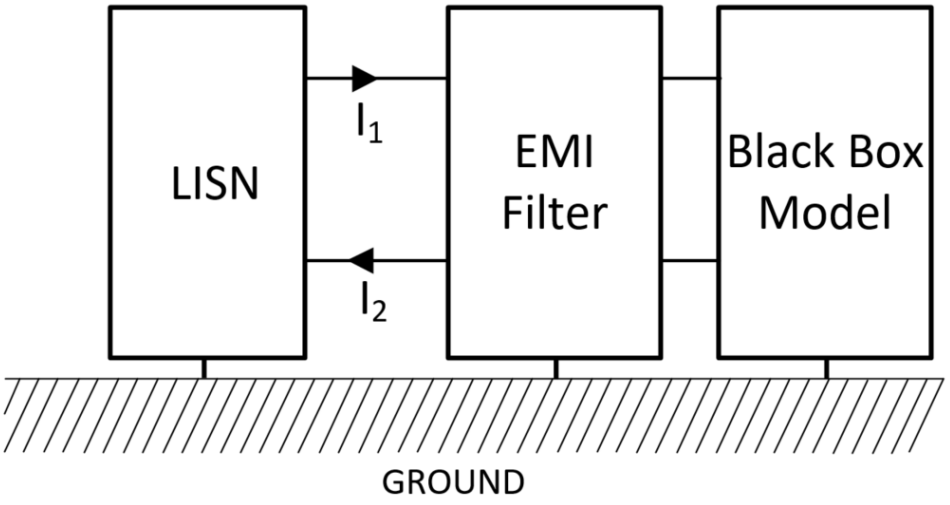

Figure II.43: Validation case "EMI Filter". Significant change of line currents according to identification process due to high attenuation of the filter.

II.5.3.1 Simulation Black Box model validation.

To validate the Black Box model identified from the time-domain simulation, three simulations have been run with different validation scenarios described in the previous section.

In each simulation line currents were recorded in order to compare them with currents computed in frequency domain from the circuit based on the Black Box model. It is worth noting that this is an actual validation of the model, since this one has been identified on a symmetric LISN, and is now used in a different configuration: either asymmetric LISN, minus to ground connection on the converter side or with EMI Filter. Moreover, the frequency-based Black Box model uses only linear equations in the frequency domain, whereas the time-domain simulation is an actual representation of the switched behaviour of the converter.

The first validation of the model was carried out with "Asymmetric gird" case. In both frequency-domain Black Box model circuit and time-domain simulation minus to ground impedance of the LISN was changed by replacing Resistor from 50Ω to 5Ω. Black Box model and time-domain simulation circuits are presented below in Fig.II.48, II.45 and Fig.II.49.

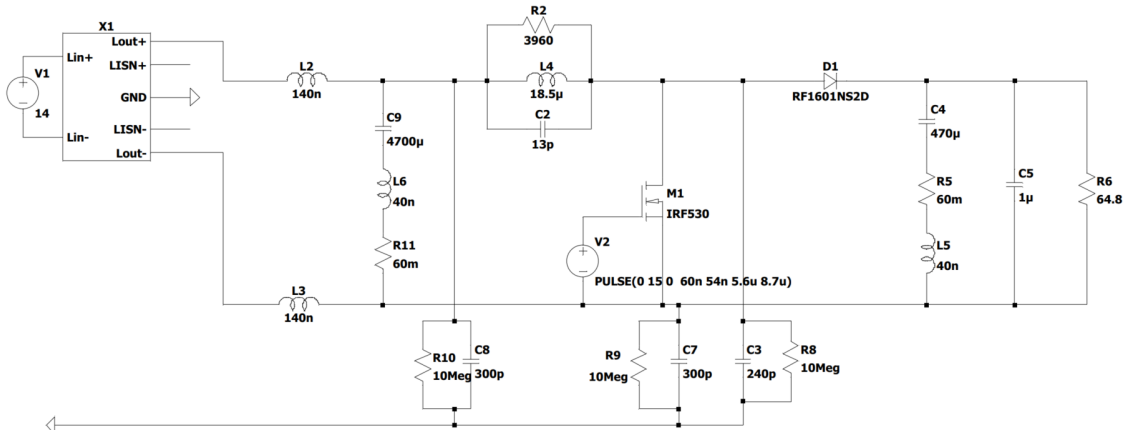

Figure II.44: Time-domain model for validation Black Box model. Case "Asymmetrical grid". LISN has line-ground impedances unbalance to introduce assymetry.

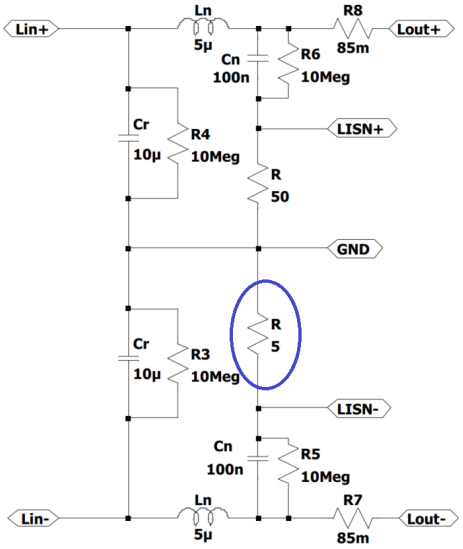

Figure II.45: Asymmetrical LISN. Changed resistor is marked blue.

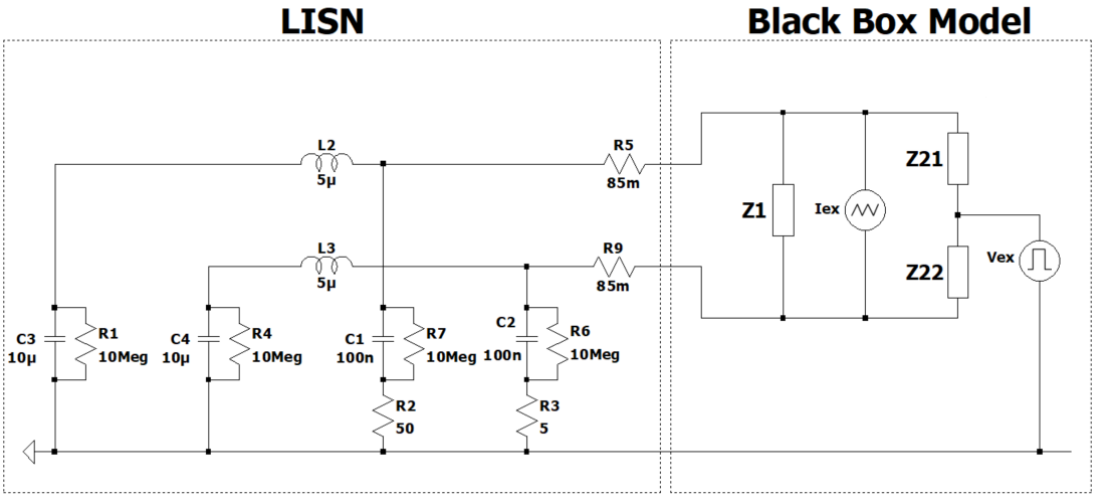

Figure II.46: Frequency-domain Black Box model circuit. Case "Asymmetrical grid".

Once the line current results were obtained from both time-domain simulation and Black Box model frequency-domain circuit, they were compared to check validity of the model in a case of asymmetry in the grid. The results are presented below in Fig.II.47. Simulation results were processed by FFT and they are presented in red colour, whereas black dots present currents obtained from Black Box model circuit, the circuit was solved for a specific frequencies only, therefore the results are discrete (peaks only).

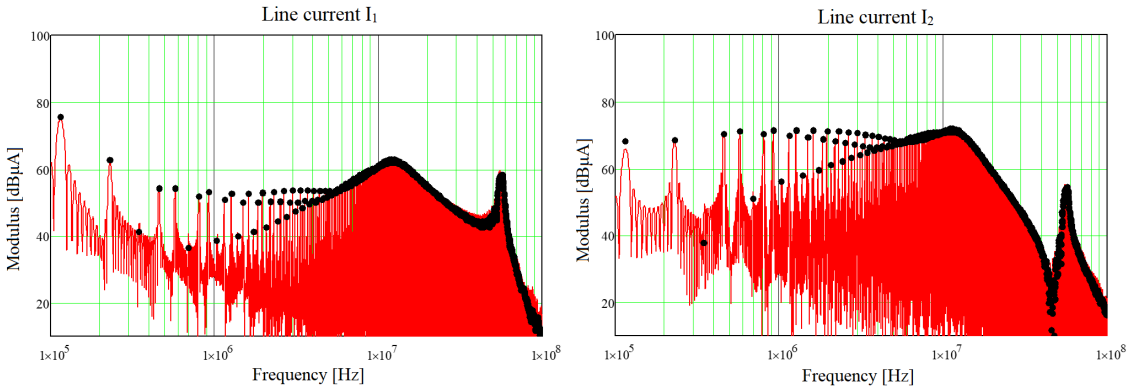

Figure II.47: Comparison between line current obtained by time-domain simulation with FFT – red coloured spectrum and line currents obtained by solving frequency-domain circuit with Black Box model representing EMI of the converter – black dots. Case "Asymmetrical grid".

The results from both cases are very similar what validates the model in asymmetrical environment. It can be noticed that I2 has a higher amplitude as I1, for harmonics higher than the fundamental. This is due to lower line to ground impedance, and therefore larger contribution of CM current, which is no more balanced in each line, due to asymmetry of the grid.

The second validation of the model was carried out with "Minus to ground" case. In both frequency-domain Black Box model circuit and time-domain simulation minus were connected to the ground with the same small but non-zero impedance to impose some high frequency current flow in minus wire. Both Black Box model and time-domain simulation circuits are presented below in Fig.II.48 and Fig.II.49.

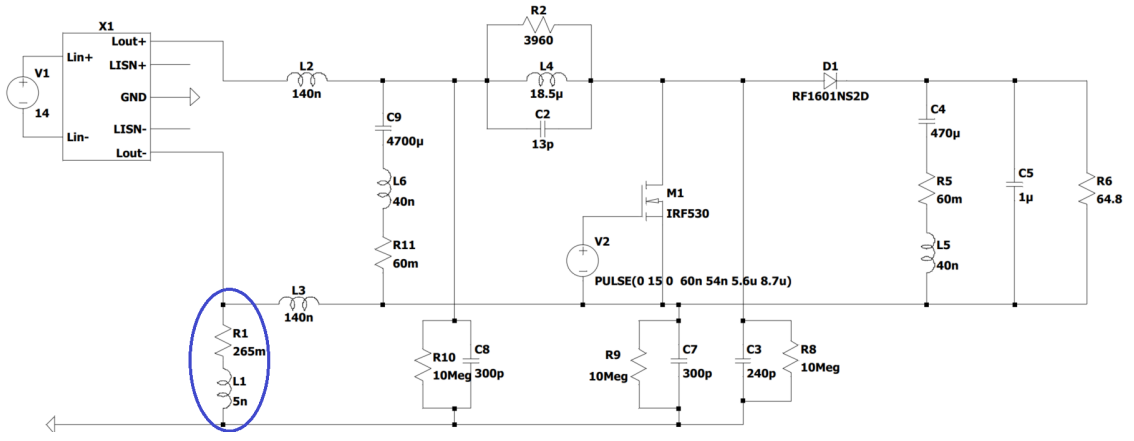

Figure II.48: Time-domain model for validation Black Box model. Case "Minus to ground". The connection impedance is marked blue.

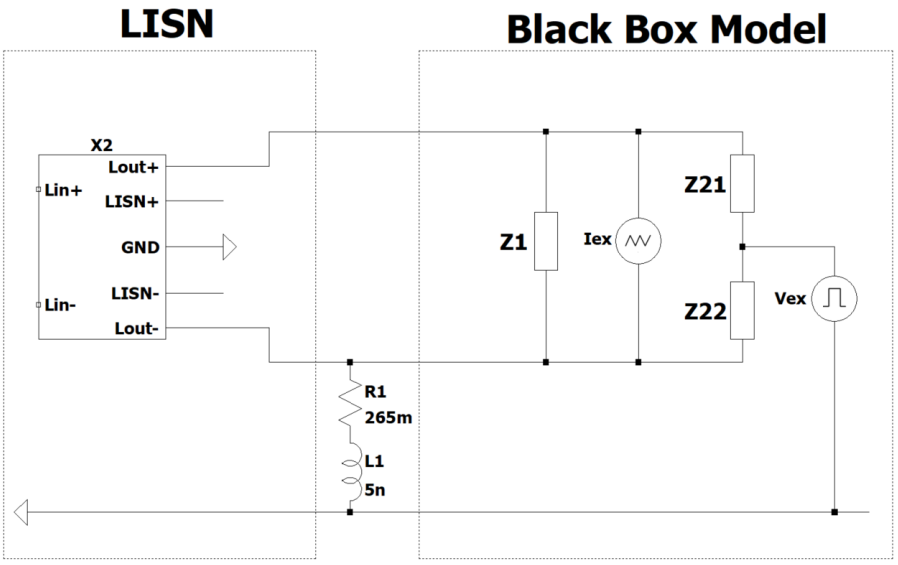

Figure II.49: Frequency-domain Black Box model circuit. Case "Minus to ground".

Again the results of line current from both time-domain simulation and Black Box model frequency-domain circuit were compared to check validity of the model in this extreme case of big line unbalance. The results are presented below in Fig.II.50. Simulation results are presented in red colour, whereas black dots present currents obtained from Black Box model circuit.

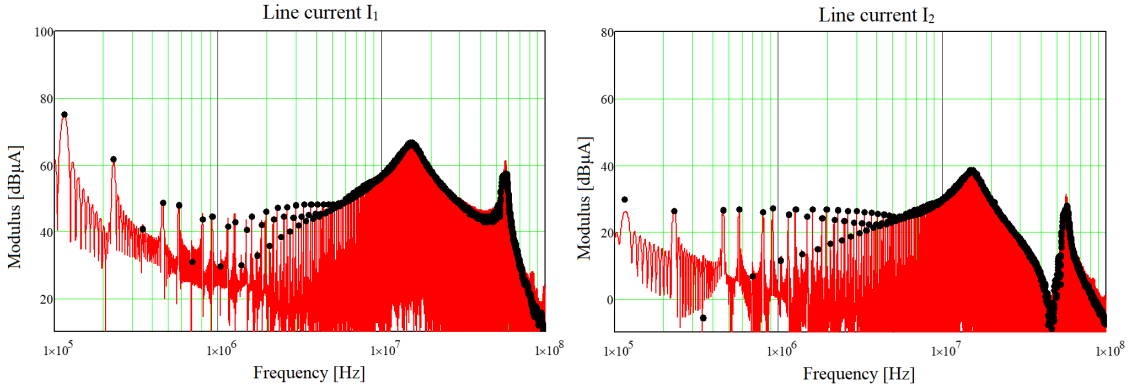

Figure II.50: Comparison between line current obtained by time-domain simulation with FFT – red coloured spectrum and line currents obtained by solving frequency-domain circuit with Black Box model representing EMI of the converter – black dots. Case "Minus to ground".

The results from both circuits are very similar which validates the model, even in this extreme case. It is worth noting that I2 current becomes very low (30 dB less than I1), since almost all current goes through the ground, and not through the minus wire. However the link between converter minus and ground is non-zero, therefore, in higher frequency current magnitude is bigger.

Third validation of the model was carried out with "EMI Filter" case. In both frequency-domain Black Box model circuit and time-domain simulation EMI filter was placed between the converter/Black Box model and the LISN. EMI filter used in the validation is the same as before (presented in Fig. II.15). Black Box model and time-domain simulation circuits are presented below in Fig.II.51 and Fig.II.52.

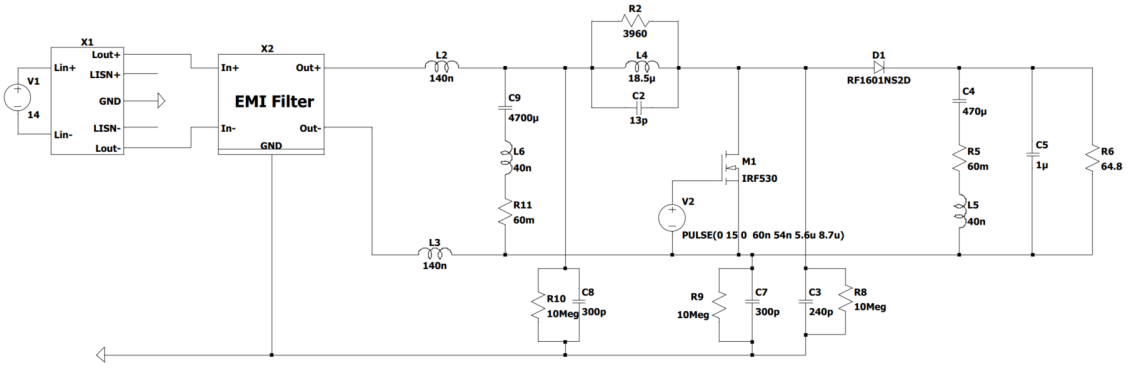

Figure II.51: Time-domain model for validation Black Box model. Case "EMI Filter".

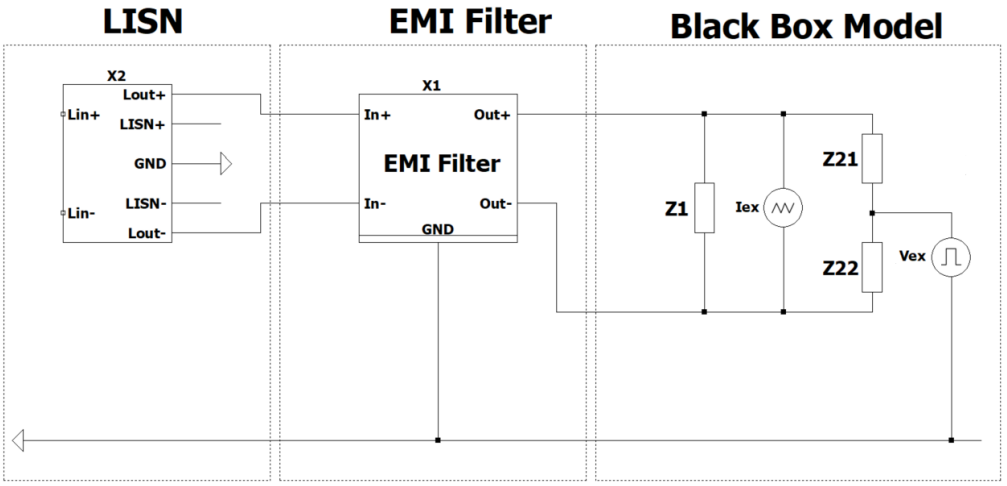

Figure II.52: Frequency-domain Black Box model circuit. Case "EMI Filter".

The results of line current from both time-domain simulation and Black Box model frequency-domain circuit were compared to check validity of the model in the case of introducing additional impedance between device and LISN. The results are presented below in Fig.II.53. Simulation results are presented in red colour, whereas black dots present currents obtained from Black Box model circuit.

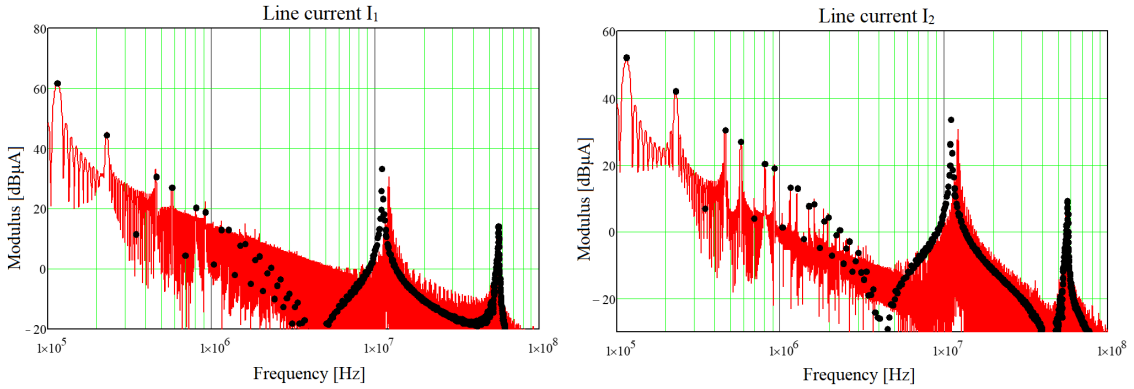

Figure II.53: Comparison between line current obtained by time-domain simulation with FFT – red coloured spectrum and line currents obtained by solving frequency-domain circuit with Black Box model representing EMI of the converter – black dots. Case "EMI Filter".

The results from both circuits are similar, however, there is some mismatch between 2-10MHz in I_1 current and 4-6MHz in I_2 current. It is most likely caused due to slight change of the actual converter operating point (since the supply circuit of the internal controller depending on the converter's input parameters) and also some numerical errors of FFT algorithm in both identification and model validation procedures. Due to high attenuation of the filter, peaks are not well captured by the algorithm and they are represented as a background noise in the spectrum. Both of the resonances were well captured but frequency of the one of them has a small mismatch comparing to the simulation case.

For all three cases EMI phenomenon in line currents is well reproduced by the model on the whole frequency range of interest (100kHz-100 MHz). The resonances in each cases are well reproduced as well. Despite the fact that the model is used in another configuration than the one used for identification, the comparison is very good. This validates the assumption of the "masking impedance" concept, which allow using impedances measured when the converter is in the off state, combined with voltage and current sources, to represent an intrinsically switching behaviour.

The interest of this validation in simulation is that the model has been identified from a converter which stray elements are perfectly defined, and no measurement errors are encountered. This contributes to the almost perfect agreement (except EMI filter case) between the frequency model and the results obtained from the time domain simulation.

II.5.3.2 Experimental Black Box model validation.

The experimental validation is really mandatory when dealing with EMC aspects since Electromagnetic Interferences are not always circulating where expected. To validate the Black Box model identified from an actual converter, similarly to the simulation validation procedure, three configurations have been checked – "Asymmetric grid", "Minus to ground" and "EMI Filter".

Line currents were recorded in the same way as in identification process, with using high-frequency current probes and oscilloscope keeping the same phase shift. Then, the data were processed with FFT. The issue which can affect the model validation accuracy is the fact that for frequency-domain circuit computation in each cases, LISN, minus to ground connection impedance and EMI Filter impedances were based on the model which were used in simulation. Moreover, for physical converter identification when computing equivalent sources, LISN impedance Z_L necessary for calculation did not consider any parasitics (just ideal R=50 Ω and C=220nF components).

The first validation of the model was carried out with "Asymmetrical grid" case. Frequency-domain Black Box model circuit is the same LISN as in simulation validation. In the experiment minus to ground impedance, which was by default terminated with 50Ω BNC connector, was replaced by 5Ω THT resistor. The experimental setup is presented below in Fig.II.54. Black Box model frequency-domain circuit for the validation remains the same as simulation validation case (Fig.II.46), however, the model itself is different since it was identified form the actual converter (difference already discussed in earlier section).

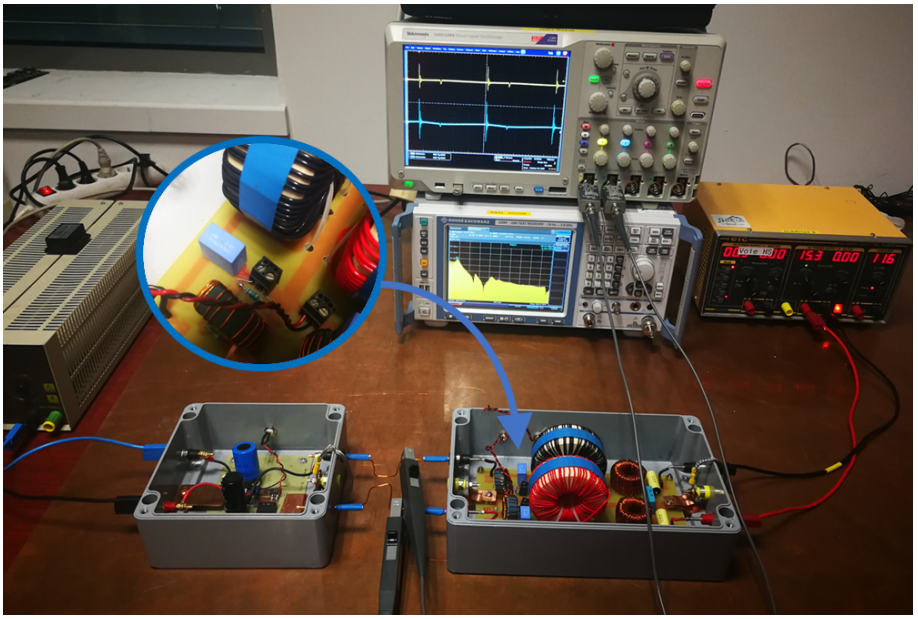

Figure II.54: Experimental validation of the Black Box model."Asymmetrical grid" case with using CISPR 16 LISN. Changed minus to ground grid impedance can be seen in zoom.

When the line currents results were obtained from experiments and Black Box model frequency-domain circuit, they were compared to check validity of the model in a case of asymmetry of the grid. The results are presented below in Fig.II.55. Recorded experimental results were processed by FFT and they are presented in red colour, whereas black dots present currents obtained from Black Box model circuit.

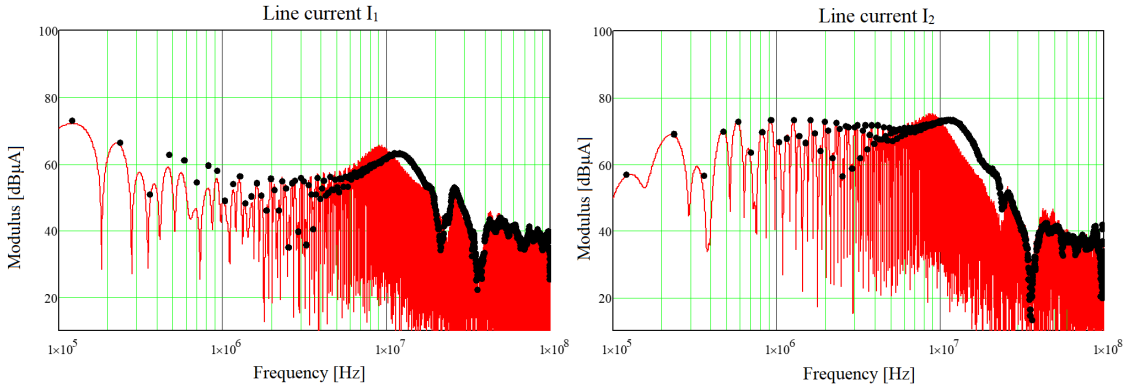

Figure II.55: Comparison between line current obtained by exepriments with FFT – red coloured spectrum and line currents obtained by solving frequency-domain circuit with Black Box model representing EMI of the converter – black dots. Case "Asymmetrical grid".

As expected the results matching is not as "perfect" as in simulation. The main differences are attributed to the model of the LISN, which is not exactly represented, due to its stray behaviour. Nevertheless, the overall results are quite good.

The second validation of the model was carried out with "Minus to ground" case. Frequency-domain Black Box model circuit is the same as in simulation validation for this case. In the experiment minus was connected to the ground with as short as possible braid cable connection, however, even with this type of connection the impedance is noticeable causing some high frequency current flow through the minus wire. Therefore, in Black Box model circuit the impedance between minus and ground has been added, and estimated based on experimental measurements with a 5nH and 265mΩ. This is why the same impedance was included in time-domain simulation for "Minus to ground" case.

The experimental setup is presented below in Fig.II.56. Black Box model frequency-domain circuit for the validation remains the same as simulation validation case (Fig.II.49), but again the model itself is different since it was identified form the actual converter.

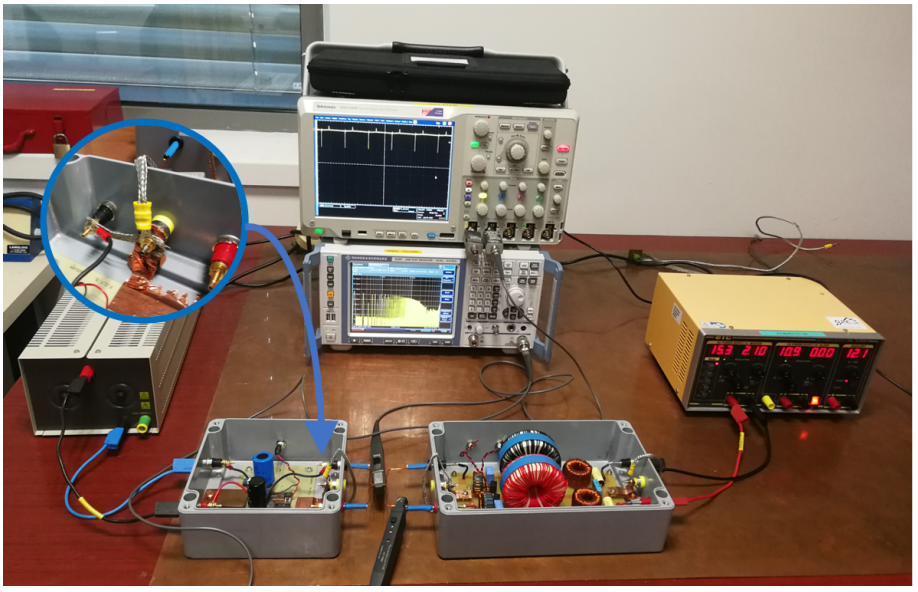

Figure II.56: Experimental validation of the Black Box model."Minus to ground" case. Minus to ground connection on the converter side can be seen in zoom.

Once the line currents results were obtained from experiments and Black Box model frequency-domain circuit, they were compared to check validity of the model in a case of current unbalance due to minus to ground connection. The results are presented below in Fig.II.57. Recorded experimental results were processed by FFT and they are presented

in red colour, whereas black dots present currents obtained from Black Box model circuit.

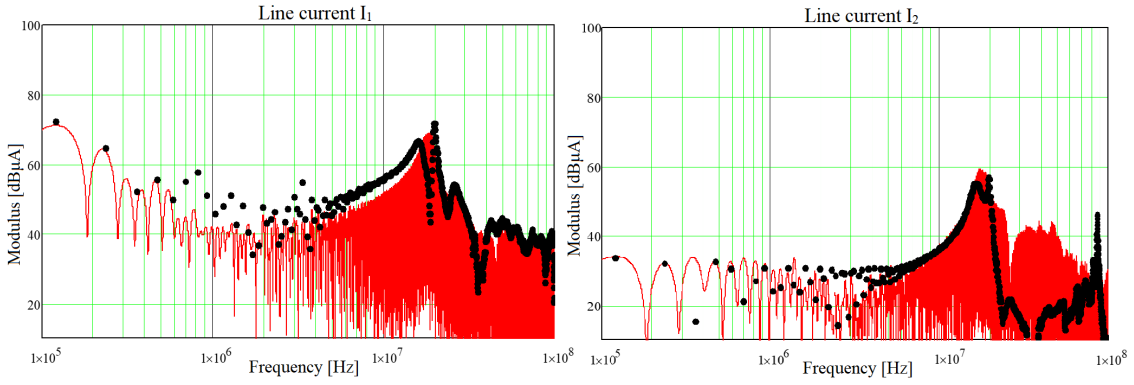

Figure II.57: Comparison between line current obtained by exepriments with FFT – red coloured spectrum and line currents obtained by solving frequency-domain circuit with Black Box model representing EMI of the converter – black dots. Case "Minus to ground".

The high frequency difference is attributed to the impact of the impedance of the short circuit which estimation have some possible errors. Moreover, in frequency-domain circuit LISN model is used that have some stray elements missing which can be responsible for high frequency behaviour. In addition, the very low value of I2 in this configuration leads to very high measurement inaccuracy due to measuring setup sensitivity and FFT numerical errors. The low frequency mismatch between 500 kHz and 3 MHz is due to a disturbance of the converter operating point: the control circuit is directly fed from the power source, and short circuiting the LISN minus results in less voltage drop and therefore a small change in input voltage and thus duty cycle. However, the global matching between the model and the measurement is quite good (except I2 current in the frequency above 20MHz), what validates the model, as well as, the identification method.

The last validation of the model which has been conducted is "EMI Filter" case. Frequency-domain Black Box model circuit has the same LISN and EMI Filter models as in simulation validation. In the experiment, physical EMI Filter, which was previously designed, were used. The filter model used in frequency-domain circuit has similar parameters to the physical one used in experiments since it was previously identified (Section II.2.3.2).

The experimental setup is presented below in Fig.II.58. Black Box model frequency-domain circuit for the validation remains the same as simulation validation case (Fig.II.52).

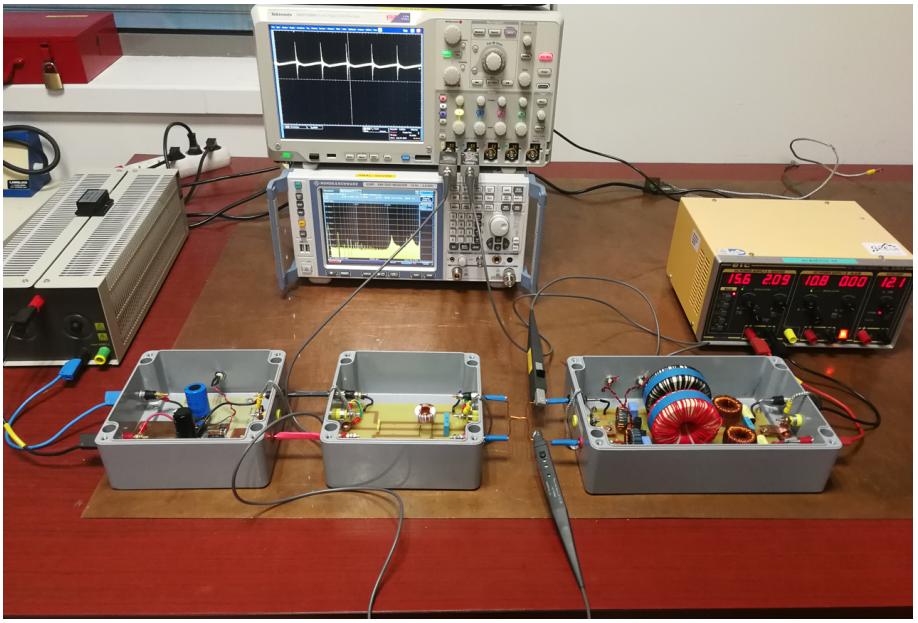

Figure II.58: Experimental validation of the Black Box model."EMI Filter" case.

Again the line currents results were obtained from experiments and Black Box model frequency-domain circuit were compared in order to check validity of the model in a case of high modification of the currents due to EMI filter attenuation. The results are presented below in Fig.II.59. Recorded experimental results were processed by FFT and they are presented in red colour, whereas black dots present currents obtained from Black Box model circuit.

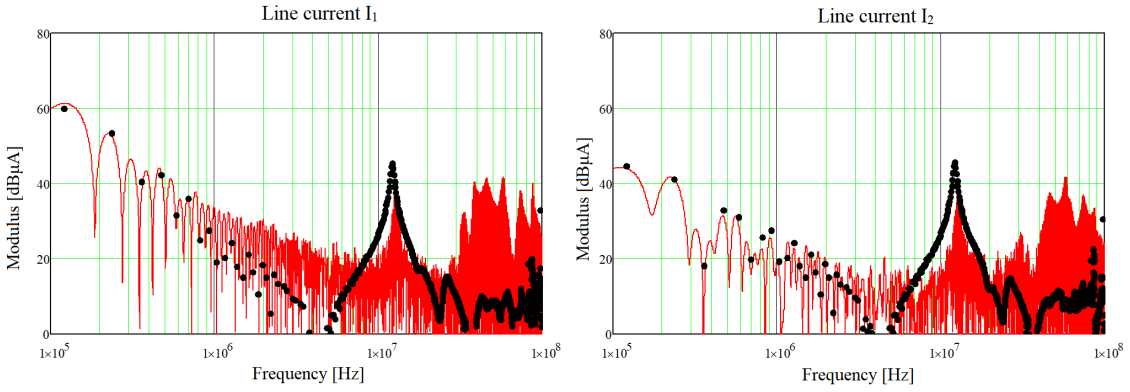

Figure II.59: Comparison between line current obtained by exepriments with FFT – red coloured spectrum and line currents obtained by solving frequency-domain circuit with Black Box model representing EMI of the converter – black dots. Case "EMI Filter".

The results of "EMI Filter" case validation are quite similar to the ones obtained from simulation validation. Due high attenuation of the filter the current level in some frequencies is very low, therefore, some measurement and FFT numerical errors could happen. Moreover, in a higher frequency above 20MHz model did not reproduce EMI behaviour correctly, however, this mismatch can have many reasons, such as inaccurate model of EMI Filter, LISN model without stray components, bad sensitivity of measurement setup in such high frequency range, also all layout impact between filter and converter, which are not taken into account in the model, there are implemented: the model of the converter, the model of the filter but there is not the model of the link between converter and filter. Nevertheless, the global matching between the model and the measurement is satisfying, the model even reproduced the resonance which occurred in 12MHz but with incorrect amplitude. Most likely with a better knowledge of EMI Filter and LISN impedance and more accurate measurement (current probes nominal working frequency up to 50MHz) the model would reproduce EMI much better.

The validation procedure proved that Black Box model can quite well reproduce EMI behaviour of the identified device. It is also valid in different environments, so one the model is identified it can be used freely as EMI source of the device. This model is very lightweight in terms of computation so it can be used in more complex cases with many devices to reproduce EMI behaviour of the whole grid.

II.6 System level EMI modelling.

The study showed that the Black Box model can pretty accurately predict EMI behaviour of the device even if it is placed in different environments. Therefore, this modelling approach can be used in EMC analysis, especially that solving the equations in frequency-domain, even if the circuit is very complex, is much faster and more lightweight in terms of computing power compared to time-domain analysis. Moreover, there is no iteration process when solving the circuit it is just solving a mathematical formula, thus, no convergence issues occur. Finally, frequency-domain modelling approach can be used not only in a single device scenario but in a whole grid allowing a fast and lightweight system-level EMI modelling.

II.6.1 The study case grid Black Box modelling.

Due to the fact that Black Box was able to predict conducted emission generated by a converter even if it was connected to non standard environment, it was decided to use it in the study case described in the one of previous chapter (II.2.2).

The models have been connected to the grid replacing the boost converters, the rest of the grid remains the same. Therefore, each of the model is connected to the EMI filter and then they are connected to DO160 LISN through cables. The figure below (Fig.II.60) shows a schematic grid based on Black Box models.

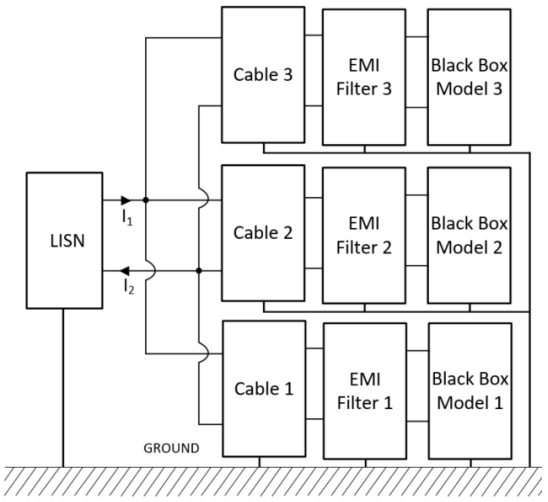

Figure II.60: Schematic view of a grid based on Black Box models.

It is worth to remind that in the Black Box model has been identified from a single converter connected only to the LISN. Thus, the environment of the grid is very different comparing to the case where converter was identified. The study case grid composed of Black Box models instead of boost converters is presented below in Fig.II.61.

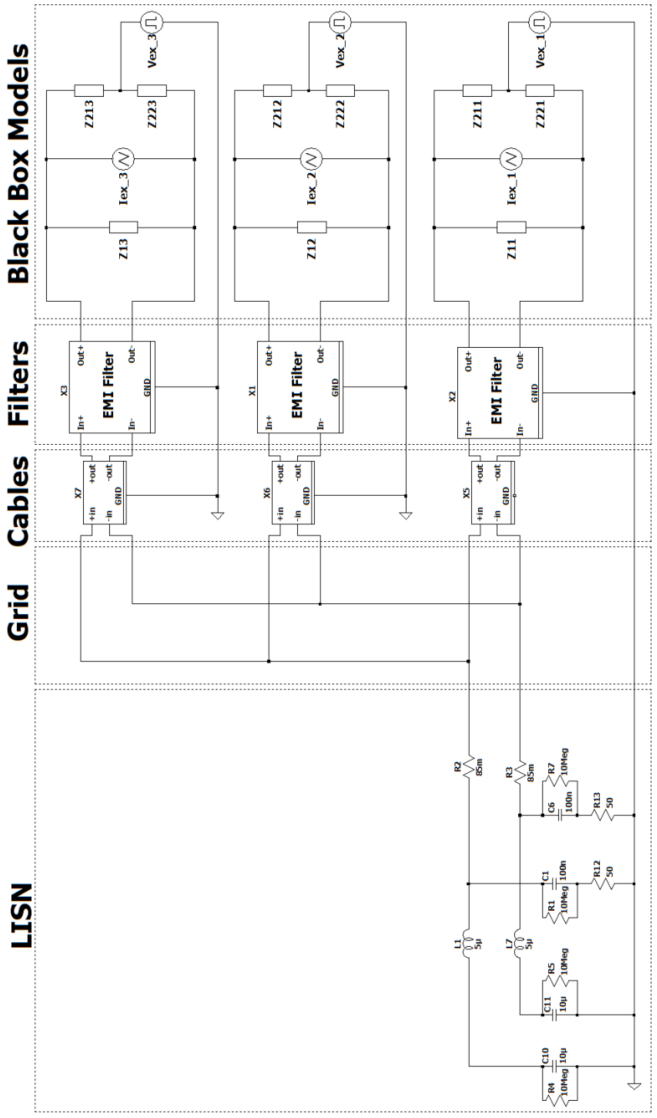

Figure II.61: Grid-level EMI modelling based on Black Box approach. Study case grid.

Once the frequency-domain grid circuit (based on Black Box models) has been solved, it was compared to the grid time-domain simulation which has been previously used for interaction analysis. Time-domain simulation results were processed by fast fourier transform in order to compare it with Black Box model grid results. The comparison of line currents flowing through LISN are presented below in Fig.II.62.

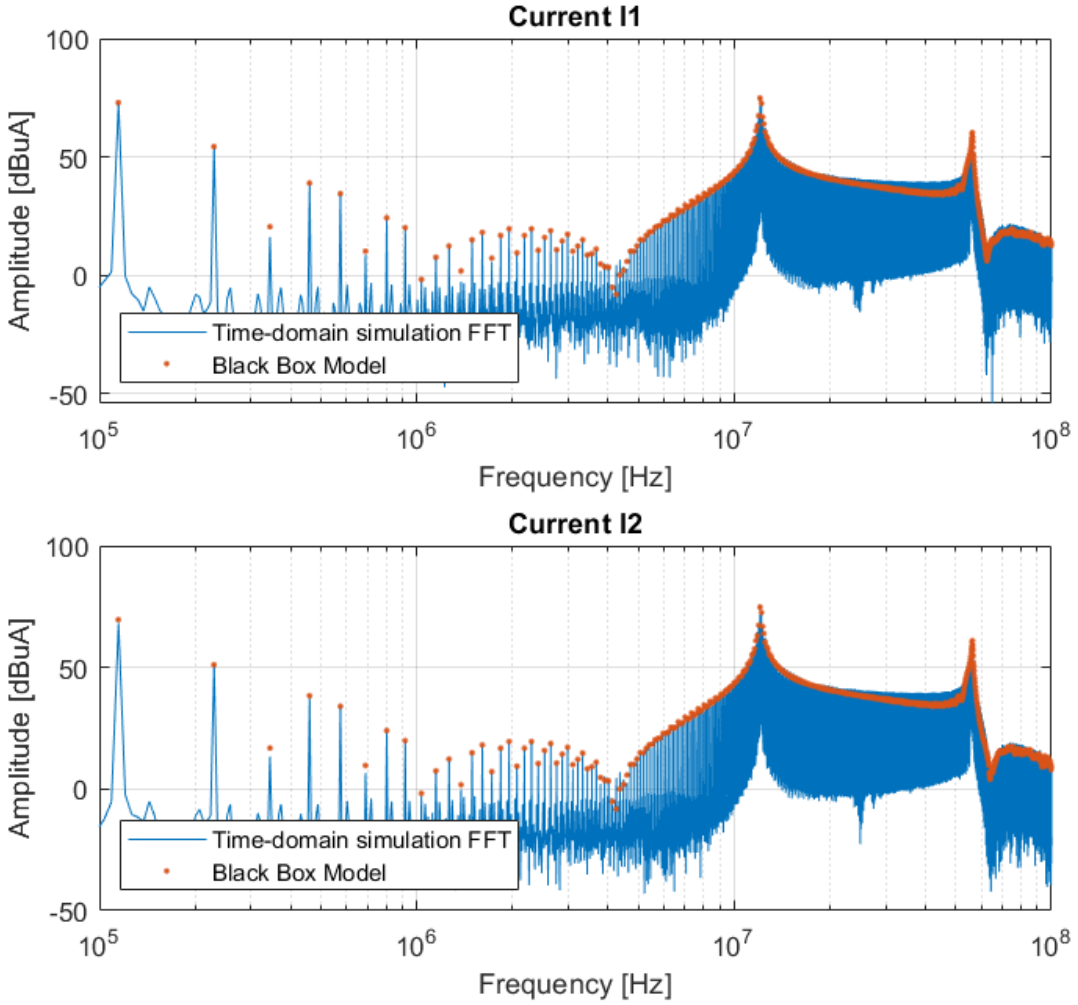

Figure II.62: Grid currents I_1 and I_2" in frequency domain. The comparison between time-domain simulation results and Black Box frequency-domain results.

It can be seen in the comparison that the line currents obtained from both time-domain simulation and frequency-domain circuit are very similar even in such a complex scenario. Even the resonances caused by EMI filters are well reproduced. There are some incompatibilities in higher frequency but it is probably caused by numerical error in FFT computation (both in identification process and in grid time-domain simulation).

This shows that Black Box modelling approach works well in gird case scenario as well. Since the emission is almost the same as in time-domain simulation it can be assumed that Black Box modelling can reproduce not only emission in a single converter but also EMI-related interaction in the grid. Thanks to its fast and lightweight computation features it can be used in some automation process like optimization design with very good accuracy.

II.7 Conclusion.

In this part an analysis of EMI interactions in a DC grid for a notional study case has been done. In the studied grid it was noticed that some interactions between grid's components occur which have influence on the actual disturbance emission to the mains supply.

A typical approach of conducted EMI measurement which is defined by the standards is either measuring the voltage between each phase and ground or line current which flows to the mains supply with a single device only. The measurement must be done on the controlled environment witch is defined impedance, for this process, usually line impedance stabilization network is used. Based on this approach EMI filter design is performed to comply the standard requirements. Nevertheless, this kind of measurement approach is not necessarily correct due to above mentioned interaction.

To properly estimate actual emission which flows to the mains supply it is necessary to consider all grid components, however, it could not be easily done, in real case condition due to hardware limitation (for example LISN rated current) or in simulation case due to computing power limitations (simulating complex cases - especially containing many parasitics is not straightforward due to aspects mentioned in the thesis). That is why it was proposed to use a novel EMI modelling approach - Black Box model with asymmetric impedances which has very lightweight features in terms of computing effort and time due to the fact that it is frequency-domain oriented.

In this work two kind of Black Box models have been identified and explained, one was based on time-domain simulation which could be used for further analysis, and the second one based on an actual converter to be able to validate the model on a real case scenario. Both models were verified with several environments and proved themselves to be pretty accurate even in higher frequencies (with some incompatibility caused by measurement and numerical errors).

The model was then used in the same study case grid in order to check whether it can reproduce grid interactions discovered in the initial study. The obtained results showed that the Black Box modelling approach is pretty accurate even if several models are used and connected together.

This modelling approach does not have disadvantages of time-domain modelling such as convergence issues and simulation time of complex models, it can be applied to some automatic design procedures.

In this case the design process based on Black Box model could be more accurate than a standard one based on a single device measurement since it could include some grid interaction.

Work which has been described in this part proved utility of the frequency-domain Black Box model. The model can be used as a basis of filter design optimization procedure making a filter even more optimal than with optimization procedure based on a single converter since grid interactions can be included. Some preliminary study of filter optimization based on the model has been done but do not described in the thesis.

In the future it is planned to extend this optimization procedure to automatic simultaneous design of several filters in the grid to find an actual optima. Then, if successful with a DC grid filter design optimization, it could be expanded to the AC-DC grid systems as the one described in Part I of the thesis. Finally, to compose together all three aspects addressed in the thesis, EMI, power quality and control in the one optimization algorithm in order to be able to optimally design several filters (both harmonics and EMI) of the gird components.

General Conclusion

The research presented in this thesis was focused on interactions that occur in electrical grids based on power electronics converters. The study described in both parts showed that the interactions indeed can have an impact on the performance of grid components in several aspects.

In the first part it was shown that the converters might interact in a way which have an influence on their dynamic performance. In fact, this impact affecting not only the control of the devices but also the harmonic filters since they have an influence on the converters' dynamic behaviour. Therefore, this kind of interaction should be taken into consideration when designing both control and harmonic filters which are connected to the common grid.

The study described in part two has shown that interactions might occur in other aspects than dynamics and harmonics. It was noticed that in grid composed of power electronics converters EMI interactions can occur. These interactions can have a significant impact on emission level injected to the grid, which in consequence affects EMI filter design process since due to the interactions, demanded attenuation of EMI filter might change. Moreover, another question arises in case of grid interactions if is better to design an individual of each converter in the grid or a common one for a group of converters to comply emission limits defined in standards.

The work presented in this thesis shows that interesting tool to have a system level approach for designing embedded grids has been developed. EMC model will have to be extended and validated for AC grids, however, some of this work has been already done and presented by different research papers such as [10], [29]. When the model will be extended to AC it could be used in study case grid described in part one or in any other grids commonly used in aircraft industry. Based on those tools an automatic design procedure including optimization can be introduced. This design process can include several aspects, such as power quality, dynamic behaviour and electromagnetic interference.

The fully developed tool would be able to simultaneously consider both all the above-mentioned aspects of the converter and the interactions. Therefore, obtained design result would be an actual optimal design.

Bibliography

[1] Cispr 16-1-2:2014 specification for radio disturbance and immunity measuring apparatus and methods - part 1-2: Radio disturbance and immunity measuring apparatus - coupling devices for conducted disturbance measurements.

[2] Cispr 16-2-1:2014+amd1:2017 specification for radio disturbance and immunity measuring apparatus and methods - part 2-1: Methods of measurement of disturbances and immunity - conducted disturbance measurements.

[3] Iec 61000-2-2:2002 environment - compatibility levels for low-frequency conducted disturbances and signalling in public low-voltage power supply systems.

[4] Khaled H Ahmed, Stephen J Finney, and Barry W Williams. Passive filter design for three-phase inverter interfacing in distributed generation. In *2007 Compatibility in Power Electronics*, pages 1–9. IEEE, 2007.

[5] Achour Ales, Jean-Luc Schanen, Djelloul Moussaoui, and James Roudet. Impedances identification of dc/dc converters for network emc analysis. *IEEE Transactions on Power Electronics*, 29(12):6445–6457, 2014.

[6] Meriem Amara, Christian Vollaire, Marwan Ali, and Francois Costa. Black box emc modeling of a three phase inverter. In *2018 International Symposium on Electromagnetic Compatibility (EMC EUROPE)*, pages 642–647. IEEE, 2018.

[7] Bruce R Archambeault, Omar M Ramahi, and Colin Brench. *EMI/EMC computational modeling handbook*, volume 630. Springer Science & Business Media, 2012.

[8] Thomas Back. *Evolutionary algorithms in theory and practice: evolution strategies, evolutionary programming, genetic algorithms*. Oxford university press, 1996.

[9] Hemant Bishnoi, Andrew Carson Baisden, Paolo Mattavelli, and Dushan Boroyevich. Analysis of emi terminal modeling of switched power converters. *IEEE Transactions on Power Electronics*, 27(9):3924–3933, 2012.

[10] Hemant Bishnoi, Paolo Mattavelli, Rolando Burgos, and Dushan Boroyevich. Emi behavioral models of dc-fed three-phase motor drive systems. *IEEE Transactions on Power Electronics*, 29(9):4633–4645, 2013.

[11] Stephen Boyd, Stephen P Boyd, and Lieven Vandenberghe. *Convex optimization*. Cambridge university press, 2004.

[12] Giovanni Lo Calzo, Alessandro Lidozzi, Luca Solero, and Fabio Crescimbini. Lc filter design for on-grid and off-grid distributed generating units. *IEEE transactions on industry applications*, 51(2):1639–1650, 2014.

[13] D. Christiansen, C.K. Alexander, and R.K. Jurgen. *Standard Handbook of Electronic Engineering, Fifth Edition*. McGraw-Hill, 2005.

[14] Richard Curran, Mark Price, Srinivasan Raghunathan, Emmanuel Bénard, Stephen Crosby, Sylvie Castagne, and Paul Mawhinney. Integrating aircraft cost modeling into conceptual design. *Concurrent Engineering*, 13(4):321–330, 2005.

[15] Blazej Czerniewski. Electromagnetic compatibility analysis for dc networks. Master's thesis, Gdansk University of Technology with G2ELab, 2017.

[16] Blazej Czerniewski, Andrea Formentini, David Dewar, Pericle Zanchetta, and Jean-Luc Schanen. Impact of converters interactions on control design in a power electronics dense network: Application to more electric aircraft. In *2019 21st European Conference on Power Electronics and Applications (EPE'19 ECCE Europe)*, pages P–1. IEEE, 2019.

[17] Blazej Czerniewski, Jean-Luc Schanen, Herve Chazal, Pericle Zanchetta, and Caio Fonseca de Freitas. Identification and validation of a non symmetrical system level emc model for power electronics converter. In *2021 IEEE Energy Conversion Congress and Exposition (ECCE)*, pages 2859–2865. IEEE, 2021.

[18] Blazej Czerniewski, Jean-Luc Schanen, and Pericle Zanchetta. Emc generation and propagation in embedded grids with multiple converters. In *2019 10th International Power Electronics, Drive Systems and Technologies Conference (PEDSTC)*, pages 433–438. IEEE, 2019.

[19] Mylene Delhommais. *Methode de pre-design par optimisation en electronique de puissance*. PhD thesis, Universite Grenoble Alpes (ComUE), 2019.

[20] David Dewar, Kang Li, Andrea Formentini, Pericle Zanchetta, and Pat Wheeler. Performance analysis of $h\_\{2\}$ optimally controlled three-phase grids. In *2018 IEEE Energy Conversion Congress and Exposition (ECCE)*, pages 2258–2264. IEEE, 2018.

[21] David Dewar, Jaime Rhoten, Andrea Formentini, and Pericle Zanchetta. Fast self-tuning decentralized variable frequency optimal controller design for three-phase embedded grids. In *IECON 2019-45th Annual Conference of the IEEE Industrial Electronics Society*, volume 1, pages 3894–3899. IEEE, 2019.

[22] Richard S Eckaus. Comparing the effects of greenhouse gas emissions on global warming. *The Energy Journal*, 13(1), 1992.

[23] K Emadi and MJIA Ehsani. Aircraft power systems: technology, state of the art, and future trends. *IEEE Aerospace and Electronic Systems Magazine*, 15(1):28–32, 2000.

[24] TDK Epcos. Film capacitors - ac capacitors cbb65a, October 2017.

[25] Mikael Foissac, Jean-Luc Schanen, and Christian Vollaire. Black box emc model for power electronics converter. In *2009 IEEE Energy Conversion Congress and Exposition*, pages 3609–3615. IEEE, 2009.

[26] Andrea Formentini, David Dewar, Pericle Zanchetta, Pat Wheeler, Dushan Boroyevich, and Jean-Luc Schanen. Optimal control of three-phase embedded power grids.

In *2016 IEEE 17th Workshop on Control and Modeling for Power Electronics (COMPEL)*, pages 1–6. IEEE, 2016.

[27] Ewald Fuchs and Mohammad AS Masoum. *Power quality in power systems and electrical machines*. Academic press, 2011.

[28] Shielding Geetha, KK Satheesh Kumar, and Rao. Emi shielding: Methods and materials–a review. *Journal of applied polymer science*, 112(4):2073–2086, 2009.

[29] Galo Guarderas, Airan Frances, Dionisio Ramirez, Rafael Asensi, and Javier Uceda. Blackbox large-signal modeling of grid-connected dc-ac electronic power converters. *Energies*, 12(6):989, 2019.

[30] Eugenio Gubía, Pablo Sanchis, Alfredo Ursúa, Jesus Lopez Taberna, and Luis Marroyo. Frequency domain model of conducted emi in electrical drives. *Power Electronics Letters, IEEE*, 3:45 – 49, 07 2005.

[31] Eldon R Hansen. Global optimization using interval analysis: the one-dimensional case. *Journal of Optimization Theory and Applications*, 29(3):331–344, 1979.

[32] Ahmet M Hava, Ufuk Ayhan, and Vahap Volkan Aban. A dc bus capacitor design method for various inverter applications. In *2012 IEEE Energy Conversion Congress and Exposition (ECCE)*, pages 4592–4599. IEEE, 2012.

[33] Silva Hiti, Dushan Boroyevich, and Carlos Cuadros. Small-signal modeling and control of three-phase pwm converters. In *Proceedings of 1994 IEEE Industry Applications Society Annual Meeting*, volume 2, pages 1143–1150. IEEE, 1994.

[34] RTCA Incorporated. Enivironmental conditions and test procedures for airborne equipment rtca do-160, March 2014.

[35] J Jahn, AA Khan, and P Zeilinger. Second-order optimality conditions in set optimization. *Journal of Optimization Theory and Applications*, 125(2):331–347, 2005.

[36] Kamran Jalili and Steffen Bernet. Design of *lcl* filters of active-front-end two-level voltage-source converters. *IEEE Transactions on Industrial Electronics*, 56(5):1674–1689, 2009.

[37] Prof. Charbel Farhat Jason Hicken, Prof. Juan Alonso. Design of aerospace systems within a formal optimization environment.

[38] W John. Remarks to the solution of emc-problems on printed-circuit-boards. In *Seventh International Conference on Electromagnetic Compatibility, 1990*, pages 68–72. IET, 1990.

[39] Joshua D Kagerbauer and TM Jahns. Development of an active dv/dt control algorithm for reducing inverter conducted emi with minimal impact on switching losses. In *2007 IEEE Power Electronics Specialists Conference*, pages 894–900. IEEE, 2007.

[40] Nikolaos V Kantartzis and Theodoros D Tsiboukis. *Modern EMC analysis techniques volume I: time-domain computational schemes*, volume 3. Morgan & Claypool Publishers, 2008.

[41] S Khalid and Bharti Dwivedi. Power quality issues, problems, standards & their effects in industry with corrective means. *International Journal of Advances in Engineering & Technology*, 1(2):1, 2011.

[42] Hyosung Kim and Seung-Ki Sul. Analysis on output lc filters for pwm inverters. In *2009 IEEE 6th International Power Electronics and Motion Control Conference*, pages 384–389. IEEE, 2009.

[43] Guanghui Lan. *First-order and Stochastic Optimization Methods for Machine Learning*. Springer, 2020.

[44] Felice Liccardo, Pompeo Marino, Castrese Schiano, and Nunzio Visciano. Active front-end design criteria. In *10th International Conference on Harmonics and Quality of Power. Proceedings (Cat. No. 02EX630)*, volume 2, pages 507–512. IEEE, 2002.

[45] Magnetics. Powder cores, 2017.

[46] Clement Marlier, Arnaud Videt, Nadir Idir, Houmam Moussa, and Régis Meuret. Frequency-domain emi noise source modeling for power converter. 05 2012.

[47] Ferran Martiacuten, Lei Zhu, Jiasheng Hong, and Francisco Medina. *BALANCED POWER DIVIDERS/COMBINERS*, pages 565–606. 2018.

[48] Ali I Maswood. A pwm voltage source inverter with pi controller for instantaneous motor current control. In *Proceedings of 1995 International Conference on Power Electronics and Drive Systems. PEDS 95*, pages 834–837. IEEE, 1995.

[49] Colonel Wm T McLyman. *Transformer and inductor design handbook*. CRC press, 2004.

[50] David Morgan. *A handbook for EMC testing and measurement*, volume 8. Iet, 1994.

[51] Ralph Morrison. *Grounding and shielding: circuits and interference*. John Wiley & Sons, 2016.

[52] S Müller, Jan Meyer, Peter Schegner, and S Djokic. Harmonic modeling of electric vehicle chargers in frequency domain. In *International conference on renewable energies and power quality (ICREPQ)*, pages 1–6, 2015.

[53] Daria Nemashkalo, Niek Moonen, and Frank Leferink. Mode decomposition in multichannel time-domain conducted emission measurements. In *2021 IEEE International Joint EMC/SI/PI and EMC Europe Symposium*, pages 643–647. IEEE, 2021.

[54] JR Nicholson and JA Malack. Rf impedance of power lines and line impedance stabilization networks in conducted interference measurements. *IEEE Transactions on Electromagnetic Compatibility*, (2):84–86, 1973.

[55] Departament of Defense. Mil-std-704, military standard: Electric power, aircraft, characteristics and utilization, December 2007.

[56] Sungjae Ohn, Jianghui Yu, Paul Rankin, Bingyao Sun, Rolando Burgos, Dushan Boroyevich, Harish Suryanarayana, and Christopher Belcastro. Three-terminal common-mode emi model for emi generation, propagation, and mitigation in a full-sic three-phase ups module. *IEEE Transactions on Power Electronics*, 34(9):8599–8612, 2019.

[57] Henry W Ott. *Electromagnetic compatibility engineering*. John Wiley & Sons, 2011.

[58] Osman ÖZKARACA. A review on usage of optimization methods in geothermal power generation. *Mugla Journal of Science and Technology*, 4(1):130–136, 2018.

[59] Ki-Bum Park, Frederick D Kieferndorf, Uwe Drofenik, Sami Pettersson, and Francisco Canales. Weight minimization of lcl filters for high-power converters: Impact of pwm method on power loss and power density. *IEEE Transactions on Industry Applications*, 53(3):2282–2296, 2017.

[60] Clayton R Paul. *Introduction to electromagnetic compatibility*. John Wiley & Sons, 2006.

[61] Elijah Polak. *Optimization: algorithms and consistent approximations*, volume 124. Springer Science & Business Media, 2012.

[62] C Poongothai and Krishna Vasudevan. Design of lcl filter for grid-interfaced pv system based on cost minimization. *IEEE Transactions on Industry Applications*, 55(1):584–592, 2018.

[63] Babak Rahrovi and Mehrdad Ehsani. A review of the more electric aircraft power electronics. pages 1–6, 2019.

[64] Atanu Roy, Saswati Ghosh, and A. Chakrabarty. Simple crosstalk model of three wires to predict nearend and farend crosstalk in an emi/emc environment to facilitate emi/emc modeling. *Progress in Electromagnetics Research B*, 8:43–58, 01 2008.

[65] Surya Santoso, Mark F McGranaghan, Roger C Dugan, and H Wayne Beaty. *Electrical power systems quality*. McGraw-Hill Education, 2012.

[66] Bulent Sarlioglu, Casey T Morris, Di Han, and Silong Li. Driving toward accessibility: a review of technological improvements for electric machines, power electronics, and batteries for electric and hybrid vehicles. *IEEE Industry Applications Magazine*, 23(1):14–25, 2016.

[67] Dan Simon. *Evolutionary optimization algorithms*. John Wiley & Sons, 2013.

[68] Bingyao Sun, Rolando Burgos, and Dushan Boroyevich. Common-mode emi unterminated behavioral model of wide-bandgap-based power converters operating at high switching frequency. *IEEE Journal of Emerging and Selected Topics in Power Electronics*, 7(4):2561–2570, 2018.

[69] Linyan Sun and Muhong Wang. Global warming and global dioxide emission: an empirical study. *Journal of Environmental Management*, 46(4):327–343, 1996.

[70] Mark A Swihart. Inductor cores–material and shape choices. *Magnetics®-www. mag-inc. com*, 2004.

[71] Mohan N Undeland, Wiliam P Robbins, and N Mohan. Power electronics. In *Converters, Applications, and Design*. John Whiley & Sons, 1995.

[72] Gerhard Venter. Review of optimization techniques. *Encyclopedia of aerospace engineering*, 2010.

[73] Adrien Voldoire. *Outil de développement et d'optimisation dédié aux onduleurs SiC de forte puissance*. PhD thesis, Université Grenoble Alpes [2020-....], 2020.

[74] Andrea Walther and Andreas Griewank. A package for the automatic differentiation of algorithms written in c/c+. *URL https://projects. coin-or. org/ADOL-C*, 2010.

[75] Timothy CY Wang, Zhihong Ye, Gautam Sinha, and Xiaoming Yuan. Output filter design for a grid-interconnected three-phase inverter. In *IEEE 34th Annual Conference on Power Electronics Specialist, 2003. PESC'03.*, volume 2, pages 779–784. IEEE, 2003.

[76] Bo Wen. *Stability analysis of three-phase ac power systems based on measured dq frame impedances*. PhD thesis, Virginia Tech, 2015.

[77] Bo Wen, Dushan Boroyevich, Rolando Burgos, Paolo Mattavelli, and Zhiyu Shen. Analysis of dq small-signal impedance of grid-tied inverters. *IEEE Transactions on Power Electronics*, 31(1):675–687, 2015.

[78] Xlinx. Zybo z7-10 zynq-7000 arm/fpga soc development board https://www.xilinx.com/products/boards-and-kits/1-pukimv.html.

[79] Xin-She Yang. *Engineering optimization: an introduction with metaheuristic applications*. John Wiley & Sons, 2010.

[80] Eckart Zitzler, Marco Laumanns, and Stefan Bleuler. A tutorial on evolutionary multiobjective optimization. *Metaheuristics for multiobjective optimisation*, pages 3–37, 2004.

Contribution to System Level Modelling of Power Quality and EMC for Design of Aircraft Grids

Abstract

Keywords *Active front-end, AFE, aerospace, Black Box, boost, conducted emission, converter control, design, EMC, EMI, harmonic filters, power quality, optimization, SQP, voltage source inverter, VSI.*

Dynamic technology development resulted in a significant increase in number of electrical devices. This growth is present in the most of engineering fields especially in science, industry and military. Usually, at least several devices are somehow connected to each other and therefore some interactions between them might occur which can lead to their the degradation of performances of the whole system. The aim of the research presented in this PhD is to study the interactions occurring in electrical grids composed of power electronic converters. The thesis presents analysis of two aircraft notional grids where the interactions were studied. The first one is a typical aircraft AC grid where the study is focused on harmonic filters interactions and their influence on system's control performance (dynamic response). The second one is a DC grid composed of several DC to DC converters with a focus on EMI-related interactions in this grid.

Part I

The first part of the thesis describes the harmonic interactions study. The research study case is a notional AC aircraft grid where two converters are connected. One of them is a Voltage Source Inverter which in fact produces the grid. The other one is an Active Front End converter connected to the grid on the input side.

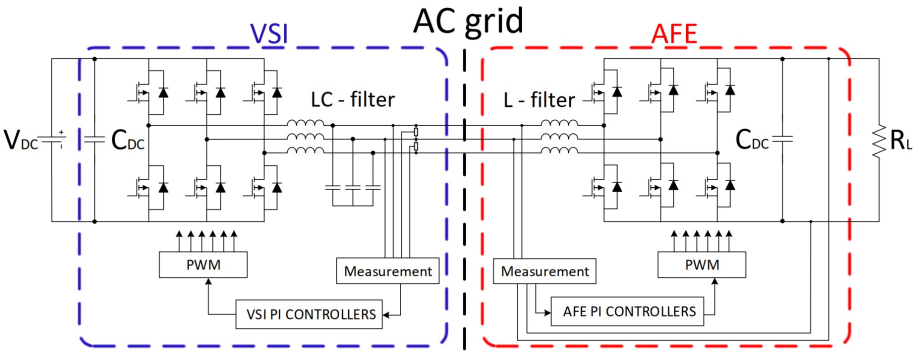

Figure II.63: Schematic of the study case AC aircraft grid.

Each converter has a filter connected to the AC grid. VSI has a LC filter connected to the its output, whereas, AFE has a L filter connected to its input. Both converters have an independent control systems based on PI controllers. The preliminary study, based on switching model simulation, showed that there are some interactions between filters, VSI filter affects AFE control performance and AFE filter affects VSI control causing issues with meeting aircraft standards requirements.

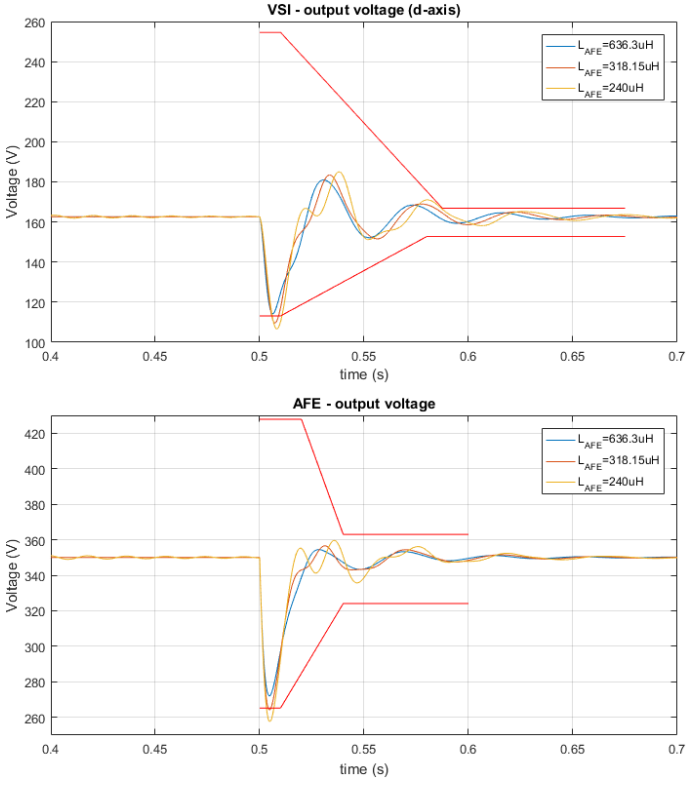

Figure II.64: Comparison of VSI and AFE output voltage response for a step load for different AFE input inductor values. Any other parameter is not changed. Red lines showing the dynamic requirements.

A conventional simulation based on a switching model which was used for preliminary study is needs a lot of computing power and is time consuming. Moreover, mathematical description of the system including a control would be a complex task due to high order of the system. Therefore it was decided to create, the dedicated simulation tool, based on small-signal average modelling approach. This tool is able to very quickly simulate systems dynamic behaviour for a given passive component values and controllers' settings. Moreover the tool automatically checks whether the avionic standard requirements are met or not.

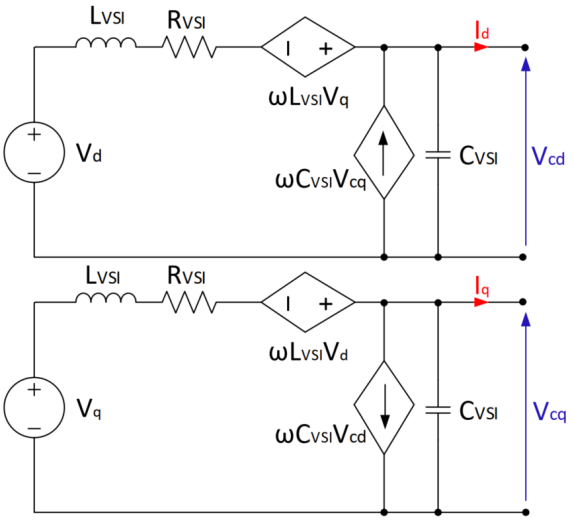

Figure II.65: Small-signal circuit dq model of the VSI converter.

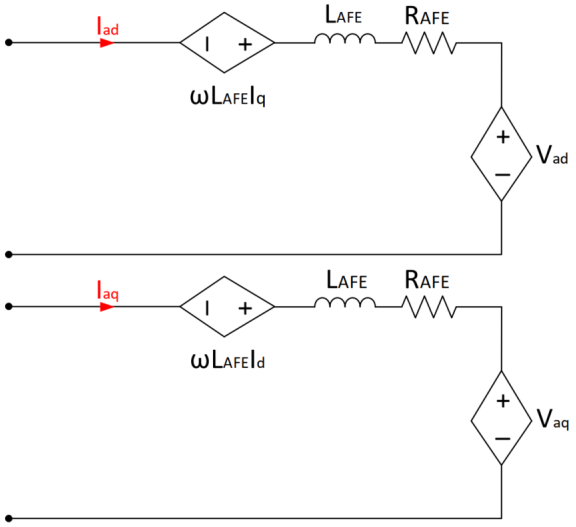

Figure II.66: Small-signal circuit dq model of the AFE converter.

Afterwards, the experimental tests have been performed in order to validate the simulation tool. The step load response have been checked for different harmonic filters values.

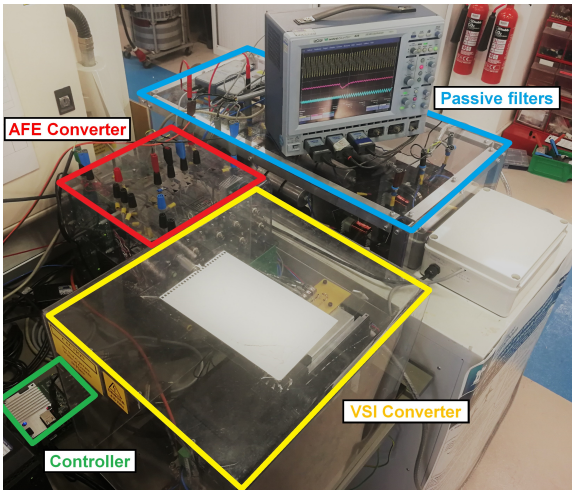

Figure II.67: View of experimental test rig.

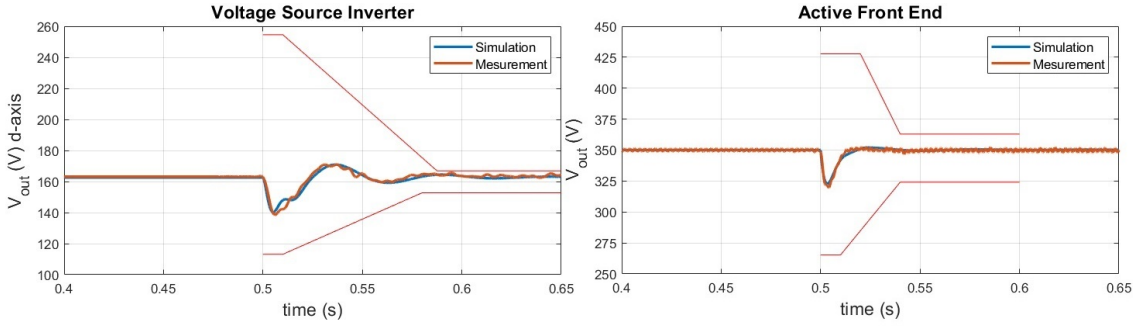

Figure II.68: Comparison between simulation and experimental results of step-load response of the system. Example result with filter parameters L_{VSI}=260μH C_{VSI}=33μF L_{AFE}=630μH.

Once the simulation tool was validated it was used to simulate all possible combinations of AC grid passive components and controller settings (in a reasonable constraints) in order to check how the filters' interactions affect the control. The results obtained from the tool allowed to create the Area of Design, a map of filter components values which are allowed to combine in order to be able to meet dynamic behaviour standards.

Then, to make Area of Design useful, harmonic filters optimization has been conducted. The optimization problem which was defined is filters mass reduction since it is related to exploitation cost of the aircraft which is crucial in avionics industry.

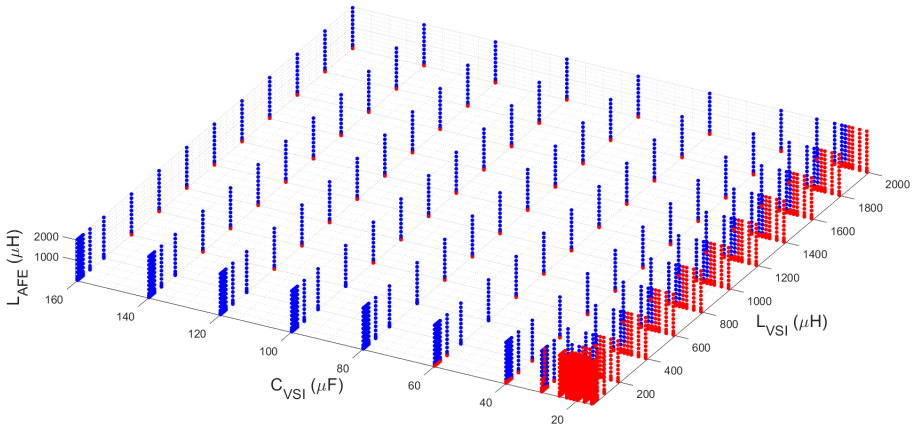

Figure II.69: Area of Design. Blue points indicates the design which meets the requirements, red which does not.

In order to optimize the filters maintaining AC grid THD requirement, it was necessary to estimate grid's harmonics, therefore, a frequency-domain grid model has been created and verified.

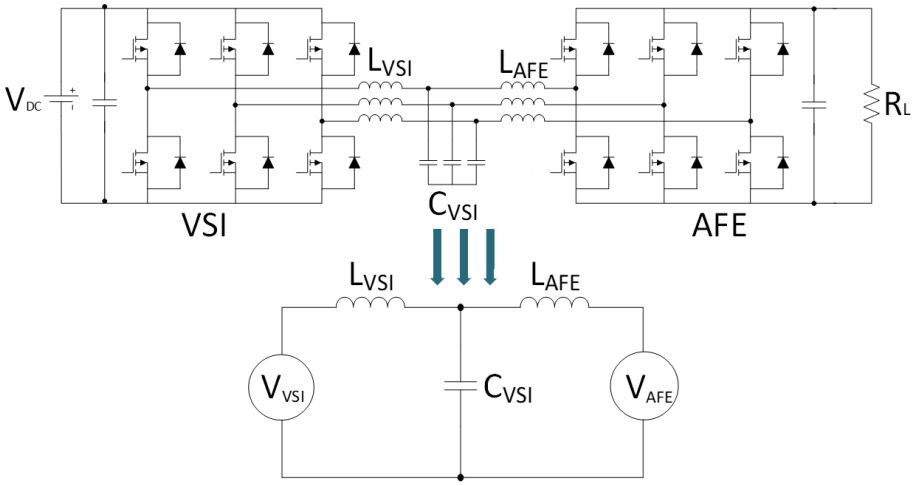

Figure II.70: Frequency-domain model of the grid.

Finally, two optimization of the harmonic filters have been performed. One with harmonic filters constraint only (grid THD) and the second with both THD and dynamic behaviour constraint (based on the Area of Design). Results show that total weight of the filters optimized only with THD constraint is smaller than the weight of the filters where both constraints were considered.

Table II.4: Comparison between the total filter mass. Before optimization, with THD constraints only and with all constraints.

Parameters	**Unit**	**Before Optimization**	**Optimization without Dynamic Constraints**	**Optimization with Dynamic Constraints**
L_{VSI}	[µH]	260	51.4	64.4
C_{VSI}	[µF]	33	23	40
L_{AFE}	[µH]	630	24.9	45.67
$FiltersMass$	[g]	1866.5	500.37	652.2
THD	[%]	0.38	4.99	2.09

The study which has been described in Part I showed that the interactions between harmonic filters are not negligible. For some filter designs if they are not considered it might happen that even if devices were meeting the standards individually (both power quality and dynamic)if they are connected to the common grid it is no longer true. This is especially important in optimization design procedures when we tend to minimize the filters which decrease their dynamic performance.

Part II

The second part describes the study of EMI interactions in a DC grid which consists of power electronics converters, in particular, how the grid interactions affect the total emission in the mains supply. The study case is a typical DC grid with three boost converters connected in parallel. In addition to converters the grid contain EMI filters connected on the each boost input and cables (also important in terms of EMC) witch connect all grid parts together.

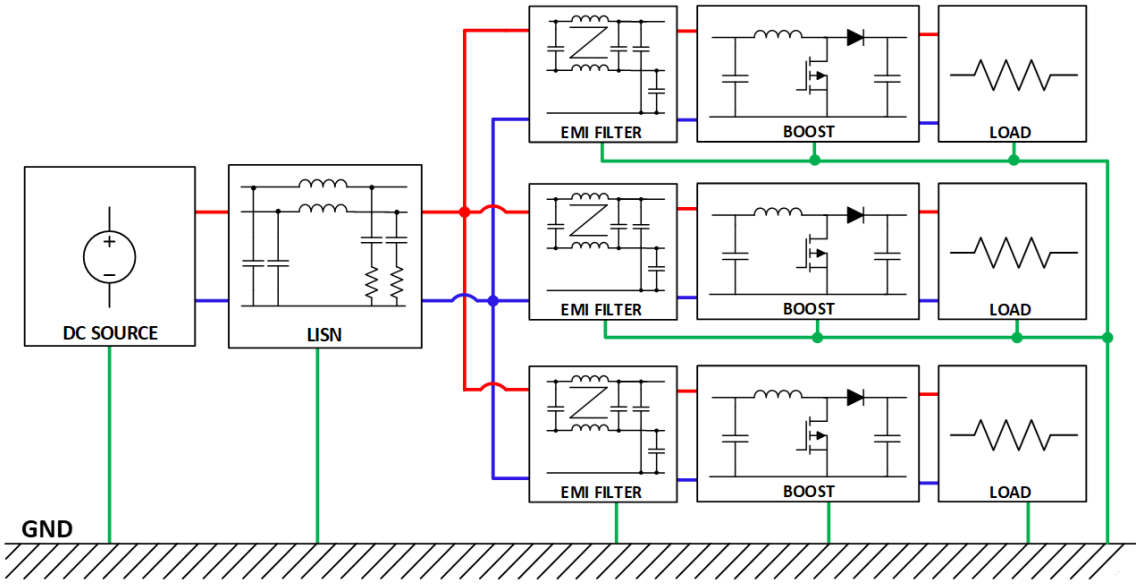

Figure II.71: Study case DC grid.

Preliminary study revealed that some EMI-related interactions occur between converters. It was noticed that there is a difference between total emission generated by a grid with parallel converters and a summation of emission generated from every converter working in a grid alone. This means that some of the disturbances flow between converters changing the expected level of emission flowing to the grid. More detailed study revealed that in fact differential mode disturbance is different when comparing both cases.

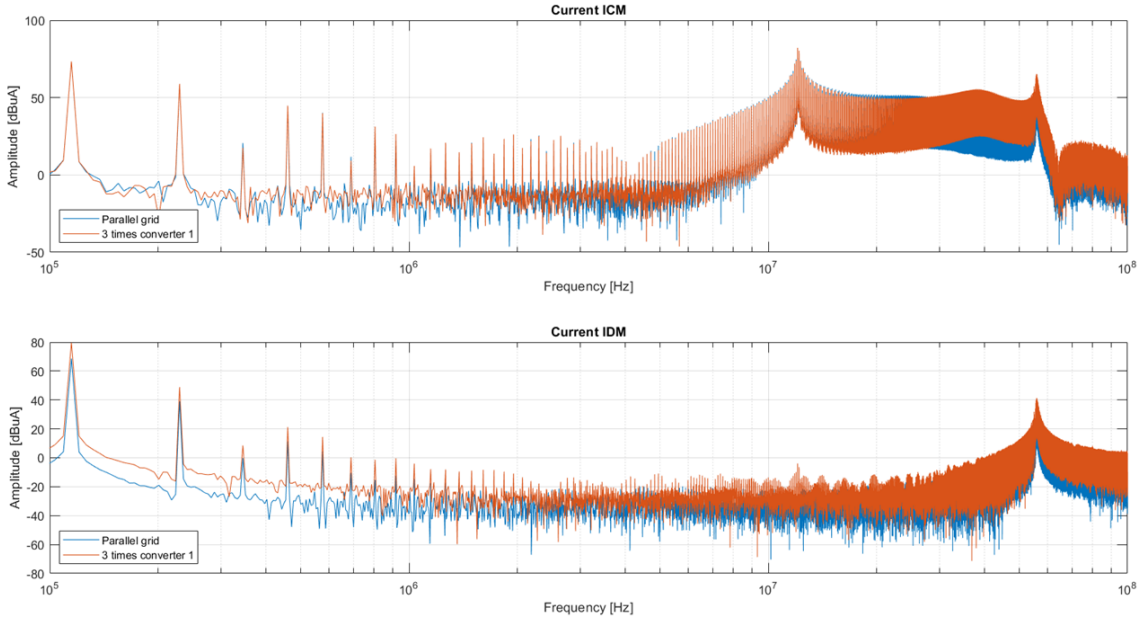

Figure II.72: Comparison between triple emission from single converter grid versus emission from grid of parallel converters for I_{CM} and I_{DM} currents in frequency-domain.

Due to the fact that the preliminary analysis was based on time-domain EMI modelling which is very rough in terms of computing power and simulation time, more detailed EMI modelling, especially with a more complex model (e.g. more complex converter and more devices in the grid) would be not suitable, therefore, another approach based on frequency-domain modelling has been introduced.

The model used in the further study is called Terminated Asymmetrical Black Box Model. It is based on input impedances of the modelled device and its excitation sources which are responsible for EMI generation in the model.

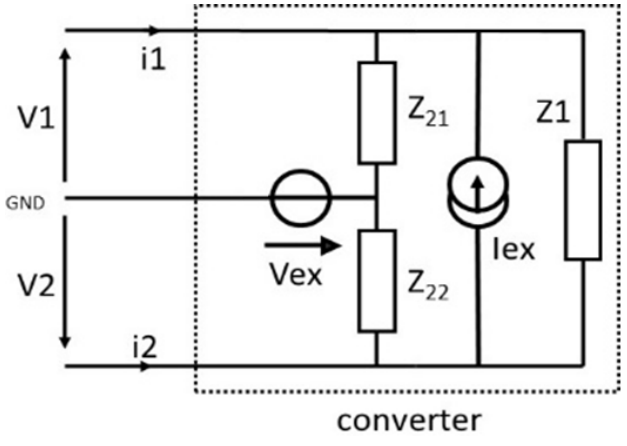

Figure II.73: Terminated Asymmetrical Black Box model.

In the further study, two different Black Box models have been identified. One model was identified on the basis of time-domain simulation model (previously used in preliminary analysis) and the second one was identified from an actual converter available in the laboratory.

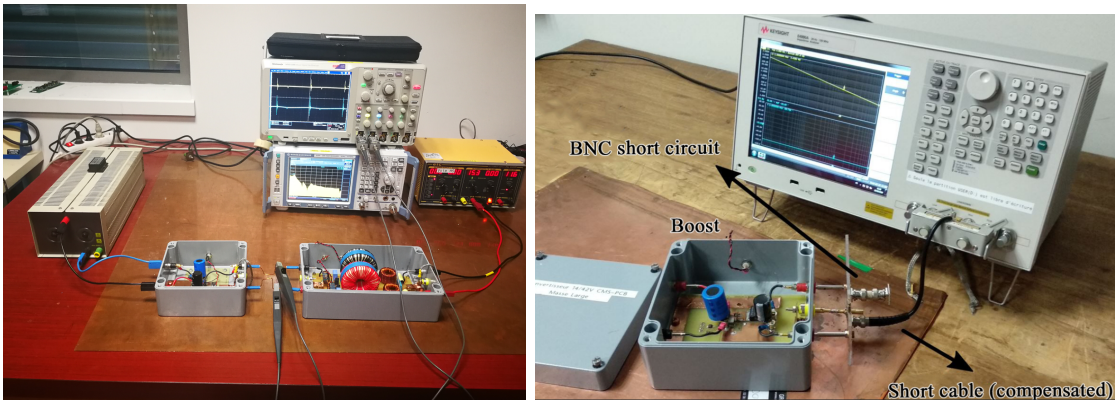

Figure II.74: Black Box model identification of the physical converter.

In order to check validity and robustness of the models, they were verified in several environments different to the one where the models were identified. The verification has been conduced for both model based on simulation and based on a the real converter in following scenarios, asymmetrical LISN, minus shorted to ground and with EMI filter.

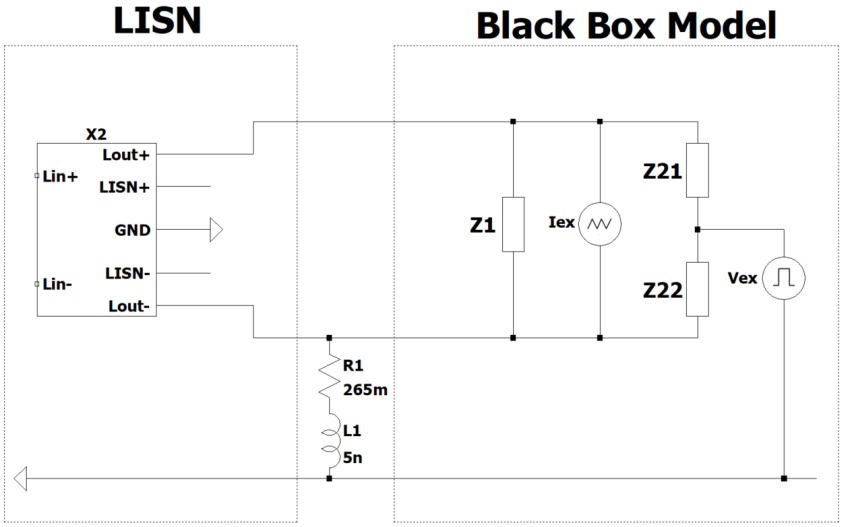

Figure II.75: Frequency-domain Black Box model circuit. Case "Minus to ground".

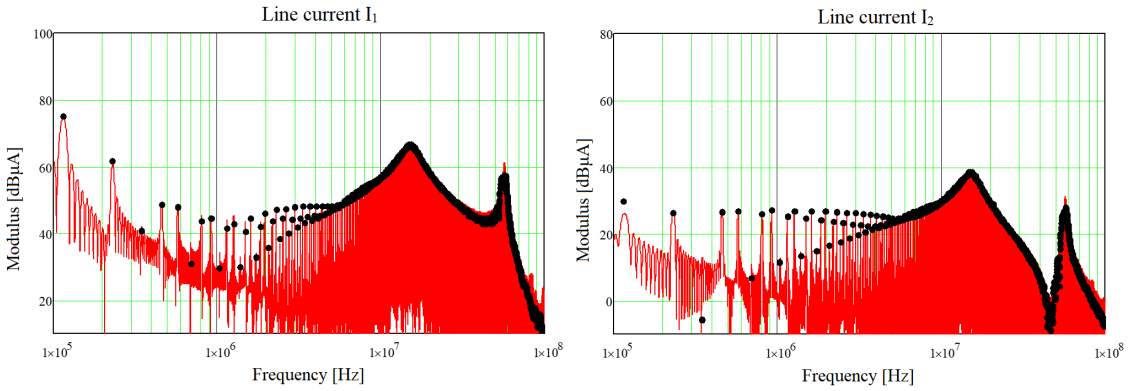

Figure II.76: Comparison between line current obtained by time-domain simulation with FFT – red coloured spectrum and line currents obtained by solving frequency-domain circuit with Black Box model representing EMI of the converter – black dots. Case "Minus to ground".

Once the Black Box modelling approach were validated, the model, which was previously identified on time-domain simulation model, was used to estimate EMI disturbances in the study case grid.

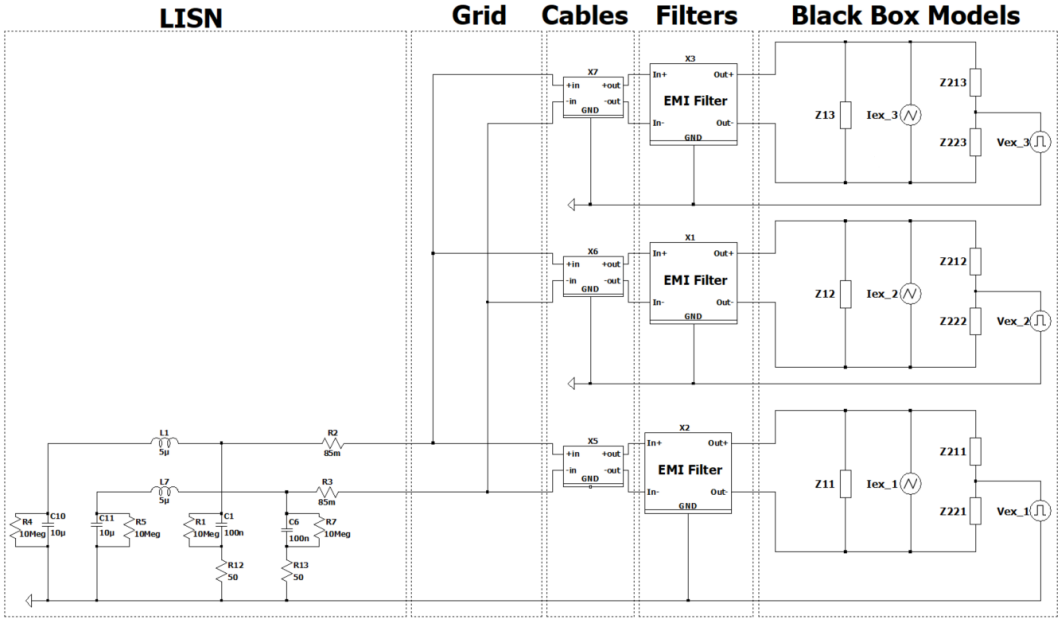

Figure II.77: Grid-level EMI modelling based on Black Box approach. Study case grid.

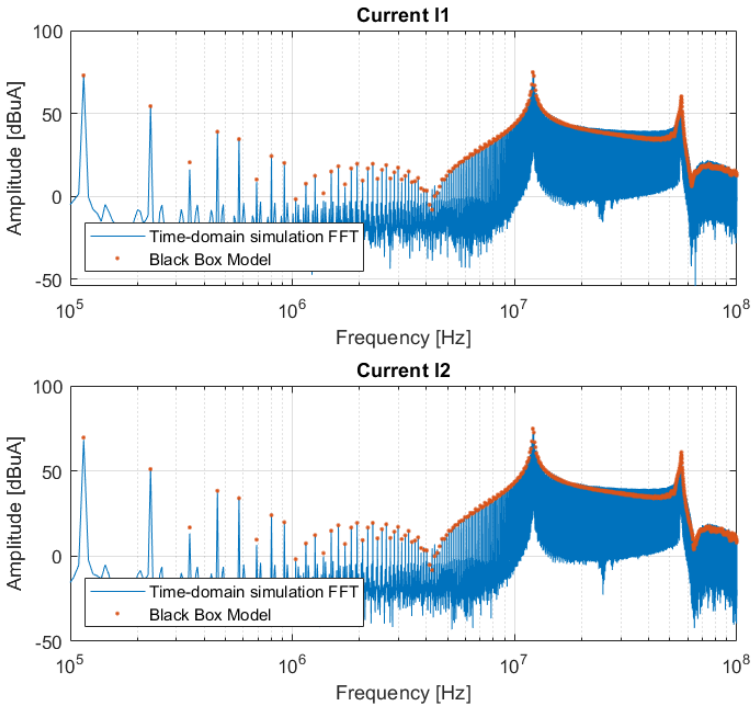

Figure II.78: Grid currents I_1 and I_2" in frequency domain. The comparison between time-domain simulation results and Black Box frequency-domain results.

The results obtained from system level Black Box modelling were compared with previously made time-domain simulation. It can be seen that both results are pretty accurately matching. Time and computing power needed for obtaining almost the same results as time-domain simulation with using Black Box frequency-domain model is much lower. This enables opportunity of system level EMI modelling even with large number of devices in the grid. Thus, it can be used in automatic design process considering EMI, with using optimization for instance.

Contribution á la modélisation systéme pour la qualité de l'energie et la CEM dans la conception des réseaux d'avions

Résumé

Mots-clés *Absorption sinusoidale, AFE, aérospatiale, Black Box, boost, CEM, émission conduite, modele CEM, controle de convertisseur, conception, filtres harmoniques, qualité de l'énergie, optimisation, SQP, voltage source inverter, VSI.*

Le développement dynamique des technologies a entraîné une augmentation significative du nombre de dispositifs électriques. Cette croissance est présente dans la plupart des domaines de l'ingénierie, en particulier dans les sciences, l'industrie et l'armée. Habituellement, au moins plusieurs dispositifs sont connectés entre eux d'une manière ou d'une autre et, par conséquent, certaines interactions entre eux peuvent se produire et conduire à une dégradation des performances de l'ensemble. L'objectif de la recherche présentée dans cette thèse est d'étudier les interactions qui se produisent dans les réseaux électriques composés de convertisseurs électroniques de puissance. La thèse présente l'analyse de deux réseaux théoriques d'avions où les interactions ont été étudiées. Le premier est un réseau alternatif typique d'avion où l'étude se concentre sur les interactions des filtres harmoniques et leur influence sur les performances de contrôle du système (réponse dynamique). Le second est un réseau DC composé de plusieurs convertisseurs DC à DC avec une attention particulière aux interactions liées aux CEM dans ce réseau.

Partie I

La première partie de la thèse décrit l'étude des interactions harmoniques. Le cas d'étude est un réseau d'avion AC élémentaire où deux convertisseurs sont connectés. L'un d'entre eux est un onduleur à source de tension qui génère le réseau. L'autre est un convertisseur à absorption sinusoidale connecté au réseau du côté de l'entrée.

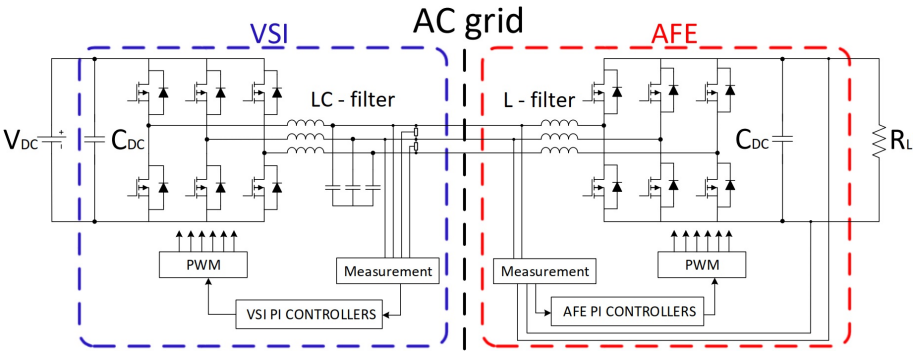

Figure II.79: Schéma de réseau de l'avion AC du cas d'étude.

Chaque convertisseur a un filtre connecté au réseau AC. Le VSI a un filtre LC connecté à sa sortie, tandis que l'AFE a un filtre L connecté à son entrée. Les deux convertisseurs ont un système de contrôle indépendant basé sur des contrôleurs PI. L'étude préliminaire, basée sur la simulation temporelle du système, a montré qu'il existe certaines interactions entre les filtres, le filtre VSI affecte les performances de contrôle de l'AFE et le filtre AFE affecte le contrôle du VSI, ce qui pose des problèmes pour répondre aux exigences des normes aéronautiques.

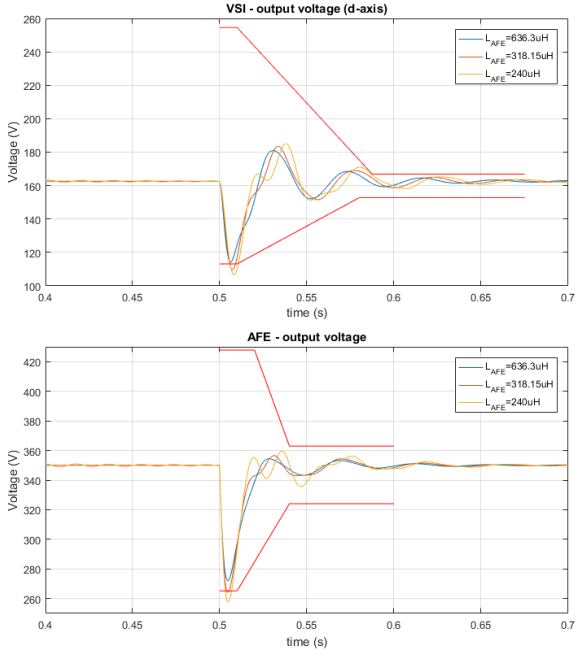

Figure II.80: Comparaison de la réponse de la tension de sortie du VSI et de l'AFE pour une charge échelonnée pour différentes valeurs d'inductance d'entrée de l'AFE. Aucun autre paramètre n'est modifié. Les lignes rouges montrent les exigences dynamiques.

Une simulation conventionnelle basée sur des simulations temporelles, qui a été utilisée pour l'étude préliminaire, nécessite une grande puissance de calcul et prend du temps. De plus, la description mathématique du système incluant une commande serait une tâche complexe en raison de l'ordre élevé du système. Il a donc été décidé de créer un outil de simulation dédié, basé sur une approche de modélisation moyenne à petits signaux. Cet outil est capable de simuler très rapidement le comportement dynamique des systèmes pour des valeurs de composants passifs et des réglages de contrôleurs donnés. De plus, l'outil vérifie automatiquement si les exigences de la norme avionique sont respectées ou non.

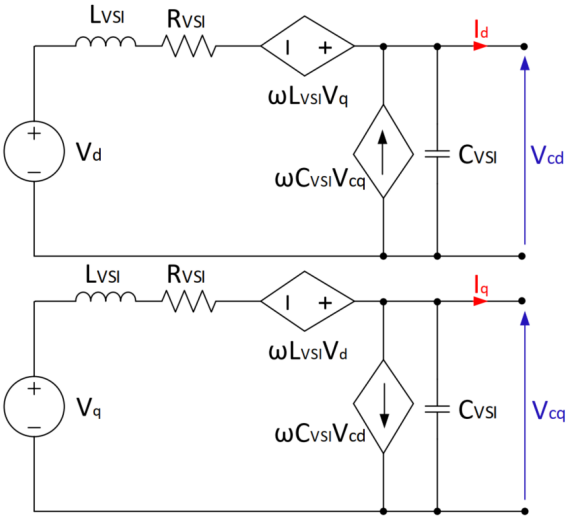

Figure II.81: Modèle dq du circuit à petits signaux du convertisseur VSI.

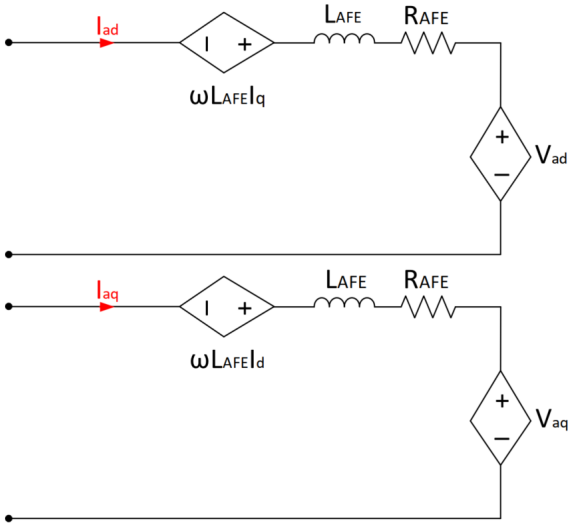

Figure II.82: Modèle de circuit à petit signal dq du convertisseur AFE.

Ensuite, les tests expérimentaux ont été réalisés afin de valider l'outil de simulation. La réponse de à un échelon de charge a été vérifiée pour différentes valeurs de filtres harmoniques.

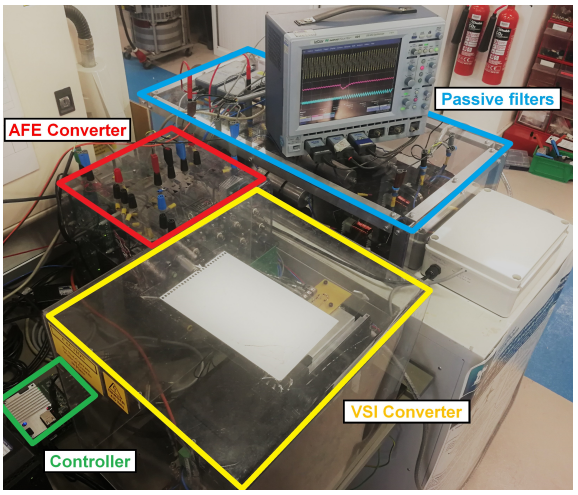

Figure II.83: Vue du banc d'essai expérimental.

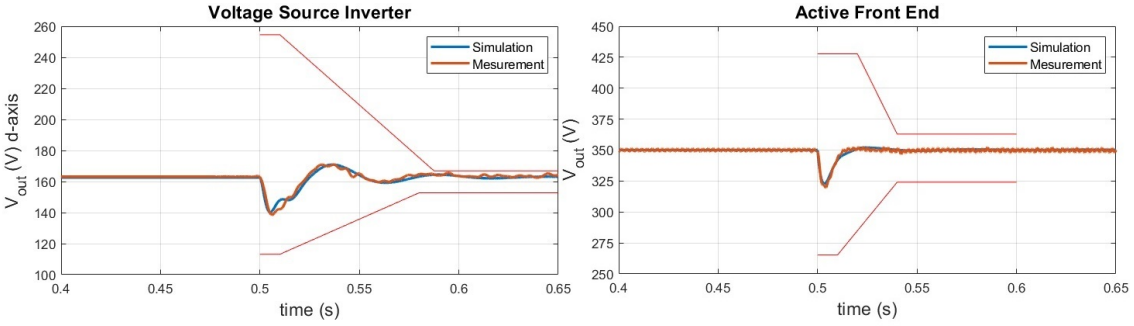

Figure II.84: Comparaison entre les résultats de la simulation et les résultats expérimentaux de la réponse du système à la charge par paliers. Exemple de résultat avec le paramètre du filtre L_{VSI}=260μH C_{VSI}=33μF L_{AFE}=630μH.

Une fois l'outil de simulation validé, il a été utilisé pour simuler toutes les combinaisons possibles de composants passifs du réseau AC et de réglages du contrôleur (dans des bornes raisonnables) afin de vérifier comment les interactions des filtres affectent le contrôle. Les résultats obtenus à partir de l'outil ont permis de créer une aire de dimensionnement„ une carte des valeurs des composants du filtre qui sont autorisés à se combiner afin de pouvoir répondre aux normes de comportement dynamique.

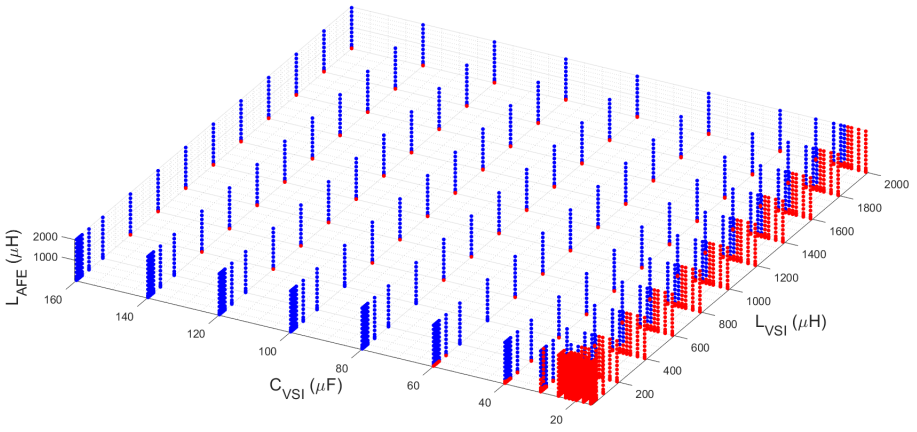

Figure II.85: Une aire de dimensionnement. Les points bleus indiquent la conception qui répond aux exigences, les rouges celle qui n'y répond pas.

Cette aire de dimensionnement a été utilisée pour optimiser des filtres harmoniques. Le problème d'optimisation qui a été défini est la réduction de la masse des filtres puisqu'elle est liée au coût d'exploitation de l'avion, ce qui est crucial dans l'industrie de l'avionique. Afin d'optimiser les filtres en maintenant les exigences de THD du réseau AC, il était nécessaire d'estimer les harmoniques du réseau, par conséquent, un modèle de réseau dans le domaine de la fréquence a été créé et vérifié.

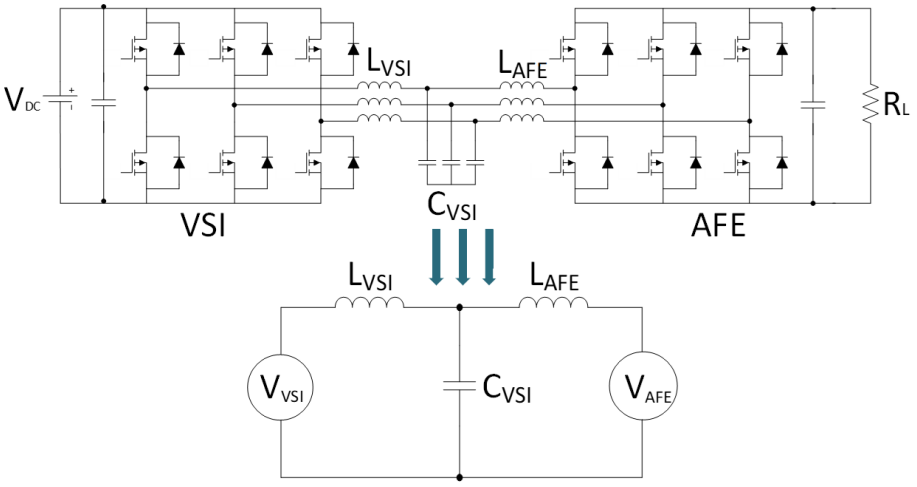

Figure II.86: Modèle de réseau dans le domaine de la fréquence.

Enfin, deux optimisations des filtres harmoniques ont été réalisées. L'une avec la seule contrainte des filtres harmoniques (THD de réseau) et la seconde avec la contrainte du THD et du comportement dynamique (basée sur l'aire de dimensionnement). Les résultats montrent que le poids total des filtres optimisés uniquement avec la contrainte THD est plus petit que le poids des filtres où les deux contraintes ont été considérées.

Table II.5: Comparaison entre la masse totale du filtre. Avant optimisation, avec les contraintes THD uniquement et avec toutes les contraintes.

Parameters	**Unit**	**Before Optimization**	**Optimization without Dynamic Constraints**	**Optimization with Dynamic Constraints**
L_{VSI}	[µH]	260	51.4	64.4
C_{VSI}	[µF]	33	23	40
L_{AFE}	[µH]	630	24.9	45.67
$FiltersMass$	[g]	1866.5	500.37	652.2
THD	[%]	0.38	4.99	2.09

L'étude qui a été décrite dans la première partie a montré que les interactions entre les filtres harmoniques ne sont pas négligeables. Pour certaines conceptions de filtres, si l'on n'en tient pas compte, il se peut que même si les dispositifs répondent aux normes individuellement (qualité de l'énergie et dynamique), s'ils sont connectés au réseau commun, ce n'est plus vrai. Ceci est particulièrement important dans les procédures de conception par optimisation, lorsque nous avons tendance à minimiser les filtres qui diminuent leurs performances dynamiques.

Partie II

La deuxième partie décrit l'étude des interactions EMI dans un réseau DC qui se compose de convertisseurs électroniques de puissance, en particulier, comment les interactions du réseau affectent l'émission totale dans l'alimentation. Le cas étudié est un réseau DC typique avec trois convertisseurs boost connectés en parallèle. En plus des convertisseurs, le réseau contient des filtres CEM connectés sur chaque entrée de boost et des câbles (également importants en termes de CEM) qui connectent toutes les parties du réseau ensemble.

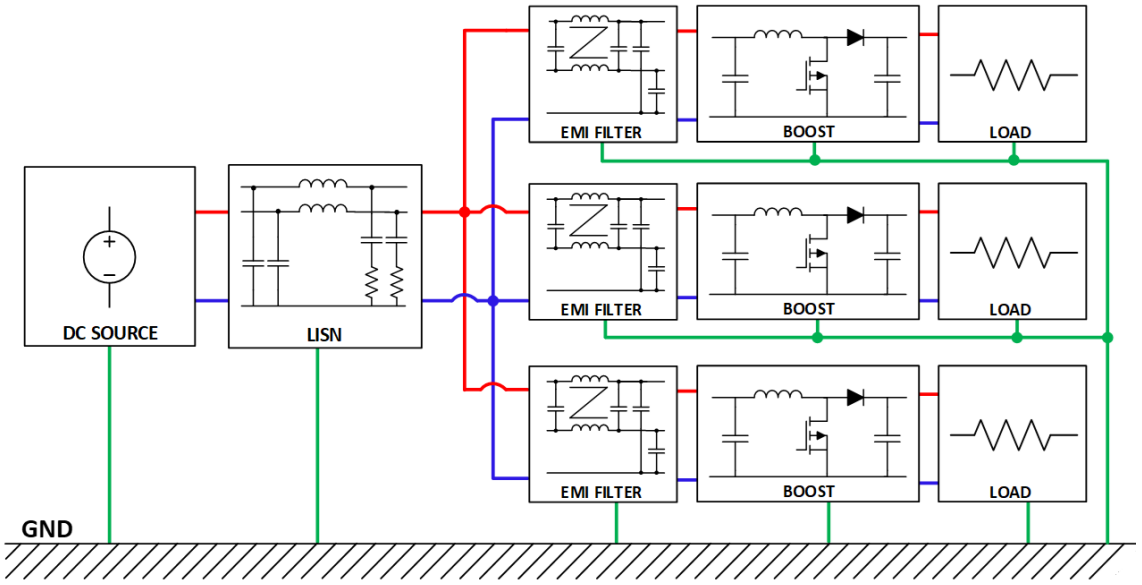

Figure II.87: Cas d'étude réseau DC.

Une étude préliminaire a révélé que certaines interactions liées aux émissions conduites se produisent entre les convertisseurs. On a remarqué qu'il y a une différence entre l'émission totale générée par un réseau avec des convertisseurs en parallèle et la somme des émissions générées par chaque convertisseur fonctionnant dans un réseau seul. Cela signifie qu'une partie des perturbations circule entre les convertisseurs, ce qui modifie le niveau prévu d'émission vers le réseau. Une étude plus détaillée a révélé qu'en fait, la perturbation en mode différentiel est différente lorsqu'on compare les deux cas.

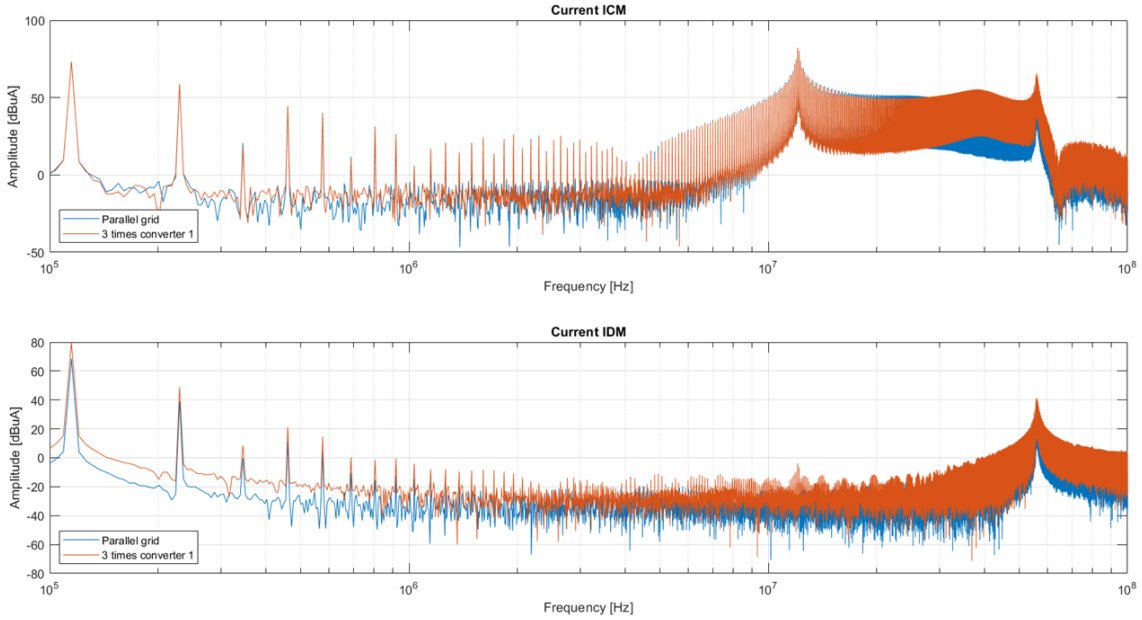

Figure II.88: Comparaison entre l'émission triple du réseau d'un seul convertisseur et l'émission du réseau de convertisseurs parallèles pour les courants I_{CM} et I_{DM} dans domaine de la fréquence.

Étant donné que l'analyse préliminaire était basée sur la modélisation des interférences électromagnétiques dans le domaine temporel, qui est très gourmande en termes de puissance de calcul et de temps de simulation, une modélisation plus détaillée des interférences électromagnétiques, en particulier avec un modèle plus complexe (par exemple, un convertisseur plus complexe et plus de dispositifs dans le réseau), ne serait pas appropriée. C'est pourquoi une autre approche basée sur la modélisation dans le domaine des fréquences a été introduite.

Le modèle utilisé dans cette étude est appelé Terminated Asymmetrical Black Box model. Il est basé sur les impédances d'entrée du dispositif modélisé et ses sources d'excitation qui sont responsables de la génération d'interférences électromagnétiques dans le modèle.

Dans la suite de l'étude, deux modèles Black Box différents ont été identifiés. Le premier modèle a été identifié sur la base du modèle de simulation dans le domaine temporel (utilisé précédemment dans l'analyse préliminaire) et le second a été identifié à partir d'un convertisseur réel disponible dans le laboratoire.

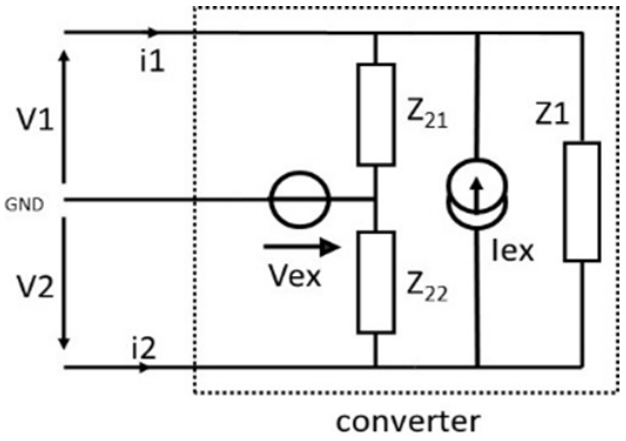

Figure II.89: Terminated Asymmetrical Black Box model.

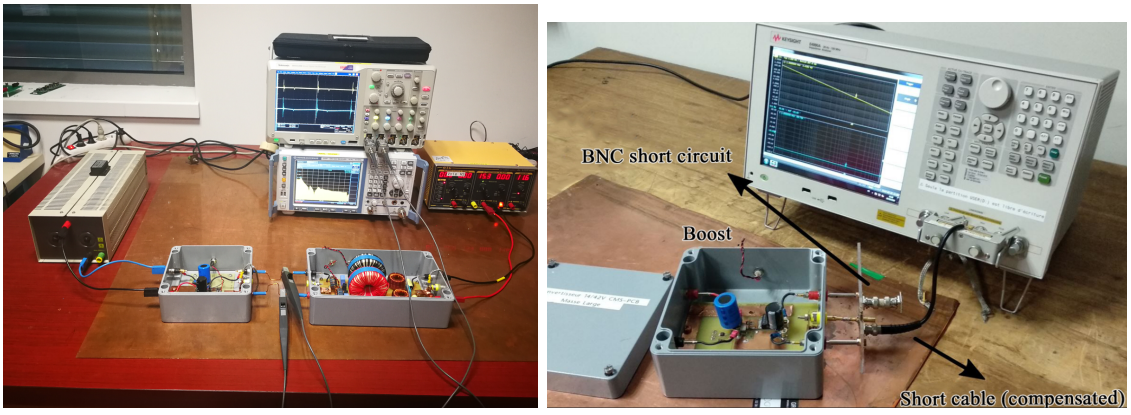

Figure II.90: Black Box model identification du convertisseur réel.

Afin de vérifier la validité et la robustesse des modèles, ceux-ci ont été vérifiés dans plusieurs environnements différents de celui où les modèles ont été identifiés. La vérification a été effectuée pour les deux modèles basés sur la simulation et sur un convertisseur réel dans les scénarios suivants, RISL asymétrique, moins court-circuité à la terre et avec un filtre d'interférence électromagnétique.

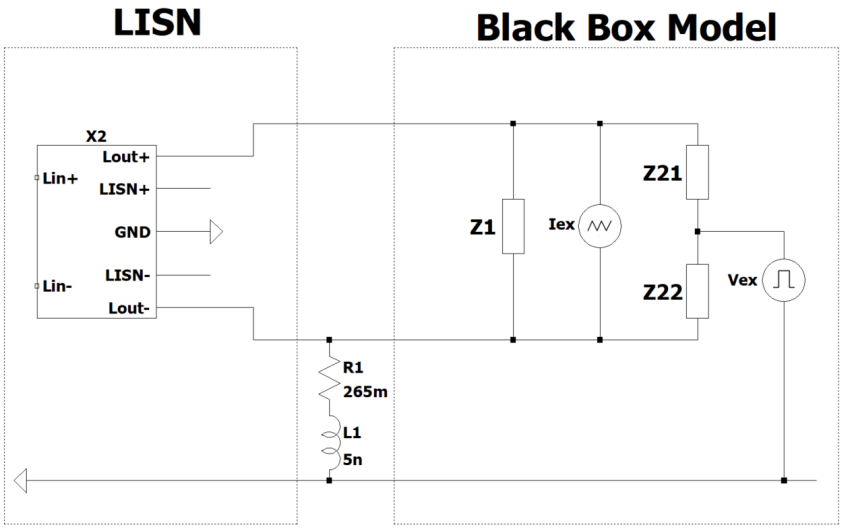

Figure II.91: Circuit modèle Black Box dans le domaine de la fréquence. Cas "Minus to ground".

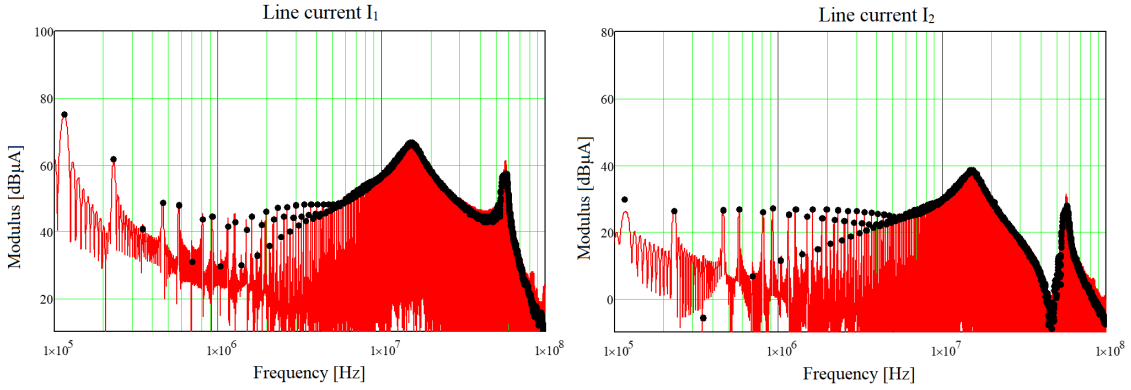

Figure II.92: Comparaison entre le courant de ligne obtenu par simulation dans le domaine temporel avec FFT – spectre de couleur rouge et les courants de ligne obtenus par la résolution du circuit dans le domaine de la fréquence avec le modèle Black Box représentant l'interférence électromagnétique du convertisseur – points noirs. Cas "Minus to ground".

Une fois que l'approche de modélisation Black Box a été validée, le modèle, qui a été précédemment identifié sur le modèle de simulation dans le domaine temporel, a été utilisé pour estimer les interférences électromagnétiques dans le réseau du cas d'étude.

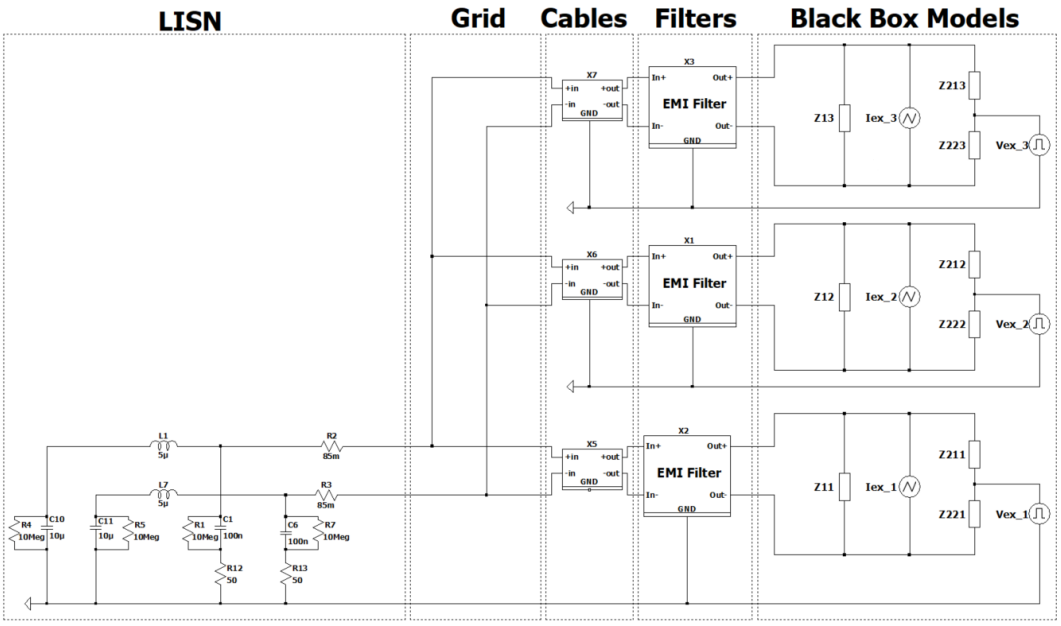

Figure II.93: Modélisation des interférences électromagnétiques au niveau du réseau basée sur l'approche Black Box. Cas d'étude réseau.

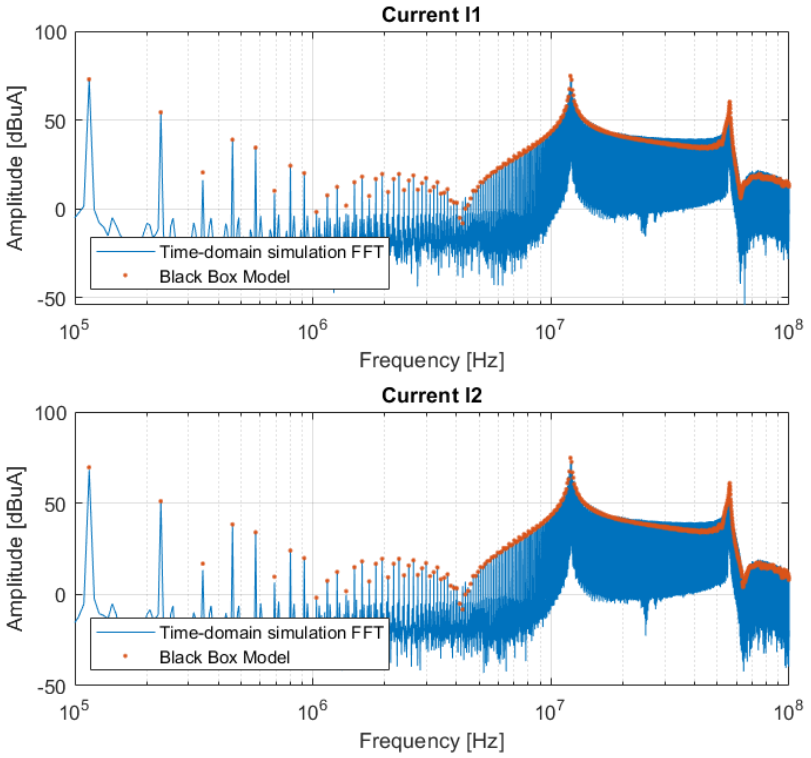

Figure II.94: Courants de réseau I_1 et I_2" dans le domaine des fréquences. La comparaison entre les résultats de la simulation dans le domaine temporel et les résultats de la Black Box dans le domaine des fréquences.

Les résultats obtenus par la modélisation Black Box au niveau du système ont été comparés à la simulation temporelle réalisée précédemment. On peut constater que les deux résultats correspondent assez fidèlement. Le temps et la puissance de calcul nécessaires pour obtenir presque les mêmes résultats que la simulation dans le domaine temporel en utilisant le modele Black Box dans le domaine de la fréquence sont beaucoup plus faibles. Cela permet de modéliser les interférences électromagnétiques au niveau du système, même avec un grand nombre de dispositifs dans le réseau. Ainsi, il peut être utilisé dans le processus de conception automatique en tenant compte des interférences électromagnétiques, en utilisant l'optimisation par exemple.

Annex-A Control System Simulation Tool – MATLAB code

```
function [set_time_VSI,set_time_AFE,undershoot_VSI,undershoot_AFE,flag] =
    VSI_AFE_SIM(x0, param, K_PI_VSI, K_PI_AFE)

    ts=1e-4; %time step

    % if ode45 iteration is longer than interrupt_time in returns error
    % which is suppresed by try catch function.

    interupt_time = 5;
    outputFun= @(t,y,flag)interuptFun(t,y,flag,interupt_time);
    opt = odeset('RelTol', ts,'OutputFcn',outputFun);
    tspan = [0 1]; %simulation time
    try
    [t,x] = ode45(@(t,x) vsi_afe_model(t, x, param, K_PI_VSI, K_PI_AFE),
    tspan, x0, opt);
    % flag = 0 unstable system - integration tolerance not met
    % flag = 1 requirements are not met
    % flag = 2 everything is fine
    % flag = 3 settling time longer than simulation time
    % flag = 4 specific case when ode45 locks so the integration is
    % interrupted after 5 secs

    sl=0.5;   %step load time (needs to be changed in the model as well)

    %Instruction that checks if simulator can run
    [~, msgid] = lastwarn;
    if strcmp(msgid, 'MATLAB:ode45:IntegrationTolNotMet')
    flag=0;
    set_time_VSI=0;
    set_time_AFE=0;
    undershoot_VSI=0;
    undershoot_AFE=0;
    lastwarn('');
    else
    % settling time search
    k=find(t>=sl&t<=sl+0.001); k=k(1);  %index of the load step interval
```

```
%VSI
w=find(x(k:end,2)<=118*sqrt(2) & x(k:end,2)>=108*sqrt(2));
ww=find(diff(w)~=1);
if isempty(ww)==1
set_time_VSI=0;
else
set_time_VSI=t(k+w(ww(end)+1)-1)-t(k);
end
%AFE
w=find(x(k:end,7)<=362.96 & x(k:end,7)>=324.07 );
ww=find(diff(w)~=1);
if isempty(ww)==1
set_time_AFE=0;
else
set_time_AFE=t(k+w(ww(end)+1)-1)-t(k);
end
%undershoot search
undershoot_VSI=min(x(k:end,2));
undershoot_AFE=min(x(k:end,7));

%% MIL-704F dynamic behaviour requirements
% time indexes searching
k1=find(t>=(sl+0.01)&t>(sl+0.0101)); k11=k1(1); k12=k1(1); k32=k1(1);
k1=find(t>=(sl+0.0875)&t>(sl+0.0876)); k21=k1(1);
k1=find(t>=(sl+0.0800)&t>(sl+0.0801)); k22=k1(1);
k1=find(t>=(sl+0.0200)&t>(sl+0.0201)); k31=k1(1);
k1=find(t>=(sl+0.0400)&t>(sl+0.0401)); k41=k1(1); k42=k1(1);

%VSI requirements functions
a1=(118*sqrt(2)-180*sqrt(2))/(t(k21)-t(k11));
b1=(180*sqrt(2))-a1*t(k11);
a2=((108*sqrt(2))-(80*sqrt(2)))/(t(k22)-t(k12));
b2=(80*sqrt(2))-a2*t(k12);
u1=a1*t(k11:k21)+b1;
u2=a2*t(k12:k22)+b2;

%AFE requirements functions
a3=(427.78-362.96)/(t(k41)-t(k31));
```

```
73      b3=427.78-a3*t(k31);
74      a4=(324.07-265.26)/(t(k42)-t(k32));
75      b4=265.26-a4*t(k32);
76      u3=a3*t(k31:k41)+b3;
77      u4=a4*t(k32:k42)+b4;
78
79      if all(x(k11:k21,2)<=u1) && all(x(k12:k22,2)>=u2) && all(x(k31:k41,7)<=
        u3) && ...
80          all(x(k32:k42,7)>=u4) && all(x(k:k11,2)<=254.5584) && all(x(k21:end
        ,2)<=166.8772) && ...
81          all(x(k:k12,2)>=113.1371) && all(x(k22:end,2)>=152.7351) && all(x(k:
        k31,7)<=427.78) && ...
82          all(x(k41:end,7)<=362.96) && all(x(k:k32,7)>=265.26) && all(x(k42:
        end,7)>=324.07)
83
84      flag=2;
85      else
86      flag=1;
87      end
88      if set_time_AFE>=0.2 || set_time_VSI>=0.2
89      flag=3;
90      end
91      end
92
93      catch ME
94      if strcmp(ME.identifier,'interuptFun:Interupt')
95      flag=4;
96      set_time_VSI=0;
97      set_time_AFE=0;
98      undershoot_VSI=0;
99      undershoot_AFE=0;
100     end
101     end
102 end
103
104 function status = interuptFun(t,y,flag,interupt_time)
105 persistent INIT_TIME;
106 status = 0;
```

```
107 switch(flag)
108     case 'init'
109         INIT_TIME = tic;
110     case 'done'
111         clear INIT_TIME;
112     otherwise
113         elapsed_time = toc(INIT_TIME);
114         if elapsed_time > interupt_time
115             clear INIT_TIME;
116             str = sprintf('%.6f',elapsed_time);
117             error('interuptFun:Interupt',...
118                 ['Interupted integration. Elapsed time is ' str ' seconds.
    ']);
119         end
120 end
121 end
122 function [xp] = vsi_afe_model(t, x, param, K_PI_VSI, K_PI_AFE)
123 
124     Iid = x(1);
125     Vcd = x(2);
126     Iiq = x(3);
127     Vcq = x(4);
128     Iad = x(5);
129     Iaq = x(6);
130     Vdca = x(7);
131     %integral states
132     wIid=x(8);
133     wVcd=x(9);
134     wIiq=x(10);
135     wVcq=x(11);
136     wIad=x(12);
137     wIaq=x(13);
138     wVdca=x(14);
139 
140     Ra = 90e-3;
141     La = param(1);
142     w = 2*pi*400;
143     Ca = 100e-6;
```

```
144     R = 120e-3;
145     L = param(2);
146     C = param(3);
147     Rl =  86;
148     Vdc = 350;
149 
150     Vcd_ref=162.6;
151     Vcq_ref=0;
152     Iaq_ref=0;
153     Vdc_ref=350;
154 
155     % LOAD
156     if(t > 0.5)
157         Il = Vdca/Rl;
158     else
159         Il = 0*Vdca/Rl;
160     end
161 %% PI controllers
162 % VSI controler
163     error_Vcd=Vcd_ref-Vcd;
164     Out_PI_Vcd=K_PI_VSI(1)*error_Vcd+K_PI_VSI(2)*wVcd;
165     wVcd=wVcd+error_Vcd;
166     error_Iid=Out_PI_Vcd-Iid;
167     Out_PI_Iid=K_PI_VSI(3)*error_Iid+K_PI_VSI(4)*wIid;
168     wIid=wIid+error_Iid;
169 
170     error_Vcq=Vcq_ref-Vcq;
171     Out_PI_Vcq=K_PI_VSI(1)*error_Vcq+K_PI_VSI(2)*wVcq;
172     wVcq=wVcq+error_Vcq;
173     error_Iiq=Out_PI_Vcq-Iiq;
174     Out_PI_Iiq=K_PI_VSI(3)*error_Iiq+K_PI_VSI(4)*wIiq;
175     wIiq=wIiq+error_Iiq;
176 
177     md = Out_PI_Iid/(0.5*Vdc);
178     mq = Out_PI_Iiq/(0.5*Vdc);
179 
180 % AFE controler
181     error_Vdca=Vdc_ref-Vdca;
```

```
    Out_PI_Vdca=K_PI_AFE(1)*error_Vdca+K_PI_AFE(2)*wVdca;
    wVdca=wVdca+error_Vdca;
    error_Iad=Out_PI_Vdca-Iad;
    Out_PI_Iad=K_PI_AFE(3)*error_Iad+K_PI_AFE(4)*wIad;
    wIad=wIad+error_Iad;

    error_Iaq=Iaq_ref-Iaq;
    Out_PI_Iaq=K_PI_AFE(3)*error_Iaq+K_PI_AFE(4)*wIaq;
    wIaq=wIaq+error_Iaq;

    pd = Out_PI_Iad/(0.5*Vdca);
    pq = Out_PI_Iaq/(0.5*Vdca);

 %% Model
    % VSI equations
    Iidp = (-R/L)*Iid + w*Iiq + (-1/L)*Vcd + (Vdc/(2*L))*md;
    Vcdp = Iid/C + w*Vcq + (-1/C)*Iad;
    Iiqp = (-w)*Iid + (-R/L)*Iiq + (-1/L)*Vcq + (Vdc/(2*L))*mq;
    Vcqp = Iiq/C + (-w)*Vcd + (-1/C)*Iaq;

    % AFE equations
    Iadp = (-Ra/La)*Iad + w*Iaq + (-1/(2*La))*Vdca*pd + Vcd/La;
    Iaqp = (-w)*Iad + (-Ra/La)*Iaq + (-1/(2*La))*Vdca*pq + Vcq/La;
    Vdcap = (3/(4*Ca))*Iad*pd + (3/(4*Ca))*Iaq*pq + (-1/Ca)*Il;
    xp = [Iidp; Vcdp; Iiqp; Vcqp; Iadp; Iaqp; Vdcap; wIid; wVcd; wIiq; wVcq
   ; wIad; wIaq; wVdca];
end
```

Annex-B Harmonic Filters Optimization - CADES code

```
import my.company:blackbox_model.FreqTool.
    Filter_optimization_2_ExternalFunction2:3.1;
import my.company:blackbox_model.FreqTool.ConstraintsCExternalFunction:3.1;
import my.company:blackbox_model.D0160G:3.1;
/*
    ********************************************************************************
    */
//New model instance:
/*
    ********************************************************************************
    */
my_Filter_optimization_2_ExternalFunction2 = new
    Filter_optimization_2_ExternalFunction2;
my_ConstraintsCExternalFunction = new ConstraintsCExternalFunction;


/*
    ********************************************************************************
    */
//Get scalar outputs:
/*
    ********************************************************************************
    */

THD = my_Filter_optimization_2_ExternalFunction2.computeFilterTHD(
    my_C_CVSI_value, my_L_LVSI_value, my_L_LAFE_value);

LminC_out_value = my_ConstraintsCExternalFunction.interpolationLminC(
    my_C_CVSI_value, my_L_LAFE_value);
Constraint1= my_L_LVSI_value-LminC_out_value;
CminC_out_value = my_ConstraintsCExternalFunction.interpolationCminC(
    my_L_LVSI_value, my_L_LAFE_value);
Constraint2= my_C_CVSI_value-CminC_out_value;
LaminC_out_value = my_ConstraintsCExternalFunction.interpolationLaminC(
    my_L_LVSI_value, my_C_CVSI_value);
Constraint3= my_L_LAFE_value-LaminC_out_value;
```

```
23
24
25 Mass_CVSI=3.28E6*my_C_CVSI_value+88.7;
26 Mass_LVSI=2.84E6*my_L_LVSI_value+59.8;
27 Mass_LAFE=2.84E6*my_L_LAFE_value+59.8;
28
29 Filters_Mass=Mass_LAFE+Mass_LVSI+Mass_CVSI;
30 /*
    ********************************************************************************
    */
```

Annex-C Computation of the Black Box model parameters

Impedances Z1 Z21 and Z22 calculation

$$Zpm = \frac{Z21 \cdot Z22}{Z21 + Z22} \qquad Zpg = \frac{Z1 \cdot Z22}{Z1 + Z22} \qquad Zmg = \frac{Z1 \cdot Z21}{Z1 + Z21}$$

$$Zmg = \frac{Z1 \cdot Z21}{Z1 + Z21} \text{ solve}, Z1 \rightarrow \frac{Z21 \cdot Zmg}{Z21 - Zmg}$$

$$Z1 := \frac{Z21 \cdot Zmg}{Z21 - Zmg}$$

$$Zpg = \frac{Z1 \cdot Z22}{Z1 + Z22} \text{ solve}, Z22 \rightarrow \frac{Z21 \cdot Zmg \cdot Zpg}{Z21 \cdot Zmg - Z21 \cdot Zpg + Zmg \cdot Zpg}$$

$$Z22 := \frac{Z21 \cdot Zmg \cdot Zpg}{Z21 \cdot Zmg - Z21 \cdot Zpg + Zmg \cdot Zpg}$$

$$Zpm = \frac{Z21 \cdot Z22}{Z21 + Z22} \text{ solve}, Z21 \rightarrow \begin{pmatrix} 0 \\ \frac{2 \cdot Zmg \cdot Zpg \cdot Zpm}{Zmg \cdot Zpg - Zmg \cdot Zpm + Zpg \cdot Zpm} \end{pmatrix}$$

$$Z1 := \frac{\frac{2 \cdot Zmg \cdot Zpg \cdot Zpm}{Zmg \cdot Zpg - Zmg \cdot Zpm + Zpg \cdot Zpm} \cdot Zmg}{\frac{2 \cdot Zmg \cdot Zpg \cdot Zpm}{Zmg \cdot Zpg - Zmg \cdot Zpm + Zpg \cdot Zpm} - Zmg} \text{ simplify} \rightarrow \frac{2 \cdot Zmg \cdot Zpg \cdot Zpm}{Zmg \cdot Zpm - Zmg \cdot Zpg + Zpg \cdot Zpm}$$

$$Z21 := \frac{2 \cdot Zmg \cdot Zpg \cdot Zpm}{Zmg \cdot Zpg - Zmg \cdot Zpm + Zpg \cdot Zpm} \text{ simplify} \rightarrow \frac{2 \cdot Zmg \cdot Zpg \cdot Zpm}{Zmg \cdot Zpg - Zmg \cdot Zpm + Zpg \cdot Zpm}$$

$$Z22 := \frac{\frac{2 \cdot Zmg \cdot Zpg \cdot Zpm}{Zmg \cdot Zpg - Zmg \cdot Zpm + Zpg \cdot Zpm} \cdot Zmg \cdot Zpg}{\frac{2 \cdot Zmg \cdot Zpg \cdot Zpm}{Zmg \cdot Zpg - Zmg \cdot Zpm + Zpg \cdot Zpm} \cdot Zmg - \frac{2 \cdot Zmg \cdot Zpg \cdot Zpm}{Zmg \cdot Zpg - Zmg \cdot Zpm + Zpg \cdot Zpm} \cdot Zpg + Zmg \cdot Zpg} \text{ simplify} \rightarrow \frac{2 \cdot Zmg \cdot Zpg \cdot Zpm}{Zmg \cdot Zpg + Zmg \cdot Zpm - Zpg \cdot Zpm}$$

$$Z1 = \frac{2 \cdot Zmg \cdot Zpg \cdot Zpm}{Zmg \cdot Zpm - Zmg \cdot Zpg + Zpg \cdot Zpm}$$

$$Z21 = \frac{2 \cdot Zmg \cdot Zpg \cdot Zpm}{Zmg \cdot Zpg - Zmg \cdot Zpm + Zpg \cdot Zpm}$$

$$Z22 = \frac{2 \cdot Zmg \cdot Zpg \cdot Zpm}{Zmg \cdot Zpg + Zmg \cdot Zpm - Zpg \cdot Zpm}$$

Computation of the excitation sources Vex and Iex

$$Zb = \begin{pmatrix} ZR1 & 0 & 0 & 0 & 0 \\ 0 & ZR2 & 0 & 0 & 0 \\ 0 & 0 & Z1 & 0 & 0 \\ 0 & 0 & 0 & Z21 & 0 \\ 0 & 0 & 0 & 0 & Z22 \end{pmatrix} \qquad M = \begin{pmatrix} 1 & -1 & -1 & 0 & 0 \\ 0 & 1 & 0 & 0 & 1 \\ 0 & 0 & 1 & -1 & -1 \end{pmatrix} \qquad Vs = \begin{pmatrix} 0 \\ Vex \\ 0 \end{pmatrix} \qquad N = \begin{pmatrix} 1 & 0 & 1 & 1 & 0 \\ 0 & 1 & -1 & 0 & -1 \end{pmatrix} \qquad Is = \begin{pmatrix} -Iex \\ Iex \end{pmatrix}$$

$$\begin{pmatrix} 1 & -1 & -1 & 0 & 0 \\ 0 & 1 & 0 & 0 & 1 \\ 0 & 0 & 1 & -1 & -1 \end{pmatrix} \cdot \begin{pmatrix} ZR1 & 0 & 0 & 0 & 0 \\ 0 & ZR2 & 0 & 0 & 0 \\ 0 & 0 & Z1 & 0 & 0 \\ 0 & 0 & 0 & Z21 & 0 \\ 0 & 0 & 0 & 0 & Z22 \end{pmatrix} \qquad \begin{pmatrix} ZR1 & -ZR2 & -Z1 & 0 & 0 \\ 0 & ZR2 & 0 & 0 & Z22 \\ 0 & 0 & Z1 & -Z21 & -Z22 \end{pmatrix} \qquad \begin{pmatrix} ZR1 & -ZR2 & -Z1 & 0 & 0 \\ 0 & ZR2 & 0 & 0 & Z22 \\ 0 & 0 & Z1 & -Z21 & -Z22 \\ 1 & 0 & 1 & 1 & 0 \\ 0 & 1 & -1 & 0 & -1 \end{pmatrix}^{-1} \cdot \begin{pmatrix} 0 \\ Vex \\ 0 \\ -Iex \\ Iex \end{pmatrix}$$

$$\begin{pmatrix} \dfrac{Vex \cdot Z1 \cdot Z22 + Vex \cdot Z1 \cdot ZR2 + Vex \cdot Z21 \cdot ZR2 + Vex \cdot Z22 \cdot ZR2 - Iex \cdot Z1 \cdot Z21 \cdot Z22 - Iex \cdot Z1 \cdot Z21 \cdot ZR2}{Z1 \cdot Z21 \cdot Z22 + Z1 \cdot Z21 \cdot ZR2 + Z1 \cdot Z22 \cdot ZR1 + Z1 \cdot ZR1 \cdot ZR2 + Z21 \cdot Z22 \cdot ZR1 + Z21 \cdot Z22 \cdot ZR2 + Z21 \cdot ZR1 \cdot ZR2 + Z22 \cdot ZR1 \cdot ZR2} \\ \dfrac{Vex \cdot Z1 \cdot Z21 + Vex \cdot Z1 \cdot ZR1 + Vex \cdot Z21 \cdot ZR1 + Vex \cdot Z22 \cdot ZR1 + Iex \cdot Z1 \cdot Z21 \cdot Z22 + Iex \cdot Z1 \cdot Z22 \cdot ZR1}{Z1 \cdot Z21 \cdot Z22 + Z1 \cdot Z21 \cdot ZR2 + Z1 \cdot Z22 \cdot ZR1 + Z1 \cdot ZR1 \cdot ZR2 + Z21 \cdot Z22 \cdot ZR1 + Z21 \cdot Z22 \cdot ZR2 + Z21 \cdot ZR1 \cdot ZR2 + Z22 \cdot ZR1 \cdot ZR2} \\ -\dfrac{Vex \cdot Z21 \cdot ZR2 - Vex \cdot Z22 \cdot ZR1 + Iex \cdot Z21 \cdot Z22 \cdot ZR1 + Iex \cdot Z21 \cdot Z22 \cdot ZR2 + Iex \cdot Z21 \cdot ZR1 \cdot ZR2 + Iex \cdot Z22 \cdot ZR1 \cdot ZR2}{Z1 \cdot Z21 \cdot Z22 + Z1 \cdot Z21 \cdot ZR2 + Z1 \cdot Z22 \cdot ZR1 + Z1 \cdot ZR1 \cdot ZR2 + Z21 \cdot Z22 \cdot ZR1 + Z21 \cdot Z22 \cdot ZR2 + Z21 \cdot ZR1 \cdot ZR2 + Z22 \cdot ZR1 \cdot ZR2} \\ -\dfrac{Vex \cdot Z1 \cdot Z22 + Vex \cdot Z1 \cdot ZR2 + Vex \cdot Z22 \cdot ZR1 + Vex \cdot Z22 \cdot ZR2 + Iex \cdot Z1 \cdot Z22 \cdot ZR1 + Iex \cdot Z1 \cdot ZR1 \cdot ZR2}{Z1 \cdot Z21 \cdot Z22 + Z1 \cdot Z21 \cdot ZR2 + Z1 \cdot Z22 \cdot ZR1 + Z1 \cdot ZR1 \cdot ZR2 + Z21 \cdot Z22 \cdot ZR1 + Z21 \cdot Z22 \cdot ZR2 + Z21 \cdot ZR1 \cdot ZR2 + Z22 \cdot ZR1 \cdot ZR2} \\ \dfrac{Vex \cdot Z1 \cdot Z21 + Vex \cdot Z1 \cdot ZR1 + Vex \cdot Z21 \cdot ZR1 + Vex \cdot Z21 \cdot ZR2 - Iex \cdot Z1 \cdot Z21 \cdot ZR2 - Iex \cdot Z1 \cdot ZR1 \cdot ZR2}{Z1 \cdot Z21 \cdot Z22 + Z1 \cdot Z21 \cdot ZR2 + Z1 \cdot Z22 \cdot ZR1 + Z1 \cdot ZR1 \cdot ZR2 + Z21 \cdot Z22 \cdot ZR1 + Z21 \cdot Z22 \cdot ZR2 + Z21 \cdot ZR1 \cdot ZR2 + Z22 \cdot ZR1 \cdot ZR2} \end{pmatrix}$$

$$\begin{pmatrix} Ip \\ In \end{pmatrix} = \begin{pmatrix} \dfrac{Vex \cdot Z1 \cdot Z22 + Vex \cdot Z1 \cdot ZR2 + Vex \cdot Z21 \cdot ZR2 + Vex \cdot Z22 \cdot ZR2 - Iex \cdot Z1 \cdot Z21 \cdot Z22 - Iex \cdot Z1 \cdot Z21 \cdot ZR2}{Z1 \cdot Z21 \cdot Z22 + Z1 \cdot Z21 \cdot ZR2 + Z1 \cdot Z22 \cdot ZR1 + Z1 \cdot ZR1 \cdot ZR2 + Z21 \cdot Z22 \cdot ZR1 + Z21 \cdot Z22 \cdot ZR2 + Z21 \cdot ZR1 \cdot ZR2 + Z22 \cdot ZR1 \cdot ZR2} \\ \dfrac{Vex \cdot Z1 \cdot Z21 + Vex \cdot Z1 \cdot ZR1 + Vex \cdot Z21 \cdot ZR1 + Vex \cdot Z22 \cdot ZR1 + Iex \cdot Z1 \cdot Z21 \cdot Z22 + Iex \cdot Z1 \cdot Z22 \cdot ZR1}{Z1 \cdot Z21 \cdot Z22 + Z1 \cdot Z21 \cdot ZR2 + Z1 \cdot Z22 \cdot ZR1 + Z1 \cdot ZR1 \cdot ZR2 + Z21 \cdot Z22 \cdot ZR1 + Z21 \cdot Z22 \cdot ZR2 + Z21 \cdot ZR1 \cdot ZR2 + Z22 \cdot ZR1 \cdot ZR2} \end{pmatrix}$$

$$\begin{pmatrix} Ip \\ In \end{pmatrix} = \begin{pmatrix} \dfrac{Z1 \cdot Z22 + Z1 \cdot ZR2 + Z21 \cdot ZR2 + Z22 \cdot ZR2}{Z1 \cdot Z21 \cdot Z22 + Z1 \cdot Z21 \cdot ZR2 + Z1 \cdot Z22 \cdot ZR1 + Z1 \cdot ZR1 \cdot ZR2 + Z21 \cdot Z22 \cdot ZR1 + Z21 \cdot Z22 \cdot ZR2 + Z21 \cdot ZR1 \cdot ZR2 + Z22 \cdot ZR1 \cdot ZR2} & \dfrac{-Z1 \cdot Z21 \cdot Z22 - Z1 \cdot Z21 \cdot ZR2}{Z1 \cdot Z21 \cdot Z22 + Z1 \cdot Z21 \cdot ZR2 + Z1 \cdot Z22 \cdot ZR1 + Z1 \cdot ZR1 \cdot ZR2 + Z21 \cdot Z22 \cdot ZR1 + Z21 \cdot Z22 \cdot ZR2 + Z21 \cdot ZR1 \cdot ZR2 + Z22 \cdot ZR1 \cdot ZR2} \\ \dfrac{Z1 \cdot Z21 + Z1 \cdot ZR1 + Z21 \cdot ZR1 + Z22 \cdot ZR1}{Z1 \cdot Z21 \cdot Z22 + Z1 \cdot Z21 \cdot ZR2 + Z1 \cdot Z22 \cdot ZR1 + Z1 \cdot ZR1 \cdot ZR2 + Z21 \cdot Z22 \cdot ZR1 + Z21 \cdot Z22 \cdot ZR2 + Z21 \cdot ZR1 \cdot ZR2 + Z22 \cdot ZR1 \cdot ZR2} & \dfrac{Z1 \cdot Z21 \cdot Z22 + Z1 \cdot Z22 \cdot ZR1}{Z1 \cdot Z21 \cdot Z22 + Z1 \cdot Z21 \cdot ZR2 + Z1 \cdot Z22 \cdot ZR1 + Z1 \cdot ZR1 \cdot ZR2 + Z21 \cdot Z22 \cdot ZR1 + Z21 \cdot Z22 \cdot ZR2 + Z21 \cdot ZR1 \cdot ZR2 + Z22 \cdot ZR1 \cdot ZR2} \end{pmatrix} \cdot \begin{pmatrix} Vex \\ Iex \end{pmatrix}$$

$$\begin{pmatrix} \dfrac{Z1 \cdot Z22 + Z1 \cdot ZR2 + Z21 \cdot ZR2 + Z22 \cdot ZR2}{Z1 \cdot Z21 \cdot Z22 + Z1 \cdot Z21 \cdot ZR2 + Z1 \cdot Z22 \cdot ZR1 + Z1 \cdot ZR1 \cdot ZR2 + Z21 \cdot Z22 \cdot ZR1 + Z21 \cdot Z22 \cdot ZR2 + Z21 \cdot ZR1 \cdot ZR2 + Z22 \cdot ZR1 \cdot ZR2} & \dfrac{-Z1 \cdot Z21 \cdot Z22 - Z1 \cdot Z21 \cdot ZR2}{Z1 \cdot Z21 \cdot Z22 + Z1 \cdot Z21 \cdot ZR2 + Z1 \cdot Z22 \cdot ZR1 + Z1 \cdot ZR1 \cdot ZR2 + Z21 \cdot Z22 \cdot ZR1 + Z21 \cdot Z22 \cdot ZR2 + Z21 \cdot ZR1 \cdot ZR2 + Z22 \cdot ZR1 \cdot ZR2} \\ \dfrac{Z1 \cdot Z21 + Z1 \cdot ZR1 + Z21 \cdot ZR1 + Z22 \cdot ZR1}{Z1 \cdot Z21 \cdot Z22 + Z1 \cdot Z21 \cdot ZR2 + Z1 \cdot Z22 \cdot ZR1 + Z1 \cdot ZR1 \cdot ZR2 + Z21 \cdot Z22 \cdot ZR1 + Z21 \cdot Z22 \cdot ZR2 + Z21 \cdot ZR1 \cdot ZR2 + Z22 \cdot ZR1 \cdot ZR2} & \dfrac{Z1 \cdot Z21 \cdot Z22 + Z1 \cdot Z22 \cdot ZR1}{Z1 \cdot Z21 \cdot Z22 + Z1 \cdot Z21 \cdot ZR2 + Z1 \cdot Z22 \cdot ZR1 + Z1 \cdot ZR1 \cdot ZR2 + Z21 \cdot Z22 \cdot ZR1 + Z21 \cdot Z22 \cdot ZR2 + Z21 \cdot ZR1 \cdot ZR2 + Z22 \cdot ZR1 \cdot ZR2} \end{pmatrix}^{-1}$$

$$\begin{pmatrix} Vex \\ Iex \end{pmatrix} = \begin{bmatrix} \dfrac{Z22 \cdot (Z21 + ZR1)}{Z21 + Z22} & \dfrac{Z21 \cdot (Z22 + ZR2)}{Z21 + Z22} \\ -\dfrac{ZR1}{Z1} - \dfrac{Z21 + ZR1}{Z21 + Z22} & \dfrac{ZR2}{Z1} + \dfrac{Z22 + ZR2}{Z21 + Z22} \end{bmatrix} \cdot \begin{pmatrix} Ip \\ In \end{pmatrix}$$

Annex-D Black Box model identification – MATLAB code

```
clc
clear

%% Data load

path='';
dir ='';
current1 = '';
current2 = '';
ZPM = '';
ZPG = '';
ZMG = '';

switching_frequency = 1.1e5;% in Hz
maximum_frequency = 100e6;%in Hz

[Freq,I1_mod,I1_phase] = PeakDetection(path,dir,current1,
    switching_frequency,maximum_frequency);
[Freq2,I2_mod,I2_phase] = PeakDetection(path,dir,current2',
    switching_frequency,maximum_frequency);

fileID = fopen(strcat(path,dir,ZPM),'r');
formatSpec = '%f %f %f';
ZPM_mes = fscanf(fileID,formatSpec,[3 Inf])';
fclose(fileID);

fileID = fopen(strcat(path,dir,ZPG),'r');
formatSpec = '%f %f %f';
ZPG_mes = fscanf(fileID,formatSpec,[3 Inf])';
fclose(fileID);

fileID = fopen(strcat(path,dir,ZMG),'r');
formatSpec = '%f %f %f';
ZMG_mes = fscanf(fileID,formatSpec,[3 Inf])';
fclose(fileID);

```

```
35
36 %% Resampling
37 %***************************
38 %Impedance resampling
39 %***************************
40 f = Freq;
41 ZPM = 10.^(interp1(log10(ZPM_mes(:,1)),log10(ZPM_mes(:,2)),log10(f))).*exp
       (1j.*interp1(ZPM_mes(:,1),ZPM_mes(:,3),f)*pi/180);
42 ZPG = 10.^(interp1(log10(ZPG_mes(:,1)),log10(ZPG_mes(:,2)),log10(f))).*exp
       (1j.*interp1(ZPG_mes(:,1),ZPG_mes(:,3),f)*pi/180);
43 ZMG = 10.^(interp1(log10(ZMG_mes(:,1)),log10(ZMG_mes(:,2)),log10(f))).*exp
       (1j.*interp1(ZMG_mes(:,1),ZMG_mes(:,3),f)*pi/180);
44 %
45 %% Computation
46 %*****************************************
47 % DO160 LISN Impedance
48 %*****************************************
49 Z_LISN1 = 1./(1j*2*pi*100e-9.*Freq) + 50;
50 Z_LISN2 = 1./(1j*2*pi*100e-9.*Freq) + 50;
51 %*****************************************
52 % Z1 Z21 Z22 computation
53 %*****************************************
54 Z1 = (2*ZMG.*ZPG.*ZPM)./((ZMG.*ZPM)-(ZMG.*ZPG)+(ZPG.*ZPM));
55 Z21 = (2*ZMG.*ZPG.*ZPM)./((ZMG.*ZPG)-(ZMG.*ZPM)+(ZPG.*ZPM));
56 Z22 = (2*ZMG.*ZPG.*ZPM)./((ZMG.*ZPG)+(ZMG.*ZPM)-(ZPG.*ZPM));
57 %************************************************
58 % Computing Vex Iex
59 %************************************************
60 I1 = complex(I1_mod.*cos(I1_phase),I1_mod.*sin(I1_phase));
61 I2 = complex(I2_mod.*cos(I2_phase),I2_mod.*sin(I2_phase));
62
63 Zz1 = (Z22.*(Z21+Z_LISN1))./(Z21+Z22);
64 Zz2 = (Z21.*(Z22+Z_LISN2))./(Z21+Z22);
65
66 Zz3 = ((-1)*(Z_LISN1./Z1))-((Z21+Z_LISN1)./(Z21+Z22));
67 Zz4 = (Z_LISN2./Z1)+((Z22+Z_LISN2)./(Z21+Z22));
68
69 Vex = I1.*Zz1+I2.*Zz2;
```

```
Iex = I1.*Zz3+I2.*Zz4;

%% Data writing
%Frequence          Module            Phase

fileID = fopen(strcat(path,dir,'Model\','Z1.txt'),'w');
fprintf(fileID,'%s\t%s\t%s\t\r\n','Frequence','Module','Phase');
formatSpec = '%7.15f\t%7.15f\t%7.15f\t\r\n';
fprintf(fileID,formatSpec,[f;abs(Z1);angle(Z1)]);
fclose(fileID);

fileID = fopen(strcat(path,dir,'Model\','Z21.txt'),'w');
fprintf(fileID,'%s\t%s\t%s\t\r\n','Frequence','Module','Phase');
formatSpec = '%7.15f\t%7.15f\t%7.15f\t\r\n';
fprintf(fileID,formatSpec,[f;abs(Z21);angle(Z21)]);
fclose(fileID);

fileID = fopen(strcat(path,dir,'Model\','Z22.txt'),'w');
fprintf(fileID,'%s\t%s\t%s\t\r\n','Frequence','Module','Phase');
formatSpec = '%7.15f\t%7.15f\t%7.15f\t\r\n';
fprintf(fileID,formatSpec,[f;abs(Z22);angle(Z22)]);
fclose(fileID);

fileID = fopen(strcat(path,dir,'Model\','Iex.txt'),'w');
fprintf(fileID,'%s\t%s\t%s\t\r\n','Frequence','Module','Phase');
formatSpec = '%7.15f\t%7.15f\t%7.15f\t\r\n';
fprintf(fileID,formatSpec,[Freq;abs(Iex);angle(Iex)]);
fclose(fileID);

fileID = fopen(strcat(path,dir,'Model\','Vex.txt'),'w');
fprintf(fileID,'%s\t%s\t%s\t\r\n','Frequence','Module','Phase');
formatSpec = '%7.15f\t%7.15f\t%7.15f\t\r\n';
fprintf(fileID,formatSpec,[Freq;abs(Vex);angle(Vex)]);
fclose(fileID);

fileID = fopen(strcat(path,dir,'Model\','I1_FFT.txt'),'w');
fprintf(fileID,'%s\t%s\t%s\t\r\n','Frequence','Module','Phase');
formatSpec = '%7.15f\t%7.15f\t%7.15f\t\r\n';
```

```
fprintf(fileID,formatSpec,[Freq;I1_mod;I1_phase]);
fclose(fileID);

fileID = fopen(strcat(path,dir,'Model\','I2_FFT.txt'),'w');
fprintf(fileID,'%s\t%s\t%s\t\r\n','Frequence','Module','Phase');
formatSpec = '%7.15f\t%7.15f\t%7.15f\t\r\n';
fprintf(fileID,formatSpec,[Freq;I2_mod;I2_phase]);
fclose(fileID);

fileID = fopen(strcat(path,dir,'Model\','harmonic_number.txt'),'w');
fprintf(fileID,'%s\t%s\t%s\t\r\n','Frequence','Module','Phase');
formatSpec = '%7.15f\t%7.15f\t%7.15f\t\r\n';
fprintf(fileID,formatSpec,[Freq(1:10);Freq(1:10)/Freq(1);0.0.*Freq(1:10)]);
fclose(fileID);

fileID = fopen(strcat(path,dir,'Model\','Ex0.txt'),'w');
fprintf(fileID,'%s\t%s\t%s\t\r\n','Frequence','Module','Phase');
formatSpec = '%7.15f\t%7.15f\t%7.15f\t\r\n';
fprintf(fileID,formatSpec,[Freq;zeros(1,size(Freq,2));zeros(1,size(Freq,2))
    ]);
fclose(fileID);
```

```
function [Freq_vector,Modulus_vector,Phase_vector] = PeakDetection(path,dir
    ,filename,f1freq,maxfreq);
%*****************************************
% Find peak values in frequency spectrum
%%*****************************************
% inputs :
% - path, dir, filename : path, directory and filename to locate the time
% measurements (example : I1_mes_t.txt)
% - ffreq : fundamental frequency in Hz
% - plotflag : plot flag (plot figures if pf = 1 (defaut 0)
plotflag = 0;
% outputs :
% - Freq_vector : Frequency at peak
% - Modulus_vector : amplitude at peak frequency
% - Phase_vector : phase at peak frequency

```

```
16
17 format long
18
19 %****************************************
20 % read raw data
21 %****************************************
22 fileID = fopen(strcat(path,dir,filename),'r');
23 formatSpec = '%f %f';
24 mes = fscanf(fileID,formatSpec,[2 Inf]);
25 fclose(fileID);
26
27 clearvars fileID formatSpec
28 %****************************************
29 % sub-sampling and resizing time acquisition
30 %****************************************
31 raw_ts = mes(1,2)-mes(1,1);                                    % raw sampling
       period
32 ssr = 1;                                                      % sub-sampling
       ratio
33 ts = ssr*raw_ts;                                              % sampling
       period
34 Fs = 1/ts;                                                    % sampling
       frequency
35 p2 = find(size(mes,2)./(2.^(1:20))<1);
36 t = mes(1,(1:ssr:2^(p2(1)-1)));                               % time vector
37 L = size(t,2);                                                % length of
       signal
38 res_mes = mes(2,(1:ssr:2^(p2(1)-1)));
39 %****************************************
40 %****************************************
41 % Fast Fourier Transform with zero padding
42 %****************************************
43 average_value = mean(res_mes);
44 res_mes = res_mes - average_value;
45 zL=2^25;
46 res_mes(zL)=0;
47 %************************
48 % test function
```

```
%tps = (0:L-1)*ts;
%tps(zL) = 0;
%res_mes = 0.3.*cos(2.*pi.*1e-2.*Fs.*tps) + 4*cos(2.*pi.*3e-2.*Fs.*tps+pi
    /3);
%************************
FFT_mes = 1/L*fft(double(res_mes),zL);
F = Fs*(0:(zL/2))/zL;
P = 1/zL/ts                                                %frequency
    resolution in Hz
Fmes = FFT_mes(1:zL/2+1);
Fmes(2:end-1) = 2*Fmes(2:end-1);
%****************************************

for n = 1:1:floor(maxfreq/f1freq);
    % h : harmonic rank -> harmonic center frequency h x freq of the
    sliding window
    h = n;

    if n==1
        ffreq = f1freq;
    end
    if n~=1
        ffreq = pf(n-1)/(h-1);
    end

    dk = 20;                    %frequency sliding window width = dk/2 x P
    d = floor(ffreq*h/P);        %index of harmonic h in the frequency
    vector

    i=(-dk:1:dk);                                                %index
    vector
    xf = F(i+d);                                                 %frequency
    vector of the sw
    yf = abs(Fmes(i+1+d));                                       %amplitude
    vector of the sw
    argf = angle(Fmes(i+1+d));                                   %Phase
    vector of the sw
    ydf = (abs(Fmes(i+1+d))-abs(Fmes(i+d)))/P;                   %derivative
```

```
    vector of the sw
79
80      xfi = (min(xf):(max(xf)-min(xf))/2^10:max(xf));              %
        interpolated frequency vector
81      ydfi = interp1(xf,ydf,xfi,'linear');                         %
        interpolated derivative vector
82      [val,ind]=min(abs(ydfi));                                    %root of
        the derivative
83
84      pf(n)= xfi(ind);
85      valf(n) = interp1(xf,yf,xfi(ind),'linear');
86      val_argf(n) = interp1(xf,argf,xfi(ind),'linear');
87
88      if (plotflag==1)&&(n==1)
89          figure;
90          subplot(2,1,1);
91          semilogx(xf,ydf,xfi(ind),val,'o');
92          subplot(2,1,2);
93          semilogx(F(i+d),abs(Fmes(i+d)),pf(n),valf(n),'o');
94      end
95      %****************************************
96  end
97
98
99  % Plot results
100 figure;
101 plot((pf./f1freq-(1:1:size(pf,2)))./(1:1:size(pf,2))*100,'square')
102 xlabel('harmonic rank : h');
103 ylabel('error on harmonic rank (%)');
104 plot(pf./f1freq,'square');hold on;plot((1:1:size(pf,2)),'r')
105 xlabel('harmonic rank : h');
106 ylabel('estimated harmonic rank');
107  figure();
108  semilogx(F,20*log10(abs(Fmes)),pf,20*log10(valf),'x',F,ones(1,size(F,2))
        .*-244);
109  xlim([1e4 30e6])
110  xlabel(['Frequency in Hz (resolution  = ' num2str(floor(P*100)/100) ' Hz)'
        ]);
```

```
 ylabel('Amplitude in dB');
figure();
semilogx(F,angle(Fmes),pf,val_argf,'x');
xlim([1e4 30e6])
xlabel(['Frequency in Hz (resolution  = ' num2str(floor(P*100)/100) ' Hz)'
    ]);
ylabel('Amplitude in dB');

Freq_vector = pf;

Modulus_vector = valf;

Phase_vector = val_argf;

end
```

Annex-E Frequency-domain circuit solver – Java code

```
/*
 * file created by the Frequency Modelling Tool - Mage - G2ELab - UGA Grenoble
 * version 2.2.0.16 of May 27th, 2020
 */

package FreqTool;

import org.gu.vesta.muse.v5.JacobianFacet;
import org.gu.vesta.muse.v5.JacobianFacet.ComputeJacobian;
import org.gu.vesta.muse.v5.MuseContainerModel;
import org.gu.vesta.muse.v5.MuseModel;
import org.gu.vesta.muse.v5.StaticFacet;
import org.gu.vesta.muse.v5.StaticFacet.Compute;
import Jampack.*;
import java.util.logging.Logger;
import java.util.logging.Level;
import org.gu.g2elab.mage.cades.One_converter_wFilter_core;

@MuseContainerModel({
@MuseModel(name="computeDBGains"),
@MuseModel(name="computeModulesArguments"),
@MuseModel(name="computeRealAndImaginaryParts")
})

public class One_converter_wFilter_external_function{
// declaration of the variables
private double f_initialValue;
private int computeValidity=1;
private int jacobianValidity=1;
private int initialisation=0;
private One_converter_wFilter_core core;

// builder of the computation kernel
public One_converter_wFilter_external_function(){
   try {
```

```
36        this.core = new One_converter_wFilter_core("\\FreqToolModel\\
      One_converter_wFilter");
37     }catch(java.lang.Exception ex){
38     }
39     computeValidity=1;
40     jacobianValidity=1;
41     initialisation=0;
42 }
43 
44 private void testChangeOfInputParameters(double f){
45 try{
46      if (initialisation==0)
47     {
48         initialisation++;
49         computeValidity++;
50     }
51 f_initialValue=testChangeOfOneInputParameter(f_initialValue,f);
52 }catch(java.lang.Exception ex){
53 }
54 }
55 
56 private double testChangeOfOneInputParameter(double initialValue, double
      value){
57     if (initialValue<1.0e-100)
58     {
59        if (Math.abs(value)>1.0e-30)
60        {
61           computeValidity++;
62           initialValue=value;
63        }
64     }
65     else
66     {
67        if (!(Math.abs((initialValue-value)/initialValue)<1.0e-15))
68         {
69            computeValidity++;
70            initialValue=value;
71         }
```

```
72      }
73      return initialValue;
74  }
75
76  @StaticFacet(museModel="computeDBGains", outputNames  = {"out"}, outputSize
        = 2 )
77  @Compute
78  public  double[] computeDBGains(double f){
79      double[] outputs;
80  try{
81      if ((initialisation==0)||(computeValidity==0)){
82          testChangeOfInputParameters(f);
83      }
84      if (computeValidity>0)
85      {
86          jacobianValidity++;
87          computeValidity=0;
88          outputs = core.computeDBGains(f);
89      }
90      else
91      {
92          outputs=core.getOutputs();
93      }
94      return outputs;
95  }catch(java.lang.Exception ex){
96  }
97  return new double[2];
98  }
99
100 @JacobianFacet(museModel="computeDBGains")
101 @ComputeJacobian
102 public double[][] jacobianDBGains(double f){
103 try{
104     double[][] outputJacobian;
105     if ((initialisation==0)||(computeValidity==0)){
106         testChangeOfInputParameters(f);
107     }
108     if (computeValidity>0){
```

```
109         computeDBGains(f);
110     }
111     if (jacobianValidity>0)
112     {
113         jacobianValidity=0;
114         outputJacobian=core.jacobianDBGains(f);
115     }
116     else
117     {
118         outputJacobian=core.getOutputJacobian();
119     }
120     return outputJacobian;
121 }catch(java.lang.Exception ex){}
122 return new double[2][1];
123 }
124 
125 @StaticFacet(museModel="computeModulesArguments", outputNames  = {"out"},
        outputSize = 4 )
126 @Compute
127 public  double[] computeModulesArguments(double f){
128     double[] outputs;
129 try{
130     if ((initialisation==0)||(computeValidity==0)){
131         testChangeOfInputParameters(f);
132     }
133     if (computeValidity>0)
134     {
135         jacobianValidity++;
136         computeValidity=0;
137         outputs = core.computeModulesArguments(f);
138     }
139     else
140     {
141         outputs=core.getOutputs();
142     }
143     return outputs;
144 }catch(java.lang.Exception ex){
145 }
```

```
146 return new double[4];
147 }
148
149 @JacobianFacet(museModel="computeModulesArguments")
150 @ComputeJacobian
151 public double[][] jacobianModulesArguments(double f){
152 try{
153     double[][] outputJacobian;
154     if ((initialisation==0)||(computeValidity==0)){
155         testChangeOfInputParameters(f);
156     }
157     if (computeValidity>0){
158         computeModulesArguments(f);
159     }
160     if (jacobianValidity>0)
161     {
162         jacobianValidity=0;
163         outputJacobian=core.jacobianModulesArguments(f);
164     }
165     else
166     {
167         outputJacobian=core.getOutputJacobian();
168     }
169     return outputJacobian;
170 }catch(java.lang.Exception ex){}
171 return new double[4][1];
172 }
173
174 @StaticFacet(museModel="computeRealAndImaginaryParts", outputNames  = {"out
    "}, outputSize = 4 )
175 @Compute
176 public  double[] computeRealAndImaginaryParts(double f){
177     double[] outputs;
178 try{
179     if ((initialisation==0)||(computeValidity==0)){
180         testChangeOfInputParameters(f);
181     }
182     if (computeValidity>0)
```

```
    {
        jacobianValidity++;
        computeValidity=0;
        outputs = core.computeRealAndImaginaryParts(f);
    }
    else
    {
        outputs=core.getOutputs();
    }
    return outputs;
}catch(java.lang.Exception ex){
}
return new double[4];
}

@JacobianFacet(museModel="computeRealAndImaginaryParts")
@ComputeJacobian
public double[][] jacobianRealAndImaginaryParts(double f){
try{
    double[][] outputJacobian;
    if ((initialisation==0)||(computeValidity==0)){
        testChangeOfInputParameters(f);
    }
    if (computeValidity>0){
        computeRealAndImaginaryParts(f);
    }
    if (jacobianValidity>0)
    {
        jacobianValidity=0;
        outputJacobian=core.jacobianRealAndImaginaryParts(f);
    }
    else
    {
        outputJacobian=core.getOutputJacobian();
    }
    return outputJacobian;
}catch(java.lang.Exception ex){}
return new double[4][1];
```

```
}

    public One_converter_wFilter_core getCore() {
        return core;
    }

}
```